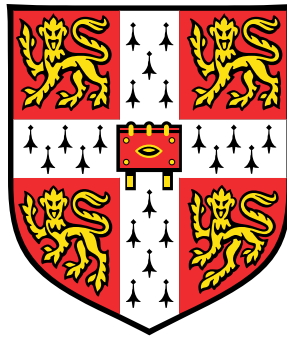


Post-inflationary Non-Gaussianities on the Cosmic Microwave Background



Shi Chun SU

Department of Applied Mathematics and Theoretical Physics

University of Cambridge

This dissertation is submitted for the degree of

Doctor of Philosophy

Trinity Hall

May 2015

This thesis is dedicated to my family for their love. It is such a fortune to have the freedom to make one's decision based on one's own interest. However, the opportunity does not come for free. When I was young, my parents devoted their lives to the family and sacrificed a lot. My siblings share the responsibility when they have grown up. As the youngest child in my family, I am so lucky to explore whatever I want. There are certainly plenty of challenges in life but I always feel so grateful for the selfless support from my family.

I would also like to dedicate this thesis to my supervisors – Eugene Lim and Paul Shellard. Eugene continuously guides and encourages me throughout the whole Ph.D. Paul gives me lots of advices and support. Without their supervision, some of the key work done in this thesis will not be possible. It is my great honor working with them.

Declaration

I declare that this dissertation is the result of my own work and contains no outcome of work done in collaboration, except where specifically indicated in the text. The contents are original and no parts have been submitted for consideration for any other qualification.

Shi Chun SU

May 2015

Acknowledgements

I would like to thank J. Fergusson for useful discussions and help with the bispectrum visualization as well as A. Kaliazin for computational support and technical advice. I would also like to thank D. Baumann, C. Bonvin, C. Fidler, D. Grin, B. Horn, W. Hu, Z. Huang, L. Hui, J. Lesgourgues, K. Nakao, G. Pettinari, C. Pitrou, T. Tram, M. LoVerde and W. Yi for advices and discussions on the researches I worked throughout the Ph.D. Moreover, I want to thank V. Assassi, T.-J. Chen, C. Lau, A. Lazanu, H. Lee, H. F. Gruetjen, M. M. Schmittfull and K. Yamamoto for sharing lots of wonderful times of Ph.D. with me. Especially, I am grateful for working on an interesting project [62] about the cosmic microwave background (CMB) B-mode polarization with D. Baumann and H. Lee.

The numerical simulations were implemented on the COSMOS supercomputer, part of the DiRAC HPC Facility which is funded by STFC and BIS.

Abstract

The cosmic microwave background (CMB) provides unprecedented details about the history of our universe and helps to establish the standard model in modern cosmology. With the ongoing and future CMB observations, higher precision can be achieved and novel windows will be opened for studying different phenomena. Non-Gaussianity is one of the most exciting effects which fascinate many cosmologists. While numerous alternative inflationary models predict detectable primordial non-Gaussianities generated during inflation, the single-field slow-roll inflation of the standard model is known to produce negligible non-Gaussianities. However, post-inflationary processes guarantee the generation of non-Gaussianities through the nonlinear evolution of our universe after inflation, regardless of the underlying inflationary theory. These non-Gaussianities not only may contaminate the potential primordial non-Gaussian signals, but also may offer independent tests for late-time physics (such as General Relativity). Therefore, it is of great interest to study them quantitatively.

In this thesis, we will study the post-inflationary non-Gaussianities in two main aspects. First, we calculate the CMB bispectrum imprinted by the 2nd-order perturbations during recombination. We carry out a numerical calculation including all the dominant effects at recombination and separate them consistently from the late-time effects. We find that the recombination bispectrum is subdominant compared to the ISW-lensing bispectrum. Although the effect will not be detectable for the Planck mission, its signal-to-noise is large enough that they present themselves as systematics. Thus, it has to be taken into account in future experiments. Second, we formulate the lensing, redshift and time-delay effects through the Boltzmann equation. The new formalism allows us to explicitly list out all the approximations implied in the canonical remapping approach. In particular, we quantify the correction of the CMB temperature power spectrum from the lens-lens couplings and confirm that the correction is small.

Table of contents

Table of contents	xi
List of figures	xv
List of tables	xix
Nomenclature	xx
1 Review of CMB Cosmology	1
2 Cosmological Perturbations and CMB Spectra	7
2.1 Coordinate System and Tetrad Basis	8
2.1.1 Coordinate System	8
2.1.2 Tetrad Basis	9
2.2 CMB Temperature and Polarization	11
2.2.1 Intensity Matrix	11
2.2.2 Stokes' Parameters	12
2.3 Governing Equations	13
2.3.1 Einstein Field Equations	13
2.3.2 Boltzmann Equation	14
2.4 Cosmology in Background Order	16
2.4.1 Friedmann–Lemaître–Robertson–Walker Metric	16
2.4.2 Λ CDM Cosmology	16
2.4.3 Friedmann Equations	17
2.5 Cosmological Perturbations in First Order	18
2.5.1 Einstein Field Equations	18
2.5.2 Boltzmann Equation	20
2.5.3 Adiabatic Initial Conditions	21

2.6	Statistics of CMB	22
2.6.1	CMB Power Spectrum	23
2.6.2	CMB Bispectrum	26
3	Cosmological Perturbations in Second Order	31
3.1	Second-order Einstein Field Equations	33
3.1.1	Gauge Choices	33
3.1.2	Multipole Decomposition of Stress-Energy Tensor	34
3.1.3	Einstein Field Equations	36
3.1.4	Continuity and Euler Equations	41
3.2	Second-order Boltzmann Equation	42
3.2.1	Liouville Operator	44
3.2.2	Collision Operator	48
3.2.3	Collision Terms for Baryons	50
3.2.4	Perturbed Optical Depth	51
3.2.5	Truncation Scheme for the Boltzmann Hierarchy	55
3.3	Numerical Implementation	55
3.3.1	Initial Conditions	56
3.3.2	Tight-coupling Approximation	58
3.3.3	Numerical Stability and Convergence	60
4	CMB Bispectrum during Recombination	65
4.1	Definition of CMB Temperature in Second Order	66
4.1.1	Brightness Temperature	67
4.1.2	Bolometric Temperature	67
4.2	Formulating Second-order Bispectrum	68
4.2.1	Second-order Line-of-sight Approach	68
4.2.2	Separation between Recombination and Late Time	69
4.2.3	Bispectrum from Second-order Perturbations	74
4.2.4	Quadratic Source Function with $m \neq 0$	79
4.3	Numerical Results	80
4.3.1	Numerical Implementation	80
4.3.2	Validation with Analytical Bispectrum	86
4.3.3	f_{NL} and Signal-to-noise	90
4.4	Conclusions and Discussion	92
5	Weak Lensing in Boltzmann Equation	93

5.1	Formalism	94
5.1.1	Lensing in Second Order	97
5.1.2	Lensing in Arbitrarily High Orders	101
5.1.3	Lensing as Dyson Series	108
5.1.4	Diagrammatic Approach	111
5.1.5	Extensions	113
5.2	Power Spectrum from Lens-lens Couplings	120
5.2.1	Diagrammatic Approach	120
5.2.2	Numerical Implementation	122
5.2.3	Other Approximations	128
5.3	Discussion and Conclusions	129
6	Discussion and Conclusions	131
6.1	Discussion	131
6.1.1	Spectral Distortions	131
6.1.2	Modified Gravity	132
6.1.3	Perturbed Optical Depth	132
6.1.4	Lensing in CMB Polarizations and Other Observables	132
6.1.5	Validation of Newtonian Approximation	133
6.2	Conclusions	133
	References	135
	Appendix A Glossary of Notations and Symbols	143
	Appendix B Table of Cosmological Parameters	149
	Appendix C Spin-weighted Spherical Harmonics	151
C.1	Properties of Spin-weighted Spherical Harmonics	151
C.2	Properties of Wigner 3-j Symbols	153
C.3	Decomposition of Spherical Harmonics	154
	Appendix D Perturbations of Tetrads and Ricci Rotation Coefficients	157
D.1	Perturbations of Tetrads	157
D.2	Perturbations of Ricci Rotation Coefficients	158

List of figures

1.1	The CMB temperature anisotropies seen by Planck [1].	2
2.1	The illustration of the pullback ϕ_λ from the physical manifold \mathcal{M}_1 onto the background manifold \mathcal{M}_0 . The dashed gray grids represent the tetrad bases. Due to the existing perturbations, the pulled-back tetrad bases on the background manifold do not align with the bases of the coordinate system (the misalignment is exaggerated in the graph).	10
2.2	The full-sky unlensed power spectra of the CMB temperature from our code (black line) and CAMB (dashed orange line) against ℓ . A perfect match is achieved. Our code uses Newtonian gauge while CAMB uses synchronous gauge.	25
3.1	The diagrammatic outline of relations between different perturbations. The corresponding evolution equations are shown in the brackets. The wavy lines denotes couplings through GR while the two headed arrow denotes the Compton scattering. We remark that the 1st-order perturbed optical depth ($\delta\tau$) is needed for the 2nd-order Compton scattering.	32
3.2	The graphs of transfer functions of the 1st-order differential optical depth $\delta\tau^{[I]}$ against the scale factor a for $k = 2 \times 10^{-5}\text{Mpc}^{-1}$ (upper panel) and $k = 0.045\text{Mpc}^{-1}$ (lower panel). Here, we ignore Helium atoms.	54
3.3	The graph of the absolute 2nd-order kernel of $\dot{\Psi}$ (solid line) against the scale factor a with $k_0 = 0.199\text{Mpc}^{-1}$, $k_1 = 0.2\text{Mpc}^{-1}$, $k_2 = 0.002\text{Mpc}^{-1}$ and $\hat{\mathbf{k}}_1 \cdot \hat{\mathbf{k}}_2 = -0.684$. The dashed line shows the absolute numerical difference in the constraint equation Eq. (3.28).	62
3.4	The graph of the absolute 2nd-order kernel of $\dot{\Psi}$ (solid line) against the scale factor a with $k_0 = 0.159\text{Mpc}^{-1}$, $k_1 = 0.2\text{Mpc}^{-1}$, $k_2 = 0.2\text{Mpc}^{-1}$ and $\hat{\mathbf{k}}_1 \cdot \hat{\mathbf{k}}_2 = -0.684$. The dashed line shows the absolute numerical difference in the constraint equation Eq. (3.28).	63

-
- 3.5 The graph of the absolute 2nd-order kernel of Ψ (solid line) against the scale factor a with $k_0 = 0.4\text{Mpc}^{-1}$, $k_1 = 0.2\text{Mpc}^{-1}$, $k_2 = 0.2\text{Mpc}^{-1}$ and $\hat{\mathbf{k}}_1 \cdot \hat{\mathbf{k}}_2 = 1$. The dashed line shows the absolute numerical difference in the constraint equation Eq. (3.28). 63
- 4.1 The graphs of the bispectra generated from the quadratic source function $S^{[1,1]}$ against ℓ for equilateral (upper) and squeezed (lower) limit. The curves correspond to different ℓ truncations of the multipoles $S_{\ell m}^{[1,1]}$. We can see that the convergence occurs when ℓ goes up to 10. 81
- 4.2 The 3D plot of the reduced bispectrum generated around recombination. The bispectrum is normalized by the coefficient $D(\ell_1, \ell_2, \ell_3)$ defined in Eq. (4.51) to remove an overall ℓ^{-4} scaling. The red regions represent positive values while the blue regions represent negative values of the recombination bispectrum. 84
- 4.3 The cross sections of the normalized reduced bispectrum in Fig. 4.2 with the conditions $\frac{1}{2}(\ell_1 + \ell_2 + \ell_3) = 400$ (upper), 1100 (middle) and 1600 (lower). 85
- 4.4 The recombination bispectrum (gray solid line) calculated numerically using Eq. (4.45) and the analytical bispectrum (black solid line) are plotted in the squeezed limit. We can see that they match with each other very well. Here, we measure the bispectrum in bolometric temperature which can be converted from the bispectrum in brightness temperature by Eq. (4.46). The ‘‘All L.T.’’ curve contains all the purely 2nd-order perturbations of the source function as shown in Eq. (4.10) while the ‘‘All Q.T.’’ curve contains all the cross products of two 1st-order perturbations of the source function as shown in Eq. (4.11). 87
- 4.5 The bispectra of the linear terms (L.T.) and quadratic terms (Q.T.) of the source function $S_{2\text{ND}}$ in squeezed limit are shown in the upper and lower panel respectively. 89
- 5.1 The diagrammatic illustration for the time-ordering of the nested integral in Eq. (5.37). The circle node indicates the source while the square nodes indicate the lenses. 105

-
- 5.2 The contributions on the temperature power spectrum from the residual diagrams of Column C and D containing lens-lens couplings in Table 5.4. The top and bottom panels show the corrections to the power spectrum from those diagrams in Column C and D respectively. In the top panel, the solid gray line corresponds to the diagram (1C) while the dashed line corresponds to the diagrams (2C) and (3C). Diagrams (2C) and (3C) have identical contributions and thus we sum them up. In the bottom panel, the solid gray line corresponds to the diagram (1D) while the dashed line corresponds to the diagram (2D). For both panels, the signs of contributions from the diagrams in Row $\langle \Theta^{[4]} \Theta^{[2]*} \rangle$ of Table 5.4, i.e. the dashed lines, are reversed to illustrate the cancellations. 126
- 5.3 The overall correction to the temperature power spectrum from the lens-lens couplings. 128

List of tables

4.1	The table of the effective f_{NLS} , F_{NLS} and S/N s of the local and equilateral templates correlated to the recombination bispectrum, as well as its total signal (auto-correlation). For ISW-lensing bispectrum, we found that its correlation with the recombination bispectrum is $\sim 30\%$. For ease of comparison, the F_{NL} quantities normalize the integrated bispectrum signal for any shape relative to the $f_{\text{NL}} = 1$ local model. We have used $\ell_{\text{max}} = 2000$ throughout.	90
4.2	The table for comparisons among the results from all the codes implementing the full recombination bispectrum.	91
5.1	The diagrams with their corresponding represented equations and their physical meanings. In the ‘‘Term’’ column, the first choice assumes Approximation 7 while the second one does not.	112
5.2	All the possible couplings of the weak lensing effects on the CMB anisotropies in the third, fourth and fifth orders. As an example, Eq. (5.62) demonstrates how to construct the formulae from the middle diagram in the first row of Table 5.2b.	114
5.3	The forbidden contractions for the lensing effects on the power spectrum. θ is the Heaviside step function. The Heaviside step functions come from replacing the integration $\int_{\eta_{\text{LSS}}}^{\eta_{N+1}} d\eta_N$ with $\int_{\eta_{\text{LSS}}}^{\eta_0} d\eta_N \theta(\eta_{N+1} - \eta_N)$	123
5.4	All the non-zero configurations for the temperature power spectrum from the next-to-leading order of the weak lensing effect. The dotted lines denote correlations while the arrows indicate the cancellations between some pairs of the diagrams.	124
A.1	Physical parameters and background quantities	143
A.2	Mathematical notations and functions	144
A.3	Notations for power spectra and bispectra	144

A.4	Coordinate-related notations and quantities	145
A.5	Perturbations	146
A.6	Quantities for EFEs and CMB photon	147
A.7	Liouville-related notations	148
A.8	Miscellaneous	148
B.1	The best-fit cosmological parameters are listed based on the Planck+WP dataset in [3]. For the primordial tensor modes, parameters come from the BICEP2's data in [2] with $n_t = 0$ and $k_* = 0.05/\text{Mpc}$. The definitions of these parameters can be found in Table 1 of [3]. As mentioned in [9], the tension between Planck and Bicep due to the tensor mode is mild. Thus, we do not re-fit the cosmological parameters using the data from the Planck and BICEP2 together.	149

Chapter 1

Review of CMB Cosmology

The origin of our universe is a question which we cannot but be lured into attempting to comprehend. In ancient time, answers to the question were descriptive and qualitative with various hypotheses. Although these answers provide innovative insights about the universe, it was hard to validate them due to the lack of observations available at that time. Until the last century, the technology became advanced enough to detect the distant signals from the sky. Different models of our universe can then be studied with experiments. After that, the study of universe thrives and the foundation of modern cosmology has been established.

In particular, after the discovery of the cosmic microwave background (CMB), cosmology has entered into an era with unprecedented precision. The CMB signals was imprinted on the sky due to the decoupling of photons from baryons when our universe was only about 380,000 years old. Even though the CMB photons traveled for 13.8 billion years before being captured by us, the contamination from foreground is acceptable. Thus, the information of the early universe contained in the CMB signals can be preserved and restored. By analyzing the CMB data, we are able to deduce the evolution history of our universe, the abundance of different components and the origin of the large-scale structures. The CMB temperature anisotropies observed by Planck is shown in Fig. 1.1.

The CMB data favour a model of universe which is almost perfectly homogeneous and isotropic with very tiny fluctuations at the early stage. Since the fluctuations are so small, the linear perturbation theory is usually sufficient for describing the dominant features of the fluctuations embedded on the CMB. Without the nonlinear evolutions, the calculation for the evolution of perturbations can be significantly simplified in the linear order. This facilitates our understanding of the early universe and the development of the standard model - Λ CDM (see [32, 105] for more details) in modern cosmology.

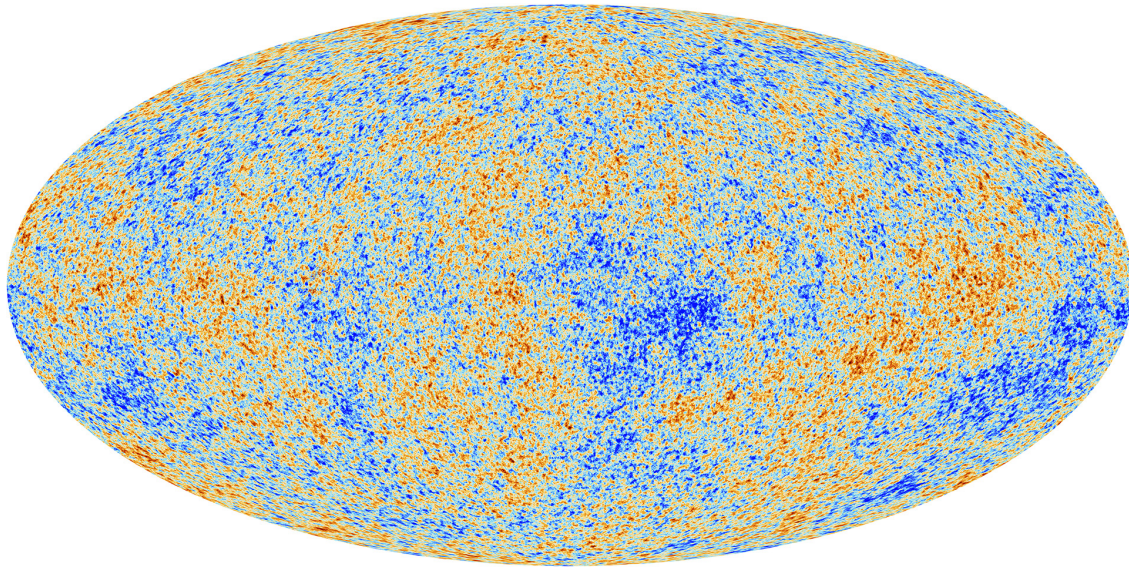


Figure 1.1 The CMB temperature anisotropies seen by Planck [1].

The idea of inflation is by far the most popular one to describe the very beginning of our universe. Not only it solves some puzzles in cosmology (e.g. flatness, homogeneity and isotropy of our universe), but it also explains the origin of the tiny perturbations as quantum fluctuations expanded to cosmological scales during inflation. Although the standard model stays consistent with current observations, it is crucial to explore alternative models and keep challenging the standard model with further observations. Hence, numerous inflationary models containing fruitful physics are proposed in literature. Identifying our universe among these possibilities becomes essential. In addition, new properties discovered about the inflationary era may deepen our understanding of fundamental physics.

Depending on the inflationary model under consideration, various distinguishable features different from the standard model can be generated. In particular, many alternative inflationary models predict significant primordial non-Gaussianities which may be detected by the current and future CMB experiments through the CMB bispectra. Comprehensive studies have been done to calculate the shapes of the bispectra from different inflationary models. These shapes can be constrained with the observational data. If any primordial non-Gaussianities are detected, it will provide us further clues about the mechanism of inflation. For example, single-field inflationary models do not produce significant non-Gaussianities of the local type [72]. A detection of the local-type bispectrum can rule out all the single-field inflationary models.

However, non-Gaussianities can also be generated through the nonlinear evolution of some physical mechanisms after inflation. Nonlinear evolution is responsible to the complex

structure formation in the late-time universe. For instance, the nonlinearity of General Relativity (GR) guarantees post-inflationary non-Gaussianities. A rough estimation expects that these non-Gaussianities should have a nonlinear coupling constant f_{NL} of order 1 at recombination. Thus, these post-inflationary non-Gaussianities can potentially contaminate the primordial non-Gaussianities from inflation. It is of importance to study the nonlinear evolutions of the cosmological perturbations quantitatively. Moreover, post-inflationary non-Gaussianities can be used as an independent test for the underlying mechanisms (e.g. GR) on cosmological scales.

One of the ways to probe non-Gaussianities is to measure the CMB bispectra. While power spectra are mainly dominated by Gaussian perturbations, bispectra vanish statistically with perfectly Gaussian perturbations. This property makes bispectra an ideal tool for detecting non-Gaussianities¹. Non-Gaussianities in the CMB bispectra can provide us extra information about the Universe. With the improving sensitivities from the current and future observations [6, 8, 16], a comprehensive study of non-Gaussianities from different mechanisms becomes necessary. In this thesis, we will focus on two different types of non-Gaussianities generated after inflation. The first one comes from the 2nd-order perturbations imprinted on the CMB at recombination while the second one is sourced by the nonlinear distortions of the CMB anisotropies due to the late-time metric perturbations, e.g. CMB lensing effect.

Calculating the CMB bispectrum from the 2nd-order perturbations at recombination is not a new problem. There are already some attempts to estimate the CMB bispectrum in literature, such as [57, 75, 87, 94]. However, most of these studies consider only some specific limits of bispectrum and particular effects². That is, a thorough calculation including the full bispectrum and all the effects at recombination is desired. More seriously, the signal-to-noises³ for detection of the amplitude of the intrinsic bispectrum claimed by different work vary within a broad range – from order of 0.1 to 10. A conclusive and precise value is yet to be obtained and a systematic calculation should be carried out to constrain the effect for future CMB experiments. This is one of the two main objectives of this thesis and the result has been published in [100]. There are other teams aiming at the similar goal but working with different and independent approaches, e.g. [52, 82].

¹Nevertheless, it is possible to generate non-Gaussianities without significant bispectra [24]. In these cases, trispectra may be used to study the non-Gaussianities.

²The exception is [87] but its calculated signal-to-noise appears to be significantly larger than those calculated afterwards.

³These signal-to-noises are calculated for cosmic-variance-limited data, assuming no primordial non-Gaussianities.

We can split the problem into two parts: analytical and numerical part. In the analytical part, we derive all the evolution equations governing the 2nd-order perturbations and formulate the CMB bispectrum for the 2nd-order perturbations imprinted at recombination. Expanding the perturbations up to 2nd order is quite straightforward but there are several techniques we need. First, we will work with both the global coordinate system on the background manifold and the tetrad basis in the tangent planes. We have to develop a transformation between them up to 2nd order. Second, to obtain the multipoles in the Boltzmann equation, we have to decompose a product of two spherical harmonics. The decomposition can be achieved by exploiting the Wigner 3-j symbols. Third, we will need to derive the evolution equation of the optical depth to 1st order.

The second part is the numerical calculation. To obtain the full bispectrum and capture all the effects at recombination, numerical implementation is inevitable and it turns out to be the most challenging part of the problem. First, the 2nd-order Einstein field equations (EFEs) are numerically unstable. It is because there exists some pairs of large terms canceling with each other and the residuals are a few orders of magnitude smaller. This undermines the numerical precisions achievable. By combining the EFEs, we can mitigate the numerical instability. The result can be verified by using the constraint equations of EFEs. Second, the original quadratic source function in 2nd order requires multipoles with infinitely high ℓ and fails to separate the effects at recombination from the late-time effects consistently. We will show that these two issues can be solved by performing integration by parts to the line-of-sight (LOS) integration. We validate the result by comparing with the analytical solution of the squeezed-limit bispectrum.

Another post-inflationary non-Gaussian effect we will study is the distortions of the CMB anisotropies from the late-time metric perturbations, which include lensing, redshift and time-delay effects. In particular, CMB lensing is the dominant effect among these distortions and will be our main focus. CMB lensing was first considered in 1987 [18] and, since then (for a review, see [67]) its contributions to the power spectra [23, 46, 89, 109], bispectra [39, 46, 69] and trispectra [27, 47] of the CMB temperature and polarizations have been studied. Recently, the first detection of the CMB lensing was achieved by cross-correlating the lensing potential reconstructed by the Wilkinson Microwave Anisotropy Probe (WMAP) data and large scale structure surveys (as suggested in [42]) [41, 98]. The detection of the power spectrum of the lensing potential was first obtained with the Atacama Cosmology Telescope (ACT) data [31] and then with the South Pole Telescope (SPT) data [102]. The first full-sky map of the lensing potential was reconstructed by the Planck data [4] and the significance of the detection has been boosted to larger than 25σ . Planck also

detected the ISW-lensing bispectrum generated by the non-Gaussian lensed CMB temperature fluctuations with significance of 2.6σ [6]. Finally, the B-mode polarization induced by lensing was detected with the SPTpol data [40] at 7.7σ significance. Driven by these sophisticated experiments, the study of the CMB lensing has entered a new era with unprecedented precision.

Furthermore, since its major contribution comes from lenses at low redshifts ($z \lesssim 10$), the lensing effect is very sensitive to the late-time evolution of the universe. By using the non-Gaussian properties of the lensing effect on the CMB temperature and polarizations, different estimators [43, 44, 56, 77] were proposed to reconstruct the lensing power spectrum from the CMB data. Measuring the lensing power spectrum with high angular resolution and high sensitivity imposes constraints [55, 64] on the neutrino masses m_ν with $\sigma(m_\nu)$ as small as 0.035 eV [64], which are much tighter compared to the one using the CMB power spectra alone and have fewer biasing issues compared to the constraints from the large-scale structures. The lensing power spectrum can also break the degeneracy between the neutrino masses and the equation of state parameter ω of the dark energy [55]. The cross-correlations between the reconstructed lensing potential and other late-time observations⁴ have been analyzed through various experiments [4, 5, 19, 45, 96]. These cross-correlations allow us to constrain the dynamics of the dark matter and the dark energy [48, 92].

In view of these applications of the CMB lensing, it is clear that an accurate computation of the lensing effect is required. In particular, it remains to be articulated the *approximations* involved in the usual lensing calculation. For example, in the canonical approach [23, 46], the lensed CMB temperature anisotropies $\tilde{\Theta}$ are expressed in terms of the unlensed CMB temperature anisotropies Θ in the remapping. The usual derivation uses a perturbed geodesic and employs some implicit approximations. While there are assessments about the fidelity of the corrections of the remapping approach especially in high orders [26, 33, 44], keeping correction terms consistently in high orders is non-trivial [61, 95] and a *systematic* study in arbitrarily high orders has not been undertaken. The main goal of our study is to derive the CMB lensing (as well as redshift and time-delay) through the Liouville (free-streaming) part of the Boltzmann equation.

The key step to derive lensing, redshift and time-delay effects through the Boltzmann equation up to arbitrarily high order is to treat these effects as higher-order actions on the CMB anisotropies. The effects can be expressed as a nested integral in the line-of-sight approach. The derivation using the Boltzmann equation allows us to explicitly list out all the

⁴For example, the integrated Sachs-Wolfe (ISW) effect, the Sunyaev-Zeldovich (SZ) effect, the Cosmic Infrared Background (CIB), galaxies and quasars.

approximations implied in the canonical remapping approach. In particular, we find some new approximations which have not been identified previously in literature. We can then assess the significance of these approximations and justify the robustness of the remapping approach. To facilitate the calculation, we develop a diagrammatic approach to keep track of the couplings of different effects in arbitrarily high orders.

This thesis is organized as follows. We review the linear cosmological perturbations and their impact on CMB in Chapter 2. We derive the Boltzmann equation and EFEs up to 2nd order and present the details about solving the 2nd-order perturbations numerically in Chapter 3. In Chapter 4, we single out the effects at recombination from the late-time effects and perform the numerical calculation for the full bispectrum at recombination. In Chapter 5, we formulate the lensing, redshift and time-delay effects through the Boltzmann equation and study the effect of lens-lens couplings on the CMB power spectrum. We discuss some potential extensions of the work in this thesis and draw the conclusion in Chapter 6. Because there are many notations and symbols used, we list out all of them in Appendix A for clarification. A table of cosmological parameters used in this thesis is shown in Appendix B. Some useful definitions and formulae of the spin-weighted spherical harmonics are presented in Appendix C. Details of the perturbations of tetrads and Ricci rotation coefficients up to 2nd order can be found in Appendix D.

Chapter 2

Cosmological Perturbations and CMB Spectra

Since the cosmic microwave background (CMB) was discovered in 1964 [79], the study of Cosmology has entered an era with unprecedentedly high precision. Properties (such as flatness, homogeneity and isotropy) of the CMB signals provide clues to the development of the big bang theory with an inflationary epoch. The homogeneity and isotropy, in particular, also support the model of a uniformly-distributed universe at early time with tiny fluctuations as seeds for the late-time structure formations. These fluctuations were imprinted in the CMB anisotropies when photons decoupled with baryons during recombination. By studying the power spectra of these CMB anisotropies obtained from observations (such as COBE, WMAP and Planck), we ought to develop the standard model in Cosmology which consists of baryon ($\sim 5\%$), dark matter ($\sim 27\%$) and dark energy ($\sim 68\%$)¹ as the main components of our universe.

In this chapter, we review the cosmological perturbation theory in the CMB study up to 1st order. We will extend the study to 2nd-order perturbations in Chapter 3 and their contribution to the CMB bispectrum at recombination in Chapter 4. First, we introduce the coordinate system and the tetrad basis used throughout this thesis in Section 2.1. Then, we define the CMB temperature and polarizations in Section 2.2. In Section 2.3, we review the governing equations of the CMB study – the Einstein field equations (EFEs) and the Boltzmann equation. We derive the background- and 1st-order governing equations for the evolution of our universe in Section 2.4 and 2.5 respectively. Finally, we discuss how information from the universe can be extracted through power spectra and bispectra of the

¹The values are based on the CMB data combination *Planck+WP* in [3].

CMB anisotropies in Section 2.6.

2.1 Coordinate System and Tetrad Basis

In this section, we construct the coordinate system for the background manifold and the tetrad basis for the tangent planes used in this thesis. The construction allows us to expand the perturbations consistently to any orders.

2.1.1 Coordinate System

The homogeneity and isotropy of the universe allow us to map the physical manifold onto a background manifold equipped with a Friedmann metric. By assuming a flat universe, we choose the coordinate system $\{x^A\} = \{\eta, x^I\}$ for $A = 0, 1, 2, 3$ and $I = 1, 2, 3$ such that

$$\begin{aligned} ds^2 &= g_{\mu\nu} dx^\mu dx^\nu \\ &= a^2(\eta) \left\{ -(1 + 2\Phi) d\eta^2 + 2\mathcal{B}_I dx^I d\eta + [(1 - 2\Psi)\delta_{IJ} + 2\mathcal{H}_{IJ}] dx^I dx^J \right\}, \end{aligned} \quad (2.1)$$

where $a(\eta)$ is the scale factor and Φ , Ψ , \mathcal{B}_I and \mathcal{H}_{IJ} are metric perturbations as functions of x^A . In this thesis, capital Roman indices (A, B, C, \dots) label the chosen coordinate system in the background manifold while Greek indices (μ, ν, ρ, \dots) represent abstract indices². All the metric perturbations in Eq. (2.1) can be considered as fields living on the background manifold. Moreover, we can further decompose \mathcal{B}_I and \mathcal{H}_{IJ} by using the scalar-vector-tensor (SVT) decomposition such that

$$\mathcal{B}_I = \partial_I \mathcal{B} + \mathcal{B}_I, \quad \mathcal{H}_{IJ} = \mathcal{H}_{IJ} + \partial_{(I} \mathcal{E}_{J)} + \partial_I \partial_J \mathcal{E}, \quad (2.2)$$

where $2\partial_{(I} \mathcal{E}_{J)} \equiv \partial_I \mathcal{E}_J + \partial_J \mathcal{E}_I$ and $\partial^I \mathcal{B}_I = \partial^I \mathcal{E}_I = \partial^I \mathcal{H}_{IJ} = 0$ and $\mathcal{H}^I_I = 0$ with $\partial_I \equiv \partial/\partial x^I$.

With the assumption of a flat Friedmann metric in the background order, the equations above hold in general and can be expanded into perturbations of different orders in the following manner

$$\mathcal{A} = \mathcal{A}^{[I]} + \frac{\mathcal{A}^{[II]}}{2!} + \frac{\mathcal{A}^{[III]}}{3!} + \dots, \quad (2.3)$$

²A more familiar notation would be to write the metric in Eq. (2.1) as $g_{AB} dx^A dx^B$. That is, the indices A and B do double duty as coordinate labels and abstract indices.

where the Roman numbers inside the square brackets of the superscripts denote the orders of perturbations.

2.1.2 Tetrad Basis

At each point on the physical manifold, we construct the tangent basis to decompose the photon momenta. It is convenient to introduce the tetrad fields $\hat{\mathbf{e}}_a$ which satisfy the orthonormality conditions

$$\begin{aligned}\hat{\mathbf{e}}_a \cdot \hat{\mathbf{e}}_b &\equiv g_{\mu\nu} e_a^\mu e_b^\nu = \eta_{ab}, \\ \hat{\mathbf{e}}^a \cdot \hat{\mathbf{e}}^b &\equiv g^{\mu\nu} e^a_\mu e^b_\nu = \eta^{ab},\end{aligned}\tag{2.4}$$

where $\eta_{ab} \equiv \text{diag}(-1, 1, 1, 1)$ is the Minkowski metric, and indices a and b are equal to 0 to 3 labeling the four tetrad vectors and forms. Since photons have null 4-momenta ($p^\mu p_\mu = 0$), their momenta can be written as

$$\mathbf{p} = p^0(\hat{\mathbf{e}}_0 + \hat{\mathbf{n}}),\tag{2.5}$$

where p^0 is the photon energy measured by an observer with the velocity $\hat{\mathbf{e}}_0$ and $\hat{\mathbf{n}}$ is a spacelike vector on the hypersurface ‘‘screen’’ denoting the direction of the photon as seen by the observer, such that $n_\mu e_0^\mu = 0$ and $n^\mu n_\mu = 1$. Furthermore, it is useful to define the screen projector

$$S_{\mu\nu}(\hat{\mathbf{e}}_0, \mathbf{p}) \equiv g_{\mu\nu} + e^0_\mu e^0_\nu - n_\mu n_\nu.\tag{2.6}$$

By foliating spacetime into hypersurfaces threaded through by the orbit defined by the observer’s velocity $\hat{\mathbf{e}}_0$, we can describe radiations by a screen-projected rank-2 tensor – the intensity matrix which lives on these hypersurfaces. We will discuss the intensity matrix in detail in Section 2.2.1.

We note that the tetrad fields $\hat{\mathbf{e}}_a$ lie on the physical manifold. Thus, we have to pull them back onto the background manifold in order to study the Boltzmann equation on the background manifold. This is achieved [21] through the pullback ϕ^* with a gauge field ξ defined by

$$\xi \hat{\mathbf{e}}_a \equiv \lim_{\lambda \rightarrow 1} \phi_{\lambda, \xi}^*(\hat{\mathbf{e}}_a) = \lim_{\lambda \rightarrow 1} \sum_{N=0}^{\infty} \frac{\lambda^N}{N!} \mathcal{L}_\xi^N \hat{\mathbf{e}}_a,\tag{2.7}$$

where λ denotes the foliations \mathcal{M}_λ of an embedding (4+1)-dimensional manifold $\mathcal{N} =$

$\mathcal{M} \times [0, 1]^3$ and \mathcal{L} is the Lie derivative. The pulled-back tetrads ${}_{\xi}\hat{\mathbf{e}}_a$ lie on the background manifold. Using the following natural background basis for vectors and forms on the background manifold

$$\bar{\mathbf{e}}_a = \frac{1}{a(\eta)} \frac{\partial}{\partial x^A}, \quad \bar{\mathbf{e}}^a = a(\eta) dx^A, \quad (2.8)$$

we can express the tetrads in the natural background basis

$${}_{\xi}\hat{\mathbf{e}}_a = {}_{\xi}X_a{}^b \bar{\mathbf{e}}_b, \quad {}_{\xi}\hat{\mathbf{e}}^a = {}_{\xi}Y_b{}^a \bar{\mathbf{e}}^b, \quad (2.9)$$

where the coefficients can be expanded into perturbations as

$${}_{\xi}X_{ab} \equiv \sum_{N=0}^{\infty} \frac{1}{N!} {}_{\xi}X_{ab}^{[N]}, \quad {}_{\xi}Y_{ab} \equiv \sum_{N=0}^{\infty} \frac{1}{N!} {}_{\xi}Y_{ab}^{[N]}. \quad (2.10)$$

After fixing the residual freedoms of the transformation, we can determine ${}_{\xi}X_{ab}^{[N]}$ and ${}_{\xi}Y_{ab}^{[N]}$ order by order. The details and the coefficients in 1st and 2nd order are shown in Appendix D.1. In Fig. 2.1, we illustrate the pullback of tetrad bases onto the background manifold \mathcal{M}_0 .

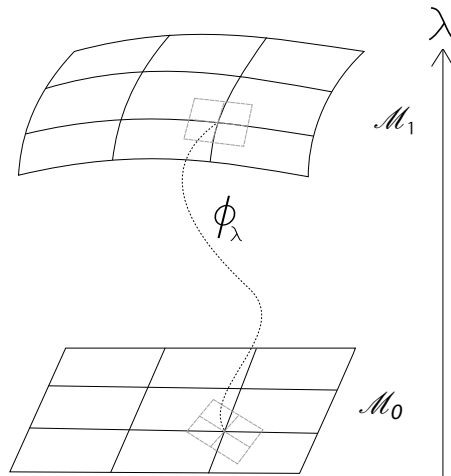


Figure 2.1 The illustration of the pullback ϕ_λ from the physical manifold \mathcal{M}_1 onto the background manifold \mathcal{M}_0 . The dashed gray grids represent the tetrad bases. Due to the existing perturbations, the pulled-back tetrad bases on the background manifold do not align with the bases of the coordinate system (the misalignment is exaggerated in the graph).

³We define the background manifold as \mathcal{M}_0 and the physical manifold as \mathcal{M}_1 with $\lambda \in [0, 1]$.

2.2 CMB Temperature and Polarization

Here, we define the intensity matrix which describes the intensity and the polarizations of the CMB photons.

2.2.1 Intensity Matrix

To encode all the information about the intensity and the polarization of the CMB photons, we define the screen-projected intensity matrix $\mathcal{P}_{\mu\nu}(x^A, p^a)$ which satisfies⁴

$$e_0^\mu \mathcal{P}_{\mu\nu}(x^A, p^a) = n^\mu \mathcal{P}_{\mu\nu}(x^A, p^a) = p^\mu \mathcal{P}_{\mu\nu}(x^A, p^a) = 0. \quad (2.11)$$

The intensity matrix of the CMB radiation can be decomposed into

$$\mathcal{P}_{\mu\nu} = \frac{1}{2} \mathcal{I} S_{\mu\nu} + \mathcal{P}_{\mu\nu}, \quad (2.12)$$

where \mathcal{I} denotes the photon intensity and the symmetric traceless polarization tensor $\mathcal{P}_{\mu\nu}$ encodes the linear polarizations of the CMB photons. Here, we ignore the circular polarization because it is not induced by Compton scattering and thus is usually neglected in the CMB studies. The polarization tensor can be further decomposed into two scalar fields [67] – E-mode \mathcal{P}_E and B-mode \mathcal{P}_B , i.e.

$$\mathcal{P}_{\mu\nu} = \tilde{\nabla}_{\langle\mu} \tilde{\nabla}_{\nu\rangle} \mathcal{P}_E + \varepsilon^\gamma_{(\mu} \tilde{\nabla}_{\gamma)} \tilde{\nabla}_{\nu} \mathcal{P}_B, \quad (2.13)$$

where $\tilde{\nabla}_\mu \equiv S_\mu{}^\nu \nabla_\nu$ is the screen-projected covariant derivative, (\dots) denotes the symmetric part, $\langle \dots \rangle$ denotes the symmetric traceless part and $\varepsilon^{\mu\nu} \equiv -i(e'^\mu_- e'^\nu_+ - e'^\nu_- e'^\mu_+)/2$ with $\mathbf{e}'_\pm \equiv \hat{\mathbf{e}}'_x \pm i\hat{\mathbf{e}}'_y$ ⁵.

The normalized energy-integrated photon intensity and polarization tensor are defined as

$$\hat{I}(x^A, \hat{\mathbf{n}}) \equiv 1 + \frac{1}{2\pi^2 \bar{I}(\eta)} \int \mathcal{I}(x^A, p^0, \hat{\mathbf{n}}) (p^0)^3 dp^0, \quad (2.14)$$

$$\hat{\mathcal{P}}_{\mu\nu}(x^A, \hat{\mathbf{n}}) \equiv \frac{1}{2\pi^2 \bar{I}(\eta)} \int \mathcal{P}_{\mu\nu}(x^A, p^0, \hat{\mathbf{n}}) (p^0)^3 dp^0, \quad (2.15)$$

⁴For details about how to construct the intensity matrix, see [101].

⁵ $\hat{\mathbf{e}}'_x$ and $\hat{\mathbf{e}}'_y$, which are orthogonal to each other, lie on the plane perpendicular to the direction $\hat{\mathbf{n}}$ of the light path and the observer's velocity $\hat{\mathbf{e}}_0$.

where

$$\bar{I}(\eta) \equiv \frac{1}{2\pi^2} \int \bar{\mathcal{I}}(\eta, p^0) (p^0)^3 dp^0, \quad (2.16)$$

with $\bar{\mathcal{I}}(\eta, p^0)$ as the homogeneous and isotropic black-body spectrum in the background order. Up to 1st order, the CMB temperature can be related to the photon intensity by

$$\hat{I}(x^A, \hat{\mathbf{n}}) = 1 + 4\Theta(x^A, \hat{\mathbf{n}}), \quad (2.17)$$

where $\Theta \equiv (T - \bar{T})/\bar{T}$ with the background CMB temperature \bar{T} . More details on defining the CMB temperature can be found in Section 4.1.

2.2.2 Stokes' Parameters

We define the normalized energy-integrated Stokes' parameters \hat{Q} and \hat{U} such that

$$\begin{aligned} (\hat{Q} + i\hat{U})(\hat{\mathbf{n}}) &\equiv e'^a_+ e'^b_+ \hat{P}_{ab}(\hat{\mathbf{n}}), \\ (\hat{Q} - i\hat{U})(\hat{\mathbf{n}}) &\equiv e'^a_- e'^b_- \hat{P}_{ab}(\hat{\mathbf{n}}), \end{aligned} \quad (2.18)$$

where \mathbf{e}'_{\pm} are defined below Eq. (2.13)⁶. We can decompose the Stokes' parameters into spin-2 spherical harmonics

$$(\hat{Q} \pm i\hat{U})(\hat{\mathbf{n}}) = \sum_{\ell m} a_{\pm 2, \ell m} {}_{\pm 2}Y_{\ell m}(\hat{\mathbf{n}}), \quad (2.19)$$

where the spin-weighted spherical harmonics ${}_s Y_{\ell m}$ s are defined in Appendix C.1. By acting the raising ($\bar{\partial}$) and lowering ($\bar{\partial}$) operators⁷ twice and making use of Eq. (C.7) and Eq. (C.8), the decompositions become

$$\begin{aligned} \bar{\partial}^2(\hat{Q} + i\hat{U})(\hat{\mathbf{n}}) &= \sum_{\ell m} \sqrt{\frac{(\ell+2)!}{(\ell-2)!}} a_{2, \ell m} Y_{\ell m}(\hat{\mathbf{n}}), \\ \bar{\partial}^2(\hat{Q} - i\hat{U})(\hat{\mathbf{n}}) &= \sum_{\ell m} \sqrt{\frac{(\ell+2)!}{(\ell-2)!}} a_{-2, \ell m} Y_{\ell m}(\hat{\mathbf{n}}). \end{aligned} \quad (2.20)$$

⁶We remark that \mathbf{e}'_x and \mathbf{e}'_y are not the same as $\bar{\mathbf{e}}_x$ and $\bar{\mathbf{e}}_y$ in Eq. (C.25). In this work, we choose $\bar{\mathbf{e}}_x$ and $\bar{\mathbf{e}}_y$ to be orthogonal to the wave vector \mathbf{k} of the 2nd-order perturbations.

⁷The raising and lowering operators are defined in Eq. (C.5) and (C.6) respectively.

The multipoles of the normalized energy-integrated \hat{E} -mode and \hat{B} -mode polarizations are defined

$$a_{\hat{E},\ell m} \equiv -\frac{1}{2}(a_{2,\ell m} + a_{-2,\ell m}), \quad a_{\hat{B},\ell m} \equiv \frac{i}{2}(a_{2,\ell m} - a_{-2,\ell m}). \quad (2.21)$$

One of the advantages to decompose the CMB polarizations into E - and B -mode is that scalar perturbations do not produce B -mode polarization [54, 108]. Thus, the B -mode polarization is a crucial probe for primordial gravitational waves⁸.

2.3 Governing Equations

In this section, we review the governing equations which are essential in studying CMB – the Boltzmann equation and the EFEs. In Section 2.4 and 2.5, we will expand the perturbations to establish the evolution equations in background and 1st order respectively. Furthermore, we will derive the 2nd-order Boltzmann equation and EFEs in Chapter 3.

2.3.1 Einstein Field Equations

To derive the governing equations, we need the EFEs

$$G_{\mu\nu} + \Lambda g_{\mu\nu} = \kappa T_{\mu\nu}, \quad (2.22)$$

where $G_{\mu\nu}$ is the Einstein tensor, Λ is the cosmological constant, $g_{\mu\nu}$ is the metric tensor, $T_{\mu\nu}$ is the stress-energy tensor and $\kappa \equiv 8\pi G/c^4$ with Newton's gravitational constant G and the speed of light c . We set the gravitational constant and the speed of light as unity throughout this thesis. Moreover, the Einstein tensor is defined as

$$G_{\mu\nu} \equiv R_{\mu\nu} - \frac{R}{2}g_{\mu\nu}, \quad (2.23)$$

where the Ricci scalar $R \equiv g^{\mu\nu}R_{\mu\nu}$ and the Ricci tensor⁹

$$R_{AB} \equiv \Gamma_{AB,C}^C - \Gamma_{AC,B}^C + \Gamma_{DC}^C \Gamma_{AB}^B - \Gamma_{DB}^C \Gamma_{AC}^D, \quad (2.24)$$

⁸We remark that vector perturbations generate B -mode polarization as well but the power spectrum produced is expected to be distinguishable from that of primordial gravitational waves.

⁹In this thesis, we use Greek letters for abstract indices and Roman alphabets for coordinates of the background Manifold.

with the Christoffel symbols

$$\Gamma_{AB}^C \equiv \frac{1}{2} g^{CD} [g_{AD,B} + g_{BD,A} - g_{AB,D}]. \quad (2.25)$$

The commas in subscripts denote partial derivatives such that $g_{AB,C} \equiv \partial g_{AB} / \partial x^C$. In general, the stress-energy tensor for a fluid can be expressed as

$$T_{\mu\nu} = \rho u_\mu u_\nu + \mathcal{P}(g_{\mu\nu} + u_\mu u_\nu) + \pi_{\mu\nu}, \quad (2.26)$$

where ρ and \mathcal{P} are the energy density and the pressure of the fluid respectively, u_μ is the fluid velocity, and $\pi_{\mu\nu}$ is the anisotropic stress. The velocity and the anisotropic stress of fluids are defined such that

$$u^\mu = \frac{dx^\mu}{ds}, \quad u^\mu u_\mu = -1, \quad u^\nu \pi_{\mu\nu} = \pi_\mu{}^\mu = 0, \quad (2.27)$$

where the proper distance s is an affine parameter. Under the chosen coordinate system of the background manifold specified in Eq. (2.1), we can apply the SVT decomposition on spatial components u_I and π_{IJ} so that

$$u_I \equiv \frac{1}{a(\eta)} (\partial_I v + v_I), \quad (2.28)$$

$$\pi_{IJ} \equiv \bar{\rho} a(\eta)^2 \left[\sigma_{I,J} - \frac{1}{3} \delta_{IJ} \sigma_{K,K} + \frac{1}{2} (\sigma_{I,J} + \sigma_{J,I}) + \sigma_{IJ} \right]. \quad (2.29)$$

where the vector modes (v_I and σ_I) and the tensor modes (σ_{IJ}) satisfy

$$\partial^I v_I = 0, \quad \partial^I \sigma_{IJ} = 0, \quad \sigma^I{}_I = 0. \quad (2.30)$$

Because of the Bianchi identity, we have the conservation of energy and momentum

$$\nabla^\mu T_{\mu\nu} = 0, \quad (2.31)$$

where ∇ is the covariant derivative.

2.3.2 Boltzmann Equation

To formulate the Boltzmann equation, we stay with the tetrad basis (denoted by indices a, b, c, \dots) and elaborate all the relevant equations onto the background manifold as what we

have done for the EFEs. The Boltzmann equation consists of two operators, the Liouville operator \mathcal{L} describing the free-streaming of photons and the collision operator \mathcal{C} describing Compton scattering. That is,

$$\mathcal{L}[\mathcal{P}_{ab}(x^A, p^0, \hat{\mathbf{n}})] = \mathcal{C}_{ab}(x^A, p^0, \hat{\mathbf{n}}), \quad (2.32)$$

where we have switched to the tetrad basis via

$$\mathcal{P}_{ab} = \mathcal{P}_{\mu\nu} e_a^\mu e_b^\nu, \quad \mathcal{C}_{ab} = \mathcal{C}_{\mu\nu} e_a^\mu e_b^\nu, \quad S_{ab} = S_{\mu\nu} e_a^\mu e_b^\nu. \quad (2.33)$$

We remark that the Boltzmann equation as a whole is gauge-invariant.

We begin with the Liouville operator, which is defined as

$$\mathcal{L} \equiv S_a^c S_b^d \frac{d}{ds} = S_a^c S_b^d \left[p^A \nabla_A + \frac{dp^e}{ds} \partial_{p^e} \right], \quad (2.34)$$

where the screen projector S_a^b is defined in Eq. (2.6), ∇_A is the covariant derivative with respect to x^A , $\partial_{p^e} \equiv \partial/\partial p^e$ and $p^A \equiv dx^A/ds$. The covariant derivative acting on the intensity matrix can be expanded into

$$\nabla_A \mathcal{P}_{cd} = \partial_A \mathcal{P}_{cd} - e_c^D e^f{}_B \Gamma_{DA}^B \mathcal{P}_{fd} - e_d^D e^f{}_B \Gamma_{DA}^B \mathcal{P}_{cf}, \quad (2.35)$$

where the Christoffel symbols Γ_{AB}^C are defined in Eq. (2.25) and coefficients e_a^A are shown in Appendix D.1. In this thesis, we use the conformal time η instead of the proper distance s . We can do so by multiplying Eq. (2.32) with the Jacobian $ds/d\eta$. Linearity of the Liouville operator preserves the decomposition of \mathcal{P}_{ab} in Eq. (2.12), i.e.

$$\mathcal{L}[\mathcal{P}_{ab}] = \frac{1}{2} \mathcal{L}[\mathcal{I}] S_{ab} + \mathcal{L}[\mathcal{P}_{ab}]. \quad (2.36)$$

That means we can write down the evolution equations of the intensity and polarizations of photons separately¹⁰.

To elaborate the Boltzmann equation, we need to know the photon trajectory, which is given by the geodesic equation

$$\frac{dp^a}{ds} + \omega_b^a{}_c p^b p^c = 0, \quad (2.37)$$

¹⁰However, the equations are coupled through Compton scattering.

where the Ricci rotation coefficients are defined as

$$\omega_b^a{}_c \equiv e^a{}_\mu e_b{}^\nu \nabla_\nu e_c{}^\mu = \Gamma_{JK}^I e_b{}^K e_c{}^J e^a{}_I + e_b{}^I e^a{}_J \partial_I e_c{}^J, \quad (2.38)$$

which are determined completely by the metric g_{AB} and the tetrads e_a^A . The perturbations of the Ricci rotation coefficients in 1st and 2nd order can be found in Appendix D.2. Meanwhile, the momentum p^A can be expressed in the tetrad basis

$$p^A = p^a e_a^A. \quad (2.39)$$

2.4 Cosmology in Background Order

Because of the homogeneity and isotropy, the evolution of our universe in background order is determined by the scale factor $a(\eta)$, which quantifies the expansion of our universe and depends on the abundances of different components.

2.4.1 Friedmann–Lemaître–Robertson–Walker Metric

The homogeneity and isotropy of our universe suggest that the background-order spacetime has a Friedmann–Lemaître–Robertson–Walker (FLRW) metric, i.e.

$$ds^2 = \bar{g}_{\mu\nu} dx^\mu dx^\nu = a^2(\eta) \left[-d\eta^2 + \frac{dr^2}{1-kr^2} + r^2 d\Omega^2 \right], \quad (2.40)$$

where the Greek letters label numbers from 0 to 3, $\bar{g}_{\mu\nu}$ is the background-order metric tensor¹¹, $a(\eta)$ is the scale factor with the conformal time η , $d\Omega^2 = d\theta^2 + \sin^2\theta d\phi^2$ and $k = -1, 0$ or 1 indicates an open, flat or close universe respectively.

2.4.2 Λ CDM Cosmology

In standard model, the universe consists of baryons, cold dark matter (CDM), dark energy, neutrinos and photons¹². All these components interact with the spacetime metric through gravity while baryons and photons also couple with each other through Compton scatterings.

¹¹We use bar to denote the background-order quantities.

¹²We denote them by the subscripts b, c, Λ , n and r respectively.

The background energy density and pressure are related by the equation of state (EOS)

$$\bar{\mathcal{P}} = \omega \bar{\rho}, \quad (2.41)$$

where

$$\omega_b \approx 0, \quad \omega_c = 0, \quad \omega_\Lambda = -1, \quad \omega_n \approx 1/3, \quad \omega_r = 1/3. \quad (2.42)$$

The pressure of baryons can be neglected because baryons are non-relativistic at the times of interest. In contrast, neutrinos are approximately massless because they are relativistic at early time.

Due to the homogeneity and isotropy, there exist preferable coordinate systems which appreciate the symmetries, e.g. (η, r, θ, ϕ) used in Eq. (2.40). Under the coordinate system (η, r, θ, ϕ) , we can find that the quantities of the stress-energy tensor defined in Eq. (2.26) are

$$\bar{\pi}_{\mu\nu} = 0, \quad (2.43)$$

$$\bar{u}^A = \frac{1}{a(\eta)} \{1, 0, 0, 0\} \quad (2.44)$$

for all components in background order.

2.4.3 Friedmann Equations

By expanding the EFEs in background order, we obtain the well-known Friedmann equations

$$\frac{1}{a^2} \mathcal{H}^2 = \frac{8\pi \bar{\rho}_{\text{tot}}}{3} + \frac{\Lambda}{3} - \frac{k}{a^2} \quad (2.45)$$

$$\frac{1}{a^2} \dot{\mathcal{H}} = -\frac{4\pi}{3} (\bar{\rho}_{\text{tot}} + 3\bar{\mathcal{P}}_{\text{tot}}) + \frac{\Lambda}{3} \quad (2.46)$$

where the dot denotes derivatives with respect to the conformal time η ¹³, $\mathcal{H} \equiv \dot{a}/a$ is the conformal Hubble parameter and $\bar{\rho}_{\text{tot}}$ and $\bar{\mathcal{P}}_{\text{tot}}$ are the total energy density and pressure of baryons, CDM, neutrinos and photons respectively. Throughout this thesis, we assume a flat universe, i.e. $k = 0$. In particular, we have $\mathcal{H} = 1/\eta$ in radiation-dominated era.

¹³The physical time is related to the conformal time by $t = \int a(\eta) d\eta$.

2.5 Cosmological Perturbations in First Order

Linear cosmological perturbation theory has been widely studied and provides us tremendous information through the CMB power spectra. A complete calculation of the linear theory requires thorough understanding of numerous physical processes, such as the nucleosynthesis, Compton scattering at recombination and reionization, General Relativity and so on. The details can be found in many textbooks (e.g. [32, 105]).

The cosmological perturbations are imprinted in the CMB anisotropies. Although these anisotropies are very tiny (of order 10^{-5}), they are detectable and are used to study the early evolution of our universe. In this section, we will review the cosmological perturbations in linear order and develop the corresponding governing equations. Apart from extending the EFEs to 1st order, we will also need the 1st-order Boltzmann equation which describes Compton scatterings between photons and baryons.

2.5.1 Einstein Field Equations

To derive the 1st-order EFEs, we keep all the perturbations in Eq. (2.1) up to 1st order, i.e. $\mathcal{A} \approx \mathcal{A}^{[1]}$ for any perturbation \mathcal{A} ¹⁴. Moreover, we fix the gauge freedom by choosing Newtonian gauge in 1st order. Thus, we have

$$\mathcal{E} = \mathcal{B} = \mathcal{E}_I = 0. \quad (2.47)$$

Under the standard model, we ignore the 1st-order vector and tensor perturbations, i.e.

$$\mathcal{B}_I = \mathcal{H}_{IJ} = 0. \quad (2.48)$$

In other words, we have only two metric perturbations in 1st order, i.e. Φ and Ψ . However, it is important to emphasize that the vector and tensor perturbations in 2nd order cannot be neglected even they vanish in 1st order. This is because 2nd-order vector and tensor perturbations can be generated by 1st-order scalar perturbations due to the nonlinear effect of General Relativity (GR). We will discuss this in detail in Chapter 3. Using the conditions

¹⁴Without confusion, we ignore the superscript [I] in the following.

in Eq. (2.27), we can find that the 1st-order quantities of the stress-energy tensor obey

$$u^O = -\frac{1}{a}\Phi, \quad (2.49)$$

$$\pi^{OO} = 0, \quad \pi^{IO} = 0, \quad \pi^I_I = 0. \quad (2.50)$$

There are four EFEs for 1st-order scalar perturbations:

Time-time: G^O_O

$$3\mathcal{H}\dot{\Psi} + k^2\Psi + 3\mathcal{H}^2\Phi + \frac{\kappa a^2}{2} \left(\sum_{X=b,c} \bar{\rho}_X \delta_X + \sum_{X=n,r} \bar{\rho}_X \hat{I}_{X,00} \right) = 0, \quad (2.51)$$

Trace space-space: G^I_I

$$\ddot{\Psi} + 2\mathcal{H}\dot{\Psi} + \mathcal{H}\dot{\Phi} + (\mathcal{H}^2 + 2\dot{\mathcal{H}})\Phi + \frac{1}{3}k^2(\Psi - \Phi) - \frac{\kappa a^2}{2} \sum_{X=n,r} c_{s,X}^2 \bar{\rho}_X \hat{I}_{X,00} = 0, \quad (2.52)$$

Traceless space-space: $(3\Delta^{-2}\partial^J\partial_I - \Delta^{-1}\delta^J_I)(3G^I_J - \delta^I_J G^K_K)$

$$\Psi - \Phi - \frac{\kappa a^2}{5k^2} \sum_{X=n,r} \bar{\rho}_X \hat{I}_{X,20} = 0, \quad (2.53)$$

Time-space: $\Delta^{-1}\partial^I G^O_I$

$$\dot{\Psi} + \mathcal{H}\Phi + \frac{\kappa a^2}{2} \sum_{X=b,c} \bar{\rho}_X (1 + \omega_X) v_X - \frac{\kappa a^2}{6k} \sum_{X=n,r} \bar{\rho}_X \hat{I}_{X,10} = 0, \quad (2.54)$$

where $\Delta \equiv \partial^I\partial_I$, the dots over symbols denote derivatives with respect to the conformal time η , $\delta \equiv \delta\rho/\bar{\rho}$, $c_s \equiv \sqrt{\delta\mathcal{P}/\delta\rho}$ is the speed of sound and the subscripts b, c, n and r represent baryons, CDM, neutrinos and photons respectively. We have transformed the quantities of stress-energy tensors into multipoles for neutrinos and photons¹⁵. We remark that two of the four EFEs are redundant due to the gauge freedom. Only two EFEs are adequate for determining the evolution of the two scalar metric perturbations, which are Φ and Ψ . However, in practice, they are useful for numerical validation.

Furthermore, we need the evolution equations for energy densities and velocities of baryons and CDM. These can be obtained by perturbing the conservation of energy and

¹⁵The details of the transformation will be presented in Section 3.1.2.

momentum in Eq. (2.31). Thus, we have the continuity and Euler equation

$$\dot{\delta}_X - k^2 v_X - 3\dot{\Psi} = 0, \quad (2.55)$$

$$k\dot{v}_X + k\mathcal{H}v_X + k\Phi = \mathfrak{C}_X^v, \quad (2.56)$$

where $X = b, c$ denotes baryons and CDM respectively and the collision term $\mathfrak{C}_c^v = 0$ for CDM and $\mathfrak{C}_b^v = -R\dot{\tau}(\hat{I}_{10}/4 + kv_b)$ for baryons¹⁶.

2.5.2 Boltzmann Equation

The Boltzmann equation describes the evolution of the multipoles of photons and neutrinos. To derive the Boltzmann equation, we need to know the differential optical depth of Compton scattering, which is defined as

$$\dot{\tau} \equiv \sigma_T a x_e n_e, \quad (2.57)$$

where σ_T is the Thomson cross-section, x_e is the fraction of free electrons and n_e is the number density of total electrons. In 1st order, we need only the background-order differential optical depth. i.e. $\dot{\tau}(\eta)$. In the following, we will present the 1st-order Boltzmann equations for photon intensity and E -mode polarization¹⁷:

$$\dot{\hat{I}}_{\ell 0} + k({}_0\mathcal{U}_{\ell 0}^0 \hat{I}_{\ell+1,0} - {}_0\mathcal{D}_{\ell 0}^0 \hat{I}_{\ell-1,0}) - 4\delta_\ell^0 \dot{\Psi} - 4\delta_\ell^1 k\Phi = \mathfrak{C}_{\ell 0}[\hat{I}], \quad (2.58)$$

$$\dot{\hat{E}}_{\ell 0} + k({}_2\mathcal{U}_{\ell 0}^0 \hat{E}_{\ell+1,0} - {}_2\mathcal{D}_{\ell 0}^0 \hat{E}_{\ell-1,0}) = \mathfrak{C}_{\ell 0}[\hat{E}], \quad (2.59)$$

where the coefficients ${}_s\mathcal{D}_{\ell m}^n$, ${}_s\mathcal{T}_{\ell m}^n$ and ${}_s\mathcal{U}_{\ell m}^n$ are defined in Appendix C.3 and the collision terms are

$$\mathfrak{C}_{\ell 0}[\hat{I}] = \dot{\tau}(-\hat{I}_{\ell 0} + \delta_\ell^0 \hat{I}_{00} + 4\delta_\ell^1 \tilde{v}_{b,(0)} + \delta_\ell^2 \hat{\Pi}), \quad (2.60)$$

$$\mathfrak{C}_{\ell 0}[\hat{E}] = \dot{\tau}(-\hat{E}_{\ell 0} - \sqrt{6}\delta_\ell^2 \hat{\Pi}), \quad (2.61)$$

with $i\tilde{v}_{(0)} = v^i \bar{e}_{(0)}^{*I}$ and

$$\hat{\Pi} \equiv \frac{1}{10}(\hat{I}_{20} - \sqrt{6}\hat{E}_{20}). \quad (2.62)$$

¹⁶The density ratio is defined as $R \equiv (4/3)\bar{\rho}_r/\bar{\rho}_b$. More discussions of the collision term can be found in Section 3.2.3.

¹⁷The detailed derivation can be found in [32, 105].

For neutrinos, we only need to consider the intensity as in Eq. (2.58) but the collision term equals to zero. We remark that only the $m = 0$ modes are required for solving 1st-order perturbations. This is because we align the wavenumber \mathbf{k} with the azimuthal direction of the multipoles.

2.5.3 Adiabatic Initial Conditions

Throughout this thesis, we assume single-field slow-roll inflation. With the single field, the initial conditions of perturbations are expected to be adiabatic. This implies two conditions¹⁸: the ratios between $\rho_b^{1/3}$, $\rho_c^{1/3}$, $\rho_n^{1/4}$ and $\rho_r^{1/4}$ at each spatial point remain constant and

$$v_b = v_c = v_n = v_r. \quad (2.63)$$

In 1st order, the conditions become

$$\frac{1}{3}\delta_b = \frac{1}{3}\delta_c = \frac{1}{4}\hat{I}_{n,00} = \frac{1}{4}\hat{I}_{r,00}, \quad (2.64)$$

$$-4k v_b = -4k v_c = \hat{I}_{n,10} = \hat{I}_{r,10}. \quad (2.65)$$

That means we only need to solve for the initial energy density and velocity of one component. The adiabatic initial conditions can be determined by the comoving curvature perturbation, which is expressed in 1st order as

$$\mathcal{R} = \Psi + \frac{2}{3(1+\omega)\mathcal{H}}(\dot{\Psi} + \mathcal{H}\Phi), \quad (2.66)$$

where ω is the equation of state of the total fluid. The comoving curvature perturbation is conserved up to 2nd order for superhorizon scales [103].

To fix the initial conditions, we consider the initial conformal time η_i deep in the radiation-dominated era such that the cosmological scales are out of horizon ($k\eta_i \ll 1$). Therefore, the conformal Hubble parameter $\mathcal{H} = 1/\eta_i$ and the energy density of the total fluid is dominated by neutrinos and photons, i.e. $\bar{\rho}_{\text{tot}} \approx \bar{\rho}_n + \bar{\rho}_r$. By ignoring $\dot{\Psi}$ ¹⁹ and terms

¹⁸These two conditions of adiabaticity also hold in 2nd order.

¹⁹By expanding the perturbations into powers of $k\eta_i$, we can show that the leading term of Ψ is a constant and thus $\dot{\Psi} \approx 0$.

with higher powers of $k\eta_i$, the initial conditions satisfy

$$\mathcal{R} = \Psi + \frac{1}{2}\Phi, \quad \dot{\hat{I}}_{n,20} = \frac{2k}{3}\hat{I}_{n,10}, \quad (2.67)$$

$$3\mathcal{H}^2\Phi = \frac{\kappa a^2}{2}(\bar{\rho}_n\hat{I}_{n,00} + \bar{\rho}_r\hat{I}_{r,00}), \quad (2.68)$$

$$\mathcal{H}\Phi = \frac{\kappa a^2}{6k}(\bar{\rho}_n\hat{I}_{n,10} + \bar{\rho}_r\hat{I}_{r,10}), \quad (2.69)$$

$$\Psi - \Phi = \frac{\kappa a^2}{5k^2}(\bar{\rho}_n\hat{I}_{n,20} + \bar{\rho}_r\hat{I}_{r,20}), \quad (2.70)$$

and $\hat{I}_{r,\ell 0} = \hat{E}_{r,\ell 0} = 0$ for $\ell \geq 2$ due to the tight coupling of Compton scattering. Moreover, higher-order moments of neutrinos are suppressed, i.e. $\hat{I}_{n,\ell 0} = 0$ for $\ell \geq 3$. This is because moments with ℓ are suppressed by $(k\eta)^\ell$. By making use of $3\mathcal{H}^2 = \kappa a^2(\bar{\rho}_n + \bar{\rho}_r)$, Eq. (2.64) and Eq. (2.65), the initial perturbations are related to the comoving curvature perturbation by

$$\Phi = \frac{10}{15 + 4f_n}\mathcal{R}, \quad \Psi = \left(1 + \frac{2}{5}f_n\right)\Phi, \quad (2.71)$$

$$\hat{I}_{n,00} = -2\Phi, \quad \hat{I}_{n,10} = 2(k\eta_i)\Phi, \quad \hat{I}_{n,20} = \frac{2}{3}(k\eta_i)^2\Phi, \quad (2.72)$$

where $f_n \equiv \bar{\rho}_n/(\bar{\rho}_n + \bar{\rho}_r)$.

2.6 Statistics of CMB

In this section, we construct power spectra and bispectra of the CMB anisotropies. In standard model, the quantum fluctuations generated during inflation have the primordial power spectrum, which is in form of

$$P_\Phi(k) = 2\pi^2 A_s \frac{k^{n_s-4}}{k_*^{n_s-1}}, \quad (2.73)$$

where A_s is the initial amplitude, k_* is the pivot wavenumber and n_s is the spectral index. The power spectrum becomes scale-invariant when $n_s = 1$. Here, we assume that the spectral index is independent of k and ignore the higher-order Taylor expansion of the primordial power spectrum, such as the running index α_s . The quantum fluctuations set the initial conditions for perturbations. Then, the perturbations evolve and are imprinted on the CMB anisotropies. By studying the evolution history, we can infer the parameters in Eq. (2.73)

by fitting the predicted CMB power spectrum with the observed one. From Planck mission [3], $A_s = 2.215 \times 10^{-9}$ and $n_s = 0.9619$ for $k_* = 0.05/\text{Mpc}$.

2.6.1 CMB Power Spectrum

Unlensed Power Spectrum

First of all, we express the Boltzmann equation in 1st order as

$$\dot{\hat{I}} + ik\mu\hat{I} - 4\dot{\Psi} + 4ik\mu\Phi = \dot{\tau} \left[-\hat{I} + \hat{I}_{00} - 4i\mu v_b + \frac{1}{20} (1 - 3\mu^2) (\hat{I}_{20} - \sqrt{6}\hat{E}_{20}) \right], \quad (2.74)$$

where the overhead dots denote the derivatives with respect to the conformal time η , $\mu \equiv \hat{\mathbf{k}} \cdot \hat{\mathbf{n}}$ and $\hat{I}(\eta, \mathbf{k}, \hat{\mathbf{n}}) \equiv I^{[\Pi]}/\bar{I}$ is defined in Eq. (2.14)²⁰. With the line of sight approach as shown in [91], we find that the photon brightness defined as $\Delta \equiv \hat{I}/4$ can be expressed as an integral

$$\begin{aligned} \Delta^{[\Pi]}(\eta, \mathbf{k}, \hat{\mathbf{n}}) &= e^{\bar{\tau}(\eta)} \int_0^\eta d\tilde{\eta} e^{ik\mu(\tilde{\eta}-\eta) - \bar{\tau}(\tilde{\eta})} \left\{ \dot{\Psi} - ik\mu\Phi + \dot{\tau} \left[\Delta_{00} - i\mu v_b + \frac{1}{2} (1 - 3\mu^2) \Pi \right] \right\} \\ &\equiv e^{\bar{\tau}(\eta)} \int_0^\eta d\tilde{\eta} e^{ik\mu(\tilde{\eta}-\eta)} \tilde{S}_T(\tilde{\eta}, \mathbf{k}, \hat{\mathbf{n}}), \end{aligned} \quad (2.75)$$

where the optical depth $\bar{\tau} \equiv \int_{\tilde{\eta}}^{\eta_0} \dot{\tau}(\eta') d\eta'$, Δ_{00} is the monopole of the fractional brightness and $\Pi \equiv (\hat{I}_{20} - \sqrt{6}\hat{E}_{20})/40$. Here, we make use of the fact that $\dot{\tau} \rightarrow \infty$ when $\eta \rightarrow 0$.

For any function X of η , we can perform the integration by parts such that

$$\int_0^{\eta_0} d\eta e^{ik\mu\eta} \mu X = \left[e^{ik\mu\eta} \frac{X}{ik} \right]_0^{\eta_0} - \int_0^{\eta_0} d\eta e^{ik\mu\eta} \frac{\dot{X}}{ik}. \quad (2.76)$$

By applying the integration by parts to Eq. (2.75), we can simplify the photon brightness at present η_0 and obtain

$$\Delta(\eta_0, \mathbf{k}, \hat{\mathbf{n}}) = \int_0^{\eta_0} d\tilde{\eta} e^{ik\mu(\tilde{\eta}-\eta_0)} S_T(\tilde{\eta}, k) \Phi(\mathbf{k}), \quad (2.77)$$

where $\Phi(\mathbf{k})$ is the primordial fluctuation of the gravitational potential and the new source

²⁰We perform the Fourier transformation to the perturbations, i.e. $X(\eta, \mathbf{x}) = \int \frac{d^3\mathbf{k}}{(2\pi)^{3/2}} e^{i\mathbf{k}\cdot\mathbf{x}} X(\eta, \mathbf{k})$.

function is defined as

$$S_T(\tilde{\eta}, k) \equiv g \left(\Delta_{00} + \Phi + \frac{v_b}{k} + \frac{\Pi}{2} + \frac{3\ddot{\Pi}}{2k^2} \right) + \dot{g} \left(\frac{v_b}{k} + \frac{3\dot{\Pi}}{k^2} \right) + \frac{3\ddot{g}\Pi}{2k^2} + e^{-\tilde{\tau}} (\dot{\Phi} + \dot{\Psi}), \quad (2.78)$$

with $g \equiv \dot{\tau} e^{-\tilde{\tau}}$.

With the temperature definition in Eq. (2.17), the temperature anisotropies observed today is

$$\Theta(\hat{\mathbf{n}}) = \int \frac{d^3\mathbf{k}}{(2\pi)^{3/2}} \int_0^{\eta_0} d\tilde{\eta} e^{-ik\mu\tilde{r}} S_T(\tilde{\eta}, k) \Phi(\mathbf{k}), \quad (2.79)$$

where the conformal distance $\tilde{r} \equiv \eta_0 - \tilde{\eta}$. The exponential function in Eq. (2.79) can be expanded by

$$e^{-ik\mu r} = \sum_{\ell} (-i)^{\ell} (2\ell + 1) j_{\ell}(kr) P_{\ell}(\mu), \quad (2.80)$$

where $j_{\ell}(kr)$ is the spherical Bessel function of the first kind and $P_{\ell}(\mu)$ is the Legendre polynomial. Using this, we can rewrite the temperature anisotropies as

$$\Theta(\hat{\mathbf{n}}) = \sum_{\ell} (-i)^{\ell} (2\ell + 1) \int \frac{d^3\mathbf{k}}{(2\pi)^{3/2}} P_{\ell}(\mu) \Delta_{\ell}(k) \Phi(\mathbf{k}), \quad (2.81)$$

with the transfer function

$$\Delta_{\ell}(k) = \int_0^{\eta_0} d\eta S_T(\eta, k) j_{\ell}(kr). \quad (2.82)$$

Moreover, we can decompose the temperature anisotropies into spherical harmonics

$$a_{\ell m} = \int d^2\hat{\mathbf{n}} \Theta(\hat{\mathbf{n}}) Y_{\ell m}^*(\hat{\mathbf{n}}). \quad (2.83)$$

With Eq. (2.81) and Eq. (C.11), we can find that

$$a_{\ell m} = (-i)^{\ell} \sqrt{\frac{2}{\pi}} \int d^3\mathbf{k} Y_{\ell m}^*(\hat{\mathbf{k}}) \Delta_{\ell}(k) \Phi(\mathbf{k}). \quad (2.84)$$

By assuming the statistical isotropy of the CMB signals, we have the correlation

$$\langle a_{\ell m} a_{\ell' m'} \rangle = (-1)^m C_{\ell} \delta_{\ell\ell'} \delta_{-mm'}, \quad (2.85)$$

where $\langle \dots \rangle$ denotes the ensemble average and C_ℓ is the power spectrum. Using $\langle \Phi(\mathbf{k})\Phi(\mathbf{k}') \rangle = \delta(\mathbf{k} + \mathbf{k}')P_\Phi(k)$, the CMB power spectrum can be expressed as

$$C_\ell = \frac{2}{\pi} \int dk k^2 P_\Phi(k) [\Delta_\ell(k)]^2. \quad (2.86)$$

In Fig. 2.2, we plot the CMB power spectrum with the best-fit parameters from Planck as shown in Appendix B.

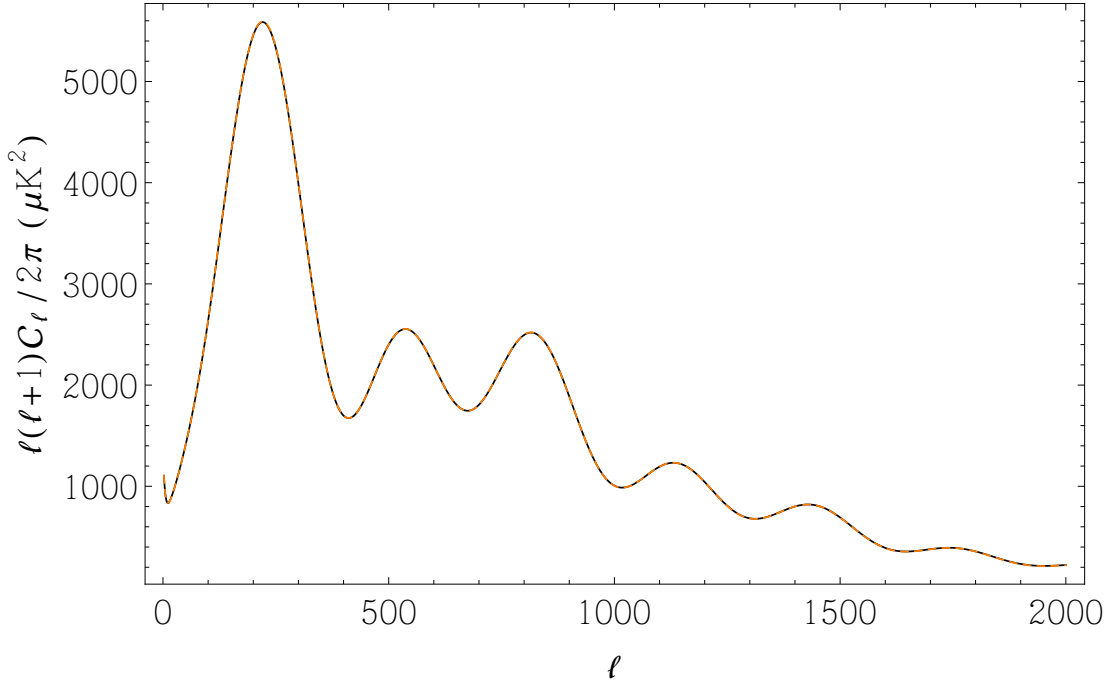


Figure 2.2 The full-sky unlensed power spectra of the CMB temperature from our code (black line) and CAMB (dashed orange line) against ℓ . A perfect match is achieved. Our code uses Newtonian gauge while CAMB uses synchronous gauge.

CMB Lensing Effect

It is known that the CMB lensing has a significant contribution to the CMB anisotropies and thus their correlations. In the canonical approach [67], the lensed CMB temperature anisotropies $\tilde{\Theta}$ are expressed in terms of the unlensed CMB temperature anisotropies Θ in the remapping²¹

$$\tilde{\Theta}(\hat{\mathbf{n}}) = \Theta(\hat{\mathbf{n}} + \boldsymbol{\alpha}). \quad (2.87)$$

²¹When similar approaches apply to CMB polarizations, geometric corrections on the spherical sky have to be considered to maintain statistical isotropy of the lensed fields [22].

The deflection angle $\boldsymbol{\alpha}$ is a perturbation defined as

$$\boldsymbol{\alpha}(\hat{\mathbf{n}}) = \nabla_{\hat{\mathbf{n}}}\psi(\hat{\mathbf{n}}) \equiv 2 \int_0^{r_{\text{LSS}}} dr \frac{r - r_{\text{LSS}}}{r r_{\text{LSS}}} \nabla_{\hat{\mathbf{n}}}\Psi_{\text{W}}(r, -r\hat{\mathbf{n}}), \quad (2.88)$$

where $\psi(\hat{\mathbf{n}})$ is known as the *lensing potential*, $\Psi_{\text{W}} \equiv (\Phi + \Psi)/2$ is the Weyl potential, r is the conformal distance between the gravitational potential and the observer, r_{LSS} is the conformal distance between the LSS and the observer and $\nabla_{\hat{\mathbf{n}}}$ is the covariant derivative on the sphere. We refer to [23, 46] and Chapter 5 for details about how lensing effects distort the CMB power spectrum.

2.6.2 CMB Bispectrum

If the CMB signals are not perfectly Gaussian, non-Gaussianities exist and may induce CMB bispectra. These non-Gaussianities can be produced during and after inflation and the treatments can be very different. In this section, we discuss the CMB bispectra from the primordial non-Gaussianities generated during inflation. The post-inflationary non-Gaussianities will be studied in Chapter 4. We remark that although the bispectra involve non-linear perturbations, the bispectra from different non-Gaussianities are separable²².

For the primordial non-Gaussianities, the leading-order effect to the CMB anisotropies can be expressed as

$$\Theta(\hat{\mathbf{n}}) = \int \frac{d^3\mathbf{k}}{(2\pi)^{3/2}} \int_0^{\eta_0} d\tilde{\eta} e^{ik\mu(\tilde{\eta}-\eta_0)} S_T(\tilde{\eta}, k) \Phi^{\text{NG}}(\mathbf{k}), \quad (2.89)$$

where $\Phi^{\text{NG}}(\mathbf{k})$ denotes the non-Gaussian fluctuation of the gravitational potential. We note that the 1st-order source function defined in Eq. (2.78) is used. That is, the leading order captures how the primordial non-Gaussianities evolve linearly over time after inflation. In Chapter 4, we will see that the nonlinear source function is necessary for studying the post-inflationary non-Gaussianities.

By decomposing the temperature anisotropies into spherical harmonics, the CMB bispectrum is the ensemble average of three coefficients $a_{\ell m s}$

$$B_{\ell_1 \ell_2 \ell_3}^{m_1 m_2 m_3} \equiv \langle a_{\ell_1 m_1} a_{\ell_2 m_2} a_{\ell_3 m_3} \rangle. \quad (2.90)$$

²²It is true at least for the leading terms of the bispectra.

The CMB angular-averaged bispectrum $B_{\ell_1\ell_2\ell_3}$ can then be defined as

$$B_{\ell_1\ell_2\ell_3} \equiv \sum_{m_1m_2m_3} \begin{pmatrix} \ell_1 & \ell_2 & \ell_3 \\ m_1 & m_2 & m_3 \end{pmatrix} B_{\ell_1\ell_2\ell_3}^{m_1m_2m_3}, \quad (2.91)$$

where the Wigner 3j-symbol $\begin{pmatrix} \ell_1 & \ell_2 & \ell_3 \\ m_1 & m_2 & m_3 \end{pmatrix}$ guarantees the satisfaction of the triangle conditions $|\ell_j - \ell_k| \leq \ell_i \leq \ell_j + \ell_k$ for any permutations of the indices $i, j, k = 1, 2, 3$. Moreover, it is convenient to use the reduced bispectrum $b_{\ell_1\ell_2\ell_3}$, which is related to the angular-averaged bispectrum by

$$B_{\ell_1\ell_2\ell_3} \equiv \sqrt{\frac{(2\ell_1+1)(2\ell_2+1)(2\ell_3+1)}{4\pi}} \begin{pmatrix} \ell_1 & \ell_2 & \ell_3 \\ 0 & 0 & 0 \end{pmatrix} b_{\ell_1\ell_2\ell_3}. \quad (2.92)$$

Using Eq. (C.24), we have the relation

$$B_{\ell_1\ell_2\ell_3}^{m_1m_2m_3} = \mathcal{G}_{\ell_1\ell_2\ell_3}^{m_1m_2m_3} b_{\ell_1\ell_2\ell_3}, \quad (2.93)$$

where the Gaunt integral is defined in Eq. (C.14).

By expressing the coefficients using Eq. (2.84), the CMB bispectrum can be written as

$$B_{\ell_1\ell_2\ell_3}^{m_1m_2m_3} = \left[\prod_{i=1}^3 (-i)^{\ell_i} \sqrt{\frac{2}{\pi}} \int d^3\mathbf{k}_i Y_{\ell_i m_i}^*(\hat{\mathbf{k}}_i) \Delta_{\ell}(\mathbf{k}_i) \right] \langle \Phi(\mathbf{k}_1) \Phi(\mathbf{k}_2) \Phi(\mathbf{k}_3) \rangle, \quad (2.94)$$

where $\langle \Phi(\mathbf{k}_1) \Phi(\mathbf{k}_2) \Phi(\mathbf{k}_3) \rangle$ is the $\Phi(\mathbf{k})$ -field bispectrum. For our interest, it is enough to define the $\Phi(\mathbf{k})$ -field bispectrum in form of

$$\langle \Phi(\mathbf{k}_1) \Phi(\mathbf{k}_2) \Phi(\mathbf{k}_3) \rangle = (2\pi)^{-3/2} \delta^3(\mathbf{k}_1 + \mathbf{k}_2 + \mathbf{k}_3) B(k_1, k_2, k_3), \quad (2.95)$$

where the Dirac delta function δ^3 ensures the conservation of momentum and $B(k_1, k_2, k_3)$ specifies the shape of the bispectrum.

Since the source function S_T is independent on the direction of \mathbf{k} (i.e. $S_T = S_T(\eta, k)$), we can simplify the bispectrum further by using Eq. (2.80), Eq. (C.11) and

$$\int d^3\mathbf{x} e^{i(\mathbf{k}_1 + \mathbf{k}_2 + \mathbf{k}_3) \cdot \mathbf{x}} = (2\pi)^3 \delta^3(\mathbf{k}_1 + \mathbf{k}_2 + \mathbf{k}_3). \quad (2.96)$$

In particular, the reduced bispectrum can be simplified as

$$b_{\ell_1 \ell_2 \ell_3} = \frac{8}{\pi^3} \int r^2 dr (k_1 k_2 k_3)^2 dk_1 dk_2 dk_3 j_{\ell_1}(k_1 r) j_{\ell_2}(k_2 r) j_{\ell_3}(k_3 r) \Delta_{\ell_1}(k_1) \Delta_{\ell_2}(k_2) \Delta_{\ell_3}(k_3) B(k_1, k_2, k_3). \quad (2.97)$$

In Chapter 4, we will see that the 2nd-order source function $S_T^{[\text{III}]}$ has more dependences other than η and k . Hence, the corresponding reduced bispectrum becomes more complicated.

We separate the temperature anisotropies into the Gaussian (G) and non-Gaussian (NG) parts, i.e.

$$a_{\ell m} = a_{\ell m}^{\text{G}} + a_{\ell m}^{\text{NG}}, \quad (2.98)$$

where $a_{\ell m}^{\text{NG}}$ can come from primordial non-Gaussianities or post-inflationary nonlinear evolution. Since the Gaussian signals do not contribute to the bispectrum, the leading-order CMB bispectrum is

$$B_{\ell_1 \ell_2 \ell_3}^{m_1 m_2 m_3} = \langle a_{\ell_1 m_1}^{\text{G}} a_{\ell_2 m_2}^{\text{G}} a_{\ell_3 m_3}^{\text{NG}} \rangle + 2 \text{ perm.} \quad (2.99)$$

In the standard model, the primordial fluctuations were originated from the Bunch-Davies vacuum state and are thus Gaussian. It can be shown that significant non-Gaussianities would not be produced from the single-field slow-roll inflation [72]. However, the question of having primordial non-Gaussianities is still open and has long been studied. Numerous mechanisms have been proposed to generate measurable non-Gaussianities [10]. The detection of these non-Gaussianities will facilitate our understanding of the very early universe and even the fundamental physics taken place in that era. The CMB bispectrum is of importance to probe the primordial non-Gaussianities from inflation. In particular, non-Gaussianities generated from different mechanisms have distinguishable features in the CMB bispectrum which can be classified into different types. Here, we review some of the most popular types of bispectrum templates – local, equilateral and orthogonal type.

Local-type Bispectrum

The primordial non-Gaussianity of the local type is a correction to the primordial Gaussian Newtonian potential $\Phi_G(\mathbf{x})$ expressed in real space as

$$\Phi(\mathbf{x}) = \Phi_G(\mathbf{x}) + f_{\text{NL}}^{\text{loc}} [\Phi_G^2(\mathbf{x}) - \langle \Phi_G^2(\mathbf{x}) \rangle], \quad (2.100)$$

where $f_{\text{NL}}^{\text{loc}}$ is the nonlinear coupling constant of the local type and the ensemble average $\langle \Phi_G(\mathbf{x}) \rangle = 0$.

In Fourier space, we decompose $\Phi(\mathbf{k}) = \Phi_G(\mathbf{k}) + \Phi_{\text{NG}}(\mathbf{k})$ with the non-Gaussian part

$$\Phi_{\text{NG}}(\mathbf{k}) \equiv f_{\text{NL}}^{\text{loc}} \left[\int \frac{d^3 \mathbf{q}}{(2\pi)^{3/2}} \Phi_G(\mathbf{k} + \mathbf{q}) \Phi_G^*(\mathbf{q}) - (2\pi)^{3/2} \delta^3(\mathbf{k}) \langle \Phi_G^2(\mathbf{x}) \rangle \right], \quad (2.101)$$

where the superscript $*$ denotes the complex conjugate and $\delta^3(\mathbf{k})$ is the Dirac delta function in three dimension²³.

If the Newtonian potential is purely Gaussian with mean zero, the $\Phi(\mathbf{k})$ -field bispectrum will simply vanish. However, due to the non-Gaussian part in Eq. (2.101), the bispectrum is non-vanishing and the leading components are²⁴

$$\langle \Phi_G(\mathbf{k}_1) \Phi_G(\mathbf{k}_2) \Phi_{\text{NG}}(\mathbf{k}_3) \rangle + 2 \text{ perm.} = (2\pi)^{-3/2} \delta^3(\mathbf{k}_1 + \mathbf{k}_2 + \mathbf{k}_3) B(k_1, k_2, k_3), \quad (2.102)$$

where

$$B(k_1, k_2, k_3) = 2f_{\text{NL}}^{\text{loc}} [P_\Phi(k_1)P_\Phi(k_2) + P_\Phi(k_2)P_\Phi(k_3) + P_\Phi(k_1)P_\Phi(k_3)]. \quad (2.103)$$

The bispectrum of the local type peaks at the squeezed-limit triangle for which one of the three modes k_i s in Fourier space is much smaller than the other two. Significant local-type bispectrum can be generated by multifield inflationary models [60], inhomogeneous reheating scenario [34] and etc. However, single-field inflationary models do not produce any measurable non-Gaussianity of the local type. For example, $f_{\text{NL}}^{\text{loc}} = (5/12)(1 - n_s) \ll 1$ for the single-field slow-roll inflation [72]. A convincing detection of $f_{\text{NL}}^{\text{loc}}$ from inflation will thus rule out the single-field inflationary models, regardless of their dynamics [30].

²³We make use of the fact that $\Phi(\mathbf{x})$ is a real quantity so that $\Phi^*(\mathbf{k}) = \Phi(-\mathbf{k})$.

²⁴Because of the second term in Eq. (2.101), Eq. (2.102) is only valid for $k_i \neq 0$.

The constraint on the local type from Planck 2013 [6] is

$$f_{\text{NL}}^{\text{loc}} = 2.7 \pm 5.8, \quad (2.104)$$

at 68% confidence level (CL).

Equilateral-type Bispectrum

Similar to the local type, the equilateral type is specified by Eq. (2.102) with

$$B(k_1, k_2, k_3) = 6f_{\text{NL}}^{\text{equ}} \left\{ -[P_{\Phi}(k_1)P_{\Phi}(k_2) + 2 \text{ perm.}] - 2[P_{\Phi}(k_1)P_{\Phi}(k_2)P_{\Phi}(k_3)]^{2/3} \right. \\ \left. + [P_{\Phi}(k_1)^{1/3}P_{\Phi}(k_2)^{2/3}P_{\Phi}(k_3) + 5 \text{ perm.}] \right\}. \quad (2.105)$$

Inflationary models, such as the Dirac-Born-Infeld (DBI) inflation, can generate significant non-Gaussianity of this type [97]. The constraint on the equilateral type from Planck 2013 [6] is

$$f_{\text{NL}}^{\text{equ}} = -42 \pm 75, \quad (2.106)$$

at 68% CL.

Orthogonal-type Bispectrum

The $\Phi(\mathbf{k})$ -field bispectrum for the orthogonal type is specified by

$$B(k_1, k_2, k_3) = 6f_{\text{NL}}^{\text{orth}} \left\{ -3[P_{\Phi}(k_1)P_{\Phi}(k_2) + 2 \text{ perm.}] - 8[P_{\Phi}(k_1)P_{\Phi}(k_2)P_{\Phi}(k_3)]^{2/3} \right. \\ \left. + 3[P_{\Phi}(k_1)^{1/3}P_{\Phi}(k_2)^{2/3}P_{\Phi}(k_3) + 5 \text{ perm.}] \right\}. \quad (2.107)$$

Significant non-Gaussianity of the orthogonal type can be produced by single-field inflationary models [25]. The constraint on the orthogonal type from Planck 2013 [6] is

$$f_{\text{NL}}^{\text{orth}} = -25 \pm 39, \quad (2.108)$$

at 68% CL.

Chapter 3

Cosmological Perturbations in Second Order

The perturbation theory is essential for studying Cosmology. For example, linear perturbations have been studied in depth for understanding the linear evolution of cosmological perturbations and their imprint on the observations. With improving precisions of measurements, higher-order perturbations from different mechanisms become important and can play a crucial role in Cosmology.

Nonlinear evolution can occur during and after inflation. Usually, non-Gaussianities are produced and can be probed by 3-point correlations of various observations, e.g. cosmic microwave background (CMB) and large-scale surveys. Although the single-field slow-roll inflation in standard Cosmology is known to have negligible non-Gaussianities [72], alternative inflationary models can generate detectable non-Gaussianities as clues about the underlying theory of inflation¹. Nevertheless, whether these primordial non-Gaussianities exist or not has to be verified by observations. In contrast, post-inflationary era guarantees the existence of nonlinear evolution through some well-known processes. In particular, the nonlinearity of General Relativity (GR) promotes the growth of nonlinear perturbations and is responsible for the formation of complex structures at late time.

Nonlinear perturbations can have profound impacts on the CMB statistics, especially bispectra and trispectra. They can contain fruitful information about the universe and thus deserve a thorough study. In this chapter, we establish all the governing equations necessary for solving the cosmological perturbations up to 2nd order, including the Boltzmann equa-

¹See [24] for a review.

tion (BE) and the Einstein field equations (EFEs). Fig. 3.1 outlines the relations between different perturbations and their corresponding evolution equations. As the leading non-linear order, 2nd-order perturbations are enough for understanding the nonlinear evolution around recombination when the perturbations in cosmological scales are still tiny compared to the background quantities and higher-order perturbations are highly suppressed. We will find that the derivation here is indispensable when we calculate the CMB bispectrum generated at recombination in the next chapter. In principle, the canonical perturbation theory breaks down at low redshifts. Thus, other approaches, such as N-body simulation and effective field theory [14], are adopted when we study the late-time large-scale evolution.

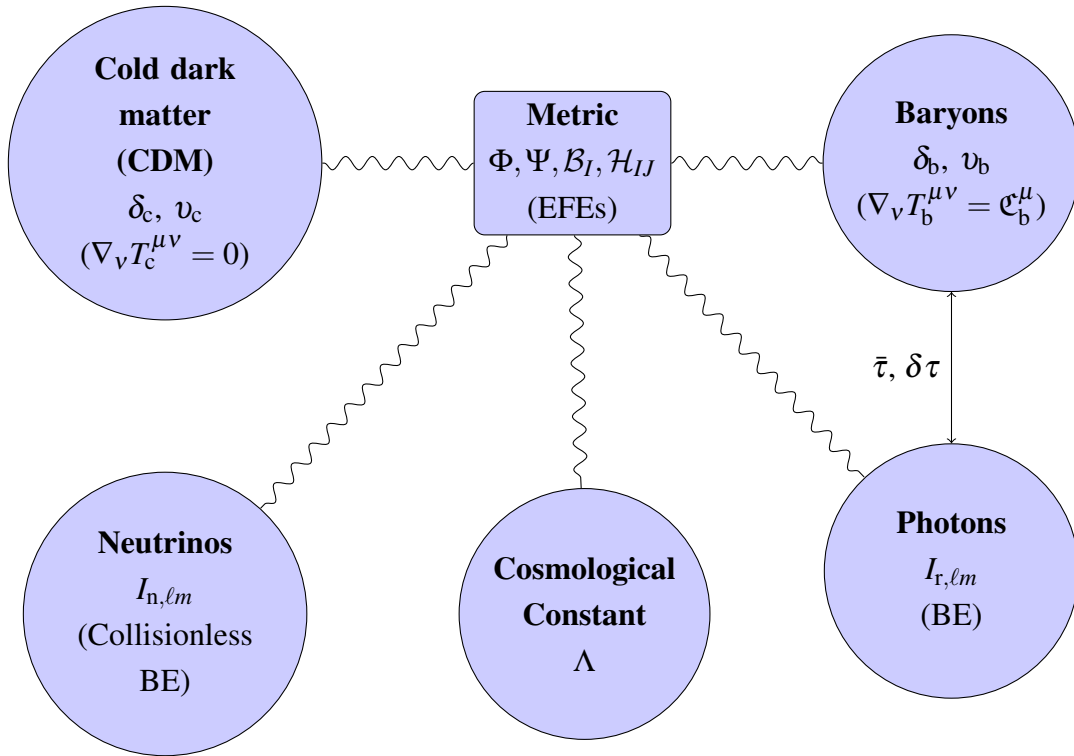


Figure 3.1 The diagrammatic outline of relations between different perturbations. The corresponding evolution equations are shown in the brackets. The wavy lines denotes couplings through GR while the two headed arrow denotes the Compton scattering. We remark that the 1st-order perturbed optical depth ($\delta\tau$) is needed for the 2nd-order Compton scattering.

This chapter is organized as follows. In Section 3.1, we extend the discussion about the coordinate system (see also Section 2.1.1) and fix the 2nd-order gauge choice to the Newtonian gauge. We then derive the EFEs, continuity equation and Euler equation in 2nd order. In Section 3.2, we derive the hierarchy of the 2nd-order Boltzmann equation, including the Liouville and collision parts. We also formulate the evolution equation of the

1st-order optical depth which is essential for the 2nd-order Compton scattering. Finally, we present the numerical calculation of the 2nd-order perturbations in Section 3.3. In particular, we set the initial conditions, apply the tight-coupling approximation (TCA) and validate the numerical results with the constraint equations.

3.1 Second-order Einstein Field Equations

Deriving the 2nd-order EFEs is rather straightforward but messy. For simplicity, we will first fix the gauge choice. Throughout this chapter, we use Newtonian gauge in both 1st and 2nd order². Then, we expand the Einstein tensor and stress-energy tensor up to 2nd order based on the equations in Section 2.3.1. The derivation is similar to what we have done in Section 2.5.1 for the 1st-order EFEs. However, there is a subtlety worth being emphasized. That is, the scalar-vector-tensor decomposition does not hold in 2nd order. For example, 1st-order scalar perturbations can induce 2nd-order vector and tensor perturbations. This is because of the existing cross terms of two 1st-order perturbations in the 2nd-order EFEs.

3.1.1 Gauge Choices

We begin with the metric in Eq. (2.1) and expand it up to 2nd order, i.e.

$$ds^2 = a^2(\eta) \left\{ -(1 + 2\Phi)d\eta^2 + 2\mathcal{B}_I dx^I d\eta + [(1 - 2\Psi)\delta_{IJ} + 2\mathcal{H}_{IJ}] dx^I dx^J \right\}, \quad (3.1)$$

where perturbations Φ , Ψ , \mathcal{B}_I and \mathcal{H}_{IJ} can be expanded in form of

$$\mathcal{A}(\eta, x^I) = \mathcal{A}^{[I]}(\eta, x^I) + \frac{1}{2}\mathcal{A}^{[II]}(\eta, x^I). \quad (3.2)$$

With the decompositions of \mathcal{B}_I and \mathcal{H}_{IJ} in Eq. (2.2), we fix the gauge freedom to Newtonian gauge up to 2nd order so that

$$\mathcal{E} = \mathcal{B} = \mathcal{E}_I = 0. \quad (3.3)$$

Different gauge choices are physically equivalent. We choose Newtonian gauge up to 2nd order mainly because this allows us to cross-check the derivation of 2nd-order evolution equations directly with other work in literature [52, 82, 87] which used Newtonian gauge

²It is possible to choose different gauges in different orders. See Section 2.1.1 for more discussions.

as well. However, different gauge choices might be different when we solve the evolution equations numerically. It turns out that the 2nd-order EFEs in Newtonian gauge are numerically unstable but the instability can be tackled by some tricks (see Section 3.3.3 for more details).

Moreover, we assume no 1st-order vector and tensor perturbations, i.e. $\mathcal{B}_I^{[1]} = \mathcal{H}_{IJ}^{[1]} = 0$. Any initial vector modes will decay due to the expansion of our universe unless there exist supports in the matters, such as cosmological defects [104], to continuously source the vector modes. Hence, vector perturbations are usually negligible. Recently, BICEP team detects B-mode polarization[2] which may originate from the primordial gravitational waves. If it is confirmed, the 1st-order tensor perturbations should be taken into account in our calculation. However, the 2nd-order vector and tensor perturbations are generally non-negligible because they can be generated by the 1st-order scalar perturbations nonlinearly.

3.1.2 Multipole Decomposition of Stress-Energy Tensor

To derive the 2nd-order EFEs, we need to calculate the stress-energy tensors of different components. For relativistic components like neutrinos and photons, we study their distribution functions and corresponding multipoles through the Boltzmann equation, instead of their stress-energy tensors through the continuity and Euler equations. That means we have to relate the stress-energy tensor with the multipoles to elaborate the EFEs.

While the EFEs and thus the stress-energy tensors are constructed under the coordinate system (η, x^I) of the background manifold, the multipoles in the Boltzmann equation are naturally expressed under the tetrad basis $(\hat{\mathbf{e}}_a)$ defined in the tangent planes of the physical manifold. When we relate the stress-energy tensor with the corresponding multipoles, we work on the background manifold consistently and pull the tetrad basis back onto the background manifold. Since the pulled-back tetrad basis does not necessarily align with the basis of the coordinate system (η, x^I) , we have to take into account the perturbations of the pulled-back tetrad³. In other words, we need to establish the following relations

$$T^{AB} \longleftrightarrow T^{ab} \longleftrightarrow \hat{I}_{\ell m}. \quad (3.4)$$

For relativistic component with an intensity distribution $\mathcal{I}(\eta, \mathbf{x}, p^0, \hat{\mathbf{n}})$, the stress-energy

³Details of the pullback are discussed in Section 2.1.2.

tensor can be expressed as

$$T^\mu{}_\nu = \frac{1}{(2\pi)^3} \int d\hat{\mathbf{n}} \int p^0 dp^0 \mathcal{I}(\eta, \mathbf{x}, p^0, \hat{\mathbf{n}}) p^\mu p_\nu. \quad (3.5)$$

The normalized energy-integrated photon intensity defined in Eq. (2.14) can be expanded into multipoles of spherical harmonics

$$\hat{I}(\hat{\mathbf{n}}) = \sum_{\ell m} \frac{1}{N_\ell} \hat{I}_{\ell m} Y_{\ell m}(\hat{\mathbf{n}}), \quad (3.6)$$

where N_ℓ is defined in Eq. (C.2). First of all, we relate the stress-energy tensor with its corresponding multipoles, both in tetrad basis. By using the fact that $p^i = p^0 n^i$ in tetrad basis as shown in Eq. (2.5) and the decomposition developed in Appendix C.3, we have⁴

$$T^0{}_0 = -T^i{}_i = -\bar{\rho} \hat{I}_{00}, \quad (3.7)$$

$$\bar{e}_{(m)}^{*i} T^i{}_0 = -\frac{i}{3} \bar{\rho} \hat{I}_{1m}, \quad (3.8)$$

$$[n^i n^j]_{2m} \left(T^i{}_j - \frac{1}{3} \delta^i{}_j T^k{}_k \right) = \frac{2}{15} \bar{\rho} \hat{I}_{2m}, \quad (3.9)$$

where $\bar{\rho} = \bar{I}(\eta)$ is the background-order energy density of the radiation.

Now, we are ready to pull stress-energy tensors back onto the background manifold using the transformation of tetrad basis discussed in Section 2.1.2, i.e.

$$T^a{}_b = T^A{}_B \xi^a{}_A \xi_b{}^B, \quad (3.10)$$

where we simply write ξT as T for the pulled-back stress-energy tensors and the perturbations of $\xi e^a{}_A$ and $\xi e_b{}^B$ can be found in Eq. (D.2) to (D.12). In 2nd order, we obtain

$$T^0{}^{[III]}_0 = T^O{}^{[III]}_O = -\delta\rho^{[III]} - 2(\bar{\rho} + \bar{P})v^I v_{,I}, \quad (3.11)$$

$$T^i{}^{[III]}_j = T^I{}^{[III]}_J = \pi^I{}_J^{[III]} + \delta P^{[III]} \delta^I{}_J + 2(\bar{\rho} + \bar{P})v^I v_{,J} - 4\Psi\pi^I{}_J, \quad (3.12)$$

$$\begin{aligned} T^i{}^{[III]}_0 &= T^I{}^{[III]}_O - (\bar{\rho} + \bar{P})\mathcal{B}^I{}^{[III]} + 2(\bar{\rho} + \bar{P})(\Phi + \Psi)v^I \\ &= -(\bar{\rho} + \bar{P})(\partial^I v^{[III]} + v^{I[III]} + \mathcal{B}^I{}^{[III]} - 2\Psi v^I) - 2(\delta\rho + \delta P)v^I - 2\pi^I{}_J v^{,J} \\ &= -(\bar{\rho} + \bar{P})v^{i[III]} - 2(\delta\rho + \delta P)v^I - 2\pi^I{}_J v^{,J}, \end{aligned} \quad (3.13)$$

⁴In tetrad basis, the upper and lower indices for spatial components are related trivially by δ_{ij} and δ^{ij} . Thus, we treat them as the same set of indices.

where the fluid quantities defined in Eq. (2.26) are expanded up to 2nd order. i.e.

$$\rho = \bar{\rho} + \delta\rho^{[\text{I}]} + \frac{1}{2}\delta\rho^{[\text{II}]}, \quad (3.14)$$

$$\mathcal{P} = \bar{\mathcal{P}} + \delta\mathcal{P}^{[\text{I}]} + \frac{1}{2}\delta\mathcal{P}^{[\text{II}]}, \quad (3.15)$$

$$u_A = a \delta^O{}_A + u_A^{[\text{I}]} + \frac{1}{2}u_A^{[\text{II}]}, \quad (3.16)$$

$$\pi_{AB} = \pi_{AB}^{[\text{I}]} + \frac{1}{2}\pi_{AB}^{[\text{II}]}, \quad (3.17)$$

with the overhead bar denoting the background quantities and the superscript O denoting the index corresponding to the conformal time η .

3.1.3 Einstein Field Equations

With the metric defined and the gauge fixed, the 2nd-order Einstein tensor can be calculated straightforwardly by expanding Eq. (2.23). For the stress-energy tensor, we define the sound speed c_s of a fluid as

$${}^{[N]}c_s^2 \equiv \frac{\delta\mathcal{P}^{[N]}}{\delta\rho^{[N]}}, \quad (3.18)$$

where $[N]$ indicates the perturbation order. The reference frame is chosen so that the observer's velocity is orthonormal to the hypersurfaces of constant time (see Appendix D.1 for the explicit definition of the reference frame). Using the conditions in Eq. (2.27), we find that, for all components,⁵

$$u^{O[\text{II}]} = \frac{1}{a} (-\Phi^{[\text{II}]} + 3\Phi\Phi + \partial_I v \partial^I v), \quad (3.19)$$

$$\pi^{OO[\text{II}]} = 0, \quad \pi^{IO[\text{II}]} = 2\pi^{IJ} \partial_J v, \quad \pi^I{}^I[\text{II}] = 0, \quad (3.20)$$

where the scalar mode v is defined in Eq. (2.28).

By substituting all these perturbations into Eq. (2.22), we can obtain the 2nd-order EFEs. Before doing so, we can expect that the 2nd-order EFEs must be in form of

$$\mathcal{D}_X[X^{[\text{II}]}] = \mathcal{C}_X[X^{[\text{I}]}], \quad (3.21)$$

⁵Henceforth, we omit the superscripts $[\text{I}]$ denoting the 1st-order perturbations whenever it is clear in the context.

where \mathcal{D} is a linear differential operator on any 2nd-order perturbations $X^{[\text{II}]}$ and the operator \mathcal{C} contains only terms with products of two 1st-order perturbations. Clearly, these are the only two ways to obtain terms in 2nd order. In particular, the linear operator \mathcal{D} has exactly the same form as the corresponding equations in 1st order. Mathematically, we can consider the 2nd-order equations as differential equations sourced by the cross terms in the operator \mathcal{C} (or the inhomogeneous part).

Moreover, it is more convenient to express the perturbations in Fourier space by the transformation

$$X^{[N]}(\eta, \mathbf{x}) = \int \frac{d^3\mathbf{k}}{(2\pi)^{3/2}} e^{i\mathbf{k}\cdot\mathbf{x}} X^{[N]}(\eta, \mathbf{k}). \quad (3.22)$$

In particular, we define the kernel $X^{[\text{III}]}(\eta, \mathbf{k}_1, \mathbf{k}_2)$ of any 2nd-order perturbations as

$$X^{[\text{III}]}(\eta, \mathbf{k}) \equiv \int \frac{d^3\mathbf{k}_1 d^3\mathbf{k}_2}{(2\pi)^{3/2}} \delta(\mathbf{k} - \mathbf{k}_1 - \mathbf{k}_2) X^{[\text{III}]}(\eta, \mathbf{k}_1, \mathbf{k}_2), \quad (3.23)$$

and the convolution operator \mathcal{T} as

$$\mathcal{T}_{\mathbf{k}_1, \mathbf{k}_2}(\mathbf{k}) \{\dots\} \equiv \int \frac{d^3\mathbf{k}_1 d^3\mathbf{k}_2}{(2\pi)^{3/2}} \delta(\mathbf{k} - \mathbf{k}_1 - \mathbf{k}_2) \dots \quad (3.24)$$

Scalar Modes

There are four EFEs for the 2nd-order scalar perturbations:⁶

Time-time: G^0_0

$$3\mathcal{H}\dot{\Psi} + k^2\Psi + 3\mathcal{H}^2\Phi + \frac{\kappa a^2}{2} \left(\sum_{X=b,c} \bar{\rho}_X \delta_X + \sum_{X=n,r} \bar{\rho}_X \hat{I}_{X,00} \right) = \mathcal{T}_{\mathbf{k}_1, \mathbf{k}_2}(\mathbf{k}) \{\mathcal{C}_1(\eta, \mathbf{k}_1, \mathbf{k}_2)\}, \quad (3.25)$$

Trace space-space: G^I_I

$$\ddot{\Psi} + 2\mathcal{H}\dot{\Psi} + \mathcal{H}\dot{\Phi} + (\mathcal{H}^2 + 2\dot{\mathcal{H}})\Phi + \frac{1}{3}k^2(\Psi - \Phi) - \frac{\kappa a^2}{2} \sum_{X=n,r} [^{\text{III}}]c_{s,X}^2 \bar{\rho}_X \hat{I}_{X,00} = \mathcal{T}_{\mathbf{k}_1, \mathbf{k}_2}(\mathbf{k}) \{\mathcal{C}_2(\eta, \mathbf{k}_1, \mathbf{k}_2)\}, \quad (3.26)$$

⁶For simplicity, we omit the label [II] for the 2nd-order quantities.

Traceless space-space: $(3\Delta^{-2}\partial^J\partial_I - \Delta^{-1}\delta^J_I)(3G^J_I - \delta^J_I G^K_K)$

$$\Psi - \Phi - \frac{\kappa a^2}{5k^2} \sum_{X=n,r} \bar{\rho}_X \hat{I}_{X,20} = \mathcal{T}_{\mathbf{k}_1, \mathbf{k}_2}(\mathbf{k}) \{\mathcal{C}_3(\eta, \mathbf{k}_1, \mathbf{k}_2)\}, \quad (3.27)$$

Time-space: $\Delta^{-1}\partial^J G^O_I$

$$\dot{\Psi} + \mathcal{H}\Phi + \frac{\kappa a^2}{2} \sum_{X=b,c} \bar{\rho}_X (1 + \omega_X) v_X - \frac{\kappa a^2}{6k} \sum_{X=n,r} \bar{\rho}_X \hat{I}_{X,10} = \mathcal{T}_{\mathbf{k}_1, \mathbf{k}_2}(\mathbf{k}) \{\mathcal{C}_4(\eta, \mathbf{k}_1, \mathbf{k}_2)\}, \quad (3.28)$$

where $\Delta \equiv \partial^J \partial_I$, the dots over symbols denote derivatives with respect to the conformal time η , $\delta \equiv \delta\rho/\bar{\rho}$ and the subscripts b, c, n and r represent baryons, CDM, neutrinos and photons respectively. Two of the four EFEs are redundant and can be used for consistency checks. We will discuss this further in Section 3.3.3. \mathcal{C}_i s for $i = 1$ to 4 contain only cross terms of two 1st-order perturbations and are defined as⁷

$$\begin{aligned} \mathcal{C}_1 \equiv & - [4(k_1^2 + k_2^2) + 3\mathbf{k}_1 \cdot \mathbf{k}_2] \Psi_1 \Psi_2 + 12\mathcal{H}^2 \Phi_1 \Phi_2 + 12\mathcal{H}(\Phi_1 - \Psi_1) \dot{\Psi}_2 \\ & + 3\dot{\Psi}_1 \dot{\Psi}_2 + \kappa a^2 \mathbf{k}_1 \cdot \mathbf{k}_2 \sum_{X=b,c} \bar{\rho}_X (1 + \omega_X) v_{X,1} v_{X,2}, \end{aligned} \quad (3.29)$$

$$\begin{aligned} \mathcal{C}_2 \equiv & - \left[\frac{4}{3}(k_1^2 + k_2^2) + \mathbf{k}_1 \cdot \mathbf{k}_2 \right] \Psi_1 \Psi_2 + \left(4\mathcal{H}^2 + 8\dot{\mathcal{H}} - \frac{2}{3}\mathbf{k}_1 \cdot \mathbf{k}_2 \right) \Phi_1 \Phi_2 - \dot{\Psi}_1 \dot{\Psi}_2 \\ & + 2\dot{\Phi}_1 \dot{\Psi}_2 + 8\mathcal{H}\Phi_1 \dot{\Phi}_2 + \left(8\mathcal{H}\dot{\Psi}_1 + 4\ddot{\Psi}_1 - \frac{4}{3}k_1^2 \Phi_1 \right) (\Phi_2 - \Psi_2) \\ & - \frac{2}{3}\mathbf{k}_1 \cdot \mathbf{k}_2 \Phi_1 \Psi_2 - \frac{\kappa a^2}{3} \mathbf{k}_1 \cdot \mathbf{k}_2 \sum_{X=b,c} \bar{\rho}_X (1 + \omega_X) v_{X,1} v_{X,2}, \end{aligned} \quad (3.30)$$

$$\begin{aligned} \mathcal{C}_3 \equiv & -4\Psi_1 \Psi_2 - 2\Phi_1 \Phi_2 \\ & - \frac{1}{k^2} \left[\mathbf{k}_1 \cdot \mathbf{k}_2 (\Phi_1 + \Psi_1) (\Phi_2 + \Psi_2) + 2k_2^2 \Psi_1 \Phi_2 \right. \\ & \left. + \kappa a^2 \mathbf{k}_1 \cdot \mathbf{k}_2 \sum_{X=b,c} \bar{\rho}_X (1 + \omega_X) v_{X,1} v_{X,2} \right] \\ & + \frac{3}{k^2} \left[(\hat{\mathbf{k}} \cdot \mathbf{k}_1) (\hat{\mathbf{k}} \cdot \mathbf{k}_2) (\Phi_1 + \Psi_1) (\Phi_2 + \Psi_2) + 2(\hat{\mathbf{k}} \cdot \mathbf{k}_2)^2 \Psi_1 \Phi_2 \right. \\ & \left. + \kappa a^2 (\hat{\mathbf{k}} \cdot \mathbf{k}_1) (\hat{\mathbf{k}} \cdot \mathbf{k}_2) \sum_{X=b,c} \bar{\rho}_X (1 + \omega_X) v_{X,1} v_{X,2} \right], \end{aligned} \quad (3.31)$$

⁷Again, we remove the superscript [1] from the 1st-order perturbations, e.g. $\Phi^{[1]}$ is replaced by simply Φ .

$$\begin{aligned}
\mathcal{C}_4 \equiv & 4\mathcal{H}\Phi_1\Phi_2 - 4\Psi_1\dot{\Psi}_2 + 2\frac{\mathbf{k}\cdot\mathbf{k}_2}{k^2}\dot{\Psi}_1\Phi_2 + 4\frac{\mathbf{k}\cdot\mathbf{k}_2}{k^2}\Phi_1\dot{\Psi}_2 \\
& + \frac{\mathbf{k}\cdot\mathbf{k}_2}{k^2}\kappa a^2 \sum_{X=b,c} \bar{\rho}_X [(1+\omega_X)(\Phi_1 + \Psi_1) - (1+[\square]c_{s,X}^2)\delta_{X,1}] v_{X,2} \\
& - \frac{\kappa a^2}{3k} \sum_{X=n,r} \bar{\rho}_X (\Phi_1 + \Psi_1) \hat{I}_{X,10}(\mathbf{k}_2),
\end{aligned} \tag{3.32}$$

where $\hat{\mathbf{k}} \equiv \mathbf{k}/k$ and the subscripts 1 and 2 on the 1st-order quantities indicate the \mathbf{k}_1 - and \mathbf{k}_2 -dependence, e.g. $\Phi_1 = \Phi(\mathbf{k}_1)$. In Eq. (3.32), we make use of the 1st-order relation that

$$\hat{I}_{1m}(\mathbf{k}') = 3(1+\omega)k'_{(m)}v(\mathbf{k}'), \tag{3.33}$$

with $k'_{(0)} = -\hat{\mathbf{k}}\cdot\mathbf{k}'$. Throughout the thesis, we align z -axis with the direction of $-\mathbf{k}$ whenever the decomposition of spherical harmonics is performed, i.e. $k_{(\pm 1)} = 0$ and $k_{(0)} = -k$. To derive Eq. (3.27), it is useful to know that the inverse

$$(3\partial^I\partial_J - \Delta\delta^I_J)^{-1} = \frac{1}{2}\Delta^{-2}\partial^J\partial_I - \frac{1}{6}\Delta^{-1}\delta^I_J, \tag{3.34}$$

which corresponds to, in Fourier space,

$$(-3k^I k_J + k^2\delta^I_J)^{-1} = -\frac{1}{2k^4}k^J k_I + \frac{1}{6k^2}\delta^I_J. \tag{3.35}$$

Alternatively, the time-space EFE in Eq. (3.28) can be obtained by $\Delta^{-1}\partial_I G^I_O$ such that

$$\dot{\Psi} + \mathcal{H}\Phi + \frac{\kappa a^2}{2} \sum_{X=b,c} \bar{\rho}_X (1+\omega_X) v_X - \frac{\kappa a^2}{6k} \sum_{X=n,r} \bar{\rho}_X \hat{I}_{X,10} = \mathcal{T}_{\mathbf{k}_1, \mathbf{k}_2}(\mathbf{k}) \{ \mathcal{C}'_4(\eta, \mathbf{k}_1, \mathbf{k}_2) \}, \tag{3.36}$$

where

$$\begin{aligned}
\mathcal{C}'_4 \equiv & \frac{\mathbf{k}\cdot\mathbf{k}_2}{k^2} \left[4\mathcal{H}(\Phi_1 - \Psi_1)\Phi_2 + 2\dot{\Psi}_1\Phi_2 - 4\dot{\Psi}_1\Psi_2 - 8\Psi_1\dot{\Psi}_2 \right] \\
& - \frac{\mathbf{k}\cdot\mathbf{k}_2}{k^2}\kappa a^2 \sum_{X=b,c} \bar{\rho}_X [(1+\omega_X)(\Phi_1 + \Psi_1) + (1+[\square]c_{s,X}^2)\delta_{X,1}] v_{X,2} \\
& + \frac{\kappa a^2}{3k} \sum_{X=n,r} \bar{\rho}_X (\Phi_1 + \Psi_1) \hat{I}_{X,10}(\mathbf{k}_2).
\end{aligned} \tag{3.37}$$

It can be shown that Eq. (3.32) and Eq. (3.37) are equivalent. Throughout this thesis, we

assume that $c_s^2 = 0$ and $\pi^{AB} = 0$ for baryons⁸ and CDM, which are valid for the cosmological scales we work on. Furthermore, we assume that $c_s^2 = 1/3$ for neutrinos and photons.

Vector Modes

There are two sets of EFEs for the two divergenceless vector perturbations in 2nd order:

Time-space:

$$\begin{aligned} \left(\mathcal{H}^2 - \dot{\mathcal{H}} + \frac{k^2}{4} \right) \tilde{\mathcal{B}}_{(\pm 1)} + \frac{\kappa a^2}{2} \sum_{X=b,c} \bar{\rho}_X (1 + \omega_X) \tilde{v}_{X,(\pm 1)} \\ + \frac{\kappa a^2}{6} \sum_{X=n,r} \bar{\rho}_X \hat{I}_{X,1\pm 1} = \mathcal{T}_{\mathbf{k}_1, \mathbf{k}_2}(\mathbf{k}) \{ \mathcal{C}_{(1,\pm 1)}(\eta, \mathbf{k}_1, \mathbf{k}_2) \}, \end{aligned} \quad (3.38)$$

Space-space:

$$\frac{k}{\sqrt{3}} \left(\dot{\tilde{\mathcal{B}}}_{(\pm 1)} + 2\mathcal{H}\tilde{\mathcal{B}}_{(\pm 1)} \right) - \frac{2\kappa a^2}{15} \sum_{X=n,r} \bar{\rho}_X \hat{I}_{X,2\pm 1} = \mathcal{T}_{\mathbf{k}_1, \mathbf{k}_2}(\mathbf{k}) \{ \mathcal{C}_{(2,\pm 1)}(\eta, \mathbf{k}_1, \mathbf{k}_2) \}, \quad (3.39)$$

where $i\tilde{\mathcal{B}}_{(\pm 1)} \equiv \mathcal{B}_{(\pm 1)} = \mathcal{B}^I \bar{e}_{(\pm 1)}^I$, $i\tilde{v}_{(m)} \equiv v_{(m)} = v^I \bar{e}_{(m)}^{*I}$ for $m = -1, 0, 1$ and

$$\begin{aligned} \mathcal{C}_{(1,\pm 1)} \equiv k_{1,(\pm 1)} \left[\Phi_1 (2\dot{\Psi}_2 - 4\mathcal{H}\Psi_2) - 4\dot{\Psi}_1 \Psi_2 \right] \\ - k_{1,(\pm 1)} \left\{ \kappa a^2 \sum_{X=b,c} \bar{\rho}_X v_{X,1} \left[(1 + \omega_X) (\Phi_2 + \Psi_2) + (1 + \square] c_{s,X}^2) \delta_{X,2} \right] \right\} \\ - \frac{\kappa a^2}{3} \sum_{X=n,r} \bar{\rho}_X \hat{I}_{X,1\pm 1}(\mathbf{k}_1) (\Phi_2 + \Psi_2) + \frac{\kappa a^2}{2} \sum_{X=b,c,n,r} \bar{\rho}_X (1 + \omega_X) \tilde{\mathcal{B}}_{(\pm 1)}, \end{aligned} \quad (3.40)$$

$$\begin{aligned} \mathcal{C}_{(2,\pm 1)} \equiv 2[\mathbf{k}_1 \mathbf{k}_2]_{2\pm 1} \left[\Phi_1 \Phi_2 - 2\Phi_1 \Psi_2 + 3\Psi_1 \Psi_2 - \sum_{X=b,c} \kappa a^2 \bar{\rho}_X (1 + \omega_X) v_{X,1} v_{X,2} \right] \\ + 4[\mathbf{k}_1 \mathbf{k}_1]_{2\pm 1} [\Phi_1 \Phi_2 - \Phi_1 \Psi_2 + 2\Psi_1 \Psi_2], \end{aligned} \quad (3.41)$$

with $k_{1,(\pm 1)} = k_1^I \bar{e}_{(\pm 1)}^{*I}$ and $[\mathbf{k}' \mathbf{k}'']_{2m} \equiv [n^i n^j]_{2m} k'_I k''_J$ which are decomposed based on Eq. (C.31) and Eq. (C.34) respectively. Similar to scalar modes, one set of the EFEs for vector modes is redundant and can be used for consistency checks.

⁸Because of baryon pressure, the sound speed of baryons deviates from zero but the correction should be tiny. See Section 5.6 of [71] for more details.

Tensor Modes

There is only one set of EFEs for the two tensor perturbations in 2nd order:

Space-space:

$$\ddot{\mathcal{H}}_{(\pm 2)} + 2\mathcal{H}\dot{\mathcal{H}}_{(\pm 2)} + k^2\mathcal{H}_{(\pm 2)} - \frac{2\kappa a^2}{15} \sum_{X=n,r} \bar{\rho}_X \hat{I}_{X,2\pm 2} = \mathcal{T}_{\mathbf{k}_1, \mathbf{k}_2}(\mathbf{k}) \{ \mathcal{C}_{(2,\pm 2)}(\eta, \mathbf{k}_1, \mathbf{k}_2) \}, \quad (3.42)$$

where $\mathcal{H}_{(\pm 2)} \equiv [n^i n^j]_{2\pm 2} \mathcal{H}_{IJ}$ and

$$\begin{aligned} \mathcal{C}_{(2,\pm 2)} \equiv & 2[\mathbf{k}_1 \mathbf{k}_2]_{2\pm 2} \left[\Phi_1 \Phi_2 - 2\Phi_1 \Psi_2 + 3\Psi_1 \Psi_2 - \sum_{X=b,c} \kappa a^2 \bar{\rho}_X (1 + \omega_X) v_{X,1} v_{X,2} \right] \\ & + 4[\mathbf{k}_1 \mathbf{k}_1]_{2\pm 2} [\Phi_1 \Phi_2 - \Phi_1 \Psi_2 + 2\Psi_1 \Psi_2]. \end{aligned} \quad (3.43)$$

For tensor modes, there is no redundant equation for consistency checks.

The EFEs derived above are used to determine the evolutions of the 2nd-order metric perturbations (see the rectangular block in Fig. 3.1). In the next subsection, we derive the continuity and Euler equations governing the energy density (δ) and velocity (v) of non-relativistic fluids, e.g. baryons and CDM. In contrast, multipole moments are required to completely describe the relativistic fluids, e.g. neutrinos and photons. We will study them comprehensively in Section 3.2 when we formulate the Boltzmann equation.

3.1.4 Continuity and Euler Equations

Baryons and CDM are non-relativistic and have only the first two moments, i.e. the energy density and velocity. The corresponding evolution equations can be derived from the conservation of stress–energy

$$\nabla_\nu T_X^{\mu\nu} \equiv T_X^{\mu\nu}{}_{,\nu} + \Gamma_{\alpha\nu}^\mu T_X^{\alpha\nu} + \Gamma_{\alpha\nu}^\nu T_X^{\mu\alpha} = \mathfrak{C}_X^\mu, \quad (3.44)$$

where $X = b$ and c stand for baryons and CDM respectively, ∇ denotes the covariant derivative and \mathfrak{C} is the collision term. Since CDM is collisionless (i.e. $\mathfrak{C}_c^\mu = 0$), its energy and momentum are conserved. In contrast, baryons couple with photons through the Compton scattering so we expect exchanges of energy and momentum between baryons and photons.

Working under the coordinate system (refer to Eq. (2.1)) of the background manifold,

we can derive the continuity equation for the 2nd-order energy density from the time component of Eq. (3.44)⁹

$$\begin{aligned} \mathfrak{E}_X^\delta &= \dot{\delta}_X^{[\text{II}]} - k^2 v_X^{[\text{II}]} - 3\dot{\Psi}^{[\text{II}]} \\ &+ \mathcal{T}_{\mathbf{k}_1, \mathbf{k}_2}(\mathbf{k}) \left\{ -6(2\Psi_1 + \delta_{X,1})\dot{\Psi}_2 - 2(\mathbf{k} \cdot \mathbf{k}_2)\delta_{X,1}v_{X,2} - 2k_2^2(\Phi_1 + \Psi_1)v_{X,2} \right. \\ &\quad \left. + 2\mathbf{k}_1 \cdot \mathbf{k}_2(2\Psi_1 - 2\Phi_1 - \mathcal{H}v_{X,1} - 2\dot{v}_{X,1})v_{X,2} \right\}, \end{aligned} \quad (3.45)$$

where the collision term \mathfrak{E}_X^δ vanishes for CDM and is expressed as in Eq. (3.91) for baryons.

Similarly, we obtain the Euler equations for the 2nd-order scalar and vector velocities (i.e. $v^{[\text{II}]}$ and $v_{(\pm 1)}^{[\text{II}]}$ respectively) from the spatial components of Eq. (3.44)¹⁰

$$\begin{aligned} \mathfrak{E}_X^v &= k\dot{v}_X^{[\text{II}]} + \mathcal{H}k v_X^{[\text{II}]} + k\Phi^{[\text{II}]} \\ &+ 2\mathcal{T}_{\mathbf{k}_1, \mathbf{k}_2}(\mathbf{k}) \left\{ \hat{\mathbf{k}} \cdot \mathbf{k}_2 [(\delta_{X,1} - \Phi_1 + \Psi_1)\dot{v}_{X,2} + \delta_{X,1}\Phi_2 + 2(\Psi_1 - \Phi_1)\Phi_2 \right. \\ &\quad \left. - (\mathbf{k}_1 \cdot \mathbf{k}_2)v_{X,1}v_{X,2} + \mathcal{H}(\delta_{X,1} - \Phi_1 + \Psi_1)v_{X,2} - \dot{\Psi}_1 v_{X,2}] \right\}, \end{aligned} \quad (3.46)$$

$$\begin{aligned} \mathfrak{E}_{X,(\pm 1)}^v &= \dot{v}_{X,(\pm 1)}^{[\text{II}]} + \mathcal{H}\tilde{v}_{X,(\pm 1)}^{[\text{II}]} \\ &+ 2\mathcal{T}_{\mathbf{k}_1, \mathbf{k}_2}(\mathbf{k}) \left\{ k_{2,(\pm 1)} [(\delta_{X,1} - \Phi_1 + \Psi_1)\dot{v}_{X,2} + \delta_{X,1}\Phi_2 + 2(\Psi_1 - \Phi_1)\Phi_2 \right. \\ &\quad \left. - (\mathbf{k}_1 \cdot \mathbf{k}_2)v_{X,1}v_{X,2} + \mathcal{H}(\delta_{X,1} - \Phi_1 + \Psi_1)v_{X,2} - \dot{\Psi}_1 v_{X,2}] \right\}, \end{aligned} \quad (3.47)$$

where the collision term \mathfrak{E}_X^v vanishes for CDM and is shown as in Eq. (3.92) and Eq. (3.93) for baryons. The discussion about the collision part of baryons will be postponed to Section 3.2.3 after we study the Compton scattering through the Boltzmann equation in Section 3.2.2. In the next section, we will develop the evolution equations for the multipoles of neutrinos and photons using the Boltzmann equation.

3.2 Second-order Boltzmann Equation

Similar to the case in 1st order, the 2nd-order Boltzmann equation is needed for two main purposes. First, we derive the governing equations of the 2nd-order multipoles from the

⁹Without confusion, we omit the notations for the 1st-order perturbations.

¹⁰For scalar mode, we elaborate $\Delta^{-1}\partial_t(\nabla_A T_X^{IA})$ under the coordinate system in Eq. (2.1).

Boltzmann equation and use these equations to solve the evolution of the multipoles of neutrinos and photons¹¹. Second, we construct the evolution equation of the photon intensity matrix from the Boltzmann equation and perform the line-of-sight approach to calculate the 2nd-order CMB anisotropies during recombination. We will focus on the former in this section and discuss the latter in Section 4.2. To begin, we classify terms in the 2nd-order Boltzmann equation into four categories

$$\mathcal{L}^{[\text{II}]} + \mathcal{L}^{[\text{I,I}]} = \mathcal{C}^{[\text{II}]} + \mathcal{C}^{[\text{I,I}]} \quad (3.48)$$

where \mathcal{L} is the Liouville operator, \mathcal{C} is the collision operator, the superscripts [II] and [I,I] denote linear terms of purely 2nd-order perturbations and quadratic terms of two 1st-order perturbations respectively. The Liouville operator conserves the phase-space distribution function along the trajectories if there are no collisions while the collision operator specifies how photons and electrons interact through the Compton scattering.

There are some subtleties when we study the 2nd-order Boltzmann equation. The quadratic terms in Eq. (3.48) contain couplings between two multipoles. The Wigner 3-j symbols or Clebsch–Gordan coefficients are thus required when we decompose multipoles of spherical harmonics in the Boltzmann equation¹². Moreover, when we solve the multipoles and perform the line-of-sight integration in Boltzmann equation, we choose the conformal time η as the unit of time. Thus, it is more convenient to redefine the Liouville and collision operator such that

$$\mathcal{L} \rightarrow \left(\frac{d\eta}{ds} \right) \mathcal{L}, \quad \mathcal{C} \rightarrow \left(\frac{d\eta}{ds} \right) \mathcal{C}. \quad (3.49)$$

This transformation is equivalent to the transformation with simply the background-order $(d\eta/ds)^{[0]}$. When we consider N th-order Boltzmann equation, $(d\eta/ds)^{[\text{L}]}$ will multiply with $(N-L)$ th-order Boltzmann equation, which vanishes[83] due to the lower-order Boltzmann equation. From now on, we will adopt this transformation in the derivation of the 2nd-order Boltzmann equation. Throughout this section, we will derive the Boltzmann equation in the tetrad basis.

¹¹For neutrinos, the Boltzmann equation is collisionless and we are interested in its intensity only.

¹²Some useful formulae for the multipole decomposition can be found in Appendix C.

3.2.1 Liouville Operator

The Liouville (free-streaming) operator acting on the intensity matrix \mathcal{P}_{ab} can be expressed as¹³

$$\mathfrak{L}[\mathcal{P}_{ab}] = S_a^c S_b^d \left(\frac{dx^A}{d\eta} \nabla_A \mathcal{P}_{cd} + \frac{dp^0}{d\eta} \frac{\partial}{\partial p^0} \mathcal{P}_{cd} + \frac{dn^i}{d\eta} \frac{\partial}{\partial n^i} \mathcal{P}_{cd} \right), \quad (3.50)$$

where the covariant derivative ∇_A can be elaborated by using Eq. (2.35) and S_{ab} is the screen projector defined in Eq. (2.6). In Tetrad basis, the screen projector contains no perturbations and is written as

$$S_{ab} = \eta_{ab} + \delta_a^0 \delta_b^0 - n_a n_b, \quad (3.51)$$

where the Minkowski metric $\eta_{ab} \equiv \text{diag}(-1, 1, 1, 1)$, $n_0 = 0$ and $n_i n^i = 1$.

Before we continue the derivation, we want to emphasize one thing. When we perform the perturbation expansion, we decompose the photon momentum \mathbf{p} into p^0 and n^i under the tetrad basis as the momentum lives on the tangent plane. Similarly, the screen projector is represented in tetrad basis, i.e. S^{ij} instead of S^{IJ} . In contrast, we express everything else in the coordinate system $\{x^A\}$ of the background manifold, such as metric perturbations (\mathcal{B}_J , \mathcal{H}_{IJ} , ...) and the spatial derivatives ($\partial/\partial x^I$). We do so because of the following reason: The photon momentum \mathbf{p} at a point of the physical manifold is measured as the quantities p^0 and n^i under a chosen basis (tetrad basis in our case) of the tangent plane. These quantities are unperturbed. On the other hand, the metric perturbations are expanded on the background manifold. We perform all the calculations consistently on the background manifold and thus we need to pull back the tetrad fields $\hat{\mathbf{e}}_a$ onto the background manifold as shown in Eq. (2.7). Due to the existing perturbations, we do not expect the pulled-back tetrads $\xi \hat{\mathbf{e}}_a$ to be perfectly aligned with the natural background basis $\bar{\mathbf{e}}_A$ (see Fig. 2.1 for an illustration). Therefore, $\xi \hat{\mathbf{e}}_a^A$, which are the coefficients of the pulled-back tetrads under the natural background basis $\bar{\mathbf{e}}^A$, are perturbative. After the perturbation expansion, implicit summations $S^{ij} \partial_j$ and $n^i \partial_I$ stand for $\xi \bar{e}_j^J S^{ij} \partial_J$ and $\xi \bar{e}_i^I n^i \partial_I$ with the alignment $\xi \bar{\mathbf{e}}_a = \bar{\mathbf{e}}_A$.

To expand the 2nd-order Liouville terms, we need to solve the geodesic equation Eq. (2.37) up to 2nd-order and obtain the following useful terms¹⁴

¹³Note that we multiply the Boltzmann equation with the Jacobian $ds/d\eta$.

¹⁴We ignore both vector and tensor perturbations in 1st order.

Background order:

$$\left(\frac{dx^I}{d\eta}\right)^{[0]} = n^i, \quad (3.52)$$

$$\left(\frac{dn^i}{d\eta}\right)^{[0]} = 0, \quad (3.53)$$

$$\left(\frac{dp^0}{d\eta}\right)^{[0]} = -\mathcal{H}p^0, \quad (3.54)$$

1st order:

$$\left(\frac{dx^I}{d\eta}\right)^{[I]} = n^i \left(\Psi^{[I]} + \Phi^{[I]}\right), \quad (3.55)$$

$$\left(\frac{dn^i}{d\eta}\right)^{[I]} = -S^{ij} \partial_j \left(\Psi^{[I]} + \Phi^{[I]}\right), \quad (3.56)$$

$$\left(\frac{dp^0}{d\eta}\right)^{[I]} = p^0 \left(\dot{\Psi}^{[I]} - n^i \partial_I \Phi^{[I]}\right), \quad (3.57)$$

2nd order:

$$\begin{aligned} \left(\frac{dp^0}{d\eta}\right)^{[II]} &= p^0 \left[\dot{\Psi}^{[II]} - n^i \partial_I \Phi^{[II]} + \left(\partial_I \mathcal{B}_J^{[II]} - \mathcal{H}_{IJ}^{[II]}\right) n^i n^j \right. \\ &\quad \left. + 2 \left(\Phi^{[I]} - \Psi^{[I]}\right) n^i \partial_I \Phi^{[I]} + 4\Psi^{[I]} \dot{\Psi}^{[I]} \right]. \end{aligned} \quad (3.58)$$

Using Eq. (2.36), we can separate Liouville parts of photon intensity and polarizations and expand them in 2nd order such that

$$\begin{aligned} \frac{\partial \mathcal{I}^{[III]}}{\partial \eta} + \left(\frac{dx^I}{d\eta}\right)^{[0]} \frac{\partial \mathcal{I}^{[III]}}{\partial x^I} + \left(\frac{dp^0}{d\eta}\right)^{[0]} \frac{\partial \mathcal{I}^{[III]}}{\partial p^0} + \left(\frac{dp^0}{d\eta}\right)^{[III]} \frac{\partial \bar{\mathcal{I}}}{\partial p^0} \\ + 2 \left(\frac{dp^0}{d\eta}\right)^{[I]} \frac{\partial \mathcal{I}^{[II]}}{\partial p^0} + 2 \left(\frac{dx^I}{d\eta}\right)^{[I]} \frac{\partial \mathcal{I}^{[II]}}{\partial x^I} + 2 \left(\frac{dn^i}{d\eta}\right)^{[I]} \frac{\partial \mathcal{I}^{[II]}}{\partial n^i}, \end{aligned} \quad (3.59)$$

$$\begin{aligned} (\nabla_\eta \mathcal{P}_{ab})^{[III]} + \left(\frac{dx^I}{d\eta}\right)^{[0]} \frac{\partial \mathcal{P}_{ab}^{[III]}}{\partial x^I} + \left(\frac{dp^0}{d\eta}\right)^{[0]} \frac{\partial \mathcal{P}_{ab}^{[III]}}{\partial p^0} \\ + 2 \left(\frac{dp^0}{d\eta}\right)^{[I]} \frac{\partial \mathcal{P}_{ab}^{[II]}}{\partial p^0} + 2 \left(\frac{dx^I}{d\eta}\right)^{[I]} \frac{\partial \mathcal{P}_{ab}^{[II]}}{\partial x^I} + 2S_a^c S_b^d \left(\frac{dn^i}{d\eta}\right)^{[I]} \frac{\partial \mathcal{P}_{cd}^{[II]}}{\partial n^i}, \end{aligned} \quad (3.60)$$

where $\bar{\mathcal{I}} = \bar{\mathcal{I}}(\eta, p^0)$ and $\bar{\mathcal{P}}_{ab} = 0$ are homogeneous and isotropic. The covariant derivative of polarizations in the first term of Eq. (3.60) can be expanded using Eq. (2.35). We do

not consider the terms with the Christoffel symbols in this thesis. However, they should be taken into account in the future. We can interpret physically the terms in Eq. (3.59) as follows. The first two terms in the first line corresponds to the 2nd-order photon intensity propagating through the spacetime on the background metric. The third term is responsible to the redshifting due to the Hubble expansion while the fourth term is responsible to the redshifting (nonlinear Sachs-Wolfe and integrated Sachs-Wolfe effects) due to the 2nd-order metric perturbations on the background-order photon intensity. Similarly, the first term in the second line is the redshifting (Sachs-Wolfe and integrated Sachs-Wolfe effects) of the 1st-order metric perturbations on the 1st-order photon intensity. The second term generates a time delay effect while the third one generates a lensing effect. Similar interpretation works for polarization in Eq. (3.60). We will discuss these effects, especially the lensing effect, in greater details in Chapter 5.

By using the decomposition of spherical harmonics in Appendix C.3 and the coefficients in Appendix D, we can derive the 2nd-order Liouville operators of different multipoles as follows:

Pure Second-order Liouville Operator $\mathcal{L}^{[II]}$

The pure 2nd-order Liouville operators have exactly the same form as the 1st-order ones without neglecting the 1st-order vector and tensor perturbations

$$\begin{aligned} \mathcal{L}_{\ell m}^{[II]}[\hat{I}] &= \dot{\hat{I}}_{\ell m} + k \left({}_0\mathcal{U}_{\ell m}^0 \hat{I}_{\ell+1,m} - {}_0\mathcal{D}_{\ell m}^0 \hat{I}_{\ell-1,m} \right) - 4\delta_\ell^0 \delta_m^0 \dot{\Psi} - 4\delta_\ell^1 \delta_m^0 k\Phi \\ &\quad + \frac{4k}{\sqrt{3}} \delta_\ell^2 \left(\delta_m^1 \tilde{\mathcal{B}}_{(1)} + \delta_m^{-1} \tilde{\mathcal{B}}_{(-1)} \right) + 4\delta_\ell^2 \left(\delta_m^2 \dot{\mathcal{H}}_{(2)} + \delta_m^{-2} \dot{\mathcal{H}}_{(-2)} \right), \end{aligned} \quad (3.61)$$

$$\mathcal{L}_{\ell m}^{[II]}[\hat{E}] = \dot{\hat{E}}_{\ell m} + k \left({}_2\mathcal{U}_{\ell m}^0 \hat{E}_{\ell+1,m} - {}_2\mathcal{D}_{\ell m}^0 \hat{E}_{\ell-1,m} - {}_2\mathcal{T}_{\ell m}^0 \hat{B}_{\ell m} \right), \quad (3.62)$$

$$\mathcal{L}_{\ell m}^{[II]}[\hat{B}] = \dot{\hat{B}}_{\ell m} + k \left({}_2\mathcal{U}_{\ell m}^0 \hat{B}_{\ell+1,m} - {}_2\mathcal{D}_{\ell m}^0 \hat{B}_{\ell-1,m} + {}_2\mathcal{T}_{\ell m}^0 \hat{E}_{\ell m} \right), \quad (3.63)$$

where the coefficients ${}_s\mathcal{D}_{\ell m}^n$, ${}_s\mathcal{T}_{\ell m}^n$ and ${}_s\mathcal{U}_{\ell m}^n$ are defined in Appendix C.3.

Quadratic Second-order Liouville Operator $\mathcal{L}^{[I,I]}(\mathbf{k})$

We define the kernel operator $\mathcal{L}^{[I,I]}(\mathbf{k}_1, \mathbf{k}_2)$ as

$$\mathcal{L}^{[I,I]}[\hat{X}](\mathbf{k}) \equiv \mathcal{F}_{\mathbf{k}_1, \mathbf{k}_2}(\mathbf{k}) \left\{ \mathcal{L}^{[I,I]}[\hat{X}](\mathbf{k}_1, \mathbf{k}_2) \right\}, \quad (3.64)$$

where \hat{X} stands for \hat{I} , \hat{E} and \hat{B} . The quadratic 2nd-order Liouville operators for photon intensity and polarizations are

$$\begin{aligned} \mathfrak{L}_{\ell m}^{[I,I]}[\hat{I}] = & -8 \sum_{n=-1}^1 k_{2,(n)} ({}_0\mathcal{U}_{\ell m}^n \hat{I}_{1,\ell+1,m-n} - {}_0\mathcal{D}_{\ell m}^n \hat{I}_{1,\ell-1,m-n}) \Phi_2 \\ & - 8 [\hat{I}_{1,\ell m} \Psi_2 + 2\delta_\ell^0 \Psi_1 \Psi_2 + \delta_\ell^1 k_{1,(m)} \Phi_1 (\Phi_2 - \Psi_2)] + \mathfrak{L}_{T,\ell m}^{[I,I]}[\hat{I}] + \mathfrak{L}_{L,\ell m}^{[I,I]}[\hat{I}], \end{aligned} \quad (3.65)$$

$$\begin{aligned} \mathfrak{L}_{\ell m}^{[I,I]}[\hat{E}] = & -8 \sum_{n=-1}^1 k_{2,(n)} ({}_2\mathcal{U}_{\ell m}^n \hat{E}_{1,\ell+1,m-n} - {}_2\mathcal{D}_{\ell m}^n \hat{E}_{1,\ell-1,m-n}) \Phi_2 \\ & - 8 \hat{E}_{1,\ell m} \Psi_2 + \mathfrak{L}_{T,\ell m}^{[I,I]}[\hat{E}] + \mathfrak{L}_{L,\ell m}^{[I,I]}[\hat{E}], \end{aligned} \quad (3.66)$$

$$\mathfrak{L}_{\ell m}^{[I,I]}[\hat{B}] = 8 \sum_{n=-1}^1 k_{2,(n)} {}_2\mathcal{T}_{\ell m}^n \hat{E}_{1,\ell,m-n} \Phi_2 + \mathfrak{L}_{T,\ell m}^{[I,I]}[\hat{B}] + \mathfrak{L}_{L,\ell m}^{[I,I]}[\hat{B}], \quad (3.67)$$

where

$$\mathfrak{L}_{T,\ell m}^{[I,I]}[\hat{I}] = -2 \sum_{n=-1}^1 k_{1,(n)} ({}_0\mathcal{U}_{\ell m}^n \hat{I}_{1,\ell+1,m-n} - {}_0\mathcal{D}_{\ell m}^n \hat{I}_{1,\ell-1,m-n}) (\Phi_2 + \Psi_2), \quad (3.68)$$

$$\mathfrak{L}_{L,\ell m}^{[I,I]}[\hat{I}] = 2 \sum_{n=-1}^1 k_{2,(n)} [{}_0\mathcal{U}_{\ell m}^n (\ell+2) \hat{I}_{1,\ell+1,m-n} + {}_0\mathcal{D}_{\ell m}^n (\ell-1) \hat{I}_{1,\ell-1,m-n}] (\Phi_2 + \Psi_2), \quad (3.69)$$

$$\mathfrak{L}_{T,\ell m}^{[I,I]}[\hat{E}] = -2 \sum_{n=-1}^1 k_{1,(n)} ({}_2\mathcal{U}_{\ell m}^n \hat{E}_{1,\ell+1,m-n} - {}_2\mathcal{D}_{\ell m}^n \hat{E}_{1,\ell-1,m-n}) (\Phi_2 + \Psi_2), \quad (3.70)$$

$$\mathfrak{L}_{L,\ell m}^{[I,I]}[\hat{E}] = 2 \sum_{n=-1}^1 k_{2,(n)} [{}_2\mathcal{U}_{\ell m}^n (\ell+2) \hat{E}_{1,\ell+1,m-n} + {}_2\mathcal{D}_{\ell m}^n (\ell-1) \hat{E}_{1,\ell-1,m-n}] (\Phi_2 + \Psi_2), \quad (3.71)$$

$$\mathfrak{L}_{T,\ell m}^{[I,I]}[\hat{B}] = 2 \sum_{n=-1}^1 k_{1,(n)} {}_2\mathcal{T}_{\ell m}^n \hat{E}_{1,\ell,m-n} (\Phi_2 + \Psi_2), \quad (3.72)$$

$$\mathfrak{L}_{L,\ell m}^{[I,I]}[\hat{B}] = -2 \sum_{n=-1}^1 k_{2,(n)} {}_2\mathcal{T}_{\ell m}^n \hat{E}_{1,\ell,m-n} (\Phi_2 + \Psi_2), \quad (3.73)$$

with $k_{1,(n)} = k_1^I \bar{e}_{(n)}^{*I}$, $k_{2,(n)} = k_2^I \bar{e}_{(n)}^{*I}$ and the subscript 1 on \hat{I} , \hat{E} and \hat{B} denoting the \mathbf{k}_1 -dependence, e.g. $\hat{I}_{1,\ell m} = \hat{I}_{\ell m}(\mathbf{k}_1)$. Since we align the azimuthal direction of the multipoles with the direction of $-\mathbf{k}$, we need to rotate multipoles of any 1st-order quantity X correspondingly such that

$$X_{\ell m}^{[I]}(\mathbf{k}') = \sqrt{\frac{4\pi}{2\ell+1}} Y_{\ell m}^*(\mathbf{k}') X_{\ell 0}^{[I]}(k') \quad (3.74)$$

where \mathbf{k}' stands for \mathbf{k}_1 or \mathbf{k}_2 and $X_{\ell 0}^{[\text{I}]}(k')$ is calculated with the azimuthal direction aligning with the direction of $-\mathbf{k}'$ ¹⁵.

3.2.2 Collision Operator

To complete the derivation of the 2nd-order Boltzmann equation, we need to study the Compton scattering between baryons and photons

$$\gamma(\mathbf{p}) + e(\mathbf{q}) \longleftrightarrow \gamma(\mathbf{p}') + e(\mathbf{q}'), \quad (3.75)$$

where a photon with momentum \mathbf{p} scatters with an electron with momentum \mathbf{q} and the outcome is a photon with momentum \mathbf{p}' and an electron with momentum \mathbf{q}' . We note that photons interact with protons as well through Compton scattering. However, the mass ratio of electron to proton (i.e. $m_e/m_p \sim 10^{-3}$) suppresses this type of scattering. Therefore, we can safely ignore protons in the collision operator. Furthermore, the strong Coulomb interaction between electrons and protons allows us to treat them as a single fluid. We will only list out the 2nd-order collision terms in the following and refer to [15, 83] for detailed derivations and discussions.

Pure Second-Order Collision Operator $\mathfrak{C}^{[\text{II}]}$

Again, the pure 2nd-order collision terms have the same forms as the corresponding collision terms in 1st-order

$$\mathfrak{C}_{\ell m}^{[\text{II}]}[\hat{I}] = \dot{\tau} \left(-\hat{I}_{\ell m} + \delta_\ell^0 \delta_m^0 \hat{I}_{00} + 4\delta_\ell^1 \tilde{v}_{\text{b},(m)} + \delta_\ell^2 \hat{\Pi}_m \right), \quad (3.76)$$

$$\mathfrak{C}_{\ell m}^{[\text{II}]}[\hat{E}] = \dot{\tau} \left(-\hat{E}_{\ell m} - \sqrt{6}\delta_\ell^2 \hat{\Pi}_m \right), \quad (3.77)$$

$$\mathfrak{C}_{\ell m}^{[\text{II}]}[\hat{B}] = -\dot{\tau} \hat{B}_{\ell m}, \quad (3.78)$$

where $\dot{\tau}(\eta)$ is the differential optical depth in the background order, $i\tilde{v}_{(m)} = v^I \tilde{e}_{(m)}^{*I}$ and

$$\hat{\Pi}_m \equiv \frac{1}{10} \left(\hat{I}_{2m} - \sqrt{6}\hat{E}_{2m} \right). \quad (3.79)$$

¹⁵As mentioned in Section 2.5.2, only $m = 0$ multipoles of 1st-order quantities are needed.

Quadratic Second-order Collision Operator $\mathfrak{C}^{[I,I]}(\mathbf{k})$

We define the kernel operator $\mathfrak{C}^{[I,I]}(\mathbf{k}_1, \mathbf{k}_2)$ as

$$\mathfrak{C}^{[I,I]}[\hat{X}](\mathbf{k}) \equiv \mathcal{T}_{\mathbf{k}_1, \mathbf{k}_2}(\mathbf{k}) \{ \mathfrak{C}^{[I,I]}[\hat{X}](\mathbf{k}_1, \mathbf{k}_2) \}, \quad (3.80)$$

where \hat{X} stands for \hat{I} , \hat{E} and \hat{B} . The quadratic 2nd-order collision operators for photon intensity and polarizations become

$$\begin{aligned} \mathfrak{C}_{\ell m}^{[I,I]}[\hat{I}] = & 2\dot{\tau} \left[\sum_{n=-1}^1 (-{}_0\mathcal{U}_{\ell m}^n \hat{I}_{1, \ell+1, m-n} + {}_0\mathcal{D}_{\ell m}^n \hat{I}_{1, \ell-1, m-n}) k_{2,(n)} \mathbf{v}_{b,2} \right. \\ & + \delta_\ell^0 \left(-\frac{4}{3} \mathbf{k}_1 \cdot \mathbf{k}_2 \mathbf{v}_{b,1} + 2 \sum_{n=-1}^1 {}_0\mathcal{U}_{00}^n \hat{I}_{1,1,-n} k_{2,(n)} \right) \mathbf{v}_{b,2} \\ & + 3\delta_\ell^1 \sum_{n=-1}^1 {}_0\mathcal{D}_{1n}^n \hat{I}_{1,0,m-n} k_{2,(n)} \mathbf{v}_{b,2} \\ & + \delta_\ell^2 \sum_{n=-1}^1 {}_0\mathcal{D}_{2m}^n \left(-\frac{1}{2} \hat{I}_{1,1,m-n} + 7k_{1,(m-n)} \mathbf{v}_{b,1} \right) k_{2,(n)} \mathbf{v}_{b,2} \\ & \left. + 5\delta_\ell^3 \sum_{n=-1}^1 {}_0\mathcal{D}_{3m}^n \hat{\Pi}_{1,m-n} k_{2,(n)} \mathbf{v}_{b,2} \right] \\ & + 2(\delta\dot{\tau}_1 + \Phi_1) \mathfrak{C}_{2,\ell m}[\hat{I}], \end{aligned} \quad (3.81)$$

$$\begin{aligned} \mathfrak{C}_{\ell m}^{[I,I]}[\hat{E}] = & 2\dot{\tau} \left[\sum_{n=-1}^1 (-2\mathcal{U}_{\ell m}^n \hat{E}_{1, \ell+1, m-n} + 2\mathcal{D}_{\ell m}^n \hat{E}_{1, \ell-1, m-n}) k_{2,(n)} \mathbf{v}_{b,2} \right. \\ & + \sqrt{6}\delta_\ell^2 \sum_{n=-1}^1 {}_0\mathcal{D}_{2m}^n \left(\frac{1}{2} \hat{I}_{1,1,m-n} - k_{1,(m-n)} \mathbf{v}_{b,1} \right) k_{2,(n)} \mathbf{v}_{b,2} \\ & \left. - 5\sqrt{6}\delta_\ell^3 \sum_{n=-1}^1 {}_2\mathcal{D}_{3m}^n \hat{\Pi}_{1,m-n} k_{2,(n)} \mathbf{v}_{b,2} \right] \\ & + 2(\delta\dot{\tau}_1 + \Phi_1) \mathfrak{C}_{2,\ell m}[\hat{E}], \end{aligned} \quad (3.82)$$

$$\mathfrak{C}_{\ell m}^{[I,I]}[\hat{B}] = -2\dot{\tau} \left[\sum_{n=-1}^1 {}_2\mathcal{T}_{\ell m}^n \left(\hat{E}_{1,\ell,m-n} - 2\sqrt{6}\delta_\ell^2 \hat{\Pi}_{1,m-n} \right) k_{2,(n)} \mathbf{v}_{b,2} \right], \quad (3.83)$$

where $\delta\dot{\tau}$ is the fraction of the 1st-order differential optical depth defined in Eq. (3.95). It is worth pointing out that there are energy exchanges (the terms in the second line of Eq. (3.81)) between electrons and photons in 2nd order, i.e. the Compton scattering is inelastic in 2nd order.

3.2.3 Collision Terms for Baryons

Here, we formulate the collision terms for baryons as shown in Eq. (3.45) to (3.47). Although there can be exchanges of energy and momentum between baryons and photons due to the Compton scattering, the stress-energy of baryons and photons as a whole has to conserve, i.e.

$$\nabla_\mu T_b^{\mu\nu} + \nabla_\mu T_r^{\mu\nu} = 0, \quad (3.84)$$

where the subscripts b and r denote baryons and photons respectively. Since the continuity and Euler equations of baryons are derived under the coordinate system (η, x^I) , the following transformations are useful

$$a \left(\nabla_A T^{AO} \right)^{[\text{III}]} = \left(\nabla_a T^{a0} \right)^{[\text{III}]} - 2\Phi^{[\text{I}]} \left(\nabla_a T^{a0} \right)^{[\text{II}]}, \quad (3.85)$$

$$a \left(\nabla_A T^{AI} \right)^{[\text{III}]} = \left(\nabla_a T^{ai} \right)^{[\text{III}]} + 2\Psi^{[\text{I}]} \left(\nabla_a T^{ai} \right)^{[\text{II}]}. \quad (3.86)$$

In tetrad basis, the covariant derivative of the stress-energy tensor of photons is related to the collision term [93] by¹⁶

$$\nabla_a T_r^{ab} = \frac{1}{(2\pi)^3} \int d\hat{\mathbf{n}} \int p^0 dp^0 p^b p^a e_a^O \mathfrak{C}[\mathcal{I}], \quad (3.87)$$

where $\mathcal{I} = \mathcal{I}(\eta, \mathbf{x}, p^0, \hat{\mathbf{n}})$ is the intensity distribution and \mathbf{e}_a is defined in Section 2.1.2. In second order, it can be shown that

$$\frac{1}{\bar{I}} \left(\nabla_a T_r^{a0} \right)^{[\text{III}]} = \frac{1}{a} \left(\mathfrak{C}_{00}^{[\text{III}]}[\hat{I}] + \mathfrak{C}_{00}^{[\text{I,II}]}[\hat{I}] - 2\Phi^{[\text{I}]} \mathfrak{C}_{00}^{[\text{II}]}[\hat{I}] \right), \quad (3.88)$$

$$\frac{1}{\bar{I}} \bar{e}_{(m)}^{*i} \left(\nabla_a T_r^{ai} \right)^{[\text{III}]} = \frac{i}{3a} \left(\mathfrak{C}_{1m}^{[\text{III}]}[\hat{I}] + \mathfrak{C}_{1m}^{[\text{I,II}]}[\hat{I}] - 2\Phi^{[\text{I}]} \mathfrak{C}_{1m}^{[\text{II}]}[\hat{I}] \right), \quad (3.89)$$

where

$$\mathfrak{C}[\hat{I}] \equiv \frac{1}{2\pi^2 \bar{I}} \int \mathfrak{C}[\mathcal{I}] (p^0)^3 dp^0. \quad (3.90)$$

¹⁶We have used the redefinition in Eq. (3.49) so that our $\mathfrak{C}[\mathcal{I}]$ is equal to $p^O C[f]$ in [93].

With the equations above, we can find that the collision terms are

$$\mathfrak{C}_b^\delta \equiv -2R\dot{\tau}\mathcal{F}_{\mathbf{k}_1, \mathbf{k}_2}(\mathbf{k}) \left\{ \sum_{n=-1}^1 \frac{(-1)^n}{4} \hat{I}_{1,1n} k_{2,(n)} v_{b,2} - (\mathbf{k}_1 \cdot \mathbf{k}_2) v_{b,1} v_{b,2} \right\}, \quad (3.91)$$

$$\mathfrak{C}_b^v \equiv -R\dot{\tau} \left(\frac{\hat{I}_{10}^{[\text{II}]}}{4} - \tilde{v}_{b,(0)}^{[\text{II}]} \right) - 2R\dot{\tau}\mathcal{F}_{\mathbf{k}_1, \mathbf{k}_2}(\mathbf{k}) \left\{ (\delta\dot{\tau}_1 + \Psi_1) \left(\frac{\hat{I}_{2,10}}{4} - \tilde{v}_{b,2,(0)} \right) - \hat{I}_{1,00} \tilde{v}_{b,2,(0)} + \frac{1}{4} \sum_{n=-1}^1 {}_0\mathcal{U}_{10}^n \hat{I}_{1,2,-n} \tilde{v}_{b,2,(n)} \right\}, \quad (3.92)$$

$$\mathfrak{C}_{b,(m)}^v \equiv R\dot{\tau} \left(\frac{\hat{I}_{1m}^{[\text{II}]}}{4} - \tilde{v}_{b,(m)}^{[\text{II}]} \right) + 2R\dot{\tau}\mathcal{F}_{\mathbf{k}_1, \mathbf{k}_2}(\mathbf{k}) \left\{ (\delta\dot{\tau}_1 + \Psi_1) \left(\frac{\hat{I}_{2,1m}}{4} - \tilde{v}_{b,2,(m)} \right) - \hat{I}_{1,00} \tilde{v}_{b,2,(m)} + \frac{1}{4} \sum_{n=-1}^1 {}_0\mathcal{U}_{1m}^n \hat{I}_{1,2,m-n} \tilde{v}_{b,2,(n)} \right\}, \quad (3.93)$$

where $m = \pm 1$, the density ratio $R \equiv (4/3)\bar{\rho}_r/\bar{\rho}_b$, $\tilde{v}_{b,(0)}^{[\text{II}]} = -k v_b$ and $\tilde{v}_{b,2,(0)} = -\hat{\mathbf{k}} \cdot \mathbf{k}_2 v_{b,2}$.

The formalism of the Boltzmann equation is almost finished. In the next subsection, we will discuss the evolution equation of the 1st-order optical depth to complete the derivation.

3.2.4 Perturbed Optical Depth

In order to elaborate the 2nd-order Compton scattering, we need to know the evolution of the optical depth up to 1st order as discussed in Section 3.2.2. Here, we will outline the formalism of the evolution equation of the 1st-order optical depth¹⁷. For what we are interested in, the perturbed optical depth is crucial for studying recombination era of the CMB. However, it can also be used to study the 21cm absorption[68].

To start with, we expand the differential optical depth up to 1st order

$$\dot{\tau} = \dot{\tau}(1 + \delta\dot{\tau}^{[\text{I}]}). \quad (3.94)$$

With the definition of differential optical depth in Eq. (2.57), its 1st-order perturbation can be written as

$$\delta\dot{\tau}^{[\text{I}]} = \frac{n_e^{[\text{I}]}}{\bar{n}_e} + \frac{x_e^{[\text{I}]}}{\bar{x}_e} = \delta_b^{[\text{I}]} + \delta x_e^{[\text{I}]}, \quad (3.95)$$

¹⁷See [65, 76, 93] for more details.

where $\delta x_e^{[1]} \equiv x_e^{[1]}/\bar{x}_e$ and the second equality holds due to the tight coupling between electrons and baryons through Coulomb scattering. That means, we need to solve the fraction of free electrons in 1st order. In principle, this can be done by formulating the Boltzmann equation of free electrons. Practically, it is not straightforward at all because many atomic transitions between many different states are involved during recombination. It was shown in [78] that hydrogen atoms during recombination can be approximated as atoms with effectively 3 levels¹⁸, i.e. ground state, first excited state and continuum state.

In the background order, the fraction of free electrons satisfies

$$\frac{\partial \bar{x}_e}{\partial \eta} = \frac{a}{\bar{n}_e} \bar{Q}[\bar{n}_{fe}, \bar{n}_b, \bar{T}_M, \bar{T}_R, \bar{H}], \quad (3.96)$$

where the overhead bar denotes the background-order quantities, $n_{fe} = n_e x_e$ is the number density of free electrons, n_b is the number density of total protons, T_M is the kinetic temperature of the electrons, T_R is the radiation temperature and H is the physical-time Hubble parameter. The function Q is defined as [93]

$$Q \equiv - \left[\alpha_B(T_M) n_{fe}^2 - \beta_B(T_R) (n_b - n_{fe}) e^{-B_{12}/(k_B T_R)} \right] C_H, \quad (3.97)$$

where k_B is the Boltzmann constant and $B_{12} \equiv E_1 - E_2$ with E_i as the ionization energy of the i -th level. The function α_B is defined as

$$\alpha_B(x) \equiv 10^{-19} F_H \frac{a y^b}{1 + c y^d} \text{m}^3 \text{s}^{-1}, \quad (3.98)$$

where $a = 4.309$, $b = -0.6166$, $c = 0.6703$, $d = 0.5300$, $y \equiv x/10^4 \text{K}$ and the fudge factor $F_H = 1.14$ accounts for non-equilibrium populations of the excited states [88]. The function β_B is defined as

$$\beta_B(T_R) \equiv \alpha_B(T_R) e^{-E_2/(k_B T_R)} \left(\frac{2\pi m_e k_B T_R}{h_P^2} \right)^{3/2}, \quad (3.99)$$

where m_e is the electron mass and h_P is the Planck constant. The function C_H is

$$C_H \equiv 1 - \frac{\beta_B(T_R)}{3PA_{21} + \Lambda_{2S \rightarrow 1S} + \beta_B(T_R)}, \quad (3.100)$$

¹⁸The approximation can be extended to Helium atoms. However, we consider only Hydrogen throughout this thesis.

where $\Lambda_{2S \rightarrow 1S} = 8.2245809\text{s}^{-1}$ and

$$3PA_{21} \approx \frac{8\pi H v_{21}^3}{(n_b - n_{fe})c^3}, \quad (3.101)$$

with v_{21} as the frequency of the Ly α photons and c as the speed of light.

In 1st order, we have

$$\frac{\partial}{\partial \eta} \delta x_e = \frac{a}{\bar{n}_{fe}} [(\Phi - \delta x_e) \bar{Q} + \delta Q], \quad (3.102)$$

where

$$\bar{Q} + \delta Q = Q [\bar{n}_{fe}(1 + \delta x_e), \bar{n}_b(1 + \delta_b), \bar{T}_M + \delta T_M, \bar{T}_R + \delta T_R, \bar{H}(1 + \delta_H)], \quad (3.103)$$

with

$$\delta T_R = \frac{\hat{I}_{00}}{4}, \quad \delta_H = -\Psi - \frac{\dot{\delta}_b}{3\mathcal{H}}. \quad (3.104)$$

If we are interested in recombination only, we can treat the temperatures of baryons and photons as the same, i.e. $T_M = T_R$. The evolutions of the 1st-order differential optical depth $\delta \tau^{[I]}$ are shown in Fig. 3.2 for different scales. It can be shown [93] that the 1st-order differential optical depth for large scales is well approximated by

$$\delta \tau^{[I]} \approx \delta_b \left(1 - \frac{\dot{x}_e}{3\mathcal{H}x_e} \right). \quad (3.105)$$

We remark that the 1st-order optical depth here is obtained by perturbing the fitting function of the background-order optical depth, which contains some fudge factors. This will undermine the accuracy of the calculated optical depth in 1st order, especially for small scales when the details of the underlying dynamics become important. For calculating the CMB bispectrum, the problem can be ignored in the squeezed limit where the contribution from the 1st-order optical depth with small scales is suppressed. To understand this, we note that the term in Boltzmann equation with the 1st-order optical depth is in form of $\delta \tau(k_1) \mathfrak{C}(k_2)$. In squeezed limit, the term is highly suppressed if $k_1 \gg k_2$ because the collision term $\mathfrak{C}(k_2)$ is negligible in large scales due to causality. However, this is not necessarily true for non-squeezed configurations. Therefore, a more sophisticated calculation for the perturbed optical depth should be considered in the future.

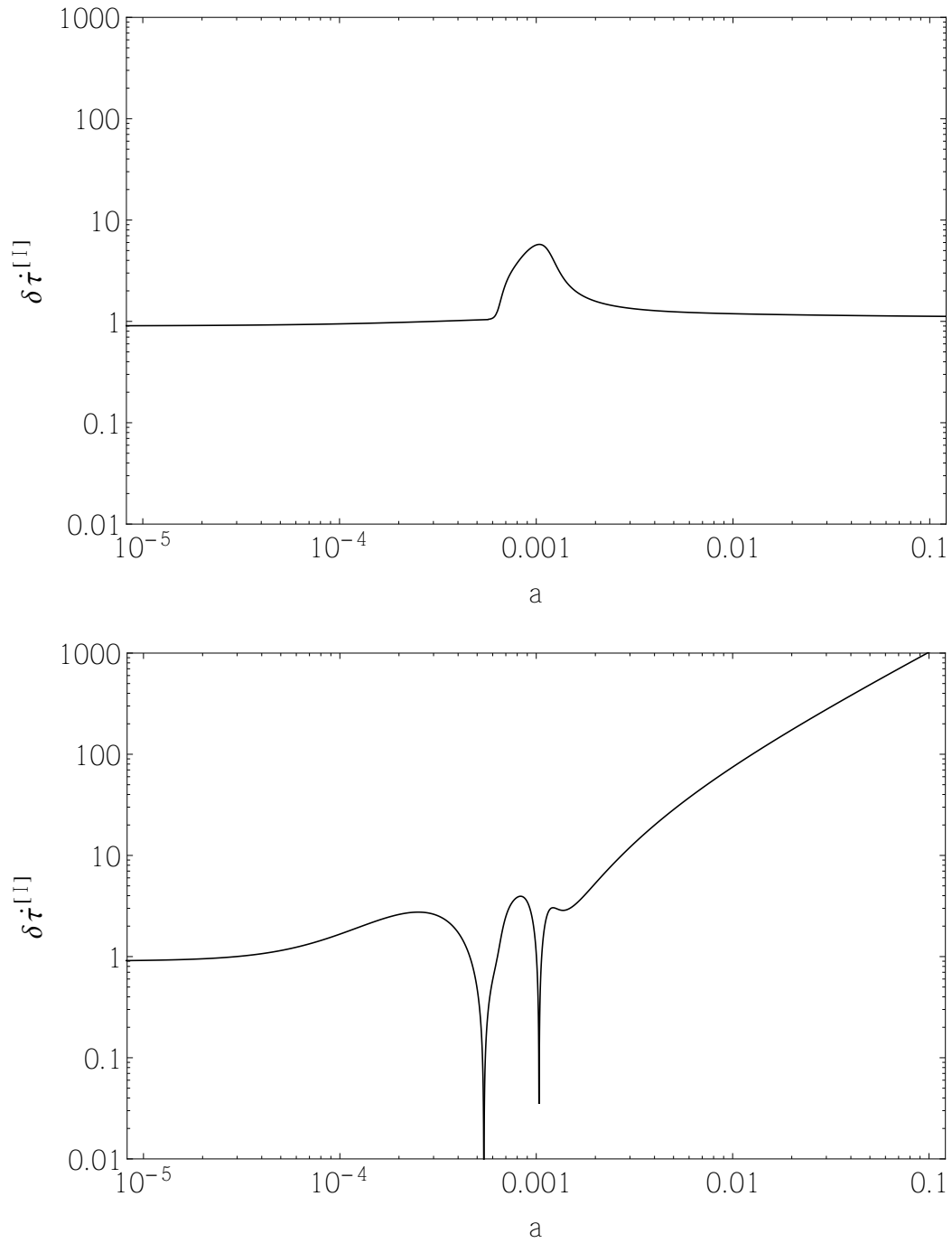


Figure 3.2 The graphs of transfer functions of the 1st-order differential optical depth $\delta\tau^{[I]}$ against the scale factor a for $k = 2 \times 10^{-5} \text{Mpc}^{-1}$ (upper panel) and $k = 0.045 \text{Mpc}^{-1}$ (lower panel). Here, we ignore Helium atoms.

3.2.5 Truncation Scheme for the Boltzmann Hierarchy

In principle, we need infinite multipoles ($\ell \rightarrow \infty$) for solving the Boltzmann equation but this is numerically infeasible. Instead, we truncate the hierarchy and solve the Boltzmann equation up to ℓ_{\max} . However, this will induce some errors. To mitigate the truncation error, we exploit the following scheme at $\ell = \ell_{\max}$ according to Appendix D of [87]

$$\hat{I}_{\ell m} = k \left[\sqrt{\frac{\ell + |m|}{\ell - |m|}} \frac{2\ell + 1}{2\ell - 1} \hat{I}_{\ell-1, m} - \frac{\ell + 1 + |m|}{k\eta} \hat{I}_{\ell m} \right], \quad (3.106)$$

$$\begin{aligned} \hat{E}_{\ell m} + i\hat{B}_{\ell m} = k & \left[\sqrt{1 - \frac{m^2}{\ell^2}} \sqrt{\frac{\ell + 2}{\ell - 1}} \frac{2\ell + 1}{2\ell - 1} (\hat{E}_{\ell-1, m} + i\hat{B}_{\ell-1, m}) \right. \\ & \left. + \left(-\frac{\ell + 3}{k\eta} + i\frac{m}{\ell} \right) (\hat{E}_{\ell m} + i\hat{B}_{\ell m}) \right]. \end{aligned} \quad (3.107)$$

3.3 Numerical Implementation

In Section 3.1 and 3.2, we have derived the 2nd-order EFEs (Eqs. (3.25)-(3.28), (3.38)-(3.39) and (3.42)), continuity and Euler equations (Eqs. (3.45)-(3.47)) and Boltzmann equation (Eqs. (3.61)-(3.63), (3.65)-(3.67), (3.76)-(3.78) and (3.81)-(3.83)), which govern the evolution of the 2nd-order perturbations. In this section, we will present the details of how to solve these evolution equations numerically. First of all, we will set the initial conditions of the 2nd-order perturbations in Section 3.3.1. Then, we generalize the TCA to 2nd order in Section 3.3.2. Finally, we discuss the numerical stability and convergence checking in Section 3.3.3.

Numerically, we solve the kernels of 2nd-order perturbations defined in Eq. (3.23) for different values of k_1 , k_2 and $\mathbf{k}_1 \cdot \mathbf{k}_2$ ¹⁹. Moreover, we rewrite all the governing equations so that they are symmetric on \mathbf{k}_1 and \mathbf{k}_2 , i.e.

$$F(\mathbf{k}_1, \mathbf{k}_2) \rightarrow \frac{1}{2} [F(\mathbf{k}_1, \mathbf{k}_2) + F(\mathbf{k}_2, \mathbf{k}_1)], \quad (3.108)$$

where F is any kernel depending on \mathbf{k}_1 and \mathbf{k}_2 . With this symmetry, we only need to solve the cases when $k_1 \geq k_2$. For the decomposition of 2nd-order multipoles, we align the azimuthal direction with the direction of $-\mathbf{k}$. However, unlike solving 1st-order perturbations,

¹⁹For our interest in the CMB bispectrum, other dependences of \mathbf{k}_1 and \mathbf{k}_2 can be integrated out. We will discuss this further in Section 4.2.

we need to solve the multipoles with $m \neq 0$ in 2nd order. As we will see in Section 4.2, multipoles with m up to 2 are enough when we calculate the CMB bispectrum using the line-of-sight approach. However, the main contribution should come from the scalar ($m = 0$) modes. Therefore, in our numerical calculation, we skip the 2nd-order vector and tensor perturbations which correspond to $m = 1$ and $m = 2$ modes respectively²⁰. We point out that evolution equations of 2nd-order perturbations with different m modes are decoupled and can be solved separately.

3.3.1 Initial Conditions

We have established all the governing equations of the 2nd-order perturbations in Section 3.1 and 3.2. To solve the equations, we need to fix the initial conditions of the perturbations up to 2nd order. The derivation of 2nd-order initial conditions is similar to that in 1st order, which is discussed in Section 2.5.3 and [71].

Non-Gaussianities can be generated during inflation as the primordial non-Gaussianities²¹ and after inflation through non-linear evolutions of the cosmological perturbations. The initial conditions in 2nd order will depend on what non-Gaussianities we consider. In this section, we consider the latter only. In particular, we assume the single-field slow-roll inflation in standard Cosmology. That is, we assume there are negligible primordial non-Gaussianities in the non-perturbative ζ [72]. The primordial non-Gaussianities of alternative inflationary models, if exist, evolve with the linear transfer function and their bispectra can be added linearly afterwards.

With the single field, the initial conditions are adiabatic and satisfy Eq. (2.64) and Eq. (2.65). In 2nd order, the energy densities and velocities of different components²²

$$\frac{1}{3}\delta_b^{[\text{II}]} = \frac{1}{3}\delta_c^{[\text{II}]} = \frac{1}{4}\hat{I}_{n,00}^{[\text{II}]} - \left(\frac{1}{4}\hat{I}_{n,00}\right)^2 = \frac{1}{4}\hat{I}_{r,00}^{[\text{II}]} - \left(\frac{1}{4}\hat{I}_{r,00}\right)^2, \quad (3.109)$$

$$-\frac{1}{4}\hat{I}_{n,10}^{[\text{II}]} = -\frac{1}{4}\hat{I}_{r,10}^{[\text{II}]} = k v_b^{[\text{II}]} + 2(\hat{\mathbf{k}} \cdot \mathbf{k}_2)\delta_{b,1} v_{b,2} = k v_c^{[\text{II}]} + 2(\hat{\mathbf{k}} \cdot \mathbf{k}_2)\delta_{c,1} v_{c,2}. \quad (3.110)$$

²⁰It has been found [52] that the vector and tensor perturbations have negligible effects on CMB bispectrum.

²¹See [24] for a review on primordial non-Gaussianities.

²²We express the initial conditions for the kernels of 2nd-order perturbations.

Moreover, the 2nd-order comoving curvature perturbation can be written as²³ [73, 87, 103]

$$\begin{aligned} \mathcal{R}^{[\text{II}]} = & \Psi^{[\text{II}]} + \frac{2}{3(1+\omega)\mathcal{H}} \left[\dot{\Psi}^{[\text{II}]} + \mathcal{H}\Phi^{[\text{II}]} - 4\mathcal{H}\Phi^2 - \frac{\dot{\Psi}^2}{\mathcal{H}} - 4(\Phi - \Psi)\dot{\Psi} \right] \\ & + (1+3c_s^2) \left[\frac{\delta}{3(1+\omega)} \right]^2 + \frac{4\Psi\delta}{3(1+\omega)}, \end{aligned} \quad (3.111)$$

where ω , c_s and δ are the equation of state, the speed of sound and the perturbed fractional energy density of the total fluid respectively. We consider the initial conformal time η_i such that $k\eta_i \ll 1$. That is, the universe is initially deep in the radiation-dominated era so that $\omega = c_s^2 = 1/3$ and $\bar{\rho}_{\text{tot}} = \bar{\rho}_n + \bar{\rho}_r$.

By ignoring $\dot{\Psi}$ up to 2nd order and terms with higher powers of $k\eta_i$, the initial kernels of 2nd-order perturbations fulfill²⁴

$$\mathcal{R}^{[\text{II}]} = \Psi^{[\text{II}]} + \frac{1}{2}\Phi^{[\text{II}]} - 2\Phi^2 + \frac{1}{8}\delta^2 + \Psi\delta, \quad (3.112)$$

$$\mathcal{C}_1 = 3\mathcal{H}^2\Phi^{[\text{II}]} + \frac{\kappa a^2}{2} \left(\bar{\rho}_n \hat{I}_{n,00}^{[\text{II}]} + \bar{\rho}_r \hat{I}_{r,00}^{[\text{II}]} \right), \quad (3.113)$$

$$\mathcal{C}_3 = \Psi^{[\text{II}]} - \Phi^{[\text{II}]} - \frac{\kappa a^2}{5k^2} \left(\bar{\rho}_n \hat{I}_{n,20}^{[\text{II}]} + \bar{\rho}_r \hat{I}_{r,20}^{[\text{II}]} \right), \quad (3.114)$$

$$\mathcal{C}_4 = \mathcal{H}\Phi^{[\text{II}]} - \frac{\kappa a^2}{6k} \left(\bar{\rho}_n \hat{I}_{n,10}^{[\text{II}]} + \bar{\rho}_r \hat{I}_{r,10}^{[\text{II}]} \right), \quad (3.115)$$

$$\hat{I}_{n,2m}^{[\text{II}]} = \frac{2k}{3} \hat{I}_{n,1m}^{[\text{II}]} + \mathfrak{L}_{2m}^{[\text{I},\text{I}]} [\hat{I}_n], \quad (3.116)$$

where \mathcal{C}_1 , \mathcal{C}_3 and \mathcal{C}_4 are defined in Eq. (3.29), (3.31) and (3.32) respectively and $\mathfrak{L}_{2m}^{[\text{I},\text{I}]} [\hat{I}]$ can be inferred by Eq. (3.65). Multipoles of neutrinos with $\ell \geq 3$ are highly suppressed by $k\eta_i$ and thus negligible. Due to the tight coupling of Compton scattering, multipoles of photons with $\ell \geq 2$ are neglected except the quadrupoles of photon intensity and E -mode polarization

$$\hat{I}_{r,2m}^{[\text{II}]} = \frac{1}{10} \left(\hat{I}_{r,2m}^{[\text{II}]} - \sqrt{6}\hat{E}_{2m}^{[\text{II}]} \right) + \mathfrak{C}_{2m}^{[\text{I},\text{I}]} [\hat{I}_r], \quad (3.117)$$

$$\hat{E}_{2m}^{[\text{II}]} = -\frac{\sqrt{6}}{10} \left(\hat{I}_{r,2m}^{[\text{II}]} - \sqrt{6}\hat{E}_{2m}^{[\text{II}]} \right) + \mathfrak{C}_{2m}^{[\text{I},\text{I}]} [\hat{E}], \quad (3.118)$$

where $\mathfrak{C}_{2m}^{[\text{I},\text{I}]} [\hat{I}]$ and $\mathfrak{C}_{2m}^{[\text{I},\text{I}]} [\hat{E}]$ can be deduced by (3.81) and (3.82) respectively. Using these

²³Due to the nonlinear relation of \mathcal{R} to the non-perturbative ζ , there are 2nd-order contributions to the initial value of \mathcal{R} . Hence, even with subsequent linear evolution only, there is a non-zero bispectrum.

²⁴Here, we use the 2nd-order EFEs and Boltzmann equations derived in Section 3.1 and 3.2.

two equations, we can find that the quadrupoles of photons are

$$\hat{I}_{r,2m}^{[\text{III}]} = \frac{5}{4} \sum_{n=-1}^1 {}_0\mathcal{D}_{2m}^n \hat{I}_{1,1(m-n)} \hat{I}_{2,1n}, \quad (3.119)$$

$$\hat{E}_{2m}^{[\text{III}]} = 0. \quad (3.120)$$

Furthermore, the solutions of Eq. (3.112) to (3.116) are

$$\begin{aligned} \Phi^{[\text{III}]} = \frac{10}{15+4f_n} & \left[\mathcal{R}^{[\text{III}]} + f_n \left(\frac{2\eta_i}{5} \mathcal{C}_4 + \frac{3}{10k^2\eta_i} \mathcal{L}_{20}^{[\text{I,I}]}[\hat{I}_n] \right) - \frac{3(1-f_n)}{5(k\eta_i)^2} \hat{I}_{r,20}^{[\text{III}]} \right. \\ & \left. - \mathcal{C}_3 + 2\Phi_1\Phi_2 - \frac{1}{8}\delta_1\delta_2 - \Psi_1\delta_2 \right], \end{aligned} \quad (3.121)$$

$$\Psi^{[\text{III}]} = \Phi^{[\text{III}]} + \frac{3}{5(k\eta_i)^2} \left[f_n \hat{I}_{n,20}^{[\text{III}]} + (1-f_n) \hat{I}_{r,20}^{[\text{III}]} \right] + \mathcal{C}_3, \quad (3.122)$$

$$\hat{I}_{n,00}^{[\text{III}]} = -2\Phi^{[\text{III}]} + \frac{2\mathcal{C}_1}{3\mathcal{H}^2}, \quad (3.123)$$

$$\hat{I}_{n,10}^{[\text{III}]} = 2k\eta_i(\Phi^{[\text{III}]} - \eta_i\mathcal{C}_4), \quad (3.124)$$

$$\hat{I}_{n,20}^{[\text{III}]} = \frac{2}{3}(k\eta_i)^2(\Phi^{[\text{III}]} - \eta_i\mathcal{C}_4) - \frac{\eta_i}{2} \mathcal{L}_{20}^{[\text{I,I}]}[\hat{I}_n], \quad (3.125)$$

where $\mathcal{R}^{[\text{III}]} \approx -2\mathcal{R}^2$ [72].

3.3.2 Tight-coupling Approximation

We develop the 2nd-order code based on CAMB[70] and use DVERK for solving the governing equations up to 2nd order²⁵. Since DVERK is a non-stiff ODE solver, it breaks down when the evolution equations are stiff. Physically, this happens when baryons and photons are tightly coupled at early time, i.e. $\tilde{\tau} \gg 1$. To tackle this numerical instability, we rewrite and solve the equations with the TCA at early time and then switch back to the full equations afterwards. In this subsection, we formulate the TCA for 1st- and 2nd-order perturbations²⁶. The key idea of TCA is to expand the Boltzmann equations into powers of the inverse $1/\tilde{\tau}$ up to a certain order depending on the precision required.

We start with the 1st-order perturbations. For energy densities of baryons and photons, we keep the corresponding evolution equations unchanged because the collision is elastic

²⁵We develop our own code for solving background- and 1st-order perturbations as well. In 1st order, we use Newtonian gauge instead of synchronous gauge in CAMB.

²⁶More details can be found in [71, 84].

and thus no terms with $\dot{\tau}$ are involved. That is, we have from Eq. (2.55) and Eq. (2.58)

$$\dot{\delta}_b - k^2 v_b - 3\dot{\Psi} = 0, \quad (3.126)$$

$$\dot{I}_{00} + \frac{k}{3}\hat{I}_{10} - 4\dot{\Psi} = 0. \quad (3.127)$$

For velocities of baryons and photons, we combine Eq. (2.56) with Eq. (2.58) and eliminate their collision terms to obtain two exact equations²⁷

$$\dot{v}_b = \frac{1}{1+R} \left[-\mathcal{H}v_b - R \left(\frac{1}{4}\hat{I}_{00} - \frac{1}{10}\hat{I}_{20} \right) + R \left(\frac{1}{4k}\dot{I}_{10} + \dot{v}_b \right) \right] - \Phi, \quad (3.128)$$

$$\dot{I}_{10} = \frac{4k}{R} (\dot{v}_b + \mathcal{H}v_b) + \frac{4k(1+R)}{R} \Phi + k \left(\hat{I}_{00} - \frac{2}{5}\hat{I}_{20} \right), \quad (3.129)$$

where we approximate Eq. (3.128) by expanding the term

$$\frac{1}{4k}\dot{I}_{10} + \dot{v}_b \approx \frac{2R\mathcal{H}}{1+R} \left(\frac{1}{4k}\hat{I}_{10} + v_b \right) - \frac{1}{(1+R)\dot{\tau}} \left[\frac{\ddot{a}}{a}v_b - \mathcal{H} \left(\frac{1}{2}\hat{I}_{00} + \Phi \right) - \frac{1}{4}\dot{I}_{00} \right] + O(\dot{\tau}^{-2}). \quad (3.130)$$

The quadrupoles of photons can be estimated by

$$\hat{I}_{20} \approx \frac{8k}{9\dot{\tau}}\hat{I}_{10}, \quad (3.131)$$

$$\hat{E}_{20} \approx -\frac{\sqrt{6}}{4}\hat{I}_{20}, \quad (3.132)$$

while higher multipoles are neglected due to the suppression of tight coupling.

For 2nd-order perturbations, we apply the TCA up to the leading order which is enough [84] for our purpose. The evolution equations of the first two moments are

$$0 = \dot{\delta}_b^{[\text{II}]} - k^2 v_b^{[\text{II}]} - 3\dot{\Psi}^{[\text{II}]} + \mathcal{L}^{[\text{I, I}]}[\delta_b], \quad (3.133)$$

$$0 = \dot{I}_{00}^{[\text{II}]} + \frac{k}{3}\hat{I}_{10}^{[\text{II}]} - 4\dot{\Psi}^{[\text{II}]} + \mathcal{L}_{00}^{[\text{I, I}]}[\hat{I}], \quad (3.134)$$

$$\begin{aligned} \dot{v}_b^{[\text{II}]} = \frac{1}{1+R} & \left[-\mathcal{H}v_b^{[\text{II}]} - R \left(\frac{1}{4}\hat{I}_{00}^{[\text{II}]} - \frac{1}{10}\hat{I}_{20}^{[\text{II}]} \right) - 2R \frac{\hat{\mathbf{k}} \cdot \mathbf{k}_2}{k} \left(\delta_1 v_2 + \delta_1 \dot{v}_2 \right) \right. \\ & \left. - \frac{1}{k} \mathcal{L}^{[\text{I, I}]}[v_b] + \frac{R}{4k} \mathcal{L}_{10}^{[\text{I, I}]}[\hat{I}] \right] - \Phi^{[\text{II}]}, \end{aligned} \quad (3.135)$$

²⁷We assume the speed of sound for baryons as zero, i.e. $c_s^2 = 0$ in Section 5.7 of [71].

$$\hat{I}_{10}^{[\text{III}]} = \frac{4k}{R} \left(\dot{v}_b^{[\text{III}]} + \mathcal{H}v_b^{[\text{III}]} \right) + \frac{4k(1+R)}{R} \Phi^{[\text{III}]} + k \left(\hat{I}_{00}^{[\text{III}]} - \frac{2}{5} \hat{I}_{20}^{[\text{III}]} \right) - \mathfrak{L}_{10}^{[\text{I,I}]}[\hat{I}] + \frac{4}{R} \mathfrak{L}^{[\text{I,I}]}[v_b], \quad (3.136)$$

where $\mathfrak{L}_{00}^{[\text{I,I}]}[\hat{I}]$ and $\mathfrak{L}_{10}^{[\text{I,I}]}[\hat{I}]$ can be evaluated by using Eq. (3.65) and

$$\begin{aligned} \mathfrak{L}^{[\text{I,I}]}[\delta_b] \equiv & -6(2\Psi_1 + \delta_{X,1})\dot{\Psi}_2 - 2(\mathbf{k} \cdot \mathbf{k}_2)\delta_{X,1}v_{X,2} - 2k_2^2(\Phi_1 + \Psi_1)v_{X,2} \\ & + 2\mathbf{k}_1 \cdot \mathbf{k}_2(2\Psi_1 - 2\Phi_1 - \mathcal{H}v_{X,1} - 2\dot{v}_{X,1})v_{X,2}, \end{aligned} \quad (3.137)$$

$$\begin{aligned} \mathfrak{L}^{[\text{I,I}]}[v_b] \equiv & \hat{\mathbf{k}} \cdot \mathbf{k}_2 [(\delta_{X,1} - \Phi_1 + \Psi_1)\dot{v}_{X,2} + \delta_{X,1}\Phi_2 + 2(\Psi_1 - \Phi_1)\Phi_2 \\ & - (\mathbf{k}_1 \cdot \mathbf{k}_2)v_{X,1}v_{X,2} + \mathcal{H}(\delta_{X,1} - \Phi_1 + \Psi_1)v_{X,2} - \dot{\Psi}_1 v_{X,2}]. \end{aligned} \quad (3.138)$$

While higher multipoles are negligible, the quadrupoles of photons in 2nd order are

$$\hat{I}_{20}^{[\text{III}]} = \frac{5}{4} \sum_{n=-1}^1 {}_0D_{20}^n \hat{I}_{1,1,n} \hat{I}_{2,1,-n}, \quad (3.139)$$

$$\hat{E}_{20}^{[\text{III}]} = 0. \quad (3.140)$$

3.3.3 Numerical Stability and Convergence

Technically, solving the 2nd-order perturbations is very similar to the case in 1st order, except two main differences. First, the quadratic terms in EFEs and Boltzmann equation require the solutions of 1st-order perturbations. Thus, we need to numerically evolve 1st-order perturbations and store the values in memory. When we elaborate the quadratic terms at a specific conformal time, we perform interpolation with the pre-calculated perturbations in 1st order. Second, since we have to solve the kernels of 2nd-order perturbations for a set of $(k_1, k_2, \hat{\mathbf{k}}_1 \cdot \hat{\mathbf{k}}_2, \eta)$ with $k_1 \geq k_2$, it is much more time-consuming compared to the 1st-order calculation with a set of (k, η) .

We will work with Newtonian gauge in the numerical calculation. However, a crucial trick is required when we solve the perturbations in Newtonian gauge, in both 1st and 2nd order. In the following, we present the trick for 2nd-order perturbations only but it is straightforward to apply the trick to 1st-order study. Instead of using either two of the 2nd-order EFEs in Eq. (3.25) to (3.28) directly²⁸, we use Eq. (3.27) and a combination of

²⁸For 1st order, the corresponding equations are Eq. (2.51) to (2.54).

Eq. (3.25) and Eq. (3.26) in form of $G^I_I + G^O_O/3$, which is rewritten as

$$\begin{aligned} & \ddot{\Psi} + 3\mathcal{H}\dot{\Psi} + \mathcal{H}\dot{\Phi} + \frac{k^2}{3}\Psi + \frac{\kappa a^2}{15} \sum_{n,r} \bar{\rho}_X \hat{I}_{X,20} + \frac{\kappa a^2}{6} \sum_{b,c} \bar{\rho}_X \delta_X + \left(\frac{\kappa a^2}{3} \sum_{b,c} \bar{\rho}_X + \frac{4\Lambda a^2}{3} \right) \Phi \\ & = \mathcal{T}_{\mathbf{k}_1, \mathbf{k}_2}(\mathbf{k}) \left\{ \frac{1}{3} \mathcal{C}'_1 + \mathcal{C}'_2 + \frac{4}{3} \left(\kappa a^2 \sum_{b,c} \bar{\rho}_X + 4\Lambda a^2 \right) \Phi_1 \Phi_2 \right\}, \end{aligned} \quad (3.141)$$

where

$$\mathcal{C}'_1 \equiv \mathcal{C}_1 - 12\mathcal{H}^2 \Phi_1 \Phi_2, \quad (3.142)$$

$$\mathcal{C}'_2 \equiv \mathcal{C}_2 - (4\mathcal{H}^2 + 8\dot{\mathcal{H}}) \Phi_1 \Phi_2. \quad (3.143)$$

The reason why the trick is essential is that either Eq. (3.25) or Eq. (3.26) contains some pairs of terms with large numerical values. However, the sum of each pair can be several orders of magnitude smaller. The cancellations boost up the numerical errors such that the solutions become unstable. Eq. (3.141) works well in the radiation-dominated era because it replaces the sums of these pairs with small quantities explicitly. To understand this physically, we notice that quantities, such as \mathcal{H}^2 and $\dot{\mathcal{H}}$, are determined by $\bar{\rho}_n$ and $\bar{\rho}_r$ exclusively during radiation-dominated era. Nevertheless, the sum $\mathcal{H}^2 + \dot{\mathcal{H}}$ is of order $\kappa a^2(\bar{\rho}_b + \bar{\rho}_c)$ which can be a few orders of magnitude smaller. Since we are interested in the evolution of 2nd-order perturbations up to recombination, Eq. (3.141) is sufficient over the time covered. For matter-dominated era, Eq. (3.26) and Eq. (3.27) can be used directly with the replacement

$$\mathcal{H}^2 + 2\dot{\mathcal{H}} = -\frac{\kappa a^2}{3}(\bar{\rho}_n + \bar{\rho}_r) + \Lambda a^2, \quad (3.144)$$

to tackle the large-value cancellations.

Solving the 2nd-order perturbations is numerically non-trivial. It is thus important to verify the calculation. One way to do so is to make use of the redundant EFEs to check if numerical errors are well controlled. In Fig. 3.3 to 3.5, we show the absolute numerical difference by elaborating the unused constraint equation Eq. (3.28). We can see that the differences are within percentage level for different configurations of k_1 , k_2 and $\mathbf{k}_1 \cdot \mathbf{k}_2$. Moreover, there are two leaps of the differences in each plot. The one at $a \sim 1.5 \times 10^{-5}$ corresponds to the turning-off of TCA in 1st-order equations while the other one at $a \sim 5 \times 10^{-5}$ comes from the turning-off of TCA in 2nd-order equations. We remark that we apply the TCA up

to the leading order only for 2nd-order perturbations²⁹. Therefore, we can expect the errors to be reduced by at least a factor of 100 if we include the next-to-leading-order correction of the TCA. This can be done in the future if higher precision is needed. However, the leading-order TCA is sufficient for calculating the CMB bispectrum at recombination. Finally, we point out that although a significant deviation of the constraint equation is shown for $a \lesssim 10^{-5}$ in Fig. 5.8 of [80], we manage to reproduce their curvature potential derivative for $a \gtrsim 10^{-5}$. We confirm that the deviation does not affect the bispectrum calculation.

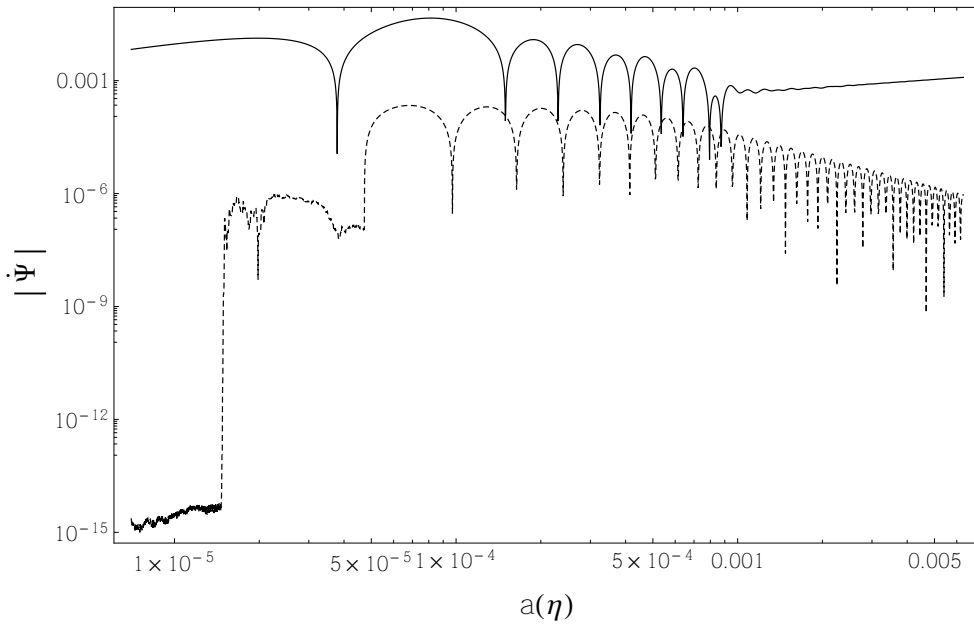


Figure 3.3 The graph of the absolute 2nd-order kernel of $\dot{\Psi}$ (solid line) against the scale factor a with $k_0 = 0.199\text{Mpc}^{-1}$, $k_1 = 0.2\text{Mpc}^{-1}$, $k_2 = 0.002\text{Mpc}^{-1}$ and $\hat{\mathbf{k}}_1 \cdot \hat{\mathbf{k}}_2 = -0.684$. The dashed line shows the absolute numerical difference in the constraint equation Eq. (3.28).

²⁹See Section 3.3.2 for more details about the TCA.

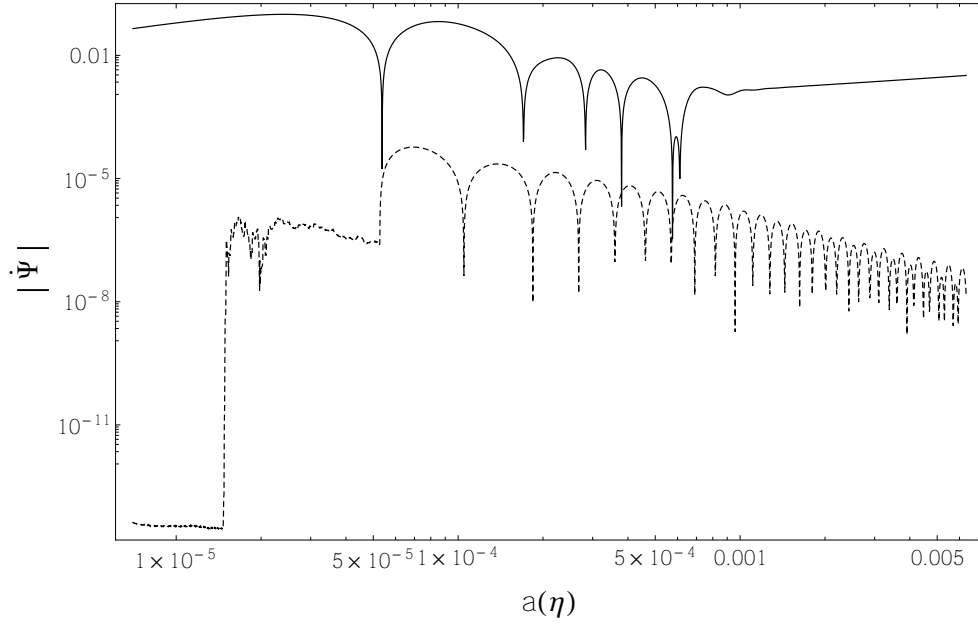


Figure 3.4 The graph of the absolute 2nd-order kernel of $\dot{\Psi}$ (solid line) against the scale factor a with $k_0 = 0.159\text{Mpc}^{-1}$, $k_1 = 0.2\text{Mpc}^{-1}$, $k_2 = 0.2\text{Mpc}^{-1}$ and $\hat{\mathbf{k}}_1 \cdot \hat{\mathbf{k}}_2 = -0.684$. The dashed line shows the absolute numerical difference in the constraint equation Eq. (3.28).

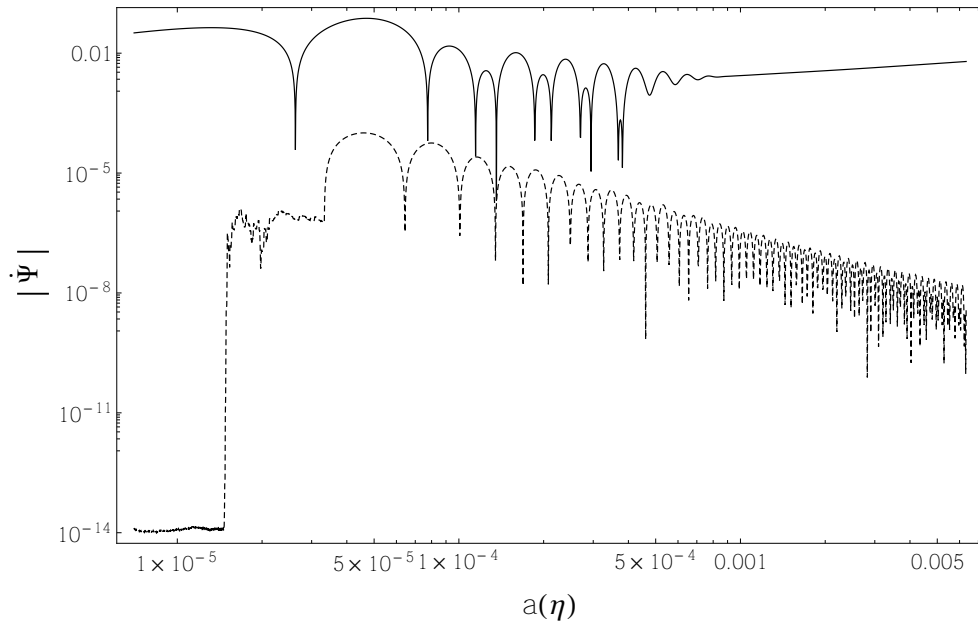


Figure 3.5 The graph of the absolute 2nd-order kernel of $\dot{\Psi}$ (solid line) against the scale factor a with $k_0 = 0.4\text{Mpc}^{-1}$, $k_1 = 0.2\text{Mpc}^{-1}$, $k_2 = 0.2\text{Mpc}^{-1}$ and $\hat{\mathbf{k}}_1 \cdot \hat{\mathbf{k}}_2 = 1$. The dashed line shows the absolute numerical difference in the constraint equation Eq. (3.28).

Chapter 4

CMB Bispectrum during Recombination

Even if the quantum fluctuations from inflation are perfectly Gaussian, non-Gaussianities can exist through the nonlinear evolution afterwards. These post-inflationary non-Gaussianities can have significant impacts on cosmic microwave background (CMB) study. Depending on when they are generated, we can classify them into two categories: recombination bispectra if they are produced during the recombination and late-time bispectra if they are imprinted from the late-time large-scale structures. Understanding the shapes of these bispectra is crucial for eliminating their contaminations to the primordial non-Gaussianities and verifying the gravitational theory in cosmological scales. While the late-time ISW-lensing¹ bispectra are known to be important [39, 46, 69], there are still discrepancies about the significance of the recombination bispectra². A complete analysis is thus desired for resolving those discrepancies and predicts the detectability of the recombination bispectra for the upcoming CMB experiments.

To study the recombination bispectra, it is necessary to calculate the cosmological perturbations up to 2nd order, which has been discussed in details in Chapter 3. In this chapter, we will focus on how these perturbations are linked to the observation – CMB temperature bispectrum. We present the numerical calculation of the bispectrum produced around recombination. More precisely, we include all the effects due to *the Compton collision at recombination and the early-time ISW-related couplings around recombination*. In order to do so, we have to distinguish the physics at recombination from the late-time mechanisms. This separation leads to a 2nd-order line-of-sight (LOS) integrand which is different from the one used in [52, 82] and provides an alternative way to calculate the CMB bispectrum

¹ISW stands for the integrated Sachs-Wolfe effect.

²See, for example, [11, 13, 20, 29, 57, 58, 66, 75, 86, 87, 94].

around recombination. Our approach interprets the quadratic 2nd-order effects as couplings of two well-known 1st-order effects in Newtonian gauge ³. This provides a clear physical picture about what effects are taken into account.

We start with several definitions of the CMB temperature in 2nd order in Section 4.1. Then, we calculate the 2nd-order CMB temperature anisotropies through the LOS approach and formulate the recombination bispectrum under the flat-sky and thin-shell approximations in Section 4.2. In particular, we present the trick to separate the effects during recombination from the late-time effects in 2nd-order in Section 4.2.2. This trick also solves the hierarchy problem of 2nd-order LOS approach. In Section 4.3, the details about the numerical calculations are given. We present the calculated bispectrum at recombination and validate it with the analytical solution in squeezed limit. Moreover, we constrain f_{NLS} for different templates and forecast the signal-to-noise for the recombination bispectrum. Finally, we discuss some potential further studies and draw the conclusion in Section 4.4.

4.1 Definition of CMB Temperature in Second Order

Since the inelastic 2nd-order Compton scattering induces the CMB spectral distortions [85], there does not exist a unique way of defining the CMB temperature in 2nd order. In this section, we will discuss several possible definitions. First, we assume that the CMB temperature T can be related to the distribution function of the CMB photons in form of the black-body spectrum

$$\mathcal{I}(\eta, \mathbf{x}, p^0, \hat{\mathbf{n}}) = \left[e^{p^0/T(\eta, \mathbf{x}, p^0, \hat{\mathbf{n}})} - 1 \right]^{-1}, \quad (4.1)$$

where the CMB temperature anisotropies Θ can be expanded into perturbations as

$$T(\eta, \mathbf{x}, p^0, \hat{\mathbf{n}}) = \bar{T}(\eta) \left[1 + \Theta^{[\text{I}]}(\eta, \mathbf{x}, \hat{\mathbf{n}}) + \frac{1}{2} \Theta^{[\text{III}]}(\eta, \mathbf{x}, p^0, \hat{\mathbf{n}}) \right], \quad (4.2)$$

with the background CMB temperature \bar{T} . We note that $\Theta^{[\text{III}]}$ depends on the photon momentum p^0 due to the spectral distortion. By applying Taylor expansion at $\Theta = 0$, we obtain

$$\mathcal{I}(\eta, \mathbf{x}, p^0, \hat{\mathbf{n}}) = \bar{\mathcal{I}} - p^0 \frac{\partial \bar{\mathcal{I}}}{\partial p^0} \Theta^{[\text{I}]} + \left[\frac{(p^0)^2}{2} \frac{\partial^2 \bar{\mathcal{I}}}{\partial p^0 \partial p^0} + p^0 \frac{\partial \bar{\mathcal{I}}}{\partial p^0} \right] (\Theta^{[\text{I}]})^2 - \frac{p^0}{2} \frac{\partial \bar{\mathcal{I}}}{\partial p^0} \Theta^{[\text{III}]}, \quad (4.3)$$

³See Section 4.2.2 for more details,

where $\bar{\mathcal{I}}(\eta, p^0)$ is the photon intensity in background order. After performing the energy integration as in Eq. (2.14), we have

$$\hat{I} = 1 + 4\Theta^{[\text{I}]}(\eta, \mathbf{x}, \hat{\mathbf{n}}) + 6[\Theta^{[\text{I}]}(\eta, \mathbf{x}, \hat{\mathbf{n}})]^2 - \frac{1}{4\pi^2\bar{I}(\eta)} \int \frac{\partial \bar{\mathcal{I}}}{\partial p^0} \Theta^{[\text{III}]}(\eta, \mathbf{x}, p^0, \hat{\mathbf{n}}) (p^0)^4 dp^0. \quad (4.4)$$

Depending on details of the spectral distortion, $\Theta^{[\text{III}]}$ in the last integral of Eq. (4.4) can have different dependences on p^0 .

4.1.1 Brightness Temperature

Because of the spectral distortion, we cannot simply fit the perturbed CMB photon spectrum with black-body spectrum to define the CMB temperature. Instead of using Eq. (4.2), we define the brightness temperature $T_I \equiv \bar{T} [1 + \Theta_I(\eta, \mathbf{x}, \hat{\mathbf{n}})]$ such that

$$\Theta_I \equiv \frac{1}{4} [\hat{I}(\eta, \mathbf{x}, \hat{\mathbf{n}}) - 1]. \quad (4.5)$$

In particular, we have $\Theta_I^{[\text{I}]} = \Theta^{[\text{I}]}$ and

$$\Theta_I^{[\text{III}]} = \frac{1}{4} \hat{I}^{[\text{III}]} = 3[\Theta^{[\text{I}]}(\eta, \mathbf{x}, \hat{\mathbf{n}})]^2 - \frac{1}{8\pi^2\bar{I}(\eta)} \int \frac{\partial \bar{\mathcal{I}}}{\partial p^0} \Theta^{[\text{III}]}(\eta, \mathbf{x}, p^0, \hat{\mathbf{n}}) (p^0)^4 dp^0. \quad (4.6)$$

4.1.2 Bolometric Temperature

We define the bolometric temperature $T_E \equiv \bar{T} [1 + \Theta_E(\eta, \mathbf{x}, \hat{\mathbf{n}})]$ by

$$(1 + \Theta_E)^4 \equiv \hat{I}(\eta, \mathbf{x}, \hat{\mathbf{n}}). \quad (4.7)$$

In 1st order, bolometric temperature is identical to brightness temperature, i.e. $\Theta_E^{[\text{I}]} = \Theta_I^{[\text{I}]}$. However, they are not the same in 2nd order

$$\begin{aligned} \Theta_E^{[\text{III}]} &= \Theta_I^{[\text{III}]} - 3\left(\Theta_I^{[\text{I}]}\right)^2 \\ &= \frac{1}{4} \hat{I}^{[\text{III}]} - \frac{3}{16} (\hat{I}^{[\text{I}]})^2. \end{aligned} \quad (4.8)$$

It can be proven that the black-body radiation with the bolometric temperature has the same energy density as the actual distribution [87]. In other words, we define the CMB tem-

perature such that the energy density of the actual distribution matches with that of the black-body radiation with the bolometric temperature. It is worth pointing out that the CMB bispectra calculated will be different when different definitions of temperature are adopted. However, these bispectra are related analytically and can be transformed from one into another straightforwardly. We will discuss this further in Section 4.2.

4.2 Formulating Second-order Bispectrum

In this section, we first extend the LOS approach to calculate the 2nd-order CMB temperature anisotropies. Then, we apply the integration by parts (IBPs) to the LOS integrand in order to separate the recombination effects from the late-time ones. Finally, we establish the formalism for the temperature bispectrum generated from 2nd-order perturbations.

4.2.1 Second-order Line-of-sight Approach

To calculate the 2nd-order temperature anisotropies, we first rewrite the 2nd-order Boltzmann equation using Eq. (3.48), (3.61) and (3.76) such that

$$\dot{\Delta}^{[\text{II}]} + i\mathbf{k} \cdot \hat{\mathbf{n}} \Delta^{[\text{II}]} + \dot{\bar{\tau}} \Delta^{[\text{II}]} = \sum_{\ell m} \frac{1}{N_\ell} e^{\bar{\tau}} \left(\tilde{S}_{\ell m}^{[\text{II}]} + \tilde{S}_{\ell m}^{[\text{I,I}]} \right) Y_{\ell m}(\hat{\mathbf{n}}), \quad (4.9)$$

where $4\Delta \equiv \hat{I}$ is the fractional brightness, $\bar{\tau} \equiv \int_{\eta}^{\eta_0} \dot{\tau}(\tilde{\eta}) d\tilde{\eta}$ is the optical depth, N_ℓ is defined in Eq. (C.2) and multipoles of the purely 2nd-order and quadratic source functions ($\tilde{S}^{[\text{II}]}$ and $\tilde{S}^{[\text{I,I}]}$ respectively) are defined as⁴

$$e^{\bar{\tau}} \tilde{S}_{\ell m}^{[\text{II}]} \equiv \delta_\ell^0 \delta_m^0 \dot{\Psi} + \delta_\ell^1 \delta_m^0 k \Phi - \frac{k}{\sqrt{3}} \delta_\ell^2 \left(\delta_m^1 \tilde{\mathcal{B}}_{(1)} + \delta_m^{-1} \tilde{\mathcal{B}}_{(-1)} \right) - \delta_\ell^2 \left(\delta_m^2 \tilde{\mathcal{H}}_{(2)} + \delta_m^{-2} \tilde{\mathcal{H}}_{(-2)} \right) + \dot{\bar{\tau}} \left(\delta_\ell^0 \delta_m^0 \Delta_{00} + \delta_\ell^1 \tilde{v}_{b,(m)} + \frac{1}{4} \delta_\ell^2 \hat{\Pi}_m \right), \quad (4.10)$$

$$e^{\bar{\tau}} \tilde{S}_{\ell m}^{[\text{I,I}]} \equiv -\frac{1}{4} \mathcal{L}_{\ell m}^{[\text{I,I}]}[\hat{I}] + \frac{1}{4} \mathbf{e}_{\ell m}^{[\text{I,I}]}[\hat{I}]. \quad (4.11)$$

⁴We omit [II] denoting the 2nd-order perturbations.

After integrating over the conformal time and wavenumbers, the 2nd-order fractional brightness can be expressed as

$$\Delta^{[\text{II}]}(\eta_0, \mathbf{k}, \hat{\mathbf{n}}) = \mathcal{T}_{\mathbf{k}_1, \mathbf{k}_2}(\mathbf{k}) \left\{ \int_0^{\eta_0} d\eta e^{-i\mathbf{k} \cdot \hat{\mathbf{n}} r} \sum_{\ell m} \frac{1}{N_\ell} \left(\tilde{S}_{\ell m}^{[\text{II}]} + \tilde{S}_{\ell m}^{[\text{I}, \text{I}]} \right) Y_{\ell m}(\hat{\mathbf{n}}) \right\}, \quad (4.12)$$

where $r \equiv \eta_0 - \eta$.

As expected, the 2nd-order source function consists of two parts: purely 2nd-order part and quadratic part. The purely 2nd-order part has the same form as the 1st-order source function [50] and requires solutions of 2nd-order perturbations. However, purely 2nd-order source terms exist up to $\ell = 2$. In contrast, the quadratic part requires solutions of 1st-order perturbations only but the source terms extend to infinitely high ℓ modes. Thus, there is a hierarchy problem when we perform the LOS approach to the quadratic source. Moreover, since we are interested in the 2nd-order effects imprinted during recombination, we have to distinguish these effects from the late-time effects (e.g. CMB lensing) consistently. In the next subsection, we will show how performing IBPs can resolve the hierarchy problem and identify the effects during recombination.

4.2.2 Separation between Recombination and Late Time

In this subsection, we demonstrate a trick to distinguish between the effects during recombination and late times. The trick also mitigates the hierarchy problem so that it is enough to truncate the multipoles of the quadratic source function at low ℓ s. Before we work on the 2nd-order source function, it is useful to review how we separate the early-time and late-time ISW effect in 1st order. The 1st-order fractional brightness at time η can be expressed in Fourier space as Eq. (2.75) with the 1st-order source function in form of⁵

$$\tilde{S}_T^{[\text{I}]} = e^{-\bar{\tau}} \left(\dot{\Psi} - i\mathbf{k} \cdot \hat{\mathbf{n}} \Phi + \dot{\bar{\tau}} \Delta + \frac{\mathcal{E}}{4} \right). \quad (4.13)$$

The first two terms generate redshift effects on the background CMB due to the linear perturbations of the metric while the last two terms contain all the effects generated at recombination due to the Compton scattering⁶. As shown in Section 2.6.1, we can use the IBPs

⁵For simplicity, we have omitted the superscript [I] on the right-hand side of the equation.

⁶We ignore the reionization and other late-time scatterings throughout this thesis.

on the second term of Eq. (4.13) such that the source term becomes

$$e^{-\bar{\tau}} \left(-\delta(\bar{\eta} - \eta) \Phi + \dot{\bar{\tau}} \Phi + \dot{\Phi} + \dot{\Psi} + \dot{\bar{\tau}} \Delta + \frac{\mathfrak{C}}{4} \right), \quad (4.14)$$

where $\delta(\eta)$ is the Dirac delta function. The first two terms encode the Sachs-Wolfe (SW) effect while the next two terms are the ISW effect.

Integration by parts are not merely mathematical tricks. Since we are replacing derivative terms in the integrand with *non-zero boundary terms*, this means that it is important where we evaluate the boundary terms at. Physically, performing the IBPs “re-distributes” the physical effects along the LOS integration. In this case, Eq. (4.14) separates the redshift effects occurring at different times physically as follows. The first two terms are the SW effect due to the difference of the gravitational potential between recombination and time η , i.e. the SW effect measured by an observer at time η . In particular, Φ in the first term is a constant when $\eta = \eta_0$. The third and fourth terms (i.e. $\dot{\Phi} + \dot{\Psi}$) include the early-time ISW effect from the time-varying gravitational potential due to the transition from radiation-dominated to matter-dominated era and the late-time ISW effect from the time-varying gravitational potential due to the domination of dark energy. In this paper, we calculate the bispectrum at and around recombination. Explicitly, it means that we include SW and early-time ISW but exclude late-time ISW. In the following, we extend the separation to the redshift-related couplings in 2nd order.

The quadratic part of the 2nd-order source function can be read in configuration space as⁷

$$\begin{aligned} \tilde{S}^{[L,I]} = 2e^{-\bar{\tau}} \left[S^{ij} \partial_j (\Phi + \Psi) \frac{\partial \Delta}{\partial n^i} - (\Phi + \Psi) n^i \partial_I \Delta + 4(-n^i \partial_I \Phi + \dot{\Psi}) \Delta \right. \\ \left. + (\Phi - \Psi) n^i \partial_I \Phi + 2\Psi \dot{\Psi} \right] + \frac{1}{4} e^{-\bar{\tau}} \mathfrak{C}^{[L,I]}[\hat{I}], \end{aligned} \quad (4.15)$$

where S^{ij} is the screen projector defined in Eq. (2.6) and $\mathfrak{C}^{[L,I]}$ is the quadratic collision operator expressed in Eq. (3.81). The first three terms in Eq. (4.15), which contain fractional brightness Δ , are numerically problematic. It is because the contributions of the LOS approach from these terms extend to late times at which high multipoles of the brightness are generated through propagation and projection onto the spherical harmonics. This means that solving these terms is numerically expensive since truncating at low multipoles is not

⁷The notation for 1st-order perturbations is omitted for simplicity.

enough. Because we focus on the contributions at and around recombination, we ignore the first and second terms in Eq. (4.15) which correspond to the lensing and time-delay effects respectively and contribute at late times. The third term in Eq. (4.15) is responsible for the 1st-order redshift effects, including the SW and ISW effects, on the 1st-order temperature anisotropies. Intuitively, it includes contributions at and around recombination (i.e. couplings with SW and early-time ISW effect) as well as late-time contributions (i.e. couplings with late-time ISW effect). The key issue here is to *physically distinguish between the early-time and late-time effects for those redshift-related couplings*. Although the quadratic collision operator $\mathfrak{C}^{[1,1]}$ contains high ℓ multipoles, its contribution is concentrated at recombination when high ℓ multipoles are still highly suppressed⁸.

From now on, we focus on the third term of Eq. (4.15). We can express its contribution (denoted by the subscript R) to the 2nd-order fractional brightness as

$$\Delta_{\text{R}}^{[\text{III}]}(\eta_0, \mathbf{k}, \hat{\mathbf{n}}) = 8 \mathcal{T}_{\mathbf{k}_1, \mathbf{k}_2}(\mathbf{k}) \left\{ \int_0^{\eta_0} d\eta e^{-i\mathbf{k} \cdot \hat{\mathbf{n}} r - \bar{\tau}} \Delta_1(\hat{\mathbf{n}}) (\Psi_2 - i\mathbf{k}_2 \cdot \hat{\mathbf{n}} \Phi_2) \right\}, \quad (4.16)$$

where the subscripts 1 and 2 denote the dependence on \mathbf{k}_1 and \mathbf{k}_2 respectively. As mentioned in Section 4.2 of [82], if we perform IBPs on the term with $\mathbf{k}_2 \cdot \hat{\mathbf{n}}$ in Eq. (4.16), we will get a time integration whose integrand contains the time derivative of the 1st-order fractional brightness $\dot{\Delta}$. We can iteratively apply IBPs on that time integration but this approach fails to single out a unique recombination contribution. More seriously, contributions from higher multipoles grow when we integrate over the time further after recombination. That is, the hierarchy problem remains unsolved.

However, there exists a unique way to separate the early-time and late-time redshift effects which is physically reasonable and allows us to calculate the bispectrum around recombination with a truncation at low ℓ s. The key is to realize that Eq. (4.16) contains a double time integration by substituting Δ_1 with Eq. (2.75). We can then exchange the inner and outer time integrations such that Eq. (4.16) is rewritten as

$$\Delta_{\text{R}}^{[\text{III}]} = 8 \mathcal{T}_{\mathbf{k}_1, \mathbf{k}_2}(\mathbf{k}) \left\{ \int_0^{\eta_0} d\tilde{\eta} e^{-i\mathbf{k}_1 \cdot \hat{\mathbf{n}} \tilde{r}} \tilde{S}_T(\tilde{\eta}, \mathbf{k}_1, \hat{\mathbf{n}}) \int_{\tilde{\eta}}^{\eta_0} d\eta e^{-i\mathbf{k}_2 \cdot \hat{\mathbf{n}} r} [\Psi_2(\eta) - i\mathbf{k}_2 \cdot \hat{\mathbf{n}} \Phi_2(\eta)] \right\}. \quad (4.17)$$

⁸In Section 4.3, we find that ℓ up to about 10 is sufficient for getting a converging bispectrum for the quadratic collision terms.

Now, we perform IBPs on the integration over η and obtain

$$\Delta_{\text{R}}^{[\text{III}]} = 8 \mathcal{T}_{\mathbf{k}_1, \mathbf{k}_2}(\mathbf{k}) \left\{ \int_0^{\eta_0} d\tilde{\eta} e^{-i\mathbf{k} \cdot \hat{\mathbf{n}} \tilde{r}} \tilde{S}_T(\tilde{\eta}, \mathbf{k}_1, \hat{\mathbf{n}}) \left\{ \Phi_2(\tilde{\eta}) + \int_{\tilde{\eta}}^{\eta_0} d\eta e^{i\mathbf{k}_2 \cdot \hat{\mathbf{n}}(\tilde{r}-r)} [\dot{\Phi}_2(\eta) + \dot{\Psi}_2(\eta)] \right\} \right\}. \quad (4.18)$$

We make use of the fact that $\mathbf{k} = \mathbf{k}_1 + \mathbf{k}_2$ to get the exponential with \mathbf{k} in the first line of Eq. (4.18). By doing so, we do not produce the problematic term with $\dot{\Delta}$ through IBPs. Note that we can ignore Φ evaluated at present η_0 because it is a constant and does not contribute to the bispectrum. The physical meaning of Eq. (4.18) is clear. Analogous to 1st-order redshift effects which come from the background-order CMB signals redshifted by the 1st-order perturbed metric, we have the 1st-order temperature anisotropies redshifted by the 1st-order SW and ISW effects to generate 2nd-order temperature anisotropies, corresponding to the first and second terms in Eq. (4.18) respectively. This trick allows us to distinguish between the early-time and late-time redshift effects similar to what we have done typically in 1st-order.

We now consistently separate the early-time and late-time redshift effects of the 1st-order source function \tilde{S}_T . For the first term of Eq. (4.18), we apply the IBPs on the term with $-i\mathbf{k}_1 \cdot \hat{\mathbf{n}} \Phi_1$ from the source function \tilde{S}_T and obtain

$$- \int_0^{\eta_0} d\tilde{\eta} e^{-i\mathbf{k} \cdot \hat{\mathbf{n}} \tilde{r} - \bar{\tau}} i\mathbf{k}_1 \cdot \hat{\mathbf{n}} \Phi_1 \Phi_2 = \int_0^{\eta_0} d\tilde{\eta} e^{-i\mathbf{k} \cdot \hat{\mathbf{n}} \tilde{r} - \bar{\tau}} \left(\dot{\Phi}_1 \Phi_2 + \frac{\dot{\bar{\tau}}}{2} \Phi_1 \Phi_2 \right), \quad (4.19)$$

for which we make use of the symmetry between the dummy variables \mathbf{k}_1 and \mathbf{k}_2 in the convolution and ignore the constant boundary term evaluated at present η_0 . For the second term of Eq. (4.18), we exchange the inner and outer time integrations and substitute the integration over $\tilde{\eta}$ with Eq. (2.75). Putting all these together, we rewrite Eq. (4.16) as

$$\Delta_{\text{R}}^{[\text{III}]} = 8 \mathcal{T}_{\mathbf{k}_1, \mathbf{k}_2}(\mathbf{k}) \left\{ \int_0^{\eta_0} d\eta e^{-i\mathbf{k} \cdot \hat{\mathbf{n}} r - \bar{\tau}} \left[(\Delta_1 + \Phi_1) (\dot{\Phi}_2 + \dot{\Psi}_2) + \frac{\dot{\bar{\tau}}}{2} \Phi_1 \Phi_2 + \left(\dot{\bar{\tau}} \Delta_1 + \frac{\mathfrak{C}_1}{4} \right) \Phi_2 \right] \right\}, \quad (4.20)$$

where

$$\Delta_1 + \Phi_1 = e^{\bar{\tau}(\eta)} \int_0^{\eta} d\tilde{\eta} e^{-i\mathbf{k}_1 \cdot \hat{\mathbf{n}}(\eta-\tilde{\eta}) - \bar{\tau}(\tilde{\eta})} \left(\dot{\bar{\tau}} \Phi_1 + \dot{\Phi}_1 + \dot{\Psi}_1 + \dot{\bar{\tau}} \Delta_1 + \frac{\mathfrak{C}_1}{4} \right). \quad (4.21)$$

Eq. (4.20) contains all possible 2nd-order couplings involving 1st-order redshift effects: the

first term includes couplings between ISW and any 1st-order CMB effects (e.g. Doppler-ISW, SW-ISW and even ISW-ISW couplings); the second term is the SW-SW coupling; the third term corresponds to couplings between CMB signals generated by Compton scattering and SW effect (e.g. Doppler-SW coupling).

At 2nd order, performing IBPs becomes tricky as mentioned in [82]. However, the approach we take uniquely separates SW, early-time ISW and late-time ISW effects along the LOS integration, as the coupling terms shown in Eq. (4.20). In contrast, [87] also performs IBPs to the third term of Eq. (4.15) but the integrand they obtained is different from that in Eq. (4.20). Since different IBPs re-distribute the redshift effects differently along the time integration, the SW and ISW effects are not manifestly separated in [87]. For example, any residual couplings between the photon brightness and $\mathbf{k} \cdot \hat{\mathbf{n}}\Phi$ in the LOS integrand do not damp out well after recombination because the term $\mathbf{k} \cdot \hat{\mathbf{n}}\Phi$ mixes up SW and ISW effects throughout the LOS integration. In particular, it is problematic when a cutoff is used to the time integration because early-time effects may be re-distributed to late times and vice versa. In other words, integrating over the early-time regime does not necessarily calculate the physical early-time effects. We speculate that this could be one of the reasons why [87] concludes a much larger signal-to-noise.

Although we perform a similar cutoff to the time integration (explicitly from $\eta = 230$ to 1050 Mpc), it is numerically stable using Eq. (4.20). Indeed, the cutoff allows us to capture the SW-related and early-time ISW-related couplings but exclude the late-time ISW-related couplings. To understand how this works, we point out that only the first term in Eq. (4.20) has non-negligible contribution (ignoring reionization) outside the chosen time range because of the ISW term ($\dot{\Phi} + \Psi$). However, ISW effect is highly suppressed after $\eta = 1050$ Mpc when our universe is matter-dominated and only becomes significant again when the dark energy dominates at late time. Indeed, the early-time ISW is suppressed well before $\eta = 1050$ Mpc and thus we find it safe to simply use a sharp cutoff at $\eta = 1050$ Mpc with negligible impact to the bispectrum. However, the extended time integration may raise some uncertainties on the early-time ISW-related couplings due to the thin-shell approximation. We will discuss about this in details in Section 4.3.

With Eq. (4.20), we can replace the quadratic part $\tilde{S}^{[L,I]}$ with $S^{[L,I]}$ which is defined in

configuration space as

$$S^{[L,I]} \equiv 2e^{-\bar{\tau}} \left[S^{ij} \partial_J (\Phi + \Psi) \frac{\partial \Delta}{\partial n^i} - (\Phi + \Psi) n^i \partial_I \Delta + 4(\dot{\Phi} + \dot{\Psi})(\Delta + \Phi) \right. \\ \left. + (\Phi - \Psi) n^i \partial_I \Phi + 2\Psi\dot{\Psi} + (4\dot{\tau}\Delta + \mathcal{C})\Phi + 2\dot{\tau}\Phi^2 \right] + \frac{1}{4} e^{-\bar{\tau}} \mathcal{C}^{[L,I]}[\hat{l}]. \quad (4.22)$$

Here, we emphasize that Eq. (4.22) uniquely separates the SW effect, the early-time and late-time ISW effect and allows us to have a early-time cutoff on the time integration to include the 2nd-order effects generated *at and around recombination*. Physically, the two terms in the first line of Eq. (4.22) are the lensing and time-delay effects respectively and will be ignored in our calculation. The IBPs performed help to distinguish SW effect from ISW effect and clarify the physical meaning of each term. For example, we can interpret $(4\dot{\tau}\Delta + \mathcal{C})\Phi$ and $2\dot{\tau}\Phi^2$ as the photon-SW and SW-SW couplings respectively. The term $(\Phi - \Psi)n^i \partial_i \Phi + 2\Psi\dot{\Psi}$ is the quadratic part of the evolution equation of photon energy p^0 in 2nd order, i.e. $(dp^0/d\eta)^{[L,I]}$. We will discuss the contributions of these effects on the bispectrum in Section 4.3.

4.2.3 Bispectrum from Second-order Perturbations

By using the 2nd-order LOS approach in Eq. (4.12) with the purely (Eq. (4.10)) and quadratic (Eq. (4.22)) 2nd-order source functions, we can calculate the 2nd-order temperature anisotropies generated at recombination. Here, we formulate the bispectrum from the 2nd-order temperature anisotropies at recombination under the flat-sky and thin-shell approximations⁹.

First of all, we define the new coefficients which are related to the reduced bispectrum by

$$\xi_{\ell_1 \ell_2 M} \equiv \sum_{\ell_3} 2L_3 \begin{pmatrix} \ell_1 & \ell_2 & \ell_3 \\ M & -M & 0 \end{pmatrix} \begin{pmatrix} \ell_1 & \ell_2 & \ell_3 \\ 0 & 0 & 0 \end{pmatrix} b_{\ell_1 \ell_2 \ell_3}, \quad (4.23)$$

where $2L \equiv 2\ell + 1$. Using Eq. (C.22), it can be shown that

$$b_{\ell_1 \ell_2 \ell_3} = \begin{pmatrix} \ell_1 & \ell_2 & \ell_3 \\ 0 & 0 & 0 \end{pmatrix}^{-1} \sum_M \begin{pmatrix} \ell_1 & \ell_2 & \ell_3 \\ M & -M & 0 \end{pmatrix} \xi_{\ell_1 \ell_2 M}. \quad (4.24)$$

Moreover, with Eq. (C.20) and Eq. (C.21), we can find that the new coefficients obey the

⁹The derivation here is based on [17].

following properties

$$\xi_{\ell_2 \ell_1 M} = \xi_{\ell_1 \ell_2 M} = \xi_{\ell_1 \ell_2 -M}. \quad (4.25)$$

Due to the statistical isotropy of the CMB, the 3-point correlation function of the brightness temperature Θ_I defined in Eq. (4.5) depends merely on the relative angles with respect to $\hat{\mathbf{n}}_3$, e.g. $(\theta_1, \phi_1, \theta_2, \phi_2)$. Thus, we can align $\hat{\mathbf{n}}_3$ with the azimuthal direction and expand the 3-point correlation function into

$$\begin{aligned} \langle \Theta(\hat{\mathbf{n}}_1) \Theta(\hat{\mathbf{n}}_2) \Theta(\hat{\mathbf{n}}_3) \rangle &= \sum_{\ell_1 \ell_2 m_1 m_2} \vartheta_{\ell_1 \ell_2 m_1 m_2} \frac{\sqrt{L_1 L_2}}{2\pi} Y_{\ell_1 m_1}(\theta_1, \phi_1) Y_{\ell_2 m_2}(\theta_2, \phi_2) \\ &= \sum_{\ell_1 \ell_2 M} \vartheta_{\ell_1 \ell_2 M - M} \frac{\sqrt{L_1 L_2}}{2\pi} Y_{\ell_1 M}(\theta_1, 0) Y_{\ell_2 -M}(\theta_2, \phi_{21}). \end{aligned} \quad (4.26)$$

In the second equality of Eq. (4.26), we make use of the fact that the rotational invariance guarantees the 3-point correlation function to be dependent on the relative phase $\phi_{21} \equiv \phi_2 - \phi_1$ instead of the absolute phases.

Now, we want to show that coefficients ξ and ϑ are identical. To do so, we perform a rotation \mathcal{R} to the two spherical harmonics in Eq. (4.26) so that $\hat{\mathbf{n}}_3$ points to (θ, ϕ) instead of the azimuthal direction, i.e.

$$Y_{\ell m}(\mathcal{R}^{-1} \hat{\mathbf{n}}) = \sum_{m'} Y_{\ell m'}(\hat{\mathbf{n}}) D_{m' m}^{\ell}(\mathcal{R}), \quad (4.27)$$

where the rotation matrices $D_{m' m}^{\ell}$ can be expressed as

$$D_{m' m}^{\ell}(\phi, \theta, \psi) = (-1)^{m'} \sqrt{\frac{4\pi}{2L}} Y_{\ell -m'}(\theta, \phi) e^{-im\psi}, \quad (4.28)$$

with Euler angles ϕ , θ and ψ . Therefore, we have by using Eq. (C.13)

$$\langle \prod_{i=1}^3 a_{\ell_i m_i} \rangle = \vartheta_{\ell_1 \ell_2 M - M} \sqrt{\frac{2L_1 L_2 L_3}{\pi}} \begin{pmatrix} \ell_1 & \ell_2 & \ell_3 \\ M & -M & 0 \end{pmatrix} \begin{pmatrix} \ell_1 & \ell_2 & \ell_3 \\ -m_1 & -m_2 & -m_3 \end{pmatrix}. \quad (4.29)$$

Applying Eq. (2.93), we can show that the reduced bispectrum becomes

$$b_{\ell_1 \ell_2 \ell_3} = \begin{pmatrix} \ell_1 & \ell_2 & \ell_3 \\ 0 & 0 & 0 \end{pmatrix}^{-1} \sum_M \begin{pmatrix} \ell_1 & \ell_2 & \ell_3 \\ M & -M & 0 \end{pmatrix} \vartheta_{\ell_1 \ell_2 M - M}. \quad (4.30)$$

By comparing with Eq. (4.24), we deduce

$$\xi_{\ell_1 \ell_2 M} = \vartheta_{\ell_1 \ell_2 M - M}. \quad (4.31)$$

Making use of $\langle \Phi(\mathbf{k}_1)\Phi(\mathbf{k}_2)\Phi(\mathbf{k}_3) \rangle = (2\pi)^{-3/2} \delta^3(\mathbf{k}_1 + \mathbf{k}_2 + \mathbf{k}_3) B(\mathbf{k}_1, \mathbf{k}_2)$, we obtain

$$\langle \Theta(\hat{\mathbf{n}}_1)\Theta(\hat{\mathbf{n}}_2)\Theta(\hat{\mathbf{n}}_3) \rangle = \int \frac{d^3\mathbf{k}_1 d^3\mathbf{k}_2}{(2\pi)^6} dr_1 dr_2 dr_3 B(\mathbf{k}_1, \mathbf{k}_2) S_T(\eta_1, \mathbf{k}_1) S_T(\eta_2, \mathbf{k}_2) S_T(\eta_3, \mathbf{k}_3) e^{-i[\mathbf{k}_1 \cdot \mathbf{r}_1 + \mathbf{k}_2 \cdot \mathbf{r}_2 - (\mathbf{k}_1 + \mathbf{k}_2) \cdot \mathbf{r}_3]}, \quad (4.32)$$

where $\mathbf{r}_i = r_i \hat{\mathbf{n}}_i$ for $i = 1, 2, 3$. We emphasize that Eq. (4.32) is valid for both primordial and post-inflationary non-Gaussianities. In flat-sky limit, $\theta_1, \theta_2 \ll 1^{10}$ and thus the argument of the exponential in Eq. (4.32) can be approximated as

$$-i \left[k_1^z (r_1 - r_3) + k_2^z (r_2 - r_3) + k_1^\perp r_1 \theta_1 \cos \beta_1 + k_2^\perp r_2 \theta_2 \cos(\beta_2 - \phi_{21}) \right], \quad (4.33)$$

where we align $\hat{\mathbf{n}}_3$ with z-axis and decompose

$$\mathbf{k}_i = (k_i^\perp \cos \beta_i, k_i^\perp \sin \beta_i, k_i^z), \quad (4.34)$$

for $i = 1, 2, 3$. With Eq. (4.26) and (4.31), the coefficients $\xi_{\ell_1 \ell_2 M}$ are

$$\frac{4\pi^2}{\sqrt{L_1 L_2}} \int \theta_1 d\theta_1 \int \theta_2 d\theta_2 \int d\phi_{21} Y_{\ell_1 - M}(\theta, 0) Y_{\ell_2 M}(\theta_2, \phi_{21}) \langle \Theta(\hat{\mathbf{n}}_1)\Theta(\hat{\mathbf{n}}_2)\Theta(\hat{\mathbf{n}}_3) \rangle. \quad (4.35)$$

By employing Bessel functions of the first kind J_M

$$J_M(x) = (-1)^M J_{-M}(x) = \frac{1}{2\pi} \int_{-\pi}^{\pi} dy e^{-i(My - x \sin y)}, \quad (4.36)$$

$$\int \theta d\theta J_M(k^\perp r \theta) J_M(L\theta) = \frac{\delta(L - k^\perp r)}{L}, \quad (4.37)$$

and the flat-sky limit of spherical harmonics

$$Y_{\ell m}(\theta, \phi) \rightarrow \sqrt{\frac{2L}{4\pi}} (-1)^M J_M(L\theta) e^{iM\phi}, \quad (4.38)$$

¹⁰Roughly speaking, this is the condition when the three directions of the 3-point correlation are close to each other so that the sphere of sky can be approximated by a flat plane.

we can derive the coefficients in the flat-sky limit¹¹

$$\xi_{\ell_1 \ell_2 M} \approx \frac{1}{(2\pi)^3} \int d\beta_{12} e^{iM\beta_{12}} \int dk_1^z dk_2^z \int dr_1 dr_2 dr_3 \frac{B(\mathbf{k}_1, \mathbf{k}_2)}{r_1^2 r_2^2} S_T(\eta_1, \mathbf{k}_1) S_T(\eta_2, \mathbf{k}_2) S_T(\eta_3, \mathbf{k}_3) e^{-ik_1^z(r_1-r_3) - ik_2^z(r_2-r_3)}, \quad (4.39)$$

where $\beta_{12} \equiv \beta_1 - \beta_2$, $k_1^\perp = L_1/r_1$ and $k_2^\perp = L_2/r_2$.

To derive the reduced bispectrum, we notice that [17]

$$\xi_{\ell_1 \ell_2 M} = \int_0^{2\pi} \frac{d\beta_{12}}{2\pi} e^{iM\beta_{12}} b_{\ell_1 \ell_2 \ell_3}, \quad (4.40)$$

where we use the approximation

$$\begin{pmatrix} \ell_1 & \ell_2 & \ell_3 \\ M & -M & 0 \end{pmatrix} \rightarrow \begin{pmatrix} \ell_1 & \ell_2 & \ell_3 \\ 0 & 0 & 0 \end{pmatrix} \cos(M\beta_{12}), \quad (4.41)$$

and the Ponzano-Regge limit

$$\begin{pmatrix} \ell_1 & \ell_2 & \ell_3 \\ 0 & 0 & 0 \end{pmatrix}^2 = \frac{1}{\pi L_1 L_2 \sin \beta_{12}}. \quad (4.42)$$

The reduced bispectrum can then be written in the flat-sky limit as

$$b_{\ell_1 \ell_2 \ell_3} \approx \frac{1}{(2\pi)^2} \int dk_1^z dk_2^z \int dr_1 dr_2 dr_3 S_T(\eta_1, \mathbf{k}_1) S_T(\eta_2, \mathbf{k}_2) S_T(\eta_3, \mathbf{k}_3) e^{-ik_1^z(r_1-r_3) - ik_2^z(r_2-r_3)} \frac{B(\mathbf{k}_1, \mathbf{k}_2)}{r_1^2 r_2^2}. \quad (4.43)$$

So far, the bispectrum formulae developed are generic for both primordial and post-inflationary non-Gaussianities. For the recombination bispectrum, we replace one of the source functions by the 2nd-order source function as in Eq. (4.12) and keep the other two in 1st order

$$b_{\ell_1 \ell_2 \ell_3}^{\text{rec}} \approx \frac{1}{(2\pi)^2} \int dk_1^z dk_2^z \int dr_1 dr_2 dr_3 S_T(\eta_1, k_1) S_T(\eta_2, k_2) S_T^{2\text{ND}}(\eta_3, \mathbf{k}_1, \mathbf{k}_2, \hat{\mathbf{n}}) e^{-ik_1^z(r_1-r_3) - ik_2^z(r_2-r_3)} \frac{P_\Phi(k_1)}{r_1^2} \frac{P_\Phi(k_2)}{r_2^2} + 2 \text{ perm.}, \quad (4.44)$$

¹¹This imposes a requirement that $B(\mathbf{k}_1, \mathbf{k}_2)$ depends solely on the relative phase β_{12} but not the absolute ones.

where $\mu \equiv \hat{\mathbf{k}}_1 \cdot \hat{\mathbf{k}}_2$, $S_T^{2\text{ND}}$ contains both the purely (Eq. (4.10)) and quadratic (Eq. (4.22)) parts of the 2nd-order source function. We emphasize that although the 2nd-order source function has more complicated dependences, the derivation in this subsection still holds. Moreover, the source function does not depend on all freedoms of $(\mathbf{k}_1, \mathbf{k}_2, \hat{\mathbf{n}})$ but we express so in Eq. (4.44) for simplicity. We will explicitly write down its dependences in Section 4.2.4. Additionally, with the thin-shell approximation, the recombination bispectrum becomes

$$b_{\ell_1 \ell_2 \ell_3}^{\text{rec}} \approx \frac{1}{(2\pi)^2} \int dk_1^z dk_2^z \left[\int dr_1 S_T(\eta_1, k_1) e^{-ik_1^z r_1} \right] \left[\int dr_2 S_T(\eta_2, k_2) e^{-ik_2^z r_2} \right] \left[\int dr_3 S_T^{2\text{ND}}(\eta_3, \mathbf{k}_1, \mathbf{k}_2, \hat{\mathbf{n}}) e^{i(k_1^z + k_2^z)r_3} \right] \frac{P_\Phi(k_1)P_\Phi(k_2)}{r_{\text{LSS}}^4} + 2 \text{ perm.}, \quad (4.45)$$

where $k_i^\perp = \ell_i/r_{\text{LSS}}$ for $i = 1, 2, 3$ with the distance r_{LSS} from the last scattering surface.

The bispectrum formulae above are measured under the brightness temperature Θ_I while the bispectra in literature are commonly based on the bolometric temperature Θ_E . However, the bispectra of these two temperature definitions can be linked straightforwardly by

$$b_{\ell_1 \ell_2 \ell_3}^{\Theta_E} = b_{\ell_1 \ell_2 \ell_3}^{\Theta_I} - 3(C_{\ell_1} C_{\ell_2} + C_{\ell_2} C_{\ell_3} + C_{\ell_1} C_{\ell_3}), \quad (4.46)$$

where the extra term comes from the second term in Eq. (4.8).

The flat-sky approximation avoids the use of the spherical Bessel function of the first kind $j_\ell(x)$ which fluctuates rapidly for high ℓ s. Thus, lower resolutions of k s are sufficient and this significantly reduces the computational power required. On the other hand, the thin-shell approximation decouples the nested integrals and simplifies the numerical integrations. However, there are drawbacks using these approximations. We expect that the bispectrum in flat-sky limit will deviate from the exact one for low ℓ s. Furthermore, since we include the early-time (but not late-time) ISW-related effects by extending the LOS integration right after recombination, the thin-shell approximation may break down for these effects. We will discuss these problems further when we compare our numerically-calculated bispectrum with the analytical one in Section 4.3.2.

Our ultimate goal is to calculate the bispectrum as observed *today*, which means that all the effects post recombination till today are ideally included in the calculation. However, since non-perturbative effects complicate the study at low redshifts ($z \lesssim 10$), an appropriate milestone towards this goal is the computation of the bispectrum *around recombination* which is what we undertake in this thesis. This means that we cut off the LOS integration

early after recombination¹², allowing us to make a definite statement about the amplitude of the bispectrum at this time clearly. In particular, we ignore contributions from lensing, time-delay and late-time ISW-related effects. The lensing and time-delay effects on bispectra have been studied elsewhere [49, 69]. The effects from the 2nd-order vector and tensor perturbations and the late-time ISW-related effects are studied in [52, 82] and are sub-dominant.

4.2.4 Quadratic Source Function with $m \neq 0$

When we decompose the purely 2nd-order source function, we need multipoles up to $\ell = 2$ only to include all scalar, vector and tensor modes. In contrast, the decomposition of the quadratic 2nd-order source function extends to arbitrarily high ℓ . This becomes a hierarchy problem. With the trick discussed in Section 4.2.2, ℓ up to about 10 is sufficient for effects at recombination. Even so, elaborating the quadratic source function is still subtle, especially for multipoles with $m \neq 0$.

The quadratic 2nd-order source function contains many terms. Here, we work only with the term

$$S_{\text{Eg},\ell m}^{[\text{I,I}]} = \frac{1}{N_\ell} Y_{\ell m}(\hat{\mathbf{n}}) \sum_{n=-1}^1 {}_0\mathcal{D}_{\ell m}^n \hat{I}_{1,\ell-1,m-n} k_{2,(n)} \Phi_2, \quad (4.47)$$

where N_ℓ is defined in Eq. (C.2) and ${}_0\mathcal{D}_{\ell m}^n$ can be found in Appendix C.3. We note that the azimuthal direction is aligned with \mathbf{k}_3 . By using Eq. (3.74) and the fact that \mathbf{k}_i for $i = 1, 2$ and 3 are in the same plane, the term becomes

$$S_{\text{Eg}}^{[\text{I,I}]} = -i^\ell \sqrt{\frac{(\ell-m)!}{(\ell+m)!}} P_\ell^m(\cos \theta_{n3}) e^{im\phi_{nk_1}} \sum_{n=-1}^1 {}_0\mathcal{D}_{\ell m}^n \sqrt{\frac{4\pi}{2\ell-1}} Y_{\ell-1,m-n}^*(\hat{\mathbf{k}}_1 \cdot \hat{\mathbf{k}}_3, 0) \sqrt{\frac{4\pi}{3}} Y_{1n}^*(\hat{\mathbf{k}}_2 \cdot \hat{\mathbf{k}}_3, \pi) \hat{I}_{\ell-1,0}(k_1) k_2 \Phi_2, \quad (4.48)$$

where $P_\ell^m(x)$ is the associated Legendre polynomial, $\cos \theta_{n3} = \hat{\mathbf{n}} \cdot \hat{\mathbf{k}}_3$ and $\phi_{nk_1} \equiv \phi_n - \phi_{k_1}$ is the relative phase between $\hat{\mathbf{n}}$ and \mathbf{k}_1 . In particular, we can find that

$$\cos \phi_{nk_1} = \frac{\cos \theta_{n1} + \cos \theta_{13} \cos \theta_{n3}}{\sin \theta_{13} \sin \theta_{n3}}, \quad (4.49)$$

¹²See Section 4.2.2 for more details about how we separate the effects around recombination from the late-time ones.

where the subscript n denotes the observation direction $\hat{\mathbf{n}}$ and the numbers $i = 1, 2$ and 3 denote \mathbf{k}_i . In the flat-sky limit, we have

$$\cos \theta_{n1} = \frac{k_1^z}{k_1}, \quad \cos \theta_{n3} = \frac{k_3^z}{k_3}, \quad \cos \theta_{13} = \frac{k_1^2 + k_3^2 - k_2^2}{2k_1k_3}. \quad (4.50)$$

Although we elaborate the term $S_{\text{Eg},\ell m}^{[I,I]}$ only, the result is generic for the quadratic source function. Indeed, all terms in the quadratic source function have the same form as the first line of Eq. (4.48), which can thus be singled out. When we calculate the 2nd-order perturbations as in Chapter 3, we need to consider merely the second line of Eq. (4.48). This explains why it is sufficient to solve the 2nd-order perturbations in a set of $(k_1, k_2, \hat{\mathbf{k}}_1 \cdot \hat{\mathbf{k}}_2)$.

4.3 Numerical Results

To calculate the bispectrum in Eq. (4.45), we solve the 1st- and 2nd-order perturbations numerically. For both cases, we use the Newtonian gauge as discussed in Section 2.5 and Chapter 3 respectively. In this section, we first describe the numerical implementations of calculating the recombination bispectrum. Then, we verify the numerical result with the analytical bispectrum in the squeezed limit. Finally, we present the constraints on $f_{\text{NL}s}$ and the signal-to-noise of the recombination bispectrum.

4.3.1 Numerical Implementation

There are two points worth being emphasized when solving the 2nd-order perturbations numerically. First, we solve and store the kernels of the 2nd-order perturbations as functions of $k_1, k_2, \hat{\mathbf{k}}_1 \cdot \hat{\mathbf{k}}_2$ and η as we explained in Section 4.2.4. For conservative convergence, the numbers of sampling points are chosen to be 180, 10, 120 for ks, μ and η respectively. In particular, making use of the flat-sky approximation allows us to simplify the numerical samplings in \mathbf{k} -space¹³. We sample $\ln k$ uniformly with k from 2.4×10^{-6} to $0.86/\text{Mpc}$ and $\ln \eta$ uniformly with η from 230 to 1050 Mpc. Moreover, we confirm the convergences of the bispectra within a few percent of errors by varying the sample sizes of ks, μ and η as well as the ranges of ks and integrated η .

¹³Because the highly-fluctuating Bessel functions are missing when calculating the bispectra with flat-sky approximation.

Second, there exist numerical instabilities in Newtonian gauge for both 1st and 2nd order arising from two large terms canceling almost perfectly with each other with the residual a few orders of magnitude smaller. This undermines the accuracies available in the numerical calculation. To tackle this problem, we use two evolution equations which are linear combinations¹⁴ of the original four scalar Einstein field equations (EFEs) as discussed in Section 3.3.3.

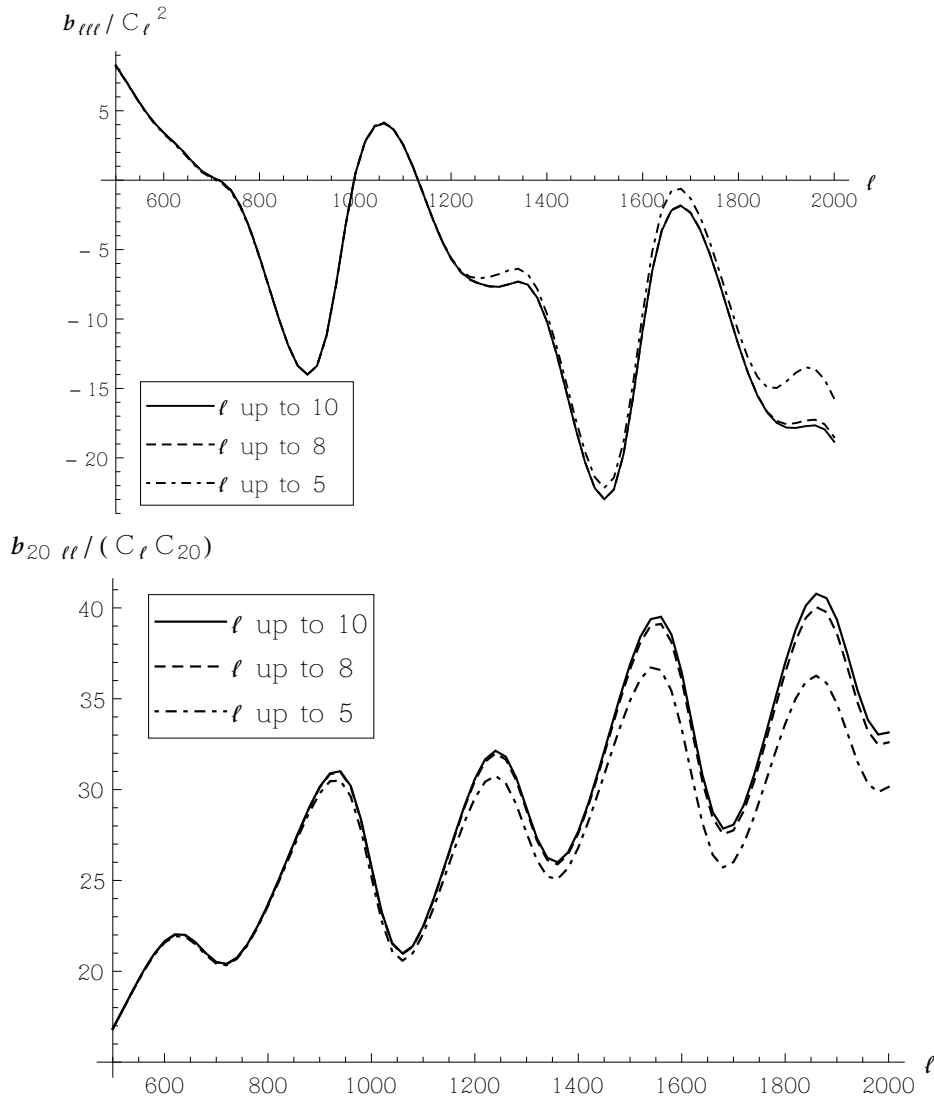


Figure 4.1 The graphs of the bispectra generated from the quadratic source function $S^{[1,1]}$ against ℓ for equilateral (upper) and squeezed (lower) limit. The curves correspond to different ℓ truncations of the multipoles $S_{\ell m}^{[1,1]}$. We can see that the convergence occurs when ℓ goes up to 10.

¹⁴This technique is first employed in the CMBQuick code introduced by Pitrou [87].

The solved 2nd-order perturbations are then fed into the purely 2nd-order source function $S^{[II]}$. Although only 1st-order perturbations are needed to compute the quadratic source function $S^{[II]}$, it has to be decomposed into multipoles $S_{\ell,m}^{[I,I]}$. In principle, closing the hierarchy requires multipoles up to infinite ℓ , but this is numerically not tractable. Hence, the usual prescription is to truncate the hierarchy once convergence is reached. The LOS integrand in Eq. (4.22) facilitates the convergence such that ℓ up to 10 is sufficient as shown in Fig. 4.1. We include all the $m \neq 0$ modes consistently up to $\ell = 10$ for the quadratic source function.

Numerical Results for Linear Perturbations

In order to calculate the 2nd-order perturbations and the corresponding CMB bispectrum, we need the linear perturbations as sources. The idea is to store all the 1st-order perturbations needed as functions of k and η into an huge array. Then, the values of those quadratic terms at different \mathbf{k}_1 , \mathbf{k}_2 and η are evaluated through the cubic spline interpolation with the array. Unfortunately, many of the 1st-order quantities, such as multipoles of photons and neutrinos, oscillate rapidly for small scales. Thus, high resolutions are required to make sure that the oscillations are captured properly. Besides, we need the 1st-order quantities all over the range of time from the initial time to the recombination.

Although the calculations on the linear perturbations have been well established in some LOS solvers, such as CAMB [70] and CLASS [63], we reproduce the calculations with our own code. One of the main reasons is that the sampling of k and η in these 1st-order quantities for evaluating the 2nd-order equations is different from those used for calculating the CMB power spectrum in these LOS solvers. For instance, the LOS solvers do not store the 1st-order quantities well before the recombination because they have negligible effects on the CMB power spectra¹⁵. In contrast, we need to store the 1st-order quantities from the initial time to the recombination when we evaluate the 2nd-order Boltzmann equation and EFEs. Thus, it is more efficient to develop our own code to control the sampling. Another reason is that the 1st-order evolution equations are simply the homogeneous parts of the 2nd-order evolution equations (see Eq. (3.21)) and provide a decent check for the linear parts of 2nd-order equations.

We developed our own code to calculate the full-sky CMB power spectrum with and without the lensing effect¹⁶. The full-sky result without the lensing effect is shown in

¹⁵Photons are tightly coupled with baryons well before the recombination and any patterns of photons at that time will be washed away by collisions.

¹⁶We also include the calculation of the unlensed power spectrum with the flat-sky approximation.

Fig. 2.2 along with that from CAMB. We obtain a very nice agreement. Although the calculation of the power spectrum is not necessary for studying the CMB bispectrum, the calculation provides us some useful guides about how high the resolutions of k and η should be used in bispectra.

Numerical Calculations of Second-Order Perturbations

Once the 1st-order perturbations are ready, the kernels of the 2nd-order perturbations can be solved by the 2nd-order EFEs and Boltzmann equations. However, there are many quadratic terms of 1st-order perturbations in these equations and it is not trivial to keep track of these terms. Besides, the solutions obtained may subject to the issue of numerical instabilities. Thus, it is important to establish a systematic check for the numerical 2nd-order solutions.

For the scalar perturbations, the verification can be achieved by using the redundancy of the EFEs. There are four EFEs for the scalar perturbations and we only need to use two of them to evolve the 2nd-order scalar metric perturbations, i.e. $\Phi^{[II]}$ and $\Psi^{[II]}$ in Newtonian gauge. However, the two redundant EFEs are consistent with the other two EFEs and can thus be used to verify the numerical solutions. For example, if a term is missing in the EFEs or the numerical instabilities grow significantly, the constraint equations will not be satisfied well (see Figs. 3.3 to 3.5). We emphasize that the verification does not work well for the collision terms of Boltzmann equation because the EFEs is sensitive only to the total energy and momentum of all components. A missing collision term may change the energies and momenta of baryons and photons but not the sum of their energies and momenta.

The 2nd-order perturbations were solved previously in [87]. However, there are some typos for the quadratic terms in the EFEs. The third term $8\mathcal{H}(\Phi - \Psi)\dot{\Psi}$ of the first line in Eq. (A.6) should be $8\mathcal{H}\Phi\dot{\Phi}$. The first term $\partial_I(\Psi + \Phi)\partial^I(\Psi + \Phi)$ in the square bracket of the second line in Eq. (A.7) should be $\partial_I(\Psi + \Phi)\partial^I(\Psi + \Phi)$. Moreover, the quadratic terms with $\sigma^{S[II]}$ in the EFEs are missing. These missing terms do not have overwhelming amplitudes compared to all the other quadratic terms¹⁷. Thus, we do not expect that the large deviation of the non-Gaussianities calculated in [87] comes from these terms.

¹⁷For example, the stress anisotropy $\sigma^{S[II]}$ is usually subdominant except for very small scales.

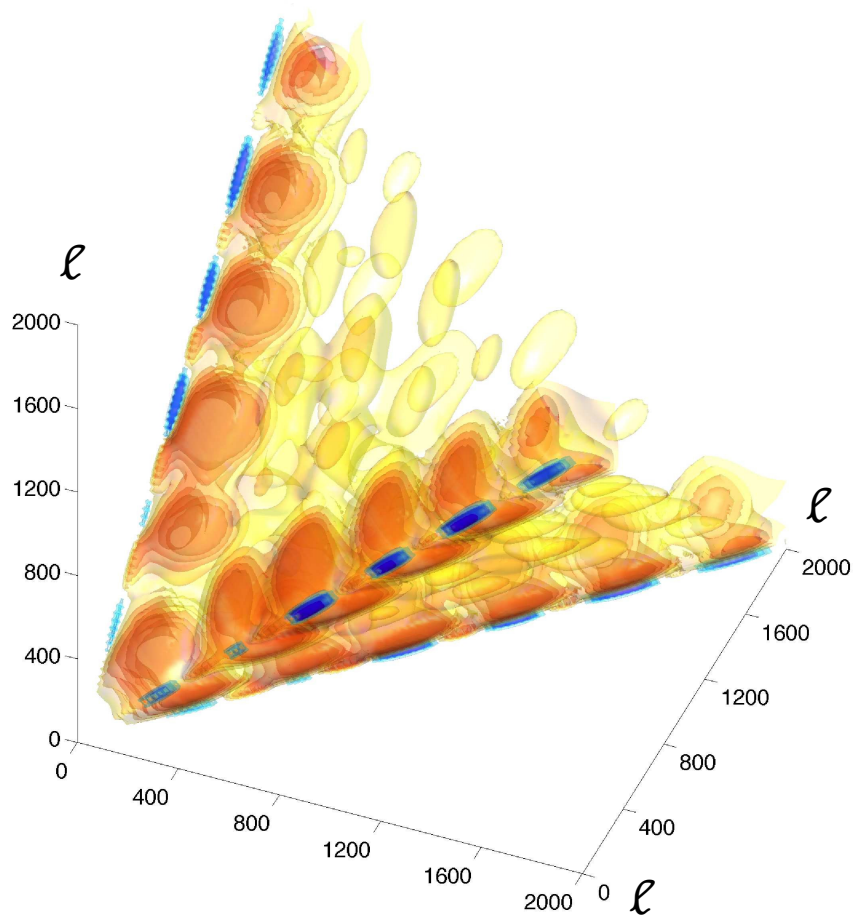


Figure 4.2 The 3D plot of the reduced bispectrum generated around recombination. The bispectrum is normalized by the coefficient $D(\ell_1, \ell_2, \ell_3)$ defined in Eq. (4.51) to remove an overall ℓ^{-4} scaling. The red regions represent positive values while the blue regions represent negative values of the recombination bispectrum.

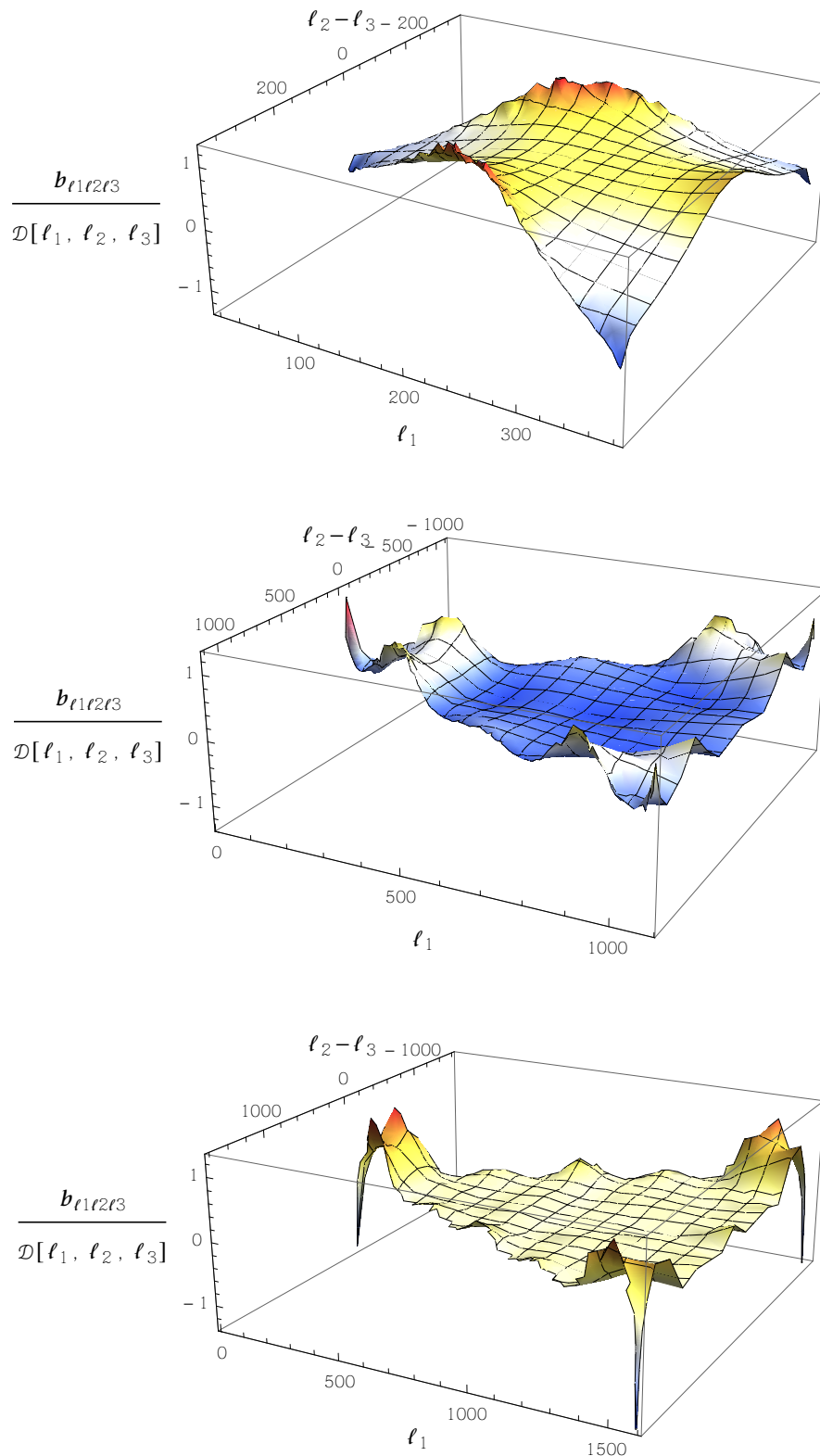


Figure 4.3 The cross sections of the normalized reduced bispectrum in Fig. 4.2 with the conditions $\frac{1}{2}(l_1 + l_2 + l_3) = 400$ (upper), 1100 (middle) and 1600 (lower).

Recombination Bispectrum

We present the full recombination bispectrum in Fig. 4.2, showing isosurfaces of the bispectrum density with the normalization factor [36]

$$D(\ell_1, \ell_2, \ell_3) \equiv \frac{1}{(2\ell_1 + 1)(2\ell_2 + 1)(2\ell_3 + 1)} \left(\frac{1}{\ell_1 + \ell_2 + \ell_3 + 3} + \frac{1}{\ell_1 + \ell_2 + \ell_3} \right). \quad (4.51)$$

Although the main contribution to the recombination bispectrum is concentrated towards the edges of the tetrahedron, the bispectrum fluctuates around zero in the squeezed limit and hence its correlation with the local-type template is somewhat suppressed. Clearly from Fig. 4.2, the bispectrum does not correlate particularly well with the popular templates – local, equilateral or orthogonal. It possesses its own distinct shape. In Fig. 4.3, we show different tetrahedral cross-sections through the full recombination bispectrum taken at different summations $\ell_1 + \ell_2 + \ell_3 = \text{const}$. On the other hand, it contains features in the squeezed limit and along the edges which reflect those appearing in the ISW-lensing bispectrum – the fluctuations along the edges of the tetrahedron. For the squeezed limit with $\ell_1 \ll \ell_2, \ell_3$, this is because they both contain a term with $d(\ell_2^2 C_{\ell_2})/d\ell_2$ (see Eq. (12) and (14) in [66]) which comes from modulations of large-scale fields. However, the ISW-lensing bispectrum possesses an extra term which fluctuates according to the angle between the small ℓ_1 and the large ℓ_2 . More precisely, they have similar shapes when $\ell_2 = \ell_3$ but look very different when $\ell_1 + \ell_2 = \ell_3$. This extra feature weakens the correlation between the ISW-lensing and the recombination bispectra, which is only $\sim 30\%$.

4.3.2 Validation with Analytical Bispectrum

To verify the numerical bispectrum we calculated, we compare it with the analytical solution available in the squeezed limit. In the squeezed limit ($\ell_1 \ll \ell_2$ and ℓ_3), the reduced bispectrum in the bolometric temperature has the simple form [12, 29]

$$b_{\ell_1 \ell_2 \ell_3}^{\Theta_E} = C_{\ell_1} C_{\ell_2} + C_{\ell_1} C_{\ell_3} + C_{\ell_2} C_{\ell_3} - \frac{C_{\ell_1}^{\Theta\zeta}}{2} \left[\frac{1}{\ell_2^2} \frac{d(\ell_2^2 C_{\ell_2})}{d \ln \ell_2} + \frac{1}{\ell_3^2} \frac{d(\ell_3^2 C_{\ell_3})}{d \ln \ell_3} \right], \quad (4.52)$$

where $C_{\ell_1}^{\Theta\zeta}$ is the correlation between the temperature anisotropies and the curvature perturbation $\zeta = \Delta_{00} - \Psi$ at recombination. Our bispectrum is in good agreement with the analytical bispectrum as shown in Fig. 4.4. We note that the flat-sky approximation performs well in the squeezed limit. The approximation breaks down only when $\ell_1 \lesssim 200$.

The breakdown occurs earlier than mentioned in [17] for the flat-sky approximation. We believe this is because the cutoff of the LOS integration is extended to $\eta = 1050$ Mpc in order to include the couplings with the early-time ISW effect. In this case, the thin-shell approximation may break down while the flat-sky approximation is still valid. However, these ISW-related couplings should contribute mildly to the total bispectrum¹⁸.

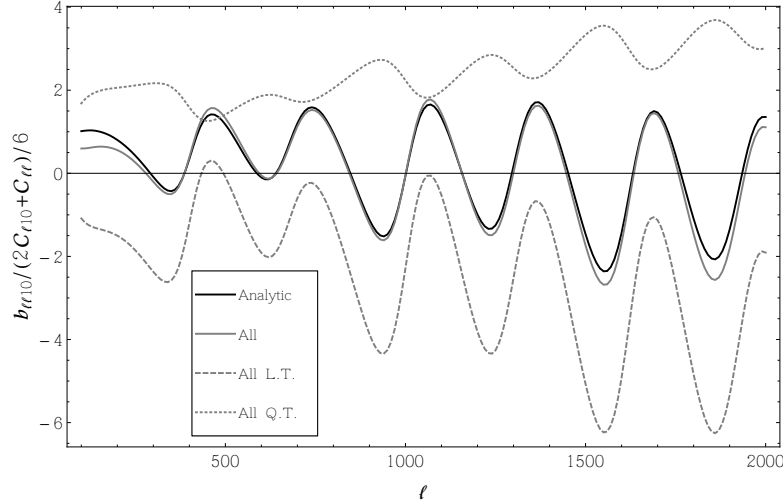


Figure 4.4 The recombination bispectrum (gray solid line) calculated numerically using Eq. (4.45) and the analytical bispectrum (black solid line) are plotted in the squeezed limit. We can see that they match with each other very well. Here, we measure the bispectrum in bolometric temperature which can be converted from the bispectrum in brightness temperature by Eq. (4.46). The “All L.T.” curve contains all the purely 2nd-order perturbations of the source function as shown in Eq. (4.10) while the “All Q.T.” curve contains all the cross products of two 1st-order perturbations of the source function as shown in Eq. (4.11).

In addition, we remark that the numerical accuracy of the multipoles $S_{\ell,m}^{[I,I]}$ with $m \neq 0$ cannot be checked with the analytical solution as they contribute negligibly in the squeezed limit. The reason is as follows. In 1st-order perturbation theory, the source function $S_T^{[I]}(\eta, \mathbf{k}, \hat{\mathbf{n}})$ can be expressed as $\tilde{S}_T^{[I]}(\eta, k, \mu)\Phi(\mathbf{k})$ where $\mu \equiv \hat{\mathbf{n}} \cdot \hat{\mathbf{k}}$ and $\Phi(\mathbf{k})$ is the primordial perturbation of the Newtonian potential. Since $\tilde{S}_T^{[I]}$ is a function of μ , it can be decomposed into spherical harmonics with only $m = 0$ modes. On the other hand, in 2nd-order perturbation theory, the kernel of quadratic source function $S^{[I,I]}$ is a function of η and $\hat{\mathbf{n}}$ as well as \mathbf{k}_1 and \mathbf{k}_2 which come from the couplings between two 1st-order perturbations. The decomposition of $S^{[I,I]}$ into spherical harmonics will contain modes with $m \neq 0$ because \mathbf{k}_1 and \mathbf{k}_2 do not necessarily align with each other. In other words, the couplings break the symmetry with $m = 0$. However, in the squeezed limit (e.g. $\mathbf{k}_1 \ll \mathbf{k}_2, \mathbf{k}_3$), the conservation

¹⁸See Fig. 1 in [66], and the SW-ISW and γ -ISW effects in the lower panel of Fig. 4.5.

law of momenta ($\mathbf{k}_3 = \mathbf{k}_1 + \mathbf{k}_2$) implies that \mathbf{k}_2 is almost parallel to \mathbf{k}_3 . Thus, modes with $m \neq 0$ are suppressed because of the much smaller \mathbf{k}_1 . In this case, we have only $m = 0$ modes when \mathbf{k}_3 is chosen to align with the azimuthal direction of the multipole decomposition. Similarly, the 2nd-order vector and tensor perturbations are negligible in the squeezed limit as they are $m = 1$ and $m = 2$ modes respectively. Having said all these, we emphasize that $m \neq 0$ modes have to be considered for non-squeezed configurations.

In Fig. 4.5, we plot the bispectra of the terms in the 2nd-order source function. We can see that the main contributions come from the effects of the Photon-SW, SW-SW and quadratic Collisions as well as the purely 2nd-order SW, Doppler and anisotropic stress effects. The sum of the Photon-SW and the SW-SW effects is roughly constant in the plot – the total bispectrum from these two effects is approximately proportional to the product of the power spectra of the long (ℓ_L) and short (ℓ_S) wavelength modes, i.e. $C_{\ell_S}C_{\ell_L}$. Moreover, this constant offset also appears in Fig. 1 of [82]. This verifies that our IBPs approach is consistent¹⁹ with the change-of-variables approach first introduced by [52]. Since we decompose the quadratic source term $S^{[I,1]}$ into different physical couplings, the physical explanation of the offset is clear: the power spectrum of the short wavelength mode comes mainly from intrinsic intensity, SW and Doppler effects while the power spectrum of the long wavelength mode is proportional to the square of the initial gravitational potential Φ (SW effect). The offset shifts the bispectrum of the purely 2nd-order source terms up and suppresses the correlation between the recombination bispectrum and that of the local type.

¹⁹The late-time ISW-related couplings are sub-dominant as expected.

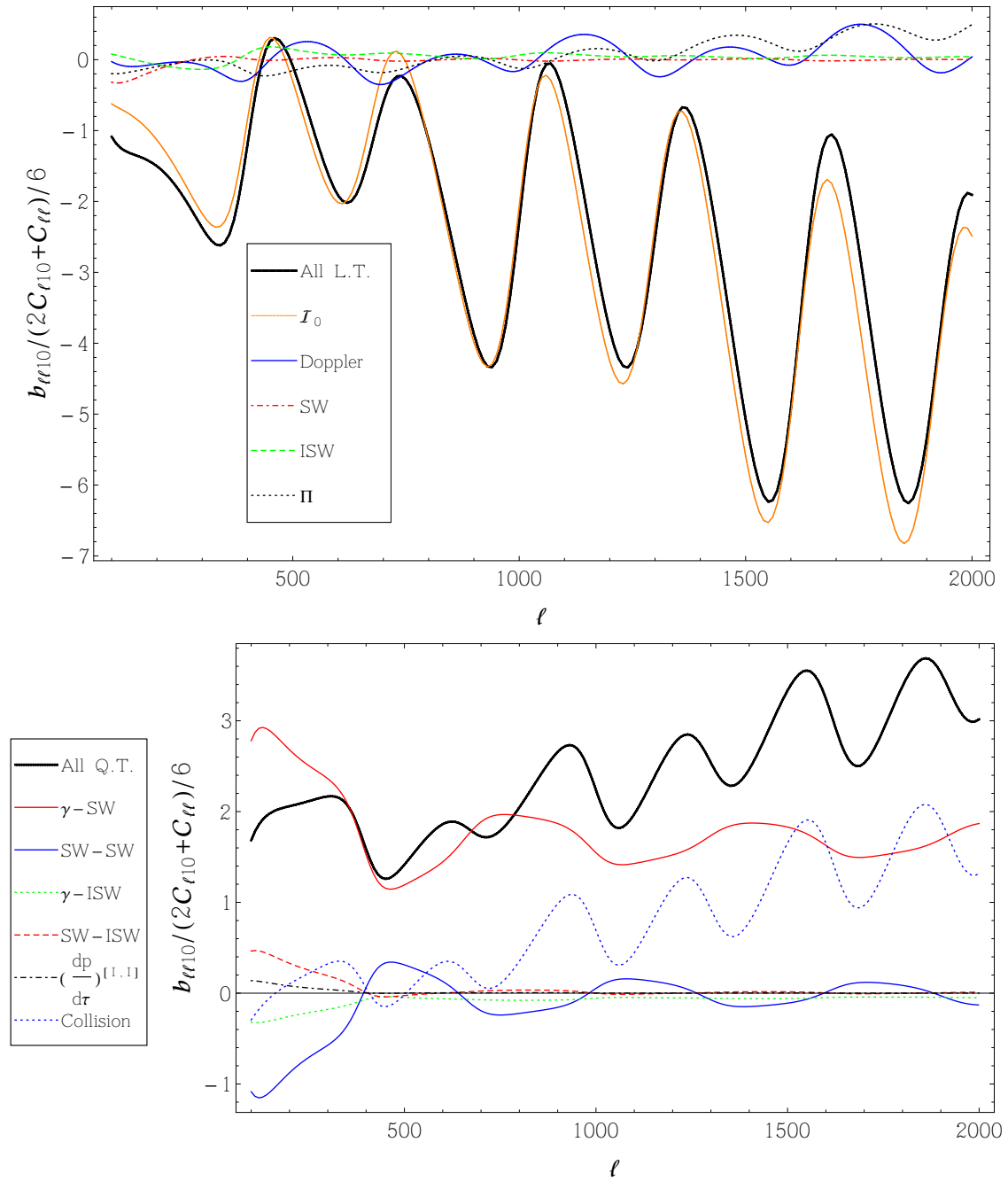


Figure 4.5 The bispectra of the linear terms (L.T.) and quadratic terms (Q.T.) of the source function $S_{2\text{ND}}$ in squeezed limit are shown in the upper and lower panel respectively.

4.3.3 f_{NL} and Signal-to-noise

In Table 4.1, we summarize the effective f_{NLS} , the normalized F_{NLS} [35] and the signal-to-noise ratios S/N which are defined as

$$f_{\text{NL}}^{\text{A}} = \frac{\mathcal{F}_{\text{A,rec}}}{\mathcal{F}_{\text{A,A}}} \quad (4.53)$$

$$F_{\text{NL}}^{\text{A}} = \sqrt{\frac{\mathcal{F}_{\text{A,A}}}{\mathcal{F}_{\text{loc,loc}}}} f_{\text{NL}}^{\text{A}} \quad (4.54)$$

$$(S/N)_{\text{A}} = \sqrt{\mathcal{F}_{\text{A,A}}} \quad (4.55)$$

where

$$\mathcal{F}_{\text{A,B}} \equiv \sum_{\ell_i} \frac{h_{\ell_1 \ell_2 \ell_3}^2}{6C_{\ell_1} C_{\ell_2} C_{\ell_3}} b_{\ell_1 \ell_2 \ell_3}^{\text{A}} b_{\ell_1 \ell_2 \ell_3}^{\text{B}} \quad (4.56)$$

$$h_{\ell_1 \ell_2 \ell_3} \equiv \sqrt{\frac{(2\ell_1 + 1)(2\ell_2 + 1)(2\ell_3 + 1)}{4\pi}} \begin{pmatrix} \ell_1 & \ell_2 & \ell_3 \\ 0 & 0 & 0 \end{pmatrix}. \quad (4.57)$$

Physically, f_{NL}^{A} measures the bias in estimating the amplitude of the A bispectrum due to the CMB bispectrum during recombination. The F_{NL} renormalizes f_{NL} with respect to the local-type bispectrum such that equitable comparisons among different templates are possible. The signal-to-noise ratio $(S/N)_{\text{A}}$ measures the detectability of the A bispectrum for unit f_{NL} . The local-type $F_{\text{NL}}^{\text{loc}}$ is small because of the fluctuating bispectrum in squeezed limit as we explained previously. The equilateral-type $F_{\text{NL}}^{\text{equ}}$ is small due to the lack of support in the interior of the recombination bispectrum. Thus, the recombination bispectrum does not correlate well with local and equilateral templates.

Model	f_{NL}	F_{NL}	(S/N)
Equilateral	5.11	0.66	0.028
Local	0.88	0.88	0.22
ISW-Lensing			7.36
Auto-correlation	—	3.19	0.69

Table 4.1 The table of the effective f_{NLS} , F_{NLS} and S/N s of the local and equilateral templates correlated to the recombination bispectrum, as well as its total signal (auto-correlation). For ISW-lensing bispectrum, we found that its correlation with the recombination bispectrum is $\sim 30\%$. For ease of comparison, the F_{NL} quantities normalize the integrated bispectrum signal for any shape relative to the $f_{\text{NL}} = 1$ local model. We have used $\ell_{\text{max}} = 2000$ throughout.

These results are consistent in the squeezed limit with [12, 29]. Moreover, we find that the equilateral type $f_{\text{NL}}^{\text{equ}} = 5.11$ ($F_{\text{NL}}^{\text{equ}} = 0.66$) which is modest but consistent with [13]. Table 4.2 compares all the codes which are capable of implementing the full recombination bispectrum. While there is a relatively good agreement on the values of $f_{\text{NL}}^{\text{equ}}$, the values of $f_{\text{NL}}^{\text{loc}}$ and S/N from different codes appear to be quite different. As we mentioned, the LOS integrand used in [87] may mix up early-time and late-time redshift couplings and fail to converge at low- ℓ truncation. This can result in the larger S/N and $f_{\text{NL}}^{\text{loc}}$ in their calculation. Although we have made some approximations, we do not think that they lead to significant uncertainties. The flat-sky approximation is validated by matching with the analytical solution in the squeezed limit as shown in Fig. 4.4. Although the thin-shell approximation may add uncertainties on the bispectrum generated by the couplings with the early-time ISW effect, these couplings are sub-dominant. The cutoff on the LOS integration allows us to separate the early-time and late-time effects consistently. In particular, we confirm that the $m \neq 0$ modes, which are included in our calculation but not in [52, 82], increase the S/N from 0.65 to 0.69. Their contribution to the bispectrum is mild.

Since the numerical calculation for the recombination bispectrum is very complicated and can depend on the details of the implementations, a comparison between different codes is essential to resolve the discrepancies among different teams in the future. This will be important for the quantitative analysis of the Planck data where this contribution should be incorporated in debiasing local and equilateral signals and in determining whether there is an overall primordial non-Gaussian signature in the data. The recombination bispectrum will combine with the ISW-lensing bispectrum at about 10% level and its correlation can affect the significance of this determination in the Planck data (recall that ISW-lensing effect can bias the local signal by as much as $f_{\text{NL}} = 9.5$ [69]). For this reason, we shall continue to incorporate more physical effects in our numerical pipeline to improve this quantitative analysis further.

	This work	Pitrou [87]	Huang [52]	Pettinari [82]
S/N	0.69	~ 1	0.47	0.47
$f_{\text{NL}}^{\text{equ}}$	5.11	~ 5	-	4.3
$f_{\text{NL}}^{\text{loc}}$	0.88	~ 5	0.82	0.5

Table 4.2 The table for comparisons among the results from all the codes implementing the full recombination bispectrum.

4.4 Conclusions and Discussion

In this chapter, we focus on the bispectrum generated around recombination across the full range of multipole combinations. We find that the effective f_{NLS} of the equilateral and local types are 5.11 and 0.88 respectively, while the overall signal-to-noise is $(S/N)_{\text{rec}} = 0.69$, all calculated using $\ell_{\text{max}} = 2000$. We note from Fig. 4.2 that the bispectrum possesses its own distinct features differentiating it from well-known templates, such as local, equilateral and ISW-lensing. To complete the full calculation of this bispectrum will require the inclusion of the time-delay and lensing effects [49, 69], the addition of the 2nd-order vector and tensor perturbations²⁰, the late-time ISW effects, and finally the terms with the Christoffel symbols in Eq. (2.35). With improving precision, this recombination bispectrum should be included in the analysis of future CMB experiments.

²⁰The 2nd-order vector and tensor perturbations have been included in [52, 82]. Their contributions are believed to be subdominant.

Chapter 5

Weak Lensing in Boltzmann Equation

Cosmic microwave background (CMB) anisotropies generated at the last scattering surface (LSS) propagating towards the present observer are inevitably distorted by the perturbed metric of the intervening spacetime. Such distortions generate higher-order fluctuations which include *lensing*, *redshift* and *time-delay effects*. Among these nonlinear effects, weak lensing has the most significant impact on the CMB.

The Planck mission has conclusively detected lensing of the CMB radiation from foreground sources to an overall significance of greater than 25σ [4]. The high precision of this measurement motivates the development of a more complete formulation of the calculation of this effect. While most effects on the CMB anisotropies are widely studied through direct solutions of the Boltzmann equation, the nonlinear effect of CMB lensing is formulated through the solutions of the geodesic equation. For the theoretical completeness, it is thus of interest to include CMB lensing in the framework of the Boltzmann equation. Practically, the new formalism can be used as a *consistency checking of the canonical remapping approach*¹.

In this chapter, we aim to fill this gap. We present a new formalism to the calculation of the lensing effect by *directly solving the Boltzmann equation*, as we did in the calculation of the CMB anisotropies at recombination. In addition to encoding the geometrical information implicit in the use of the geodesic equations, our approach using the Boltzmann equation also manifestly contains additional interactions, such as redshift effects and Compton scattering. We will discuss how these effects couple with lensing in high orders. From our formalism, we explicitly re-derive the remapping approach in Eq. (2.88) and identify

¹See Section 2.6.1 for a brief review or [67] for details.

the implicit approximations used in the remapping approach. Moreover, we developed a diagrammatic approach to efficiently keep track of all the interaction terms and calculate all possible non-trivial correlations to arbitrarily high orders. One of the primary benefits of our approach is that the meaning of each physical term is clear and unambiguous. This allows us to point out additional unexplored corrections implied in the remapping approach. To demonstrate the formalism, we calculate explicitly the corrections to the temperature power spectrum from lens-lens couplings, which are neglected in standard calculations. Without going through the quantitative calculations of other approximations, we assess their contributions to the CMB power spectrum. The work in this chapter is mainly based on [99].

This chapter is organized as follows. In section 5.1, we first derive the CMB weak lensing effect from the 2nd-order Boltzmann equation. Then, we generalize the derivation to arbitrarily high orders to establish the complete formalism and recover the remapping approach in literature from our formalism by identifying the approximations required. After that, we show how to express the lensing effect in form of Dyson Series and represent the formalism through a diagrammatic approach. Finally, we discuss how the formalism can be extended to study time-delay and redshift effects. In Section 5.2, we extend the diagrammatic approach to calculations of the lensed CMB power spectrum. Focusing on the corrections from lens-lens couplings, we illustrate how these diagrams can facilitate the calculation of the lensing effects on the CMB power spectrum. We find that the correction is $\lesssim 0.1\%$ of the CMB temperature power spectrum for ℓ up to 3000 and thus is comparable to the cosmic variance.

5.1 Formalism

To study the CMB lensing effect, we start with the Boltzmann equation as in Eq. (2.32)²

$$\mathcal{L}[\mathcal{P}_{ab}(x^A, p^0, \hat{\mathbf{n}})] = \mathfrak{C}_{ab}(x^A, p^0, \hat{\mathbf{n}}), \quad (5.1)$$

with the Liouville operator \mathcal{L} , the collision operator \mathfrak{C} and the screen-projected intensity matrix \mathcal{P}_{ab} . The Liouville operator, which describes the free-streaming of the CMB photons, can be expressed under the chosen coordinate system and tetrad basis³ as Eq. (2.34),

²See Section 2.3.2 for a brief review on Boltzmann equation.

³See Section 2.1 for how we choose the coordinate system and the tetrad basis.

i.e.

$$\mathfrak{L}[\mathcal{P}_{ab}] = S_a^c S_b^d \left(\frac{dx^A}{d\eta} \nabla_A \mathcal{P}_{cd} + \frac{dp^0}{d\eta} \frac{\partial}{\partial p^0} \mathcal{P}_{cd} + \frac{dn^i}{d\eta} \frac{\partial}{\partial n^i} \mathcal{P}_{cd} \right), \quad (5.2)$$

where the screen projector S_a^b is defined in Eq. (2.6). As we will soon see, the first term contains time-delay effect and Born approximation, the second term corresponds to redshift effects including Sachs-Wolfe (SW) and integrated Sachs-Wolfe (ISW) effects and the third term corresponds to lensing effect. To elaborate these terms, we need to know the geodesic equation given in Eq. (2.37) and the metric of spacetime in Eq. (2.1). Hereafter, we use the conformal time η instead of the affine parameter s by redefining the Liouville and collision operators

$$\mathfrak{L} \rightarrow \left(\frac{d\eta}{ds} \right) \mathfrak{L}, \quad \mathfrak{C} \rightarrow \left(\frac{d\eta}{ds} \right) \mathfrak{C}. \quad (5.3)$$

That means, we restrict the calculation to the particular choice of coordinate system. However, this transformation is found convenient when we perform the line of sight integration over the conformal time, e.g. in Eq. (5.14). As mentioned in Section 3.2.1, the transformation is equivalent to the transformation with simply the background-order $(d\eta/ds)^{[0]}$.

To solve the dynamics of the CMB photons, we perturb the Boltzmann equation and the Einstein field equations (EFEs), and then solve these differential equations. As demonstrated in Chapter 3 for the 2nd-order perturbations, quantities in lower orders are treated as sources (or inhomogeneous parts) of the higher-order differential equations. That is, we can start from the lowest (background) order and iteratively solve the equations order by order until we get the precision required. Explicitly, we expand the quantities into perturbations as

$$\frac{dX}{ds} = \left(\frac{dX}{ds} \right)^{[0]} + \left(\frac{dX}{ds} \right)^{[I]} + \frac{1}{2!} \left(\frac{dX}{ds} \right)^{[II]} + \frac{1}{3!} \left(\frac{dX}{ds} \right)^{[III]} + \dots, \quad (5.4)$$

$$\mathcal{P}_{ab} = \bar{\mathcal{P}}_{ab} + \mathcal{P}_{ab}^{[I]} + \frac{1}{2!} \mathcal{P}_{ab}^{[II]} + \frac{1}{3!} \mathcal{P}_{ab}^{[III]} + \dots, \quad (5.5)$$

where X denotes η , x^I , p^0 or n^i .

The same expansion can be done for the collision terms \mathfrak{C}_{ab} but we will focus on the damping term $-\dot{\tau} \mathcal{P}_{ab}$ in Compton scattering with the residual terms collected in \mathfrak{D}_{ab} , i.e.

$$\mathfrak{C}_{ab}(x^A, p^0, \hat{\mathbf{n}}) = -\dot{\tau}(\eta) \mathcal{P}_{ab}(x^A, p^0, \hat{\mathbf{n}}) + \mathfrak{D}_{ab}(x^A, p^0, \hat{\mathbf{n}}), \quad (5.6)$$

where $\dot{\tau}(\eta)$ is the differential optical depth in the background order. The term $-\dot{\tau}\mathcal{P}_{ab}$ is responsible for the damping effect on the CMB anisotropies. The N th-order residual term $\mathfrak{D}_{ab}^{[N]}$ contains only contributions from the low multipoles (at most $\ell = 2$) of the N th-order intensity matrix and cross terms of lower-order perturbations. For example, the low multipoles contribute to intrinsic intensity and Doppler effect in N th order. Pragmatically, these low multipoles are calculated through the Boltzmann equation and the EFEs in N th order with a truncated value of ℓ . Then, they are fed back into the Boltzmann equation, which we will then solve using the line of sight approach. Moreover, the residual term $\mathfrak{D}_{ab}^{[N]}$ also contains the perturbed differential optical depth $\delta\tau(x^A)$. This is only important when we care about the nonlinear dynamics of Compton scattering. Since our focus is the CMB weak lensing, the linear-order $\mathfrak{D}_{ab}^{[1]}$ is sufficient. See Approximation 1 in Section 5.1.2 for a more detailed discussion. Nevertheless, we emphasize that there is no dependence of $\mathcal{P}_{ab}^{[N]}$ inside the residual term $\mathfrak{D}_{ab}^{[N]}$ so it can be treated as a source term in the evolution equations of $\mathcal{P}_{ab}^{[N]}$.

Putting together both the Liouville terms Eq. (5.2) and the collision terms Eq. (5.6), we can formulate the solution of the N th-order intensity matrix $\mathcal{P}_{ab}^{[N]}$ by using the line of sight approach as follows. The Boltzmann equation in N th order can be written as

$$S_a^c S_b^d \left\{ \sum_{L=0}^N \binom{N}{L} \left[\left(\frac{dx^I}{d\eta} \right)^{[L]} \frac{\partial \mathcal{P}_{cd}^{[N-L]}}{\partial x^I} + \left(\frac{dp^0}{d\eta} \right)^{[L]} \frac{\partial \mathcal{P}_{cd}^{[N-L]}}{\partial p^0} + \left(\frac{dn^i}{d\eta} \right)^{[L]} \frac{\partial \mathcal{P}_{cd}^{[N-L]}}{\partial n^i} \right] \right\} + (\nabla_\eta \mathcal{P}_{ab})^{[N]} = -\dot{\tau} \mathcal{P}_{ab}^{[N]} + \mathfrak{D}_{ab}^{[N]}, \quad (5.7)$$

where $\binom{N}{L}$ is the Binomial coefficient. The covariant derivative in Eq. (5.7) can be expanded using Eq. (2.35). Here, we make an approximation by ignoring the terms with the Christoffel symbols in Eq. (2.35) as Approximation 0, i.e. $\nabla_\eta \mathcal{P}_{ab} \approx \partial \mathcal{P}_{ab} / \partial \eta$. We rearrange Eq. (5.7) by putting all the terms with $\mathcal{P}_{ab}^{[N]}$ on the left-hand side, such that

$$\frac{\partial \mathcal{P}_{ab}^{[N]}}{\partial \eta} + n^i \frac{\partial \mathcal{P}_{ab}^{[N]}}{\partial x^I} - \mathcal{H} p^0 \frac{\partial \mathcal{P}_{ab}^{[N]}}{\partial p^0} + \dot{\tau} \mathcal{P}_{ab}^{[N]} = S_a^c S_b^d Q_{cd}^{[N]}, \quad (5.8)$$

where we have collected all the source terms in $Q_{ab}^{[N]}$ which is defined as

$$\mathfrak{D}_{ab}^{[N]} - \sum_{L=1}^N \binom{N}{L} \left[\left(\frac{dx^I}{d\eta} \right)^{[L]} \frac{\partial \mathcal{P}_{ab}^{[N-L]}}{\partial x^I} + \left(\frac{dp^0}{d\eta} \right)^{[L]} \frac{\partial \mathcal{P}_{ab}^{[N-L]}}{\partial p^0} + \left(\frac{dn^i}{d\eta} \right)^{[L]} \frac{\partial \mathcal{P}_{ab}^{[N-L]}}{\partial n^i} \right]. \quad (5.9)$$

Henceforth, the term $\xi \bar{e}^I_i$ will be omitted in all contractions between i and I , e.g. $n^i \partial / \partial x^I$ in the second term of Eq. (5.8). Performing the Fourier transform such that any function of \mathbf{x} transforms as

$$f(\mathbf{x}) = \int \frac{d^3 \mathbf{k}}{(2\pi)^{3/2}} e^{i\mathbf{k} \cdot \mathbf{x}} f(\mathbf{k}), \quad (5.10)$$

we obtain

$$\frac{\partial \hat{\mathcal{P}}_{ab}^{[N]}}{\partial \eta} + i\mathbf{k} \cdot \hat{\mathbf{n}} \hat{\mathcal{P}}_{ab}^{[N]} + \dot{\bar{\tau}} \hat{\mathcal{P}}_{ab}^{[N]} = S_a^c S_b^d \hat{\mathcal{Q}}_{cd}^{[N]}, \quad (5.11)$$

where $\hat{\mathcal{P}}_{ab}$ and $\hat{\mathcal{Q}}_{ab}$ are defined as

$$\hat{\mathcal{P}}_{ab}(\eta, \mathbf{k}, \hat{\mathbf{n}}) \equiv \frac{1}{\bar{I}(\eta)} \int dp^0 (p^0)^3 \mathcal{P}_{ab}(\eta, \mathbf{k}, p^0, \hat{\mathbf{n}}), \quad (5.12)$$

$$\hat{\mathcal{Q}}_{ab}(\eta, \mathbf{k}, \hat{\mathbf{n}}) \equiv \frac{1}{\bar{I}(\eta)} \int dp^0 (p^0)^3 \mathcal{Q}_{ab}(\eta, \mathbf{k}, p^0, \hat{\mathbf{n}}), \quad (5.13)$$

with the background-order energy-integrated photon intensity $\bar{I}(\eta)$ defined in Eq. (2.16). Strictly speaking, we note that $\mathbf{k} \cdot \hat{\mathbf{n}} = n^i k_I \xi \bar{e}^I_i$ and contains no perturbations.

By integrating Eq. (5.11) over the line of sight, the N th-order intensity matrix at present ($\eta = \eta_0$) can be expressed as

$$\hat{\mathcal{P}}_{ab}^{[N]}(\eta_0, \mathbf{k}, \hat{\mathbf{n}}) = \int_0^{\eta_0} d\eta e^{-i\mathbf{k} \cdot \hat{\mathbf{n}} r - \bar{\tau}(\eta)} S_a^c S_b^d \hat{\mathcal{Q}}_{cd}^{[N]}(\eta, \mathbf{k}, \hat{\mathbf{n}}), \quad (5.14)$$

with the background-order optical depth $\bar{\tau}(\eta)$ and the conformal distance $r \equiv \eta_0 - \eta$. We remark that all the quantities in $\hat{\mathcal{Q}}_{ab}^{[N]}$ can be determined either by solving the Einstein field equations and the Boltzmann equation with a low truncated ℓ for up to N th order or by performing the line of sight integral for $\hat{\mathcal{P}}_{ab}^{[M]}$ with $M < N$ [83]. In other words, we can extend the calculation to any orders we want iteratively, limited only by computational power and human frailty.

5.1.1 Lensing in Second Order

In this subsection, we warm up by deriving the weak lensing effect on the CMB from the 2nd-order Boltzmann equation. We will match our result with the previous approach using the remapping approach, i.e. Eq. (2.87), explicitly stating the assumptions needed for the

matching, and explaining their physical meanings. We will generalize the derivation to arbitrarily high orders in the next subsection. For an alternative approach at formulating the 2nd-order lensing effect through the 2nd-order Boltzmann equation, see [53].

First of all, we expand the 2nd-order source term $Q_{ab}^{[II]}$ of Eq. (5.9) into

$$\mathcal{D}_{ab}^{[II]} - 2 \left(\frac{dp^0}{d\eta} \right)^{[I]} \frac{\partial \mathcal{P}_{ab}^{[I]}}{\partial p^0} - \left(\frac{dp^0}{d\eta} \right)^{[II]} \frac{\partial \bar{\mathcal{P}}_{ab}}{\partial p^0} - 2 \left(\frac{dx^I}{d\eta} \right)^{[I]} \frac{\partial \mathcal{P}_{ab}^{[I]}}{\partial x^I} - 2 \left(\frac{dn^i}{d\eta} \right)^{[I]} \frac{\partial \mathcal{P}_{ab}^{[I]}}{\partial n^i}. \quad (5.15)$$

The first term in Eq. (5.15) corresponds to Compton scattering, the second and third terms are related to the redshifts due to the perturbed metric along the light path, the fourth term is responsible with the time-delay effect, and the last term is the weak lensing effect. Physically, the second and third terms can be interpreted as redshift effects of the 1st-order perturbed metric on the 1st-order CMB anisotropies and the 2nd-order perturbed metric on the background-order CMB respectively.

Dropping all the other terms except the weak lensing term, considering only the 1st-order Compton scattering⁴, and after performing Fourier transformation and energy integration, we have⁵

$$\hat{Q}_{ab}^{[II]}(\eta, \mathbf{k}, \hat{\mathbf{n}}) = \mathcal{T}_{\mathbf{k}_1, \mathbf{k}_2}(\mathbf{k}) \left\{ 2i S^{ij} k_{1,j} [\Phi(\eta, \mathbf{k}_1) + \Psi(\eta, \mathbf{k}_1)] \frac{\partial}{\partial n^i} \hat{\mathcal{P}}_{ab}(\eta, \mathbf{k}_2, \hat{\mathbf{n}}) \right\}, \quad (5.16)$$

where \mathcal{T} is the convolution operator defined in Eq. (3.24) and S^{ij} is the screen projector in tetrad basis. Here, we express $(dn^i/d\eta)^{[I]}$ with Eq. (3.56) and replace the background-order $k_{1,J} = \xi \bar{e}^j_J k_{1,j}$ with $k_{1,j}$. We refer to Section 2.1 for a general review on coordinate system, tetrad basis and manipulations of their corresponding indices.

From now on, we focus on the photon intensity only. This can be done by the contraction

$$\hat{I}(\eta, \mathbf{k}, \hat{\mathbf{n}}) = S^{ab} \hat{\mathcal{P}}_{ab}(\eta, \mathbf{k}, \hat{\mathbf{n}}). \quad (5.17)$$

Moreover, we define the CMB temperature anisotropies Θ as

$$1 + 4\Theta(\eta, \mathbf{k}, \hat{\mathbf{n}}) \equiv \hat{I}(\eta, \mathbf{k}, \hat{\mathbf{n}}). \quad (5.18)$$

⁴The correction of the direction $\hat{\mathbf{n}}$ in the Doppler term $\hat{\mathbf{n}} \cdot \mathbf{v}_b$ is neglected when we ignore the 2nd-order Compton scattering.

⁵From now on, we omit the superscript [I] denoting 1st-order perturbations whenever it is clear in the context.

In general, the definition of temperature is not unique, especially in nonlinear order with existing CMB spectral distortions. However, if we care about only lensing effects in nonlinear order, there are no spectral distortions induced and thus the lensed CMB temperature can be defined as usual in linear order. For more discussions on the temperature definition, see Section 4.1.

With the 1st-order expression of Θ in Eq. (2.75), and after several integration by parts, we obtain

$$\frac{\partial \Theta^{[\text{I}]}}{\partial n^i}(\eta, \mathbf{k}, \hat{\mathbf{n}}) = ik_i \left[e^{\bar{\tau}(\eta)} \int_0^\eta d\tilde{\eta} e^{ik\mu(\tilde{\eta}-\eta)} (\tilde{\eta}-\eta) S_T(\tilde{\eta}, \mathbf{k}) + \frac{3}{2k^2} \dot{\bar{\tau}}(\eta) \Pi(\eta, \mathbf{k}) \right], \quad (5.19)$$

where the source term S_T is defined in Eq. (2.78).

To solve the 2nd-order lensed temperature anisotropies $\tilde{\Theta}^{[\text{II}]}(\hat{\mathbf{n}})$, we substitute Eq. (5.16) into Eq. (5.14) and replace $\hat{\mathcal{P}}_{ab}$ with temperature anisotropies Θ . Then, by using Eq. (5.19), the lensed temperature anisotropies can be written as

$$\begin{aligned} \tilde{\Theta}^{[\text{II}]}(\hat{\mathbf{n}}) = & \int \frac{d^3 \mathbf{k}_1 d^3 \mathbf{k}_2}{(2\pi)^3} \int_0^{\eta_0} dr 2k_1 k_2 (\mu - \mu_1 \mu_2) [\Phi(\eta, \mathbf{k}_1) + \Psi(\eta, \mathbf{k}_1)] e^{-ik_1 \mu_1 r} \\ & \times \left[\int_r^{\eta_0} d\tilde{r} e^{-ik_2 \mu_2 \tilde{r}} (\tilde{r} - r) S_T(\tilde{\eta}, \mathbf{k}_2) - \frac{3}{2k_2^2} e^{-ik_2 \mu_2 r} g(\eta) \Pi(\eta, \mathbf{k}_2) \right], \quad (5.20) \end{aligned}$$

where

$$\mu \equiv \hat{\mathbf{k}}_1 \cdot \hat{\mathbf{k}}_2, \quad \mu_1 \equiv \hat{\mathbf{n}} \cdot \hat{\mathbf{k}}_1, \quad \mu_2 \equiv \hat{\mathbf{n}} \cdot \hat{\mathbf{k}}_2, \quad r \equiv \eta_0 - \eta, \quad \tilde{r} \equiv \eta_0 - \tilde{\eta}. \quad (5.21)$$

We will now re-derive the remapping formula Eq. (2.87) and Eq. (2.88) of the weak lensing from the Boltzmann equation. Unlike the familiar approach [23] where the lensing deflection is calculated via solving the geodesic equations given the metric perturbations, we *explicitly solve the 2nd-order Boltzmann equation using Green's function method*. This means that we have full control over the entire evolution of the photon distribution from the LSS to today, allowing us to make clear the exact approximations required to recover Eq. (2.87) and Eq. (2.88) as follows:

1. We neglect the term with Π in Eq. (5.20) and re-write the equation as

$$\begin{aligned} \tilde{\Theta}^{[\text{II}]}(\hat{\mathbf{n}}) = & -2S^{ij} \int_0^{\eta_0} dr \frac{\partial}{\partial n^i} \left\{ \int \frac{d^3 \mathbf{k}_1}{(2\pi)^{3/2}} e^{-i\mathbf{k}_1 \cdot \hat{\mathbf{n}} r} [\Phi(\eta, \mathbf{k}_1) + \Psi(\eta, \mathbf{k}_1)] \right\} \\ & \times \int_r^{\eta_0} d\tilde{r} \frac{\tilde{r} - r}{r\tilde{r}} \frac{\partial}{\partial n^j} \left[\int \frac{d^3 \mathbf{k}_2}{(2\pi)^{3/2}} e^{-i\mathbf{k}_2 \cdot \hat{\mathbf{n}} \tilde{r}} S_T(\tilde{\eta}, \mathbf{k}_2) \right]. \quad (5.22) \end{aligned}$$

From the integration limits of the double integral, we can see that the lenses at r can only distort the signals of sources further away, i.e. from r to η_0 , as expected. The neglected term here comes from the boundary condition when we perform the integration by parts in Eq. (5.19). In general, these boundary terms appear only for those terms with modes $\ell \geq 2$ in the source function \tilde{S}_T defined in Eq. (2.75).

2. Then, we replace $(\tilde{r} - r)/\tilde{r}$ with $(r_{\text{LSS}} - r)/r_{\text{LSS}}$, contract $\int_0^{\eta_0} dr$ to $\int_0^{r_{\text{LSS}}} dr$ and extend $\int_r^{\eta_0} d\tilde{r}$ to $\int_0^{\eta_0} d\tilde{r}$ (i.e. effectively uncoupling the two integrals). We get

$$\tilde{\Theta}^{[\Pi]}(\hat{\mathbf{n}}) = 2S^{ij} \frac{\partial}{\partial n^i} \psi(\hat{\mathbf{n}}) \frac{\partial}{\partial n^j} \Theta(\hat{\mathbf{n}}) = 2\nabla_{\hat{\mathbf{n}}} \psi(\hat{\mathbf{n}}) \cdot \nabla_{\hat{\mathbf{n}}} \Theta(\hat{\mathbf{n}}), \quad (5.23)$$

where $\psi(\hat{\mathbf{n}})$ is the lensing potential defined in Eq. (2.88) and we have used the fact that the screen-projected directional derivative

$$S^{ij} \frac{\partial}{\partial n^j} = (\nabla_{\hat{\mathbf{n}}})^i \quad (5.24)$$

in the second equality. This approximation implies that we first integrate all the unlensed CMB signals – including late-time effects, such as the ISW effect and Compton scattering at reionization – and then we treat those unlensed signals as a single source at the LSS and distort them by lenses between the LSS and the observer. This approximation is motivated by the fact that most unlensed CMB signals are generated at recombination and thus can be treated as a single source. Moreover, the lensing on the late-time effects can be ignored. For example, the ISW effect is dominant at low ℓ where the lensing effect is negligible.

If we do not perform the integration by parts to replace $\tilde{S}_T(\eta, \mathbf{k}, \hat{\mathbf{n}})$ with $S_T(\eta, \mathbf{k})$, the first approximation will not be needed⁶. In other words, the first approximation can be folded into the second approximation. Here, we separate them in order to compare our result to previous studies. This “single-source approximation” has been evaluated in [107] for the weak lensing effect on the CMB power spectra. At 2nd order, their equation (Eq. (7)) for redshift-varying sources is exactly the same as Eq. (5.22). However, the term with Π is missing in their study. In principle, we have to take into account the missing boundary terms when we assume the single-source approximation.

⁶See the generalized derivation for high orders in Section 5.1.2.

5.1.2 Lensing in Arbitrarily High Orders

We will now extend the calculation of the lensing effect to arbitrarily high orders and complete the formalism. At 3rd and higher orders, the lensing effect can couple with other effects non-trivially. For example, the 2nd-order lensed photons can be redshifted by linear metric perturbations included in the term

$$\left(\frac{dp^0}{d\eta}\right)^{[I]} \frac{\partial \mathcal{P}_{ab}^{[II]}}{\partial p^0}. \quad (5.25)$$

Thus, it can be ambiguous to distinguish the lensing effect from other effects in high orders.

We will demonstrate how to derive the usual remapping approach [23] by explicitly solving the Boltzmann equation. Throughout the derivation, we will clarify all the assumptions needed. Validations of these approximations can be found in Section 5.2. We start with the source term Eq. (5.9) and make the following approximations:

1. *Ignore nonlinear collision terms:* We include only the 1st-order $\mathcal{D}_{ab}^{[I]}$ from Compton scattering in Eq. (5.6). Nevertheless, we remark that other collision-related effects can be important, such as the SZ effect on small scales at late time. However, the lensing effects on them are believed to be negligibly small [106] and thus these effects can be studied separately⁷. Without these collision terms, there are no distortions on the frequency spectra of \mathcal{P}_{ab} . In other words, there exists a unique definition of temperature anisotropies (see Section 4.1 for more details).
2. *No time-delay:* We drop all the perturbations on $dx^I/d\eta$, i.e.

$$\frac{dx^I}{d\eta} \approx n^i. \quad (5.26)$$

This means that when we accumulate the lensing effects, we perform the time integration along straight lines in the spacetime of the background manifold. This approximation is responsible for ignoring the time-delay effect and the Born approximation.

⁷See [28, 39] for the SZ effect on bispectrum.

The leading time-delay effect is a 2nd-order effect and corresponds to the term⁸

$$\left(\frac{dx^I}{d\eta}\right)^{[I]} \frac{\partial \mathcal{P}_{ab}^{[I]}}{\partial x^I}. \quad (5.27)$$

Physically, it is the effect of the 1st-order perturbed light paths on the 1st-order CMB anisotropies. In contrast, the corrections from the Born approximation are at least 3rd-order [67] and include terms like

$$\left(\frac{dx^I}{d\eta}\right)^{[I]} \frac{\partial \tilde{\mathcal{P}}_{ab}^{[II]}}{\partial x^I}, \quad (5.28)$$

where $\tilde{\mathcal{P}}_{ab}^{[II]}$ is the 2nd-order lensed CMB signals. This is the effect of the 1st-order perturbed light paths on the lensed CMB signals. Here, we emphasize that couplings between different effects (e.g. lensing, redshift and time-delay effects) are possible in higher orders and thus it can be ambiguous to distinguish between the time-delay effect and Born corrections beyond their leading orders. Therefore, we instead clarify what terms are neglected as in Eq. (5.26).

3. *No redshifting by metric perturbations at nonlinear orders:* Similarly, we drop all the perturbations on $dp^0/d\eta$ except

$$\left(\frac{dp^0}{d\eta}\right)^{[I]} \frac{\partial \bar{\mathcal{P}}_{ab}}{\partial p^0}, \quad (5.29)$$

which is responsible for the SW and ISW effects in linear order. In other words, we ignore any contributions due to redshifting beyond the linear order. In principle, redshift-related late-time effects, such as the Rees-Sciama (RS) effect, may be important⁹. In Section 5.2.3, we will see that the high-order couplings between the lensing effect and the late-time redshifting are subdominant compared to the pure lensing effect.

4. *Ignore cross terms between metric perturbations:* We approximate the term $dn^i/d\eta$

⁸In this chapter, we do not re-derive the previous approach [49] of the time-delay effect from the Boltzmann equation explicitly as we will for the remapping approach of the lensing effect in Section 5.1.1 and 5.1.2. Instead, we will argue that the interaction operator Eq. (5.69) responsible for the time-delay effect and the Born approximation is negligible compared to that of the lensing effect, which is consistent with [49].

⁹See [90] and [74] for the RS effect on the CMB power spectrum and bispectrum respectively.

as

$$\frac{dn^i}{d\eta} = \sum_{N=1}^{\infty} \frac{1}{N!} \left(\frac{dn^i}{d\eta} \right)^{[N]} \approx - \sum_{N=1}^{\infty} \frac{S^{ij}}{N!} \partial_J (\Psi^{[N]} + \Phi^{[N]}) \equiv -S^{ij} \partial_J (\Psi^{\text{NL}} + \Phi^{\text{NL}}). \quad (5.30)$$

At N th order, it means that we ignore all the cross terms of lower-order (less than N) perturbations. We call this the *Newtonian approximation* because we drop the cross terms and linearize General Relativity (GR) as if in Newtonian gravity.

With these approximations, the source term \mathcal{Q}_{ab} from Eq. (5.9) is simplified to

$$\mathcal{Q}_{ab} = \mathfrak{D}_{ab}^{[I]} - \left(\frac{dp^0}{d\eta} \right)^{[I]} \frac{\partial \bar{\mathcal{P}}_{ab}}{\partial p^0} + 2S^{ij} \partial_J \Psi_{\text{W}}^{\text{NL}} \frac{\partial \mathcal{P}_{ab}}{\partial n^i}, \quad (5.31)$$

where the nonlinear Weyl potential $\Psi_{\text{W}}^{\text{NL}} \equiv (\Psi^{\text{NL}} + \Phi^{\text{NL}})/2$. Physically, the first three approximations imply that we consider only the pure lensing effects acting on the 1st-order intensity matrix. In principle, we have to consider the nonlinear intensity matrix, especially when we calculate the N -point correlation at large N . Having said that, we expect that the lensing effects on the 2nd-order (and higher-order) intensity matrix generated at recombination are negligible in the CMB temperature power spectrum and bispectrum. For the power spectrum, it is because $|\Theta^{[I]}| \gg |\Theta^{[II]}|$. On the other hand, the 2nd-order temperature anisotropies $\Theta^{[II]}$ at recombination generate a mild bispectrum [52, 82, 100]. Thus, the lensing effect on $\Theta^{[II]}$ at recombination is expected to be subdominant.

We will solve Eq. (5.31) order by order in perturbation theory as follows. First, we expand the intensity matrix order by order

$$\hat{\mathcal{P}}_{ab}(\eta_0, \mathbf{k}, \hat{\mathbf{n}}) = \sum_{N=1}^{\infty} \frac{1}{N!} \hat{\mathcal{P}}_{ab}^{[N]}(\eta_0, \mathbf{k}, \hat{\mathbf{n}}). \quad (5.32)$$

Now we impose the condition, which follows from Approximations 1 and 3, that the 1st-order intensity matrix is sourced by the 1st-order collision term $\mathfrak{D}_{ab}^{[I]}$ and redshifting $\left(\frac{dp^0}{d\eta} \right)^{[I]}$, i.e. using Eq. (5.11)

$$\frac{\partial \hat{\mathcal{P}}_{ab}^{[I]}}{\partial \eta} + i\mathbf{k} \cdot \hat{\mathbf{n}} \hat{\mathcal{P}}_{ab}^{[I]} + \dot{\tau} \hat{\mathcal{P}}_{ab}^{[I]} = S_a^c S_b^d \hat{\mathcal{D}}_{cd}^{[I]} + 2S_{ab} (\Psi D_o - i\mathbf{k} \cdot \hat{\mathbf{n}} \Phi). \quad (5.33)$$

On the right hand side of Eq. (5.33), we have made use of the fact that there are no polarizations in the background order, i.e. $\bar{\mathcal{P}}_{ab} = (1/2)\bar{L}S_{ab}$. Reinserting the solution $\hat{\mathcal{P}}_{ab}^{[I]}$ back into Eq. (5.11) with Approximations 1 to 4, and omitting for simplicity the \mathbf{k} dependence of

$\hat{\mathcal{P}}_{ab}^{[\text{II}]}$, we get

$$\frac{\partial \hat{\mathcal{P}}_{ab}^{[\text{III}]}}{\partial \eta} + \mathbf{k} \cdot \hat{\mathbf{n}} \hat{\mathcal{P}}_{ab}^{[\text{III}]} + \dot{\tau} \hat{\mathcal{P}}_{ab}^{[\text{III}]} = 2S_a^c S_b^d \mathcal{T}_{\mathbf{k}', \mathbf{k}''}(\mathbf{k}) \left\{ 2iS^{ij} k'_j \Psi_{\mathbf{W}}^{\text{NL}}(\mathbf{k}') \frac{\partial \hat{\mathcal{P}}_{cd}^{[\text{I}]}(\mathbf{k}'')}{\partial n^i} \right\}. \quad (5.34)$$

Iterating this, we get at each $N \geq 1$

$$\begin{aligned} & \frac{\partial \hat{\mathcal{P}}_{ab}^{[N+1]}}{\partial \eta} + \mathbf{k} \cdot \hat{\mathbf{n}} \hat{\mathcal{P}}_{ab}^{[N+1]} + \dot{\tau} \hat{\mathcal{P}}_{ab}^{[N+1]} \\ &= \frac{(N+1)!}{N!} S_a^c S_b^d \mathcal{T}_{\mathbf{k}', \mathbf{k}''}(\mathbf{k}) \left\{ 2iS^{ij} k'_j \Psi_{\mathbf{W}}^{\text{NL}}(\mathbf{k}') \frac{\partial \hat{\mathcal{P}}_{cd}^{[M]}(\mathbf{k}'')}{\partial n^i} \right\}. \end{aligned} \quad (5.35)$$

From now on, we focus on the temperature anisotropies. Similar to Eq. (5.14), we use the line of sight approach and Eq. (5.31) to solve Eq. (5.35) as

$$\begin{aligned} & \frac{1}{(N+1)!} \hat{I}^{[N+1]}(\eta_{N+1}, \mathbf{k}_{N+1}, \hat{\mathbf{n}}) \\ &= e^{i\mathbf{k}_{N+1} \cdot \hat{\mathbf{n}} r_{N+1} + \bar{\tau}(\eta_{N+1})} \int_0^{\eta_{N+1}} d\eta_N \left(-\frac{2}{r_N} \right) \mathcal{T}_{\mathbf{k}'_N, \mathbf{k}_N}(\mathbf{k}_{N+1}) \left\{ \nabla_{\hat{\mathbf{n}}}^{i_N} \left[e^{-i\mathbf{k}'_N \cdot \hat{\mathbf{n}} r_N} \Psi_{\mathbf{W}}^{\text{NL}}(\eta_N, \mathbf{k}'_N) \right] \right. \\ & \quad \left. \times \left(\frac{\partial}{\partial n^{i_N}} + ik_{N, i_N} r_N \right) \left[e^{-i\mathbf{k}_N \cdot \hat{\mathbf{n}} r_N - \bar{\tau}(\eta_N)} \frac{1}{N!} \hat{I}^{[N]}(\eta_N, \mathbf{k}_N, \hat{\mathbf{n}}) \right] \right\}, \end{aligned} \quad (5.36)$$

where $N \geq 1$ denotes the N th time of iteration, $r_N \equiv \eta_0 - \eta_N$ and $\hat{I}^{[1]}(\eta_1, \mathbf{k}_1, \hat{\mathbf{n}})$ is the 1st-order photon intensity, i.e. $4\Theta^{[1]}(\eta_1, \mathbf{k}_1, \hat{\mathbf{n}})$ in Eq. (2.75). For $\eta_{N+1} = \eta_0$ at present, we can write the $(N+1)$ th iteration explicitly as the following N -nested integral

$$\begin{aligned} & \frac{1}{(N+1)!} \hat{I}^{[N+1]}(\eta_0, \mathbf{k}_{N+1}, \hat{\mathbf{n}}) = \int_0^{\eta_0} d\tilde{\eta} \left\{ \right. \\ & \int_{\tilde{\eta}}^{\eta_0} d\eta_N \left(-\frac{2}{r_N} \right) \mathcal{T}_{\mathbf{k}'_N, \mathbf{k}_N}(\mathbf{k}_{N+1}) \left\{ \nabla_{\hat{\mathbf{n}}}^{i_N} \left[e^{-i\mathbf{k}'_N \cdot \hat{\mathbf{n}} r_N} \Psi_{\mathbf{W}}^{\text{NL}}(\eta_N, \mathbf{k}'_N) \right] \left(\frac{\partial}{\partial n^{i_N}} + ik_{N, i_N} r_N \right) \left\{ \dots \right. \right. \\ & \int_{\tilde{\eta}}^{\eta_3} d\eta_2 \left(-\frac{2}{r_2} \right) \mathcal{T}_{\mathbf{k}'_2, \mathbf{k}_2}(\mathbf{k}_3) \left\{ \nabla_{\hat{\mathbf{n}}}^{i_2} \left[e^{-i\mathbf{k}'_2 \cdot \hat{\mathbf{n}} r_2} \Psi_{\mathbf{W}}^{\text{NL}}(\eta_2, \mathbf{k}'_2) \right] \left(\frac{\partial}{\partial n^{i_2}} + ik_{2, i_2} r_2 \right) \left\{ \right. \right. \\ & \int_{\tilde{\eta}}^{\eta_2} d\eta_1 \left(-\frac{2}{r_1} \right) \mathcal{T}_{\mathbf{k}'_1, \mathbf{k}_1}(\mathbf{k}_2) \left\{ \nabla_{\hat{\mathbf{n}}}^{i_1} \left[e^{-i\mathbf{k}'_1 \cdot \hat{\mathbf{n}} r_1} \Psi_{\mathbf{W}}^{\text{NL}}(\eta_1, \mathbf{k}'_1) \right] \left(\frac{\partial}{\partial n^{i_1}} + ik_{1, i_1} r_1 \right) \left\{ \right. \right. \\ & \quad \left. \left. e^{-i\mathbf{k}_1 \cdot \hat{\mathbf{n}} \bar{\tau}} 4\tilde{\mathcal{S}}_T(\tilde{\eta}, \mathbf{k}_1, \hat{\mathbf{n}}) \right\} \right\} \dots \left. \right\} \left. \right\}. \end{aligned} \quad (5.37)$$

In Eq. (5.37), we have used a familiar strategy often encountered in quantum field theory to

rearrange the order of the integration limits

$$\int_0^{\eta_{M+1}} d\eta_M \int_0^{\eta_M} d\tilde{\eta} = \int_0^{\eta_{M+1}} d\tilde{\eta} \int_{\tilde{\eta}}^{\eta_{M+1}} d\eta_M \quad (5.38)$$

to pull out the innermost integration with respect to $\tilde{\eta}$ which integrates over the sources. This trick allows us to explicitly expose the physical meaning of the nested integral – the lens at η_N , which generates the $(N + 1)$ th-order intensity from the N th-order intensity, must be located *after* the lenses at η_M ($M < N$) but *before* the observer at η_0 . The time-ordering is illustrated in Fig. 5.1.

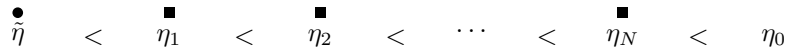


Figure 5.1 The diagrammatic illustration for the time-ordering of the nested integral in Eq. (5.37). The circle node indicates the source while the square nodes indicate the lenses.

Following Eq. (5.32), the lensed photon intensity at present is the sum of all possible iterations, i.e.

$$\hat{I}(\eta_0, \mathbf{k}, \hat{\mathbf{n}}) = \sum_{N=1}^{\infty} \frac{1}{N!} \hat{I}^{[N]}(\eta_0, \mathbf{k}, \hat{\mathbf{n}}). \quad (5.39)$$

Eq. (5.37) and Eq. (5.39) form the complete formula for the pure lensing effect on the 1st-order photon intensity and include all possible ways to distort the 1st-order photon intensity with the weak lensing effect.

In the following, we proceed to recover the remapping approach of the lensing effect in Eq. (2.87) and Eq. (2.88) from the formulae shown in Eq. (5.37) and Eq. (5.39). Several further approximations have to be made and we will clarify them explicitly. Before we do that, we first commute the terms $\partial/\partial n^i + ik_i r$ with the terms $\nabla_{\hat{\mathbf{n}}}^i [e^{-ik' \cdot \hat{\mathbf{n}} r} \Psi_{\mathbf{W}}^{\text{NL}}(\eta, \mathbf{k}')]]$ and rearrange the former to the right hand side of the latter in Eq. (5.37). The commutation can be achieved by using¹⁰

$$\begin{aligned} & \left(\frac{\partial}{\partial n^{iN}} + ik_{N,iN} r_N \right) \left\{ \nabla_{\hat{\mathbf{n}}}^{iM} \left[e^{-ik'_M \cdot \hat{\mathbf{n}} r_M} \Psi_{\mathbf{W}}^{\text{NL}}(\eta_M, \mathbf{k}'_M) \right] F(\cdot) \right\} \\ &= \frac{\partial S^{iM jM}}{\partial n^{iN}} \frac{\partial e^{-ik'_M \cdot \hat{\mathbf{n}} r_M}}{\partial n^{jM}} \Psi_{\mathbf{W}}^{\text{NL}} F(\cdot) + \nabla_{\hat{\mathbf{n}}}^{iM} \left[e^{-ik'_M \cdot \hat{\mathbf{n}} r_M} \Psi_{\mathbf{W}}^{\text{NL}} \right] \left(\frac{\partial}{\partial n^{iN}} - ik'_{M,iN} r_M + ik_{N,iN} r_N \right) F(\cdot) \end{aligned} \quad (5.40)$$

iteratively for $M < N$, with $F(\cdot)$ as some arbitrary function and we have used Eq. (5.24) to

¹⁰We omit the dependences of $\Psi_{\mathbf{W}}^{\text{NL}}$ on the right hand side of Eq. (5.40).

commute the two derivatives

$$\frac{\partial}{\partial n^{iN}} (\nabla_{\hat{\mathbf{n}}})^{iM} = \frac{\partial}{\partial n^{iN}} \left(S^{iMjM} \frac{\partial}{\partial n^{jM}} \right) = \frac{\partial S^{iMjM}}{\partial n^{iN}} \frac{\partial}{\partial n^{jM}} + S^{iMjM} \frac{\partial}{\partial n^{iN}} \frac{\partial}{\partial n^{jM}}. \quad (5.41)$$

Now, we list out the extra approximations needed:

5. *Neglect the directional derivative of the screen projector:* This means that

$$\frac{\partial S^{iMjM}}{\partial n^{iN}} \approx 0. \quad (5.42)$$

We can then move all the partial derivatives into the innermost integrand to act on $\tilde{S}_T(\tilde{\eta})$, and rewrite Eq. (5.37) as

$$\begin{aligned} & \frac{1}{(N+1)!} \hat{f}^{[N+1]}(\eta_0, \mathbf{k}_{N+1}, \hat{\mathbf{n}}) \\ &= \int_0^{\eta_0} d\tilde{\eta} \left\{ \int_{\tilde{\eta}}^{\eta_0} d\eta_N \left(-\frac{2}{r_N} \right) \mathcal{T}_{\mathbf{k}'_N, \mathbf{k}_N}(\mathbf{k}_{N+1}) \left\{ \nabla_{\hat{\mathbf{n}}}^{iN} \left[e^{-i\mathbf{k}'_N \cdot \hat{\mathbf{n}} r_N} \Psi_W^{\text{NL}}(\eta_N, \mathbf{k}'_N) \right] \right\} \left\{ \dots \right. \right. \\ & \quad \int_{\tilde{\eta}}^{\eta_3} d\eta_2 \left(-\frac{2}{r_2} \right) \mathcal{T}_{\mathbf{k}'_2, \mathbf{k}_2}(\mathbf{k}_3) \left\{ \nabla_{\hat{\mathbf{n}}}^{i2} \left[e^{-i\mathbf{k}'_2 \cdot \hat{\mathbf{n}} r_2} \Psi_W^{\text{NL}}(\eta_2, \mathbf{k}'_2) \right] \right\} \left\{ \right. \\ & \quad \left. \int_{\tilde{\eta}}^{\eta_2} d\eta_1 \left(-\frac{2}{r_1} \right) \mathcal{T}_{\mathbf{k}'_1, \mathbf{k}_1}(\mathbf{k}_2) \left\{ \nabla_{\hat{\mathbf{n}}}^{i1} \left[e^{-i\mathbf{k}'_1 \cdot \hat{\mathbf{n}} r_1} \Psi_W^{\text{NL}}(\eta_1, \mathbf{k}'_1) \right] \right\} \left\{ \right. \\ & \quad \left[\frac{\partial}{\partial n^{iN}} + i \sum_{M=1}^{N-1} k'_{M,iN} (r_N - r_M) + ik_{1,iN} r_N \right] \dots \left[\frac{\partial}{\partial n^{i2}} + ik'_{1,i2} (r_2 - r_1) + ik_{1,i2} r_2 \right] \\ & \quad \left. \times \left[\frac{\partial}{\partial n^{i1}} + ik_{1,i1} r_1 \right] e^{-i\mathbf{k}_1 \cdot \hat{\mathbf{n}} r_1} 4\tilde{S}_T(\tilde{\eta}, \mathbf{k}_1, \hat{\mathbf{n}}) \right\} \left. \right\} \left. \right\} \dots \left. \right\} \left. \right\}. \quad (5.43) \end{aligned}$$

This approximation is related to the fact that the argument $(\hat{\mathbf{n}} + \boldsymbol{\alpha})$ in Eq. (2.87) is not a unit vector. This approximation is implied in the remapping approach and has been clarified in [22]. Nevertheless, the leading correction from this approximation is at 3rd order¹¹ and thus we do not expect significant corrections on the CMB power spectra and bispectra. In Section 5.2.1, we will develop a set of diagrams to represent different couplings in Eq. (5.43). In addition, we show that Eq. (5.43) can formally be expressed as a Dyson series in Section 5.1.3.

6. *Ignore lens-lens couplings:* Operationally, this means that we drop all the terms with

¹¹The directional derivative of the screen projector requires $\partial/\partial n^i$ from a lens acting on $\nabla_{\hat{\mathbf{n}}}^j$ of another lens as shown in Eq. (5.37). Therefore, the photon intensity is at least in 3rd order including the 1st-order source term \tilde{S}_T .

integrals as follows

$$\begin{aligned}
& \frac{1}{(N+1)!} \hat{I}^{[N+1]}(\eta_0, \hat{\mathbf{n}}) \\
&= 2 \int_{\eta_{\text{LSS}}}^{\eta_0} d\eta_N \left(\frac{r_N - r_{\text{LSS}}}{r_N r_{\text{LSS}}} \right) \nabla_{\hat{\mathbf{n}}}^{i_N} [\Psi_{\text{W}}^{\text{NL}}(\eta_N, -\hat{\mathbf{n}}r_N)] \left\{ \dots \right. \\
&\quad 2 \int_{\eta_{\text{LSS}}}^{\eta_3} d\eta_2 \left(\frac{r_2 - r_{\text{LSS}}}{r_2 r_{\text{LSS}}} \right) \nabla_{\hat{\mathbf{n}}}^{i_2} [\Psi_{\text{W}}^{\text{NL}}(\eta_2, -\hat{\mathbf{n}}r_2)] \left\{ \right. \\
&\quad \quad 2 \int_{\eta_{\text{LSS}}}^{\eta_2} d\eta_1 \left(\frac{r_1 - r_{\text{LSS}}}{r_1 r_{\text{LSS}}} \right) \nabla_{\hat{\mathbf{n}}}^{i_1} [\Psi_{\text{W}}^{\text{NL}}(\eta_1, -\hat{\mathbf{n}}r_1)] \left\{ \right. \\
&\quad \quad \quad \left. \frac{\partial}{\partial n^{i_N}} \dots \frac{\partial}{\partial n^{i_2}} \frac{\partial}{\partial n^{i_1}} \left[\int \frac{d^3 \mathbf{k}_1}{(2\pi)^{3/2}} \int_0^{\eta_0} d\tilde{\eta} e^{-i\mathbf{k}_1 \cdot \hat{\mathbf{n}}\tilde{r}} 4S_T(\tilde{\eta}, \mathbf{k}_1) \right] \right\} \left. \right\} \dots \left. \right\} \\
&= \frac{4}{N!} \alpha^{i_N} \dots \alpha^{i_2} \alpha^{i_1} \frac{\partial}{\partial n^{i_N}} \dots \frac{\partial}{\partial n^{i_2}} \frac{\partial}{\partial n^{i_1}} \Theta(\hat{\mathbf{n}}), \tag{5.48}
\end{aligned}$$

where the deflection angle $\boldsymbol{\alpha}$ is expressed as

$$\boldsymbol{\alpha}(\hat{\mathbf{n}}) = 2 \int_0^{r_{\text{LSS}}} dr \frac{r - r_{\text{LSS}}}{r r_{\text{LSS}}} \nabla_{\hat{\mathbf{n}}} \Psi_{\text{W}}^{\text{NL}}(\eta, -\hat{\mathbf{n}}r) \tag{5.49}$$

and the unlensed temperature anisotropies are

$$\Theta(\hat{\mathbf{n}}) = \int \frac{d^3 \mathbf{k}_1}{(2\pi)^{3/2}} \int_0^{\eta_0} d\tilde{\eta} e^{-i\mathbf{k}_1 \cdot \hat{\mathbf{n}}\tilde{r}} S_T(\tilde{\eta}, \mathbf{k}_1). \tag{5.50}$$

Finally, summing up all orders, we recover the remapping approach of the weak lensing effect on the photon intensity [23], i.e.

$$\begin{aligned}
\hat{I}(\eta_0, \hat{\mathbf{n}}) - 1 &= \sum_{N=1}^{\infty} \frac{1}{N!} \hat{I}^{[N]}(\eta_0, \hat{\mathbf{n}}) = \sum_{N=0}^{\infty} \frac{4}{N!} \alpha^{i_N} \dots \alpha^{i_2} \alpha^{i_1} \frac{\partial}{\partial n^{i_N}} \dots \frac{\partial}{\partial n^{i_2}} \frac{\partial}{\partial n^{i_1}} \Theta(\hat{\mathbf{n}}) \\
&= 4\Theta(\hat{\mathbf{n}} + \boldsymbol{\alpha}) = 4\tilde{\Theta}(\hat{\mathbf{n}}), \tag{5.51}
\end{aligned}$$

where $\tilde{\Theta}$ denotes the lensed temperature anisotropies.

5.1.3 Lensing as Dyson Series

The Dyson series is a perturbative series which is used often to expand perturbations in different orders when we study scattering theory. Here, we demonstrate how to formulate the CMB lensing effect into a Dyson series. In this way, we start with the Boltzmann equa-

and the vector operator $\hat{\square}_{\hat{\mathbf{n}},r}$ is defined such that it is non-zero only when it acts on \mathcal{X}

$$(\hat{\square}_{\hat{\mathbf{n}},r})_i \mathcal{X}(\boldsymbol{\eta}', -\hat{\mathbf{n}}r') \equiv 2 \frac{r-r'}{r r'} \frac{\partial}{\partial n^i} \mathcal{X}(\boldsymbol{\eta}', -\hat{\mathbf{n}}r'), \quad (5.55)$$

with \mathcal{X} denoting $\Psi_{\text{W}}^{\text{NL}}$ or S_T . Physically, acting $\hat{\square}_{\hat{\mathbf{n}},r}$ on $\Psi_{\text{W}}^{\text{NL}}$ corresponds to lens-lens couplings while acting on S_T corresponds to lensing the sources. The diagrammatic approach in Section 5.1.4 immediately applies to Eq. (5.53) by representing \bullet_0 as S_T instead of Θ .

Now, we introduce the *interaction operator* \hat{V} and the evolution operator \hat{U} as

$$\hat{V}(\boldsymbol{\eta}, \hat{\mathbf{n}}) \equiv \nabla_{\hat{\mathbf{n}}}^i [\Psi_{\text{W}}^{\text{NL}}(\boldsymbol{\eta}, -\hat{\mathbf{n}}r)] (\hat{\square}_{\hat{\mathbf{n}},r})_i, \quad (5.56)$$

$$\hat{U}(\boldsymbol{\eta}_0, \tilde{\boldsymbol{\eta}}, \hat{\mathbf{n}}) \equiv 1 + \sum_{N=1}^{\infty} \hat{U}_N(\boldsymbol{\eta}_0, \tilde{\boldsymbol{\eta}}, \hat{\mathbf{n}}) = \mathcal{T} \left[e^{\int_{\tilde{\boldsymbol{\eta}}}^{\boldsymbol{\eta}_0} d\boldsymbol{\eta} \hat{V}(\boldsymbol{\eta}, \hat{\mathbf{n}})} \right], \quad (5.57)$$

where $r \equiv \eta_0 - \eta$, \mathcal{T} is the time-ordering operator, and

$$\hat{U}_N(\boldsymbol{\eta}_0, \tilde{\boldsymbol{\eta}}, \hat{\mathbf{n}}) \equiv \frac{1}{N!} \int_{\tilde{\boldsymbol{\eta}}}^{\boldsymbol{\eta}_0} d\boldsymbol{\eta}_N \dots \int_{\tilde{\boldsymbol{\eta}}}^{\boldsymbol{\eta}_0} d\boldsymbol{\eta}_2 \int_{\tilde{\boldsymbol{\eta}}}^{\boldsymbol{\eta}_0} d\boldsymbol{\eta}_1 \mathcal{T} [\hat{V}(\boldsymbol{\eta}_N, \hat{\mathbf{n}}) \dots \hat{V}(\boldsymbol{\eta}_2, \hat{\mathbf{n}}) \hat{V}(\boldsymbol{\eta}_1, \hat{\mathbf{n}})]. \quad (5.58)$$

Formally, this means that the evolution operator is the solution to the following equation

$$\frac{d}{d\boldsymbol{\eta}} \hat{U}(\boldsymbol{\eta}, \tilde{\boldsymbol{\eta}}, \hat{\mathbf{n}}) = \hat{V}(\boldsymbol{\eta}, \hat{\mathbf{n}}) \hat{U}(\boldsymbol{\eta}, \tilde{\boldsymbol{\eta}}, \hat{\mathbf{n}}). \quad (5.59)$$

Using the evolution operator, Eq. (5.53) can be expressed as the following integral

$$\frac{1}{(N+1)!} \hat{I}^{[N+1]}(\boldsymbol{\eta}_0, \hat{\mathbf{n}}) = 4 \int_0^{\eta_0} d\tilde{\boldsymbol{\eta}} \hat{U}_N(\boldsymbol{\eta}_0, \tilde{\boldsymbol{\eta}}, \hat{\mathbf{n}}) S_T(\tilde{\boldsymbol{\eta}}, -\hat{\mathbf{n}}\tilde{r}). \quad (5.60)$$

Thus, the lensed CMB anisotropies observed today are

$$\tilde{\Theta}(\hat{\mathbf{n}}) = \frac{\hat{I}(\boldsymbol{\eta}_0, \hat{\mathbf{n}})}{4} = \int_0^{\eta_0} d\tilde{\boldsymbol{\eta}} \hat{U}(\boldsymbol{\eta}_0, \tilde{\boldsymbol{\eta}}, \hat{\mathbf{n}}) S_T(\tilde{\boldsymbol{\eta}}, -\hat{\mathbf{n}}\tilde{r}). \quad (5.61)$$

Cast in this form, it is clear that we can interpret Eq. (5.61) as the accumulated lensing effect on the CMB sources at different time $\tilde{\boldsymbol{\eta}}$.

5.1.4 Diagrammatic Approach

In this subsection, we develop a set of rules as a book-keeping tool to compute any N th-order lensed CMB anisotropies. This facilitates the expansion of the lensing effect to higher orders for calculations of the corresponding CMB power spectra and bispectra. In Section 5.2.1, we will demonstrate the calculation of the lensed CMB temperature power spectrum by using the diagrammatic approach. Although we develop the diagrammatic approach based on Eq. (5.53), we note that the diagrams are compatible with Eq. (5.78) which considers fixed sources at the LSS by applying Approximation 7 in Section 5.1.2. Moreover, similar diagrams can be developed to include the redshift and time-delay effects which will be discussed in Section 5.1.5.

As we can see in Eq. (5.53), the $(N + 1)$ th-order photon intensity contains time-ordered integrals over two types of interaction terms – the unlensed source term S_T (diagrammatically $\overset{\bullet}{\underset{0}{\square}}$ where the 0 below denotes the ordering)¹² and the N th potential term $\nabla_{\hat{\mathbf{n}}}[\Psi_{\mathbf{W}}^{\text{NL}}(\eta_N)]$ (diagrammatically \blacksquare_N where the label N indicates the time-ordering of the potential terms). With $N > M$, it means that the N th potential term is located *later* in time compared to the M th potential term. We write down the time-ordered terms from left to right in a row. For example, the 4th-order photon intensity $\hat{I}^{[4]}$ is expressed as

$$\overset{\bullet}{\underset{0}{\square}} \blacksquare_1 \blacksquare_2 \blacksquare_3$$

which is simply a simplified expression of Fig. 5.1.

In addition to the interaction terms, there is an ‘‘action’’ term in Eq. (5.55), i.e. the vector operator $\hat{\square}_{\hat{\mathbf{n}},r}$ acting on either interaction term S_T or $\nabla_{\hat{\mathbf{n}}}[\Psi_{\mathbf{W}}^{\text{NL}}]$. We denote the action

by an over-arc, i.e.  for action of $\hat{\square}_{\hat{\mathbf{n}},r_N}$ on S_T and  for action of $\hat{\square}_{\hat{\mathbf{n}},r_N}$ on $\nabla_{\hat{\mathbf{n}}}[\Psi_{\mathbf{W}}^{\text{NL}}(\eta_M)]$. For each N th action, there is an N th time integral $\int_{\tilde{\eta}}^{\eta_{N+1}} d\eta_N$ associated with it¹³. We summarize these rules in Table 5.1.

Hence, the prescription to writing down the integrals in Eq. (5.53) is to construct *all possible actions from the left to the right*. Physically, an N th node acting on an M th node for $N > M$ means that the object closer to us at N is lensing the object further away at M . In our formalism, \blacksquare is a lens and thus an overarc between two lenses denotes a *lens-lens*

¹²With Approximation 7 in Section 5.1.2, the circle node represents Θ instead of $\int_0^{\eta_0} d\tilde{\eta} S_T(\tilde{\eta})$.

¹³Here, $\tilde{\eta}$ locates the source term S_T and integrates from 0 to η_0 . With Approximation 7 in Section 5.1.2, we replace $\tilde{\eta}$ by η_{LSS} .

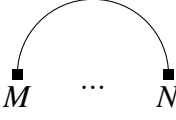
Diagram	Term	Physical Meaning
$\overset{\bullet}{0}$	$\Theta(\hat{\mathbf{n}})$ or $\int_0^{\eta_0} d\tilde{\eta} S_T(\tilde{\eta}, -\hat{\mathbf{n}}\tilde{r})$	Unlensed source generated at node 0.
$\overset{\blacksquare}{N}$	$\nabla_{\hat{\mathbf{n}}}^{i_N} [\Psi_{\mathbf{W}}^{\text{NL}}(\eta_N, -\hat{\mathbf{n}}r_N)]$	Lens at node N .
	$\int_{\eta_{\text{LSS}}}^{\eta_{N+1}} d\eta_N \nabla_{\hat{\mathbf{n}}}^{i_N} [\Psi_{\mathbf{W}}^{\text{NL}}(\eta_N)] \frac{r_N - r_{\text{LSS}}}{r_N r_{\text{LSS}}} \frac{\partial \Theta(\hat{\mathbf{n}})}{\partial n^{i_N}}$ or $\int_0^{\eta_0} d\tilde{\eta} \int_{\tilde{\eta}}^{\eta_{N+1}} d\eta_N \nabla_{\hat{\mathbf{n}}}^{i_N} [\Psi_{\mathbf{W}}^{\text{NL}}(\eta_N)] \frac{r_N - \tilde{r}}{r_N \tilde{r}} \frac{\partial S_T(\tilde{\eta})}{\partial n^{i_N}}$	The lens at node N distorts the unlensed source, i.e. lens-source coupling.
	$\int_{\eta_{\text{LSS}}}^{\eta_{N+1}} d\eta_N \nabla_{\hat{\mathbf{n}}}^{i_N} [\Psi_{\mathbf{W}}^{\text{NL}}(\eta_N)] \frac{r_N - r_M}{r_N r_M} \nabla_{\hat{\mathbf{n}}}^{i_M} \frac{\partial \Psi_{\mathbf{W}}^{\text{NL}}(\eta_M)}{\partial n^{i_N}}$ or $\int_{\tilde{\eta}}^{\eta_{N+1}} d\eta_N \nabla_{\hat{\mathbf{n}}}^{i_N} [\Psi_{\mathbf{W}}^{\text{NL}}(\eta_N)] \frac{r_N - r_M}{r_N r_M} \nabla_{\hat{\mathbf{n}}}^{i_M} \frac{\partial \Psi_{\mathbf{W}}^{\text{NL}}(\eta_M)}{\partial n^{i_N}}$	The lens at node N distorts the lens at node M , i.e. lens-lens coupling.

Table 5.1 The diagrams with their corresponding represented equations and their physical meanings. In the “Term” column, the first choice assumes Approximation 7 while the second one does not.

coupling. We emphasize that, although we have considered only the lensing effect here, it is easy to generalize our diagrammatic approach to other types of interaction terms such as the redshift and time-delay effects as will be discussed in Section 5.1.5 by adding more node types.

As an example, we list out all the possible diagrams for the third-, forth- and fifth-order terms of the lensed temperature anisotropies $\tilde{\Theta}$ in Table 5.2. In fact, except the upper left diagram in each of Table 5.2a, 5.2b and 5.2c, all the other diagrams involve the lens-lens couplings. Ignoring these couplings is equivalent to applying Approximation 6 in Section 5.1.2.

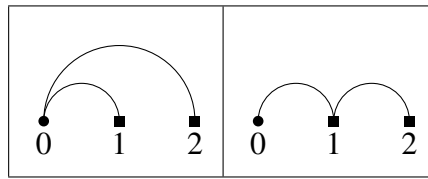
To illustrate the rules summarized in Table 5.1, we demonstrate how to construct the formulae for the middle diagram in the first row of Table 5.2b. From the diagram, there are one circle node and three square nodes, i.e. one source and three lenses. The lenses at node 1 and 2 distort the source while the lens at node 3 distorts the lens at node 1. Based on the rules in Table 5.1, the integral associated with this diagram is

$$\begin{aligned}
\tilde{\Theta}^{[4]}(\hat{\mathbf{n}}) &\supset \begin{array}{c} \bullet \\ \circlearrowleft \\ \blacksquare \quad \blacksquare \quad \blacksquare \\ 0 \quad 1 \quad 2 \quad 3 \end{array} \\
&= \int_0^{\eta_0} d\tilde{\eta} \int_{\tilde{\eta}}^{\eta_0} d\eta_3 \nabla_{\hat{\mathbf{n}}}^{i_3} [\Psi_{\mathbf{W}}^{\text{NL}}(\eta_3, -\hat{\mathbf{n}}r_3)] \left\{ \right. \\
&\quad \int_{\tilde{\eta}}^{\eta_3} d\eta_2 \nabla_{\hat{\mathbf{n}}}^{i_2} [\Psi_{\mathbf{W}}^{\text{NL}}(\eta_2, -\hat{\mathbf{n}}r_2)] \left\{ \right. \\
&\quad \int_{\tilde{\eta}}^{\eta_2} d\eta_1 \left(2 \frac{r_3 - r_1}{r_3 r_1} \right) \nabla_{\hat{\mathbf{n}}}^{i_1} \left[\frac{\partial}{\partial n^{i_3}} \Psi_{\mathbf{W}}^{\text{NL}}(\eta_1, -\hat{\mathbf{n}}r_1) \right] \left\{ \right. \\
&\quad \left. \left(2 \frac{r_2 - \tilde{r}}{r_2 \tilde{r}} \right) \left(2 \frac{r_1 - \tilde{r}}{r_1 \tilde{r}} \right) \frac{\partial}{\partial n^{i_2}} \frac{\partial}{\partial n^{i_1}} S_T(\tilde{\eta}, -\hat{\mathbf{n}}\tilde{r}) \right. \left. \left. \right\} \right\} \left. \right\}. \quad (5.62)
\end{aligned}$$

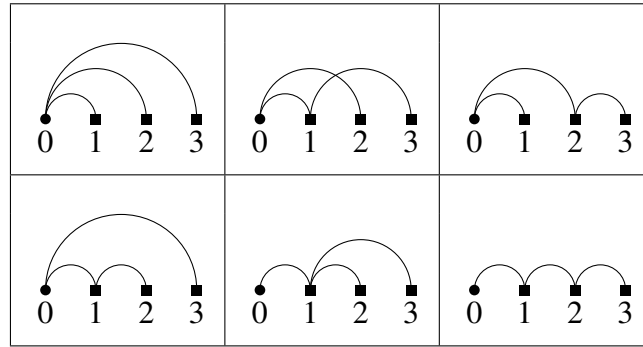
While these diagrams may seem frivolous, its power arises when we want to compute the two-point *correlation functions*, e.g. $\langle \Theta^{[N]} \Theta^{[M]} \rangle$ to all possible actions in the N th and M th orders. To see that, we need a new rule to encapsulate *contractions* between all possible interaction terms (either \blacksquare or \bullet), which will be introduced in Section 5.2.1.

5.1.5 Extensions

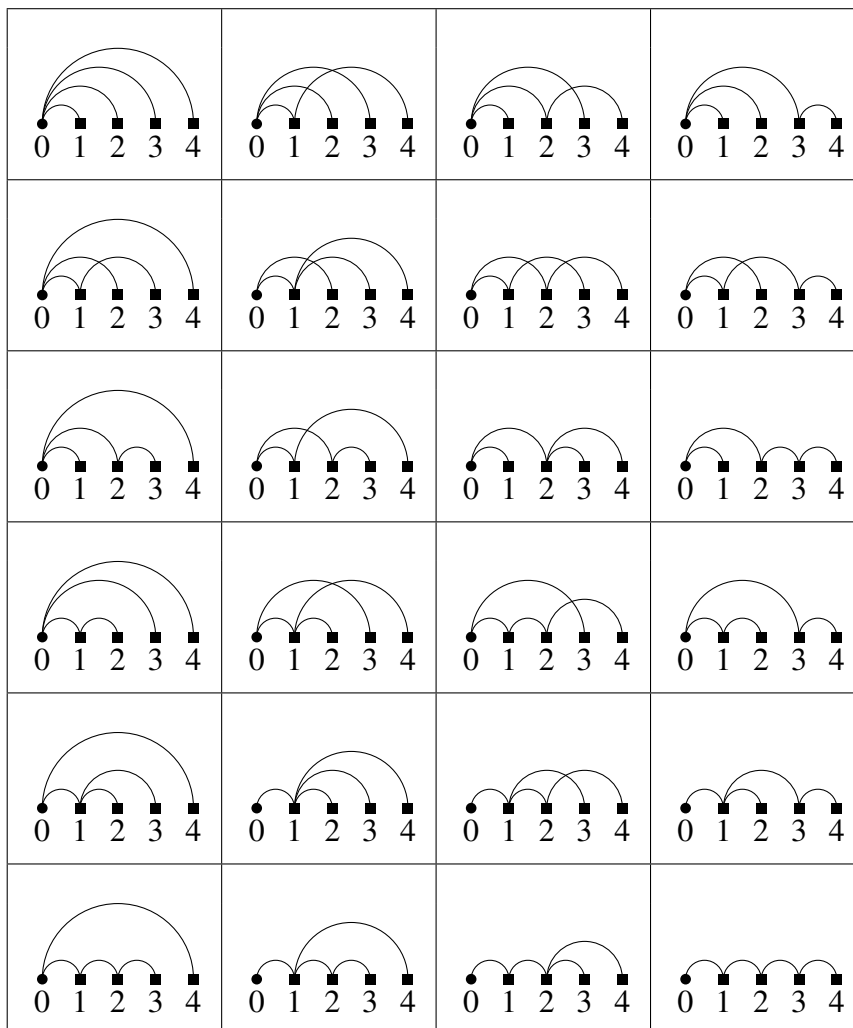
In this subsection, we extend the formalism and the diagrammatic approach developed for the weak lensing effect to study the redshift and time-delay effects. We will derive their



(a) The third iteration



(b) The fourth iteration



(c) The fifth iteration

Table 5.2 All the possible couplings of the weak lensing effects on the CMB anisotropies in the third, forth and fifth orders. As an example, Eq. (5.62) demonstrates how to construct the formulae from the middle diagram in the first row of Table 5.2b.

corresponding interaction operators, following what we have done in Section 5.1.3. We will also show how the formalism can be used to systematically estimate their contributions to the CMB signals, especially for higher orders in which the redshift and time-delay effects can couple with the lensing effect. The extension here can be treated as the relaxation of Approximations 2 and 3 in Section 5.1.2. Nonetheless, we argue that the pure lensing effect dominates in arbitrarily high orders. With the extension to the redshift and time-delay effects, the developed formalism becomes a comprehensive solution of the Liouville operator (collisionless part) of the Boltzmann equation in arbitrarily high orders. We emphasize that the formalism is generic and can be used to study the lensing, redshift and time-delay effects of other observations – such as galaxy surveys.

Time Delay Effect and Born Correction

By ignoring $dx^I/d\eta$ (Approximation 2 in Section 5.1.2) in the Boltzmann equation, we apply the Born approximation [44, 95] and neglect the time-delay effect [49]. Here, we relax this approximation in our formalism. For simplicity, we first consider it without the lensing terms. That is, Eq. (5.31) becomes

$$\mathcal{Q}_{ab} = \mathfrak{D}_{ab}^{[1]} - \left(\frac{dp^0}{d\eta} \right)^{[1]} \frac{\partial \bar{\mathcal{P}}_{ab}}{\partial p^0} - 2n^i \Psi_{\text{W}}^{\text{NL}} \frac{\partial \mathcal{P}_{ab}}{\partial x^I}, \quad (5.63)$$

with the Newtonian approximation (Approximation 4 in Section 5.1.2) modified as

$$\frac{dx^I}{d\eta} = \sum_{N=0}^{\infty} \frac{1}{N!} \left(\frac{dx^I}{d\eta} \right)^{[N]} \approx n^i + \sum_{N=1}^{\infty} \frac{n^i}{N!} (\Psi^{[N]} + \Phi^{[N]}) \equiv n^i + 2n^i \Psi_{\text{W}}^{\text{NL}}. \quad (5.64)$$

Combining Eq. (5.11) and Eq. (5.63), we can find the recursive solution of the normalized intensity matrix, by the line of sight approach

$$\frac{1}{(N+1)!} \hat{\mathcal{P}}_{ab}^{[N+1]}(\eta_{N+1}, \mathbf{k}_{N+1}, \hat{\mathbf{n}}) = e^{i\mathbf{k}_{N+1} \cdot \hat{\mathbf{n}} r_{N+1} + \bar{\tau}(\eta_{N+1})} \int_0^{\eta_{N+1}} d\eta_N \mathcal{T}_{\mathbf{k}'_N, \mathbf{k}_N}(\mathbf{k}_{N+1}) \left\{ \right. \\ \left. - 2i\mathbf{k}_N \cdot \hat{\mathbf{n}} \left[e^{-i\mathbf{k}'_N \cdot \hat{\mathbf{n}} r_N} \Psi_{\text{W}}^{\text{NL}}(\eta_N, \mathbf{k}'_N) \right] \left[e^{-i\mathbf{k}_N \cdot \hat{\mathbf{n}} r_N - \bar{\tau}(\eta_N)} \frac{1}{N!} \hat{\mathcal{P}}_{ab}^{[N]}(\eta_N, \mathbf{k}_N, \hat{\mathbf{n}}) \right] \right\}, \quad (5.65)$$

where $N \geq 1$.

Now, we focus on the temperature anisotropies only. The $(N+1)$ th iteration of the

photon intensity at present (η_0) is

$$\begin{aligned}
& \frac{1}{(N+1)!} \hat{I}^{[N+1]}(\eta_0, \mathbf{k}_{N+1}, \hat{\mathbf{n}}) \\
&= \int_0^{\eta_0} d\tilde{\eta} \left\{ \int_{\tilde{\eta}}^{\eta_0} d\eta_N \mathcal{T}_{\mathbf{k}'_N, \mathbf{k}_N}(\mathbf{k}_{N+1}) \left\{ \left[e^{-i\mathbf{k}'_N \cdot \hat{\mathbf{n}} r_N} \Psi_W^{\text{NL}}(\eta_N, \mathbf{k}'_N) \right] (-2i\mathbf{k}_N \cdot \hat{\mathbf{n}}) \left\{ \dots \right. \right. \right. \\
& \quad \int_{\tilde{\eta}}^{\eta_3} d\eta_2 \mathcal{T}_{\mathbf{k}'_2, \mathbf{k}_2}(\mathbf{k}_3) \left\{ \left[e^{-i\mathbf{k}'_2 \cdot \hat{\mathbf{n}} r_2} \Psi_W^{\text{NL}}(\eta_2, \mathbf{k}'_2) \right] (-2i\mathbf{k}_2 \cdot \hat{\mathbf{n}}) \left\{ \right. \right. \\
& \quad \int_{\tilde{\eta}}^{\eta_2} d\eta_1 \mathcal{T}_{\mathbf{k}'_1, \mathbf{k}_1}(\mathbf{k}_2) \left\{ \left[e^{-i\mathbf{k}'_1 \cdot \hat{\mathbf{n}} r_1} \Psi_W^{\text{NL}}(\eta_1, \mathbf{k}'_1) \right] (-2i\mathbf{k}_1 \cdot \hat{\mathbf{n}}) \left\{ \right. \right. \\
& \quad \left. \left. \left. \left. \left. \left. e^{-i\mathbf{k}_1 \cdot \hat{\mathbf{n}} \tilde{r}} 4\tilde{S}_T(\tilde{\eta}, \mathbf{k}_1, \hat{\mathbf{n}}) \right\} \right\} \right\} \dots \right\} \right\}. \quad (5.66)
\end{aligned}$$

Similar to Approximation 1 in Section 5.1.1, we replace $\tilde{S}_T(\tilde{\eta}, \mathbf{k}_1, \hat{\mathbf{n}})$ with $S_T(\tilde{\eta}, \mathbf{k}_1)$ by ignoring the boundary terms of $\Theta^{[1]}(\eta, \mathbf{k}_1, \hat{\mathbf{n}})$ generated by integration by parts when $\eta \neq \eta_0$. Following the derivation in Section 5.1.3, the $(N+1)$ th iteration of the photon intensity from the time-delay effect can be written in configuration space as

$$\begin{aligned}
& \frac{1}{(N+1)!} \hat{I}^{[N+1]}(\eta_0, \hat{\mathbf{n}}) \\
&= \int_0^{\eta_0} d\tilde{\eta} \left\{ \int_{\tilde{\eta}}^{\eta_0} d\eta_N [n^{i_N} \Psi_W^{\text{NL}}(\eta_N, -\hat{\mathbf{n}} r_N)] (\hat{\diamond}_{\hat{\mathbf{n}}, r_N})_{i_N} \left\{ \dots \right. \right. \\
& \quad \int_{\tilde{\eta}}^{\eta_3} d\eta_2 [n^{i_2} \Psi_W^{\text{NL}}(\eta_2, -\hat{\mathbf{n}} r_2)] (\hat{\diamond}_{\hat{\mathbf{n}}, r_2})_{i_2} \left\{ \right. \\
& \quad \left. \int_{\tilde{\eta}}^{\eta_2} d\eta_1 [n^{i_1} \Psi_W^{\text{NL}}(\eta_1, -\hat{\mathbf{n}} r_1)] (\hat{\diamond}_{\hat{\mathbf{n}}, r_1})_{i_1} \left\{ 4S_T(\tilde{\eta}, -\hat{\mathbf{n}} \tilde{r}) \right\} \right\} \dots \left. \right\}, \quad (5.67)
\end{aligned}$$

where $\Psi_W^{\text{NL}}(\eta_N, -\hat{\mathbf{n}} r_N)$ and $S_T(\tilde{\eta}, -\hat{\mathbf{n}} \tilde{r})$ are defined in Eq. (5.45) and Eq. (5.54) respectively, and the vector operator $\hat{\diamond}_{\hat{\mathbf{n}}, r}$ is defined such that it is non-zero only when it acts on \mathcal{X}

$$(\hat{\diamond}_{\hat{\mathbf{n}}, r})_i \mathcal{X}(\eta', -\hat{\mathbf{n}} r') \equiv \frac{2}{r'} \frac{\partial}{\partial n^i} \mathcal{X}(\eta', -\hat{\mathbf{n}} r'), \quad (5.68)$$

with \mathcal{X} denoting Ψ_W^{NL} or S_T . We notice that the r -dependence of the vector operator $\hat{\diamond}$ is redundant but we keep it as a consistent notation with Eq. (5.55). Furthermore, we can define the interaction operator of the time-delay effect as

$$\hat{V}_x(\eta, \hat{\mathbf{n}}) \equiv n^i \Psi_W^{\text{NL}}(\eta, -\hat{\mathbf{n}} r) (\hat{\diamond}_{\hat{\mathbf{n}}, r})_i, \quad (5.69)$$

where the subscript x denotes that this term comes from the derivative with respect to space-like coordinates x^I of the background manifold in the Liouville operator. To include the lensing effect, we can simply add the interaction operators of the lensing and time-delay effects together to the Dyson series in Eq. (5.61). Moreover, the diagrammatic approach in Section 5.1.4 can be extended straightforwardly by introducing a new node $\blacklozenge_{\mathbf{N}}$ to represent the interactions of the time-delay effect.

To understand why the lensing effect dominates over the corrections from Born approximation and the time-delay effect, we consider the ratio of the norms of the two interaction operators in Eq. (5.56) and Eq. (5.69), i.e. $R \equiv \|\hat{V}_x\|/\|\hat{V}\|$. With the flat-sky approximation, we can replace $\nabla_{\hat{n}}$ with ℓ in Fourier space and have $R \sim r/(r' - r)/\ell$ where $\ell = |\ell|$ and $|n^i|$ is of order 1. For lens-source couplings which dominate the lensing effect, $r/(r' - r)$ is of order 1 and thus $R \sim 1/\ell$ with $\ell \sim 40$ at the peak of the power spectrum of the lensing potential¹⁴. This estimation is consistent with [49]. The argument here is made with the interaction operator and is valid throughout the hierarchy, not just in the lowest orders as verified previously in literature. That is, we can safely ignore any high-order couplings involving the redshift and time-delay effects as the pure lensing effect dominates.

Redshift

Similarly, we relax Approximation 3 in Section 5.1.2 by including the redshift effects in nonlinear orders so that

$$\mathcal{Q}_{ab} = \mathfrak{D}_{ab}^{[1]} - p^0 (\partial_\eta \Psi^{\text{NL}} - n^i \partial_I \Phi^{\text{NL}}) \frac{\partial \mathcal{P}_{ab}}{\partial p^0}, \quad (5.70)$$

where the Newtonian approximation (Approximation 4 in Section 5.1.2) becomes

$$\begin{aligned} \frac{dp^0}{d\eta} &= \sum_{N=0}^{\infty} \frac{1}{N!} \left(\frac{dp^0}{d\eta} \right)^{[N]} \\ &\approx -\mathcal{H}p^0 + \sum_{N=1}^{\infty} \frac{p^0}{N!} (\partial_\eta \Psi^{[N]} - n^i \partial_I \Phi^{[N]}) \equiv -\mathcal{H}p^0 + p^0 (\partial_\eta \Psi^{\text{NL}} - n^i \partial_I \Phi^{\text{NL}}). \end{aligned} \quad (5.71)$$

Here, we ignore the lensing and time-delay effects for simplicity but it is straightforward to include them. Substituting Eq. (5.70) into Eq. (5.11), the recursive solution of the normal-

¹⁴More precisely, lenses at redshifts $z \lesssim 10$ dominate the lensing effect [67]. For these lenses, $r/(r' - r) \lesssim 2$ and the argument holds as well.

ized intensity matrix can be written as

$$\begin{aligned} \frac{1}{(N+1)!} \hat{\mathcal{P}}_{ab}^{[N+1]}(\eta_{N+1}, \mathbf{k}_{N+1}, \hat{\mathbf{n}}) &= e^{i\mathbf{k}_{N+1} \cdot \hat{\mathbf{n}} r_{N+1} + \bar{\tau}(\eta_{N+1})} \int_0^{\eta_{N+1}} d\eta_N \mathcal{T}_{\mathbf{k}'_N, \mathbf{k}_N}(\mathbf{k}_{N+1}) \left\{ 4 \right. \\ &\quad \times \left[\partial_{\eta_N} \left(e^{-i\mathbf{k}'_N \cdot \hat{\mathbf{n}} r_N} \Phi^{\text{NL}}(\eta_N, \mathbf{k}'_N) \right) - 2e^{-i\mathbf{k}'_N \cdot \hat{\mathbf{n}} r_N} \partial_{\eta_N} \Psi_{\text{W}}^{\text{NL}}(\eta_N, \mathbf{k}'_N) \right] \\ &\quad \left. \times \left[e^{-i\mathbf{k}_N \cdot \hat{\mathbf{n}} r_N - \bar{\tau}(\eta_N)} \frac{1}{N!} \hat{\mathcal{P}}_{ab}^{[N]}(\eta_N, \mathbf{k}_N, \hat{\mathbf{n}}) \right] \right\}, \end{aligned} \quad (5.72)$$

where $N \geq 1$ and $\Psi_{\text{W}}^{\text{NL}}$ is the nonlinear Weyl potential. In Eq. (5.72), the term with Φ^{NL} corresponds to the SW effect while the term with $\Psi_{\text{W}}^{\text{NL}}$ corresponds to the ISW effect. Similar trick is used in Section 4.2.2 when we separate the SW and ISW effects in the 2nd-order Boltzmann equation.

The $(N+1)$ th iteration of the photon intensity at present is

$$\begin{aligned} \frac{1}{(N+1)!} \hat{I}^{[N+1]}(\eta_0, \mathbf{k}_{N+1}, \hat{\mathbf{n}}) &= \int_0^{\eta_0} d\tilde{\eta} \left\{ \right. \\ &\int_{\tilde{\eta}}^{\eta_0} d\eta_N \mathcal{T}_{\mathbf{k}'_N, \mathbf{k}_N}(\mathbf{k}_{N+1}) \left\{ \left[\partial_{\eta_N} \left(e^{-i\mathbf{k}'_N \cdot \hat{\mathbf{n}} r_N} \Phi^{\text{NL}}(\eta_N, \mathbf{k}'_N) \right) - 2e^{-i\mathbf{k}'_N \cdot \hat{\mathbf{n}} r_N} \partial_{\eta_N} \Psi_{\text{W}}^{\text{NL}}(\eta_N, \mathbf{k}'_N) \right] \left\{ \dots \right. \right. \\ &\quad \int_{\tilde{\eta}}^{\eta_3} d\eta_2 \mathcal{T}_{\mathbf{k}'_2, \mathbf{k}_2}(\mathbf{k}_3) \left\{ \left[\partial_{\eta_2} \left(e^{-i\mathbf{k}'_2 \cdot \hat{\mathbf{n}} r_2} \Phi^{\text{NL}}(\eta_2, \mathbf{k}'_2) \right) - 2e^{-i\mathbf{k}'_2 \cdot \hat{\mathbf{n}} r_2} \partial_{\eta_2} \Psi_{\text{W}}^{\text{NL}}(\eta_2, \mathbf{k}'_2) \right] \left\{ \right. \\ &\quad \int_{\tilde{\eta}}^{\eta_2} d\eta_1 \mathcal{T}_{\mathbf{k}'_1, \mathbf{k}_1}(\mathbf{k}_2) \left\{ \left[\partial_{\eta_1} \left(e^{-i\mathbf{k}'_1 \cdot \hat{\mathbf{n}} r_1} \Phi^{\text{NL}}(\eta_1, \mathbf{k}'_1) \right) - 2e^{-i\mathbf{k}'_1 \cdot \hat{\mathbf{n}} r_1} \partial_{\eta_1} \Psi_{\text{W}}^{\text{NL}}(\eta_1, \mathbf{k}'_1) \right] \left\{ \right. \\ &\quad \left. \left. \left. \left. \left. e^{-i\mathbf{k}_1 \cdot \hat{\mathbf{n}} r} 4\tilde{\mathcal{S}}_T(\tilde{\eta}, \mathbf{k}_1, \hat{\mathbf{n}}) \right\} \right\} \right\} \dots \right\} \right\} \left. \right\}. \end{aligned} \quad (5.73)$$

In configuration space, the $(N+1)$ th iteration of the photon intensity from the redshift effect

can be written as¹⁵

$$\begin{aligned} & \frac{1}{(N+1)!} \hat{f}^{[N+1]}(\eta_0, \hat{\mathbf{n}}) \\ &= \int_0^{\eta_0} d\tilde{\eta} \left\{ \int_{\tilde{\eta}}^{\eta_0} d\eta_N \left[\partial_{\eta_N} \Phi^{\text{NL}}(\eta_N, -\hat{\mathbf{n}}r_N) - 2\dot{\Psi}_{\text{W}}^{\text{NL}}(\eta_N, -\hat{\mathbf{n}}r_N) \right] \left\{ \dots \right. \right. \\ & \quad \left. \int_{\tilde{\eta}}^{\eta_3} d\eta_2 \left[\partial_{\eta_2} \Phi^{\text{NL}}(\eta_2, -\hat{\mathbf{n}}r_2) - 2\dot{\Psi}_{\text{W}}^{\text{NL}}(\eta_2, -\hat{\mathbf{n}}r_2) \right] \left\{ \right. \right. \\ & \quad \left. \left. \int_{\tilde{\eta}}^{\eta_2} d\eta_1 \left[\partial_{\eta_1} \Phi^{\text{NL}}(\eta_1, -\hat{\mathbf{n}}r_1) - 2\dot{\Psi}_{\text{W}}^{\text{NL}}(\eta_1, -\hat{\mathbf{n}}r_1) \right] \left\{ 4S_T(\tilde{\eta}, -\hat{\mathbf{n}}\tilde{r}) \right\} \right\} \dots \right\}, \end{aligned} \quad (5.74)$$

where

$$\Phi^{\text{NL}}(\eta_N, -\hat{\mathbf{n}}r_N) \equiv \int \frac{d^3\mathbf{k}'_N}{(2\pi)^{3/2}} e^{-i\mathbf{k}'_N \cdot \hat{\mathbf{n}}r_N} \Phi^{\text{NL}}(\eta_N, \mathbf{k}'_N), \quad (5.75)$$

$$\dot{\Psi}_{\text{W}}^{\text{NL}}(\eta_N, -\hat{\mathbf{n}}r_N) \equiv \int \frac{d^3\mathbf{k}'_N}{(2\pi)^{3/2}} e^{-i\mathbf{k}'_N \cdot \hat{\mathbf{n}}r_N} \partial_{\eta_N} \Psi_{\text{W}}^{\text{NL}}(\eta_N, \mathbf{k}'_N). \quad (5.76)$$

Moreover, we define the interaction operator of the redshift effect as

$$\hat{V}_r(\eta, \hat{\mathbf{n}}) \equiv \partial_{\eta} \Phi^{\text{NL}}(\eta, -\hat{\mathbf{n}}r) - 2\dot{\Psi}_{\text{W}}^{\text{NL}}(\eta, -\hat{\mathbf{n}}r), \quad (5.77)$$

with the subscript r denoting the redshift effect. Here, we note that the interaction operator of the redshift effect is just a scalar quantity. For the diagrammatic approach in Section 5.1.4, it does not have the ‘‘action’’ term represented by an over-arc and can be indicated by solely a new node $\hat{\mathbf{N}}$.

We point out that the interaction potential $|\hat{V}_r|$ suppresses the redshift couplings due to an extra order of perturbations (see the discussion below Eq. (5.20)). This is expected because \hat{V}_r is exactly the source term for the SW and ISW effects when we perform the line of sight approach for 1st-order perturbations. The only difference is the range of the conformal time integration - we consider some subsets of the full range from 0 to η_0 here. Thus, the amplitude of CMB anisotropies will be suppressed by roughly an order of 10^{-5} when coupling with the redshift effect to one higher order. This explains why the redshift effect is subdominant compared to the lensing effect.

¹⁵We replace $\tilde{S}_T(\tilde{\eta}, \mathbf{k}_1, \hat{\mathbf{n}})$ with $S_T(\tilde{\eta}, \mathbf{k}_1)$ in order to keep the notation consistent with Eq. (5.53) and Eq. (5.67). However, unlike lensing and time-delay effects, it is not necessary for pure redshift effects.

5.2 Power Spectrum from Lens-lens Couplings

In Section 5.1.2, we develop a new formalism to study the lensing effect through the Boltzmann equation and explicitly enumerate all the approximations (Approximations 1 to 7) required to recover the canonical remapping approach reviewed in Section 2.6.1. The formalism is then extended to the redshift and time-delay effects in Section 5.1.5 in order to validate Approximation 2 and 3. In this section, we discuss the legitimacy of other approximations. In particular, we calculate quantitatively the correction of the lens-lens couplings on the temperature power spectrum and demonstrate how the diagrammatic approach in Section 5.1.4 can facilitate the calculations of the power spectra.

We start with Eq. (5.53) and impose Approximation 7 to single out the lens-lens couplings from other approximations. We can then express the $(N + 1)$ th-order lensed temperature anisotropies in configuration space as¹⁶

$$\begin{aligned} \tilde{\Theta}^{[N+1]}(\hat{\mathbf{n}}) = & \int_{\eta_{\text{LSS}}}^{\eta_0} d\eta_N \nabla_{\hat{\mathbf{n}}}^{i_N} [\Psi_{\text{W}}^{\text{NL}}(\eta_N, -\hat{\mathbf{n}}r_N)] (\hat{\square}_{\hat{\mathbf{n}},r_N})_{i_N} \left\{ \dots \right. \\ & \int_{\eta_{\text{LSS}}}^{\eta_3} d\eta_2 \nabla_{\hat{\mathbf{n}}}^{i_2} [\Psi_{\text{W}}^{\text{NL}}(\eta_2, -\hat{\mathbf{n}}r_2)] (\hat{\square}_{\hat{\mathbf{n}},r_2})_{i_2} \left\{ \right. \\ & \left. \int_{\eta_{\text{LSS}}}^{\eta_2} d\eta_1 \nabla_{\hat{\mathbf{n}}}^{i_1} [\Psi_{\text{W}}^{\text{NL}}(\eta_1, -\hat{\mathbf{n}}r_1)] (\hat{\square}_{\hat{\mathbf{n}},r_1})_{i_1} \Theta(\hat{\mathbf{n}}) \right\} \dots \left. \right\}, \end{aligned} \quad (5.78)$$

where the unlensed temperature anisotropies $\Theta(\hat{\mathbf{n}})$ are given by Eq. (5.50) and the vector operator $\hat{\square}_{\hat{\mathbf{n}},r}$ is redefined such that it is non-zero only when it acts on \mathcal{X}

$$(\hat{\square}_{\hat{\mathbf{n}},r})_i \mathcal{X}(\eta', -\hat{\mathbf{n}}r') \equiv 2 \frac{r - r'}{r r'} \frac{\partial}{\partial n^i} \mathcal{X}(\eta', -\hat{\mathbf{n}}r'), \quad (5.79)$$

with \mathcal{X} denoting $\Psi_{\text{W}}^{\text{NL}}$ or Θ ¹⁷. Physically, acting $\hat{\square}_{\hat{\mathbf{n}},r}$ on $\Psi_{\text{W}}^{\text{NL}}$ corresponds to lens-lens couplings while acting on Θ corresponds to lensing the sources. We will develop a set of diagrams to calculate the corresponding power spectrum in the following.

5.2.1 Diagrammatic Approach

To simplify the numerical calculation, we work in the limit of flat-sky, use the Limber approximation and consider only the linear part of the Weyl potential¹⁸ (i.e. $\Psi_{\text{W}}^{\text{NL}} \rightarrow \Psi_{\text{W}}^{[\text{I}]}$).

¹⁶Here, the lensed temperature anisotropies are expanded as $\tilde{\Theta}(\hat{\mathbf{n}}) = \sum_{N=1}^{\infty} \tilde{\Theta}^{[N]}(\hat{\mathbf{n}})$.

¹⁷With Approximation 7, r' is replaced by r_{LSS} when $\hat{\square}_{\hat{\mathbf{n}},r}$ acts on Θ .

¹⁸For simplicity, we omit the superscript [I] from now on.

However, we remark that these extra approximations are not necessary to the diagrammatic approach. Moreover, we do not expect these approximations to change the results significantly. Operationally, the approximations work as follows. Recall that for any function $f(\hat{\mathbf{n}})$, we can perform the Fourier transformation

$$f(\hat{\mathbf{n}}) = \int \frac{d\boldsymbol{\ell}}{2\pi} f(\boldsymbol{\ell}) e^{i\boldsymbol{\ell} \cdot \hat{\mathbf{n}}}. \quad (5.80)$$

With the assumption of statistical isotropy, it can be shown that

$$\langle \Theta(\boldsymbol{\ell}) \Theta^*(\boldsymbol{\ell}') \rangle = \delta(\boldsymbol{\ell} - \boldsymbol{\ell}') C_\ell^\Theta, \quad (5.81)$$

$$\langle \Psi_{\text{W}}(\boldsymbol{\eta}, \boldsymbol{\ell}) \Psi_{\text{W}}^*(\boldsymbol{\eta}', \boldsymbol{\ell}') \rangle = \delta(\boldsymbol{\ell} - \boldsymbol{\ell}') \delta(\boldsymbol{\eta} - \boldsymbol{\eta}') C_\ell^{\Psi_{\text{W}}}(\boldsymbol{\eta}), \quad (5.82)$$

where the angle brackets denote the ensemble averages. C_ℓ^Θ is the unlensed temperature power spectrum expressed in Eq. (2.86) while $C_\ell^{\Psi_{\text{W}}}(\boldsymbol{\eta})$ is the equal-time power spectrum of the Weyl potential.

With the flat-sky and Limber approximations, we can find

$$C_\ell^{\Psi_{\text{W}}}(\boldsymbol{\eta}) = \frac{1}{r^2} P_\Phi \left(\frac{\ell}{r} \right) \left[\mathcal{T}_{\Psi_{\text{W}}} \left(\boldsymbol{\eta}, \frac{\ell}{r} \right) \right]^2, \quad (5.83)$$

where $r \equiv \eta_0 - \eta$, $P_\Phi(k)$ is the primordial power spectrum defined in Eq. (2.73) and $\mathcal{T}_{\Psi_{\text{W}}}(\boldsymbol{\eta}, k)$ is the transfer function of the Weyl potential. Particularly, the Dirac delta function $\delta(\boldsymbol{\eta} - \boldsymbol{\eta}')$ in Eq. (5.82) comes from the Limber approximation using

$$\int dk k^2 j_\ell(kr) j_\ell(kr') = \frac{\pi}{2r^2} \delta(r - r'), \quad (5.84)$$

where $j_\ell(x)$ is the spherical Bessel function of the first kind. This is valid for high ℓ s when the term $P_\Phi(k) [\mathcal{T}_{\Psi_{\text{W}}}(\boldsymbol{\eta}, k)]^2$ varies slowly compared to the spherical Bessel functions [67]. As mentioned in [67], the Limber approximation is rather good for lensing potential with lens-source couplings. Thus, we expect the approximation does well for lens-lens couplings because at least one ℓ -mode of source is replaced by a ℓ -mode of lenses. It means that the main contribution of the ℓ -mode integration of lenses in the lensed power spectrum will shift to even higher ℓ . Additionally, we ignore the correlation between the temperature anisotropies and the Weyl potential, i.e.

$$\langle \Psi_{\text{W}}(\boldsymbol{\eta}, \boldsymbol{\ell}) \Theta^*(\boldsymbol{\ell}') \rangle \approx 0. \quad (5.85)$$

It is a very good approximation because only the ISW effect of the temperature anisotropies

correlates well with the Weyl potential at low- ℓ modes ($\ell \lesssim 100$) for which the cosmic variance is overwhelming due to the limited modes available.

Now, we introduce some extra rules to extend the diagrammatic approach for the calculation of power spectra. Diagrammatically, we represent the correlation function $\langle \dots \rangle$ by a dotted line connecting two nodes. For example, $\blacksquare \cdots \blacksquare$ denotes $\langle \Psi_{\mathbf{W}} \Psi_{\mathbf{W}}^* \rangle$. Due to the presence of the Dirac delta function $\delta(\eta - \eta')$ in Eq. (5.82), many possible configurations are forbidden because we cannot place the lens further than the lensed object from the observer. In Table 5.3, we summarize all the forbidden contractions in the diagrams, the corresponding terms in the formula and their physical meanings. Because of the forbidden contractions, the lens-lens couplings do not contribute to the 4th-order power spectrum. In order to assess effects from the lens-lens couplings, we study the 6th-order power spectrum. We itemize all the non-zero configurations for the 6th-order power spectrum as shown in Table 5.4. There exist cancellations between some pairs of the diagrams which are crossed out by the arrows. To understand this, we perform the Fourier transformation such that

$$(\nabla_{\hat{\mathbf{n}}})_i \approx \frac{\partial}{\partial n^i} \rightarrow i l_i. \quad (5.86)$$

In Fourier space, each pair of these cancelled diagrams looks exactly the same except that one contains $(\boldsymbol{\ell}_M \cdot \boldsymbol{\ell}_X) \delta(\boldsymbol{\ell}_M + \boldsymbol{\ell}_N)$ while another one contains $(\boldsymbol{\ell}_N \cdot \boldsymbol{\ell}_X) \delta(\boldsymbol{\ell}_M + \boldsymbol{\ell}_N)$. The difference comes from an overarc acting on either one of two correlated lenses. The pairs are eliminated because $\boldsymbol{\ell}_M = -\boldsymbol{\ell}_N$.

5.2.2 Numerical Implementation

Among the rest of the diagrams in Table 5.4, diagrams (1A), (1B), (2A), (2B) and (4A) do not involve the lens-lens couplings. They correspond to the expanded terms in the Taylor series of the remapping approach in Eq. (2.87) which can be calculated non-perturbatively [23]. In contrast, other residual terms, which are in Column C and D, contain the lens-lens couplings. To do the numerical calculation, we write down the temperature power spectrum

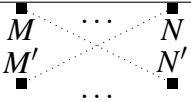
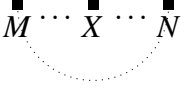
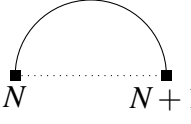
Forbidden Contractions	Term	Physical Meaning
	$\langle \Psi_W(\eta, \ell) \Theta^*(\ell') \rangle$	The CMB temperature anisotropies correlate weakly with the Weyl potential.
	$\theta(\eta_N - \eta_M) \theta(\eta_{N'} - \eta_{M'}) \delta(\eta_N - \eta_{M'}) \delta(\eta_{N'} - \eta_M)$	Lens at η_N must be placed after any lens at $\eta_M (< \eta_N)$.
	$\theta(\eta_N - \eta_X) \theta(\eta_X - \eta_M) \delta(\eta_N - \eta_M)$	Lens at η_X cannot be placed before and after the lenses at $\eta_M = \eta_N$ simultaneously.
	$(r_{N+1} - r_N) \delta(\eta_{N+1} - \eta_N)$	No lensing effect if the lens is placed at the same location as the lensed object.

Table 5.3 The forbidden contractions for the lensing effects on the power spectrum. θ is the Heaviside step function. The Heaviside step functions come from replacing the integration $\int_{\eta_{LSS}}^{\eta_{N+1}} d\eta_N$ with $\int_{\eta_{LSS}}^{\eta_0} d\eta_N \theta(\eta_{N+1} - \eta_N)$.

Correlations	Diagrams
$\langle \Theta^{[3]} \Theta^{[3]*} \rangle$	
$\langle \Theta^{[4]} \Theta^{[2]*} \rangle$	
$\langle \Theta^{[5]} \Theta^{[1]*} \rangle$	

Table 5.4 All the non-zero configurations for the temperature power spectrum from the next-to-leading order of the weak lensing effect. The dotted lines denote correlations while the arrows indicate the cancellations between some pairs of the diagrams.

represented by all the residual diagrams

$$\tilde{C}_\ell^{\Theta(6)} = \int \frac{d\ell_1 d\ell_2}{(2\pi)^4} \left\{ \mathcal{K}_0(\ell_1, \ell_2) \left\{ \frac{1}{2}(\ell_1 \cdot \ell)^2 (\ell_2 \cdot \ell)^2 C_\ell^\Theta \right. \right. \\ \left. \left. - [\ell_1 \cdot (\ell - \ell_1)]^2 [\ell_2 \cdot (\ell - \ell_1)]^2 C_{|\ell - \ell_1|}^\Theta \right. \right. \\ \left. \left. + \frac{1}{2}(\ell_1 \cdot \ell)^2 (\ell_2 \cdot \ell)^2 C_\ell^\Theta \right\} \right. \quad (5.87)$$

$$+ \mathcal{K}_0(\ell_1, \ell_2) \left\{ [\ell_1 \cdot (\ell - \ell_1 - \ell_2)]^2 [\ell_2 \cdot (\ell - \ell_1 - \ell_2)]^2 C_{|\ell - \ell_1 - \ell_2|}^\Theta \right. \\ \left. - [\ell_1 \cdot (\ell - \ell_1)]^2 [\ell_2 \cdot (\ell - \ell_1)]^2 C_{|\ell - \ell_1|}^\Theta \right\} \quad (5.88)$$

$$+ \mathcal{K}_1(\ell_1, \ell_2) \left\{ 2[\ell_1 \cdot (\ell - \ell_1 - \ell_2)]^2 [\ell_2 \cdot (\ell - \ell_1 - \ell_2)] (\ell_2 \cdot \ell_1) C_{|\ell - \ell_1 - \ell_2|}^\Theta \right. \\ \left. - [\ell_1 \cdot (\ell - \ell_1)]^2 [\ell_2 \cdot (\ell - \ell_1)] (\ell_2 \cdot \ell_1) C_{|\ell - \ell_1|}^\Theta \right. \\ \left. - [\ell_1 \cdot (\ell - \ell_1)]^2 [\ell_2 \cdot (\ell - \ell_1)] (\ell_2 \cdot \ell_1) C_{|\ell - \ell_1|}^\Theta \right\} \quad (5.89)$$

$$+ \mathcal{K}_2(\ell_1, \ell_2) \left\{ [\ell_1 \cdot (\ell - \ell_1 - \ell_2)]^2 (\ell_2 \cdot \ell_1)^2 C_{|\ell - \ell_1 - \ell_2|}^\Theta \right. \\ \left. - [\ell_1 \cdot (\ell - \ell_1)]^2 (\ell_2 \cdot \ell_1)^2 C_{|\ell - \ell_1|}^\Theta \right\} \left. \right\}, \quad (5.90)$$

where the functions $\mathcal{K}_i(\ell_1, \ell_2)$ are defined as

$$\int_{\eta_{\text{LSS}}}^{\eta_0} d\eta_1 4C_{\ell_1}^{\Psi^w}(\eta_1) \left(\frac{r_{\text{LSS}} - r_1}{r_{\text{LSS}} r_1} \right)^2 \int_{\eta_1}^{\eta_0} d\eta_2 4C_{\ell_2}^{\Psi^w}(\eta_2) \begin{cases} \left(\frac{r_{\text{LSS}} - r_2}{r_{\text{LSS}} r_2} \right)^2, & \text{if } i = 0, \\ \left(\frac{r_{\text{LSS}} - r_2}{r_{\text{LSS}} r_2} \right) \left(\frac{r_1 - r_2}{r_1 r_2} \right), & \text{if } i = 1, \\ \left(\frac{r_1 - r_2}{r_1 r_2} \right)^2, & \text{if } i = 2. \end{cases} \quad (5.91)$$

Eq. (5.87) to Eq. (5.90) correspond to Column A, B, C and D of the residual diagrams in Table 5.4 respectively.

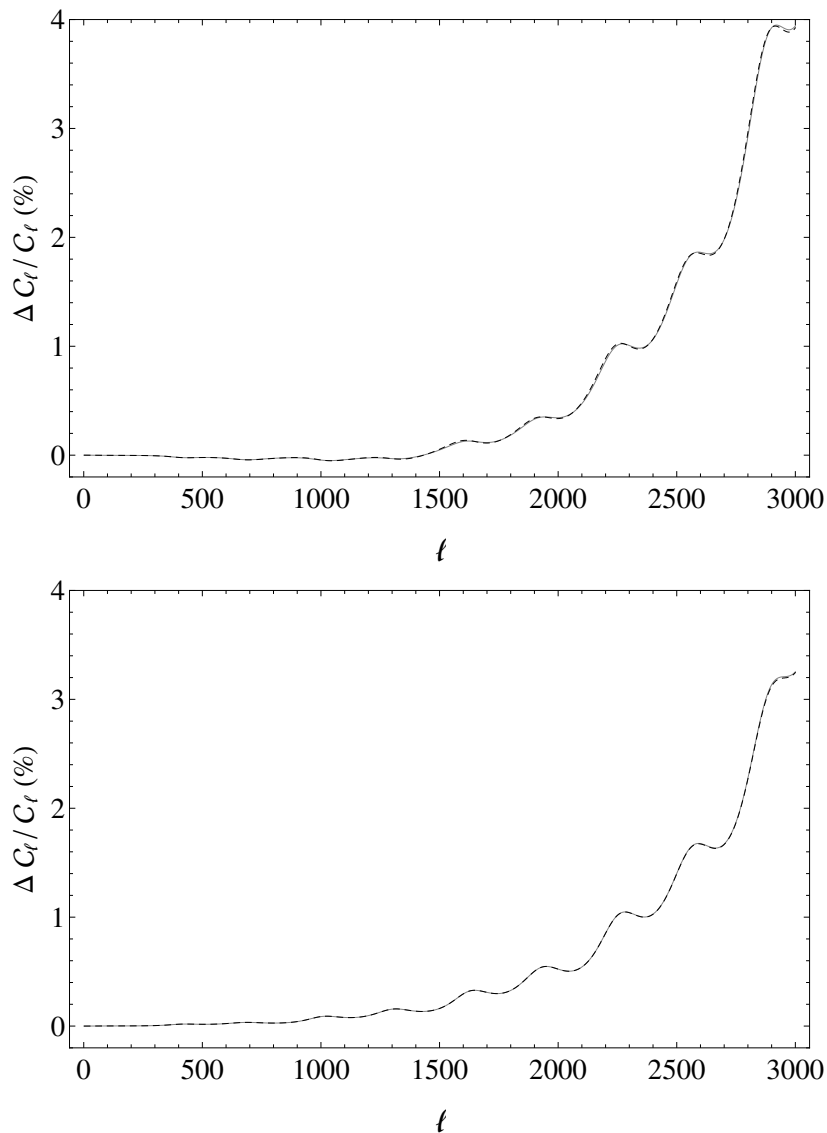


Figure 5.2 The contributions on the temperature power spectrum from the residual diagrams of Column C and D containing lens-lens couplings in Table 5.4. The top and bottom panels show the corrections to the power spectrum from those diagrams in Column C and D respectively. In the top panel, the solid gray line corresponds to the diagram (1C) while the dashed line corresponds to the diagrams (2C) and (3C). Diagrams (2C) and (3C) have identical contributions and thus we sum them up. In the bottom panel, the solid gray line corresponds to the diagram (1D) while the dashed line corresponds to the diagram (2D). For both panels, the signs of contributions from the diagrams in Row $\langle \Theta^{[4]} \Theta^{[2]*} \rangle$ of Table 5.4, i.e. the dashed lines, are reversed to illustrate the cancellations.

Since we want to study the effects of lens-lens couplings, we now focus on Column C and D of Table 5.4. In Fig. 5.2 and 5.3, we plot the contributions to the temperature

power spectrum from the residual diagrams in Column C and D. From Fig. 5.2, we see that the total contribution of each column is suppressed by cancellations and is at least an order of magnitude smaller than that from an individual diagram in the same column. The cancellations are due to the conservation of the power spectrum from the weak lensing effect. Physically, the positive terms in Eq. (5.87) to Eq. (5.90) are the power redistributed to the mode ℓ while the negative terms are the power redistributed away from the mode ℓ .

In summary, as shown in Fig. 5.3, the overall correction from the lens-lens couplings is of order 0.1% for ℓ up to 3000 and thus is comparable to the cosmic variance. It can be a systematic effect on CMB studies. We remark that the correction calculated here is for the power spectrum of the CMB temperature anisotropies. This is different from the correction of the cosmic shear power spectrum calculated in [61] which quantifies the correction of the deflection angle in the remapping approach. Moreover, the order of magnitude for the correction from the lens-lens coupling can be understood as follows: we can check that the lensing correction of the CMB temperature power spectrum from the lens-source coupling (captured by the canonical remapping approach) can exceed 20% and 2% of the unlensed power spectrum in the leading and next-to-leading orders respectively[23] for ℓ up to 3000. From Table 5.4, we can see that the difference to the corrections of CMB power spectrum from lens-source coupling and lens-lens coupling in the next-to-leading order comes mainly from replacing one of ℓ modes of the source with ℓ_i (i.e. ℓ modes of the lenses)¹⁹. With the peak of the lensing power spectrum at $\ell_i \sim 40$, it means that the correction of CMB power spectrum from lens-lens coupling can be a few of 0.01%.

¹⁹For example, compare (2B) and (2C) in Table 5.4.

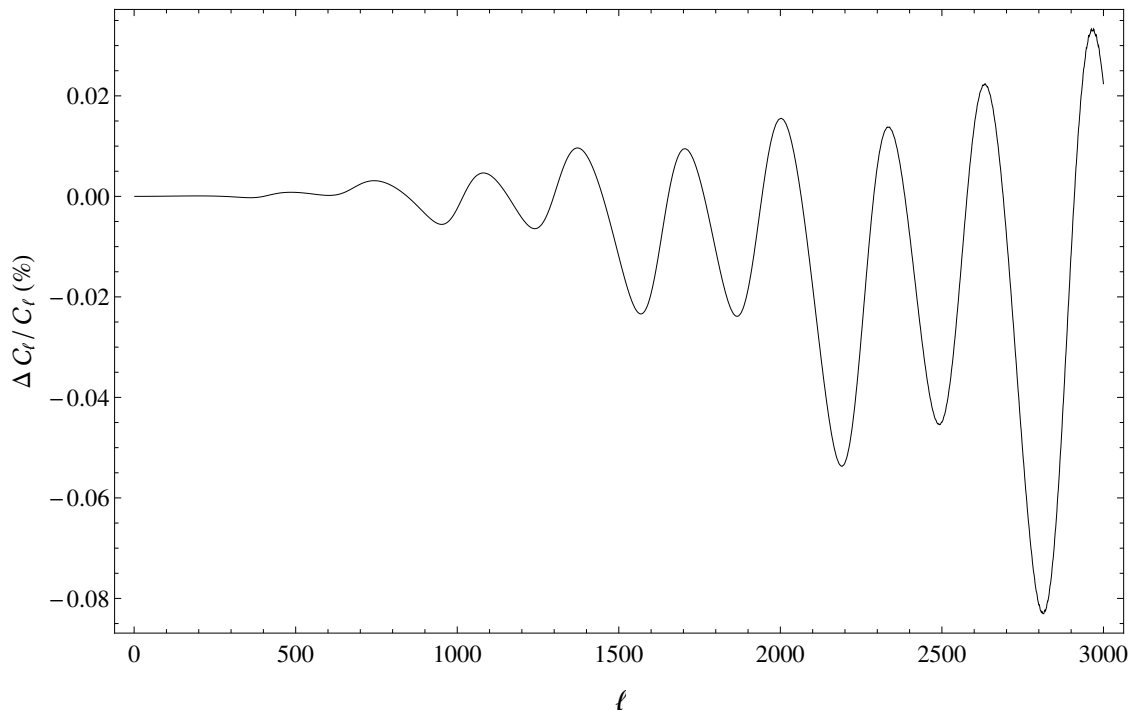


Figure 5.3 The overall correction to the temperature power spectrum from the lens-lens couplings.

5.2.3 Other Approximations

In Section 5.1.5, we qualitatively validate Approximation 2 and 3 of Section 5.1.2. In Section 5.2, we also calculate the correction from the lens-lens couplings corresponding to Approximation 6 of Section 5.1.2. In this section, we will discuss the other approximations implied when we recover the remapping approach.

Some of these approximations have been studied and their impacts on the CMB are believed to be small. The single-source approximation, which is Approximation 2 in Section 5.1.1 and Approximation 7 in Section 5.1.2, was evaluated in [107] using the flat-sky approach. Its corrections to the TT temperature power, the EE polarization power and the TE cross power spectra are of order 0.01% while the correction to the BB polarization power spectrum is about 0.4%, for ℓ up to 2000. The pure time-delay effect, included in Approximation 2 of Section 5.1.2, has been studied in [49] where the effect is estimated to be of order 0.1% correction to the TE cross power spectrum and $\lesssim 0.01\%$ corrections to the TT , EE and BB power spectra, for $\ell \sim 1000$. The 2nd-order Compton scattering at recombination, which is ignored in Approximation 1 of Section 5.1.2, is studied in [37, 52, 53, 81, 82, 100].

It have negligible effects on the CMB power spectra but systematic contaminations on the CMB bispectra. Thus, it is expected that higher-order couplings of the scattering with lensing or other effects are negligible. More details can be found in Chapter 3 and 4.

Approximation 1 in Section 5.1.1 has not been discussed previously and is first identified in [99]. However, we expect the contribution on the CMB power spectra to be negligible. It is because the correction to Approximation 1 in Section 5.1.1 is proportional to $\ell = 2$ multipoles (the term with Π in Eq. (5.20)) which is very tiny compared to other intrinsic CMB effects. Thus, the correction should be highly suppressed.

Among all the approximations, the Newtonian approximation as shown in Approximation 4 of Section 5.1.2 is the most difficult one to be assessed. On one hand, it relies heavily on the accuracy of the large-scale studies to obtain the nonlinear gravitational potentials. On the other hand, the Newtonian approximation performs well in small scales where the evolution is local and the GR effect is negligible. Thus, we can linearize Eq. (5.30) and ignore the cross terms. However, the scale of the time integration in the line of sight approach along the lensing effects is comparable to the Hubble radius. The CMB lensing is clearly not a local effect and its GR corrections can be important. Further assessment is needed in the future.

5.3 Discussion and Conclusions

In this chapter, we formulate the lensing, redshift and time-delay effects from the Liouville terms of the Boltzmann equation and express them as interaction operators in Dyson series. Focusing on the lensing effect, we demonstrate how the new formalism helps to explicitly enumerate and assess the required approximations for recovering the canonical remapping approach. Moreover, we develop a diagrammatic approach to keep track of the couplings of different effects for arbitrarily high orders. In particular, we found that the correction from the lens-lens couplings to the temperature power spectrum is $\lesssim 0.1\%$ for ℓ up to 3000 and thus is comparable to the cosmic variance. We emphasize that the formalism can be treated as a comprehensive solution of the collisionless Boltzmann equation in arbitrarily high orders. In principle, it can be used to study the lensing, redshift and time-delay effects of observations other than the CMB – such as galaxy surveys.

Chapter 6

Discussion and Conclusions

6.1 Discussion

Here, we discuss some potential extensions of our current work.

6.1.1 Spectral Distortions

As we mentioned in Section 4.1, 2nd-order Compton scattering induces spectral distortion from the blackbody spectrum such that there is no longer a unique definition of cosmic microwave background (CMB) temperature. Although the spectral distortion complicates the calculation of CMB bispectrum at recombination, it provides extra information about the evolution history of our universe. While tightest constraints on the spectral distortion come from the two-decade-old COBE/FIRAS [38], the future experiment - Pixie [59] can improve the measurement by 2-3 orders of magnitude. In particular, the 2nd-order Boltzmann equation developed in Section 3.2 can be used straightforwardly to study the y -distortion at recombination. This has been studied in [85] and the effect is subdominant compared to the y -distortion generated by the thermal Sunyaev-Zeldovich effect. The similar effect also occurs at reionization and is worth to be considered. However, since reionization happened at low redshift ($z \sim 10$) when the evolution is highly nonlinear, it is uncertain how well the 2nd-order equations perform during reionization. Furthermore, there are other types of spectral distortions which can be produced before recombination. It may be worth to formulate them through the 2nd-order Boltzmann equation with collisions other than Compton scattering. This might provide an alternative way to study these distortions along with the

typical energy-injection approach.

6.1.2 Modified Gravity

In Chapter 4, we find that the CMB bispectrum generated by 2nd-order perturbations at recombination is mild and will be treated as systematics in future CMB experiments. Since the calculation is based on General Relativity (GR), the result can be very different if modified gravity models are considered. In other words, the recombination bispectrum can be used to provide independent constraints for the alternative gravity models during recombination. There are some remarks for this application. To have an appealing gravity model, it has to be compatible with other observations, e.g. CMB power spectra. This can be done by refitting the cosmological parameters. However, if we assume single-field inflation, the recombination bispectrum in squeezed limit will be fixed and determined by power spectrum (see Eq. (4.52)), which is tightly constrained by CMB observations. Nevertheless, alternative gravity models can contribute to the non-squeezed configurations of recombination bispectrum. This should not be a concern if multi-field inflations are considered.

6.1.3 Perturbed Optical Depth

As we mentioned in Section 3.2.4, the 1st-order optical depth calculated is based on perturbing the fitting function of the background-order optical depth. Even though the approximation works well for large scales, it is not necessarily true for small scales. At small scales, the details of the underlying dynamics, which are not captured by the three-level approximation, can be important. Thus, it is of interest to study the perturbed optical depth in more comprehensive ways. One possibility is to consider atoms with multi-levels [7] and to perturb their corresponding evolution equations. This can be achieved by numerical calculations.

6.1.4 Lensing in CMB Polarizations and Other Observables

In Chapter 5, we formulate the lensing, redshift and time-delay effects on the CMB temperature anisotropies through the Boltzmann equation. The derivation can be easily extended to study the same effects on the CMB polarizations. Since the unlensed power spectra of polarizations have very different shapes compared to the unlensed power spectrum of temperature anisotropies. The corrections from the implied approximations in the remapping

approach can behave differently. Especially, the corrections are expected to be relatively stronger for B-mode polarization because there is no ‘intrinsic’ power spectrum of B-mode generated at recombination. The dominant B-mode polarization¹ comes from the lensed E-mode which is 2nd-order effects at least. On the other hand, it is of interest to check if there exist any new approximations which have not been discovered and validate the remapping approach. Similarly, it may be worth to extend the derivation to study lensing, redshift and time-delay effects on other observations, e.g. galaxy surveys. This can be done by replacing the CMB source terms with the background galaxy power spectrum and hence generalizing the approach of [61].

6.1.5 Validation of Newtonian Approximation

In Approximation 4 of Section 5.1.2, we drop the cross terms and linearize GR as if in Newtonian gravity. However, the scale of the time integration in the line of sight approach along the lensing effects is comparable to the Hubble radius. The CMB lensing is clearly not a local effect and its GR corrections can be important. Further assessment is needed in the future. To tackle the problem, highly nonlinear evolution may have to be considered but this is practically too difficult. A less rigorous checking can be achieved by considering the term in Eq. (5.30) up to 2nd order and studying its effect on the linear-order temperature anisotropies. This will give us some insights on how the cross terms affect the lensing effect in the leading third order.

6.2 Conclusions

In this thesis, we study cosmological perturbations by solving the governing Boltzmann and EFEs up to 2nd order, and calculate the corresponding CMB bispectrum during recombination. We include all the 2nd-order Liouville and collision terms, truncating the multipole hierarchy at $\ell = 10$, consistently including $m \neq 0$ terms when calculating the bispectrum with the flat-sky and thin-shell approximation. At this stage, we focus on contributions at and around recombination and thus neglect 2nd-order vector and tensor perturbations, lensing effects, and late-time non-linear ISW effects. We find that the signal-to-noise for the bispectrum is 0.69 for $\ell_{\max} = 2000$, yielding an overall signal $F_{\text{NL}} = 3.19$ (normalized relative to the local model). The effective f_{NLS} of the equilateral and local type are 5.11

¹Here, we ignore the vector and tensor perturbations in linear order.

and 0.88 respectively. The recombination bispectrum should be included in the analysis of future CMB experiments as systematics.

Moreover, we present a new formalism to calculate the lensing effect by directly solving the Boltzmann equation. This allows us to explicitly keep track of *all known physical effects* through the entire time of flight of a CMB photon from recombination to the present observer. Using this formalism and focusing on temperature anisotropies, we explicitly articulate the approximations required to recover the usual remapping approach used in current studies of the CMB lensing. We discover two new approximations which have not been studied previously although we do not expect that they contribute significantly under the current limits from observations. In addition, we calculate the correction to the CMB temperature power spectrum for the *lens-lens* coupling effects and find that the correction is $\lesssim 0.1\%$ for ℓ up to 3000. It is comparable to the cosmic variance and should be taken into account as systematics.

References

- [1] Refer to http://www.esa.int/spaceinimages/Images/2013/03/Planck_CMB.
- [2] Ade, P. et al. (2014a). Detection of B-Mode Polarization at Degree Angular Scales by BICEP2. *Phys.Rev.Lett.*, 112:241101.
- [3] Ade, P. et al. (2014b). Planck 2013 results. XVI. Cosmological parameters. *Astron.Astrophys.*, 571:A16.
- [4] Ade, P. et al. (2014c). Planck 2013 results. XVII. Gravitational lensing by large-scale structure. *Astron.Astrophys.*, 571:A17.
- [5] Ade, P. et al. (2014d). Planck 2013 results. XVIII. Gravitational lensing-infrared background correlation. *Astron.Astrophys.*, 571:A18.
- [6] Ade, P. et al. (2014e). Planck 2013 Results. XXIV. Constraints on primordial non-Gaussianity. *Astron.Astrophys.*, 571:A24.
- [7] Ali-Haïmoud, Y. and Hirata, C. M. (2011). HyRec: A fast and highly accurate primordial hydrogen and helium recombination code. *Phys.Rev.*, D83:043513.
- [8] Andre, P. et al. (2013). PRISM (Polarized Radiation Imaging and Spectroscopy Mission): A White Paper on the Ultimate Polarimetric Spectro-Imaging of the Microwave and Far-Infrared Sky. arXiv:1306.2259.
- [9] Audren, B., Figueroa, D. G., and Tram, T. (2014). A note of clarification: BICEP2 and Planck are not in tension. arXiv:1405.1390.
- [10] Bartolo, N., Komatsu, E., Matarrese, S., and Riotto, A. (2004). Non-Gaussianity from inflation: Theory and observations. *Phys.Rept.*, 402:103–266.
- [11] Bartolo, N., Matarrese, S., and Riotto, A. (2006). The full second-order radiation transfer function for large-scale cmb anisotropies. *JCAP*, 0605:010.
- [12] Bartolo, N., Matarrese, S., and Riotto, A. (2012). Non-Gaussianity in the Cosmic Microwave Background Anisotropies at Recombination in the Squeezed limit. *JCAP*, 1202:017.
- [13] Bartolo, N. and Riotto, A. (2009). On the non-Gaussianity from Recombination. *JCAP*, 0903:017.

- [14] Baumann, D., Nicolis, A., Senatore, L., and Zaldarriaga, M. (2012). Cosmological Non-Linearities as an Effective Fluid. *JCAP*, 1207:051.
- [15] Beneke, M. and Fidler, C. (2010). Boltzmann hierarchy for the cosmic microwave background at second order including photon polarization. *Phys.Rev.*, D82:063509.
- [16] Bennett, C. et al. (2013). Nine-Year Wilkinson Microwave Anisotropy Probe (WMAP) Observations: Final Maps and Results. *Astrophys.J.Suppl.*, 208:20.
- [17] Bernardeau, F., Pitrou, C., and Uzan, J.-P. (2011). CMB spectra and bispectra calculations: making the flat-sky approximation rigorous. *JCAP*, 1102:015.
- [18] Blanchard, A. and Schneider, J. (1987). Gravitational lensing effect on the fluctuations of the cosmic background radiation. *Astron.Astrophys.*, 184:1–6.
- [19] Bleem, L., van Engelen, A., Holder, G., Aird, K., Armstrong, R., et al. (2012). A Measurement of the Correlation of Galaxy Surveys with CMB Lensing Convergence Maps from the South Pole Telescope. *Astrophys.J.*, 753:L9.
- [20] Boubekeur, L., Creminelli, P., D’Amico, G., Norena, J., and Vernizzi, F. (2009). Sachs-Wolfe at second order: the CMB bispectrum on large angular scales. *JCAP*, 0908:029.
- [21] Bruni, M., Matarrese, S., Mollerach, S., and Sonego, S. (1997). Perturbations of space-time: Gauge transformations and gauge invariance at second order and beyond. *Class.Quant.Grav.*, 14:2585–2606.
- [22] Challinor, A. and Chon, G. (2002). Geometry of weak lensing of CMB polarization. *Phys.Rev.*, D66:127301.
- [23] Challinor, A. and Lewis, A. (2005). Lensed CMB power spectra from all-sky correlation functions. *Phys.Rev.*, D71:103010.
- [24] Chen, X. (2010). Primordial Non-Gaussianities from Inflation Models. *Adv.Astron.*, 2010:638979.
- [25] Cheung, C., Creminelli, P., Fitzpatrick, A. L., Kaplan, J., and Senatore, L. (2008). The Effective Field Theory of Inflation. *JHEP*, 0803:014.
- [26] Cooray, A. and Hu, W. (2002). Second order corrections to weak lensing by large scale structure. *Astrophys.J.*, 574:19.
- [27] Cooray, A. and Kesden, M. (2003). Weak lensing of the CMB: Extraction of lensing information from the trispectrum. *New Astron.*, 8:231–253.
- [28] Cooray, A. R. and Hu, W. (2000). Imprint of reionization on the cosmic microwave background bispectrum. *Astrophys.J.*, 534:533–550.
- [29] Creminelli, P., Pitrou, C., and Vernizzi, F. (2011). The CMB bispectrum in the squeezed limit. *JCAP*, 1111:025.
- [30] Creminelli, P. and Zaldarriaga, M. (2004). Single field consistency relation for the 3-point function. *JCAP*, 0410:006.

- [31] Das, S., Sherwin, B. D., Aguirre, P., Appel, J. W., Bond, J. R., et al. (2011). Detection of the Power Spectrum of Cosmic Microwave Background Lensing by the Atacama Cosmology Telescope. *Phys.Rev.Lett.*, 107:021301.
- [32] Dodelson, S. (2003). *Modern Cosmology*. Academic Press.
- [33] Dodelson, S., Kolb, E. W., Matarrese, S., Riotto, A., and Zhang, P. (2005). Second order geodesic corrections to cosmic shear. *Phys.Rev.*, D72:103004.
- [34] Dvali, G., Gruzinov, A., and Zaldarriaga, M. (2004). A new mechanism for generating density perturbations from inflation. *Phys.Rev.*, D69:023505.
- [35] Fergusson, J., Liguori, M., and Shellard, E. (2012). The CMB Bispectrum. *JCAP*, 1212:032.
- [36] Fergusson, J. and Shellard, E. (2009). The shape of primordial non-Gaussianity and the CMB bispectrum. *Phys.Rev.*, D80:043510.
- [37] Fidler, C., Pettinari, G. W., Beneke, M., Crittenden, R., Koyama, K., et al. (2014). The intrinsic B-mode polarisation of the Cosmic Microwave Background. *JCAP*, 07:011.
- [38] Fixsen, D. J. and Mather, J. C. (2002). The Spectral Results of the Far-Infrared Absolute Spectrophotometer Instrument on COBE. *Astrophys.J.*, 581:817–822.
- [39] Goldberg, D. M. and Spergel, D. N. (1999). Microwave background bispectrum. 2. A probe of the low redshift universe. *Phys.Rev.*, D59:103002.
- [40] Hanson, D. et al. (2013). Detection of B-mode Polarization in the Cosmic Microwave Background with Data from the South Pole Telescope. *Phys.Rev.Lett.*, 111(14):141301.
- [41] Hirata, C. M., Ho, S., Padmanabhan, N., Seljak, U., and Bahcall, N. A. (2008). Correlation of CMB with large-scale structure: II. Weak lensing. *Phys.Rev.*, D78:043520.
- [42] Hirata, C. M., Padmanabhan, N., Seljak, U., Schlegel, D., and Brinkmann, J. (2004). Cross-correlation of CMB with large-scale structure: Weak gravitational lensing. *Phys.Rev.*, D70:103501.
- [43] Hirata, C. M. and Seljak, U. (2003a). Analyzing weak lensing of the cosmic microwave background using the likelihood function. *Phys.Rev.*, D67:043001.
- [44] Hirata, C. M. and Seljak, U. (2003b). Reconstruction of lensing from the cosmic microwave background polarization. *Phys.Rev.*, D68:083002.
- [45] Holder, G., Viero, M., Zahn, O., Aird, K., Benson, B., et al. (2013). A Cosmic Microwave Background Lensing Mass Map and Its Correlation with the Cosmic Infrared Background. *Astrophys.J.*, 771:L16.
- [46] Hu, W. (2000). Weak lensing of the CMB: A harmonic approach. *Phys.Rev.*, D62:043007.
- [47] Hu, W. (2001). Angular trispectrum of the CMB. *Phys.Rev.*, D64:083005.

- [48] Hu, W. (2002). Dark synergy: Gravitational lensing and the CMB. *Phys.Rev.*, D65:023003.
- [49] Hu, W. and Cooray, A. (2001). Gravitational time delay effects on cosmic microwave background anisotropies. *Phys.Rev.*, D63:023504.
- [50] Hu, W., Seljak, U., White, M. J., and Zaldarriaga, M. (1998). A complete treatment of CMB anisotropies in a FRW universe. *Phys.Rev.*, D57:3290–3301.
- [51] Hu, W. and White, M. J. (1997). CMB anisotropies: Total angular momentum method. *Phys.Rev.*, D56:596–615.
- [52] Huang, Z. and Vernizzi, F. (2013). Cosmic Microwave Background Bispectrum from Recombination. *Phys.Rev.Lett.*, 110(10):101303.
- [53] Huang, Z. and Vernizzi, F. (2014). The full CMB temperature bispectrum from single-field inflation. *Phys.Rev.*, D89:021302.
- [54] Kamionkowski, M., Kosowsky, A., and Stebbins, A. (1997). Statistics of cosmic microwave background polarization. *Phys.Rev.*, D55:7368–7388.
- [55] Kaplinghat, M., Knox, L., and Song, Y.-S. (2003). Determining neutrino mass from the CMB alone. *Phys.Rev.Lett.*, 91:241301.
- [56] Kesden, M. H., Cooray, A., and Kamionkowski, M. (2003). Lensing reconstruction with CMB temperature and polarization. *Phys.Rev.*, D67:123507.
- [57] Khatri, R. and Wandelt, B. D. (2009). Crinkles in the last scattering surface: Non-Gaussianity from inhomogeneous recombination. *Phys.Rev.*, D79:023501.
- [58] Khatri, R. and Wandelt, B. D. (2010). More on crinkles in the last scattering surface. *Phys.Rev.*, D81:103518.
- [59] Kogut, A., Fixsen, D., Chuss, D., Dotson, J., Dwek, E., et al. (2011). The Primordial Inflation Explorer (PIXIE): A Nulling Polarimeter for Cosmic Microwave Background Observations. *JCAP*, 1107:025.
- [60] Komatsu, E., Spergel, D. N., and Wandelt, B. D. (2005). Measuring primordial non-Gaussianity in the cosmic microwave background. *Astrophys.J.*, 634:14–19.
- [61] Krause, E. and Hirata, C. M. (2010). Weak lensing power spectra for precision cosmology: Multiple-deflection, reduced shear and lensing bias corrections. *Astron.Astrophys.*, 523:28.
- [62] Lee, H., Su, S., and Baumann, D. (2015). The Superhorizon Test of Future B-mode Experiments. *JCAP*, 1502(02):036.
- [63] Lesgourgues, J. (2011). The Cosmic Linear Anisotropy Solving System (CLASS) I: Overview. arXiv:1104.2932.
- [64] Lesgourgues, J., Perotto, L., Pastor, S., and Piat, M. (2006). Probing neutrino masses with cmb lensing extraction. *Phys.Rev.*, D73:045021.

- [65] Lewis, A. (2007). Linear effects of perturbed recombination. *Phys.Rev.*, D76:063001.
- [66] Lewis, A. (2012). The full squeezed CMB bispectrum from inflation. *JCAP*, 1206:023.
- [67] Lewis, A. and Challinor, A. (2006). Weak gravitational lensing of the cmb. *Phys.Rept.*, 429:1–65.
- [68] Lewis, A. and Challinor, A. (2007). The 21cm angular-power spectrum from the dark ages. *Phys.Rev.*, D76:083005.
- [69] Lewis, A., Challinor, A., and Hanson, D. (2011). The shape of the CMB lensing bispectrum. *JCAP*, 1103:018.
- [70] Lewis, A., Challinor, A., and Lasenby, A. (2000). Efficient computation of CMB anisotropies in closed FRW models. *Astrophys.J.*, 538:473–476.
- [71] Ma, C.-P. and Bertschinger, E. (1995). Cosmological perturbation theory in the synchronous and conformal Newtonian gauges. *Astrophys.J.*, 455:7–25.
- [72] Maldacena, J. M. (2003). Non-Gaussian features of primordial fluctuations in single field inflationary models. *JHEP*, 0305:013.
- [73] Malik, K. A. and Wands, D. (2004). Evolution of second-order cosmological perturbations. *Class.Quant.Grav.*, 21:L65–L72.
- [74] Mangilli, A. and Verde, L. (2009). Non-Gaussianity and the CMB Bispectrum: confusion between Primordial and Lensing-Rees Sciama contribution? *Phys.Rev.*, D80:123007.
- [75] Nitta, D., Komatsu, E., Bartolo, N., Matarrese, S., and Riotto, A. (2009). CMB anisotropies at second order III: bispectrum from products of the first-order perturbations. *JCAP*, 0905:014.
- [76] Novosyadlyj, B. (2006). Perturbations of ionization fractions at the cosmological recombination epoch. *Mon.Not.Roy.Astron.Soc.*, 370:1771–1782.
- [77] Okamoto, T. and Hu, W. (2003). CMB lensing reconstruction on the full sky. *Phys.Rev.*, D67:083002.
- [78] Peebles, P. (1968). Recombination of the Primeval Plasma. *Astrophys.J.*, 153:1.
- [79] Penzias, A. A. and Wilson, R. W. (1965). A Measurement of excess antenna temperature at 4080-Mc/s. *Astrophys.J.*, 142:419–421.
- [80] Pettinari, G. W. (2014). The intrinsic bispectrum of the Cosmic Microwave Background (Ph.D. thesis). arXiv:1405.2280.
- [81] Pettinari, G. W., Fidler, C., Crittenden, R., Koyama, K., Lewis, A., et al. (2014). Impact of polarization on the intrinsic cosmic microwave background bispectrum. *Phys.Rev.*, D90(10):103010.
- [82] Pettinari, G. W., Fidler, C., Crittenden, R., Koyama, K., and Wands, D. (2013). The intrinsic bispectrum of the Cosmic Microwave Background. *JCAP*, 1304:003.

- [83] Pitrou, C. (2009). The Radiative transfer at second order: A Full treatment of the Boltzmann equation with polarization. *Class.Quant.Grav.*, 26:065006.
- [84] Pitrou, C. (2011). The tight-coupling approximation for baryon acoustic oscillations. *Phys.Lett.*, B698:1–5.
- [85] Pitrou, C., Bernardeau, F., and Uzan, J.-P. (2010a). The y-sky: diffuse spectral distortions of the cosmic microwave background. *JCAP*, 1007:019.
- [86] Pitrou, C., Uzan, J.-P., and Bernardeau, F. (2008). Cosmic microwave background bispectrum on small angular scales. *Phys.Rev.*, D78:063526.
- [87] Pitrou, C., Uzan, J.-P., and Bernardeau, F. (2010b). The cosmic microwave background bispectrum from the non-linear evolution of the cosmological perturbations. *JCAP*, 1007:003.
- [88] Seager, S., Sasselov, D. D., and Scott, D. (2000). How exactly did the universe become neutral? *Astrophys.J.Suppl.*, 128:407–430.
- [89] Seljak, U. (1996). Gravitational lensing effect on cosmic microwave background anisotropies: A Power spectrum approach. *Astrophys.J.*, 463:1.
- [90] Seljak, U. (2009). Rees-Sciama Effect in a Cold Dark Matter Universe. *Astrophys.J.*, 460:549.
- [91] Seljak, U. and Zaldarriaga, M. (1996). A Line of sight integration approach to cosmic microwave background anisotropies. *Astrophys.J.*, 469:437–444.
- [92] Seljak, U. and Zaldarriaga, M. (1999). Direct signature of evolving gravitational potential from cosmic microwave background. *Phys.Rev.*, D60:043504.
- [93] Senatore, L., Tassev, S., and Zaldarriaga, M. (2009a). Cosmological Perturbations at Second Order and Recombination Perturbed. *JCAP*, 0908:031.
- [94] Senatore, L., Tassev, S., and Zaldarriaga, M. (2009b). Non-Gaussianities from Perturbing Recombination. *JCAP*, 0909:038.
- [95] Shapiro, C. and Cooray, A. (2006). The born and lens-lens corrections to weak gravitational lensing angular power spectra. *JCAP*, 0603:007.
- [96] Sherwin, B. D., Das, S., Hajian, A., Addison, G., Bond, J. R., et al. (2012). The Atacama Cosmology Telescope: Cross-Correlation of CMB Lensing and Quasars. *Phys.Rev.*, D86:083006.
- [97] Silverstein, E. and Tong, D. (2004). Scalar speed limits and cosmology: Acceleration from D-cceleration. *Phys.Rev.*, D70:103505.
- [98] Smith, K. M., Zahn, O., and Dore, O. (2007). Detection of Gravitational Lensing in the Cosmic Microwave Background. *Phys.Rev.*, D76:043510.
- [99] Su, S. C. and Lim, E. A. (2014). Formulating Weak Lensing from the Boltzmann Equation and Application to Lens-lens Couplings. *Phys.Rev.*, D89:123006.

- [100] Su, S.-C., Lim, E. A., and Shellard, E. P. S. (2014). Cosmic microwave background bispectrum from nonlinear effects during recombination. *Phys. Rev. D*, 90:023004.
- [101] Tsagas, C. G., Challinor, A., and Maartens, R. (2008). Relativistic cosmology and large-scale structure. *Phys.Rept.*, 465:61–147.
- [102] van Engelen, A., Keisler, R., Zahn, O., Aird, K., Benson, B., et al. (2012). A measurement of gravitational lensing of the microwave background using South Pole Telescope data. *Astrophys.J.*, 756:142.
- [103] Vernizzi, F. (2005). On the conservation of second-order cosmological perturbations in a scalar field dominated Universe. *Phys.Rev.*, D71:061301.
- [104] Vilenkin, A. and Shellard, E. P. S. (1995). *Cosmic Strings and Other Topological Defects*. Cambridge University Press.
- [105] Weinberg, S. (2008). *Cosmology*. OUP Oxford.
- [106] Wu, X.-P. (2004). Weak lensing of the Sunyaev-Zel'dovich sky. *Mon.Not.Roy.Astron.Soc.*, 349:816.
- [107] Yu, B. and Lu, T. (2009). Weak Gravitational Lensing of CMB - Revisit. *Astrophys.J.*, 698:1771–1777.
- [108] Zaldarriaga, M. and Seljak, U. (1997). An all sky analysis of polarization in the microwave background. *Phys.Rev.*, D55:1830–1840.
- [109] Zaldarriaga, M. and Seljak, U. (1998). Gravitational lensing effect on cosmic microwave background polarization. *Phys.Rev.*, D58:023003.

Appendix A

Glossary of Notations and Symbols

Table A.1 Physical parameters and background quantities

Symbol	Description	Equation
c	Speed of light	
G	Gravitational constant	
h_P	Planck constant	
k_B	Boltzmann constant	
m_e	Electron mass	
κ		$\kappa \equiv 8\pi G/c^4$
Λ	Cosmological constant	Eq. (2.22)
A_s	Amplitude of initial power spectrum	Eq. (2.73)
k_*	Pivot wavenumber	Eq. (2.73)
n_s	Spectral index	Eq. (2.73)
σ_T	Thomson cross section	
ω	Equation of state of fluid	Eq. (2.41)
c_s	Speed of sound of fluid	Eq. (3.18)
a or $a(\eta)$	Scale factor	Eq. (2.1)
\mathcal{H}	Conformal Hubble function	Below Eq. (2.45)
\bar{T}	Background CMB temperature	
g		$\dot{\tau} e^{-\bar{\tau}}$
R	Density ratio	$(4/3)\bar{\rho}_r/\bar{\rho}_b$
f_n	Neutrino fraction of total radiations	$\bar{\rho}_n/(\bar{\rho}_n + \bar{\rho}_r)$

Table A.2 Mathematical notations and functions

Symbol	Description	Equation
∇	Covariant derivative	
$\nabla_{\hat{\mathbf{n}}}$	Screen-projected directional derivative	Eq. (5.24)
$\theta(x)$	Heaviside step function	
$\delta_{ij}, \delta^{ij}, \delta^i_j$	The Kronecker delta	
$\delta^3(\mathbf{k})$	The Dirac delta function	
$J_M(x)$	Bessel function of the first kind	
$j_\ell(x)$	Spherical Bessel function of the first kind	
$P_\ell(x)$	Legendre polynomial	
${}_s Y_{\ell m}(\hat{\mathbf{n}})$	Spin-weighted spherical harmonics	
$D_{m'm}^\ell$	rotation matrices	Eq. (4.28)
$\mathcal{G}_{\ell_1 \ell_2 \ell_3}^{m_1 m_2 m_3}$	The Gaunt integral	Eq. (C.14)
$h_{\ell_1 \ell_2 \ell_3}$		Eq. (4.57)
$\begin{pmatrix} \ell_1 & \ell_2 & \ell_3 \\ m_1 & m_2 & m_3 \end{pmatrix}$	The Wigner 3-j symbols	Eq. (C.13)

Table A.3 Notations for power spectra and bispectra

Symbol	Description	Equation
$\langle \dots \rangle$	Ensemble average	
$a_{\ell m}$	Components of spherical harmonics on temperature anisotropies	Eq. (2.83)
$P_\Phi(k)$	Primordial power spectrum of Newtonian potential	Above Eq. (2.86)
C_ℓ	CMB power spectrum	Eq. (2.85)
$B_{\ell_1 \ell_2 \ell_3}^{m_1 m_2 m_3}$	3-point correlator of $a_{\ell m}$ s	Eq. (2.90)
$B_{\ell_1 \ell_2 \ell_3}$	CMB angular-averaged bispectrum	Eq. (2.91)
$b_{\ell_1 \ell_2 \ell_3}$	Reduced bispectrum	Eq. (2.92)
$B(k_1, k_2, k_3),$ $B(\mathbf{k}_1, \mathbf{k}_2)$	Shape of bispectrum	Eq. (2.95), above Eq. (4.32)
$f_{\text{NL}}^{\text{loc}}, f_{\text{NL}}^{\text{equ}}, f_{\text{NL}}^{\text{orth}}$	Nonlinear coupling constants for local, equilateral and orthogonal type	Eq. (2.103), (2.105), (2.107), (4.53)
F_{NL}	Normalized nonlinear coupling constants	Eq. (4.54)
(S/N)	Signal-to-noise of bispectra	Eq. (4.55)
$\mathcal{F}_{\text{A,B}}$		Eq. (4.56)

Table A.4 Coordinate-related notations and quantities

Symbol	Description	Equation
Sub/Superscripts Greek letters	Abstract indices for tensors	
Sub/Superscripts A, B, C, \dots	Coordinates in background Manifold	
Sub/Superscripts I, J, K, \dots	Spacelike coordinates in background Manifold	
Sub/Superscripts a, b, c, \dots	Indices for tetrad basis	
Sub/Superscripts i, j, k, \dots	Spacelike indices for tetrad basis	
Superscripts [I], [II], ... , [N]	Orders of perturbations	
η	Conformal time	Eq. (2.1)
η_i	Initial conformal time	See Section 2.5.3, 3.3.1
t	Physical time	$\int a(\eta) d\eta$
r	Conformal distance from present	$\eta_0 - \eta$
r_{LSS}	Conformal distance to last scattering surface	
p^0	Photon energy in tetrad basis	Eq. (2.5)
$\hat{\mathbf{n}}$	Direction of photon path	Eq. (2.5)
$\hat{\mathbf{e}}_0$	Observer's velocity	Eq. (2.5)
$\hat{\mathbf{e}}_a, \hat{\mathbf{e}}^a$	Tetrad fields	Eq. (2.4)
$\bar{\mathbf{e}}_{(m)}$	For $m = -1, 0, 1$	Eq. (C.25)
$[\hat{\mathbf{n}}\hat{\mathbf{n}}]_{\ell m}$	Decomposition into spherical harmonics	Eq. (C.34)
$k_{(\pm 1)}$	Multipole decomposition of wavenumber	$k^I \bar{e}_{(\pm 1)}^{*I}$
$[\mathbf{k}'\mathbf{k}'']_{2m}$	Multipole decomposition of two wavenumbers	$[n^i n^j]_{2m} k'_I k''_J$
$\eta_{\mu\nu}$	Minkowski metric	diag(-1, 1, 1, 1)
$g_{\mu\nu}$	Metric	Eq. (2.1)
$S_{\mu\nu}$	Screen projector	Eq. (2.6)

Table A.5 Perturbations

Symbol	Description	Equation
\mathcal{R}	Comoving curvature perturbations	Eq. (2.66), (3.111)
Φ	Newtonian gravitational potential	Eq. (2.1)
Ψ	Another scalar metric perturbation in Newtonian gauge	Eq. (2.1)
\mathcal{B}_I	Vector metric perturbation in Newtonian gauge	Eq. (2.1), (2.2)
$\tilde{\mathcal{B}}_{(\pm 1)}$	Multipole decomposition of \mathcal{B}_I	$i\tilde{\mathcal{B}}_{(\pm 1)} = \mathcal{B}^I \bar{e}_{(m)}^{*I}$
\mathcal{H}_{IJ}	Tensor metric perturbation in Newtonian gauge	Eq. (2.1), (2.2)
$\mathcal{H}_{(\pm 2)}$	Multipole decomposition of \mathcal{H}_{IJ}	$[n^I n^J]_{2\pm 2} \mathcal{H}_{IJ}$
δ	Density perturbation	$\delta\rho/\bar{\rho}$
$\hat{I}_{\ell m}$	Intensity multipoles for photons and neutrinos	
$\hat{E}_{\ell m}, \hat{B}_{\ell m}$	Polarization multipoles	
v, v_I	Scalar and vector perturbation of fluid velocity	Eq. (2.28)
$\tilde{v}_{(m)}$	Multipole decomposition of fluid velocity	$i\tilde{v}_{(m)} = v^I \bar{e}_{(m)}^{*I}$
$\sigma, \sigma_I, \sigma_{IJ}$	Scalar, vector and tensor perturbation of anisotropic stress	Eq. (2.29)
$\delta\hat{\tau}$	Fraction of 1st-order differential optical depth	Eq. (3.95)
$\delta x_e^{[I]}$	Fraction of 1st-order free electrons	$x_e^{[I]}/\bar{x}_e$
Θ	Temperature anisotropies	Eq. (4.5), (4.7)
Δ	Photon brightness	Eq. (2.75)
\tilde{S}_T, S_T	Source functions	Eq. (2.75), (2.78), (4.10), (4.11)
$\Delta_\ell(k)$	Transfer function	Eq. (2.82)
α	Deflection angle	Eq. (2.88)
$\psi(\hat{\mathbf{n}})$	Lensing potential	Eq. (2.88)
Ψ_W	Weyl potential	$(\Phi + \Psi)/2$

Table A.6 Quantities for EFEs and CMB photon

Symbol	Description	Equation
$G_{\mu\nu}$	Einstein tensor	Eq. (2.23)
$R_{\mu\nu}, R$	Ricci tensor and scalar	Eq. (2.24)
$\Gamma_{\alpha\beta}^{\mu}$	Christoffel symbols	Eq. (2.25)
$T_{\mu\nu}$	Stress-energy tensor	Eq. (2.26)
ρ	Energy density of fluid	Eq. (2.26)
\mathcal{P}	Pressure of fluid	Eq. (2.26)
u_{μ}	Fluid velocity	Eq. (2.26)
$\pi_{\mu\nu}$	Anisotropies stress	Eq. (2.26)
$\hat{\Pi}$	A quantity defined with $\ell = 2$ multipoles	Eq. (3.79)
Π		$\Pi = \hat{\Pi}/4$
$\omega_b^a{}_c$	Ricci rotation coefficients	Eq. (2.38)
$\mathcal{C}_1, \mathcal{C}_2, \mathcal{C}_3, \mathcal{C}_4, \mathcal{C}'_4$	Quadratic terms in 2nd-order scalar EFEs	Eq. (3.29), (3.30), (3.31), (3.32), (3.37)
$\mathcal{C}_{(1,\pm 1)}, \mathcal{C}_{(2,\pm 1)}, \mathcal{C}_{(2,\pm 2)}$	Quadratic terms in 2nd-order vector and tensor EFEs	Eq. (3.40), (3.41), (3.43)
\mathcal{L}	Liouville operator	Eq. (2.34)
$\mathcal{C}_{\mu\nu}$	Collision operator	Eq. (2.32)
\mathcal{C}^{δ}	Collision terms for continuity equation	Eq. (3.45)
$\mathcal{C}_{(m)}^v$	Collision terms for Euler equation	Eq. (2.56), (3.46), (3.47)
\mathcal{D}_{ab}	Residual collision operator	Eq. (5.6)
$\mathcal{P}_{\mu\nu}$	Screen-projected intensity matrix	Eq. (2.11)
\mathcal{I}	Photon intensity	Eq. (2.12)
$\mathcal{P}_{\mu\nu}$	Symmetric traceless polarization tensor	Eq. (2.12)
\hat{I}	Normalized energy-integrated photon intensity	Eq. (2.14)
$\hat{P}_{\mu\nu}$	Normalized energy-integrated polarization tensor	Eq. (2.15)
\hat{Q}, \hat{U}	Normalized energy-integrated Stokes' parameters	Eq. (2.18)
$\hat{\tau}$	Differential optical depth	Eq. (2.57)
n_e	Number density of electrons	
x_e	Fraction of free electrons	

Table A.7 Liouville-related notations

Symbol	Description	Equation
\mathcal{Q}_{ab}	Source terms for line of sight approach	Eq. (5.9)
\mathcal{T}	Time-ordering operator	
$\hat{\square}_{\hat{\mathbf{n}},r}$	Vector operator for lensing effect	Eq. (5.55) and (5.79)
$\hat{\diamond}_{\hat{\mathbf{n}},r}$	Vector operator for time-delay effect	Eq. (5.68)
$\hat{V}(\boldsymbol{\eta}, \hat{\mathbf{n}})$	Interaction operator for lensing effect	Eq. (5.56)
$\hat{V}_x(\boldsymbol{\eta}, \hat{\mathbf{n}})$	Interaction operator for time-delay effect	Eq. (5.69)
$\hat{V}_r(\boldsymbol{\eta}, \hat{\mathbf{n}})$	Interaction operator for redshift effect	Eq. (5.77)
$\hat{U}(\boldsymbol{\eta}_0, \tilde{\boldsymbol{\eta}}, \hat{\mathbf{n}})$	Evolution operator for lensing effect	Eq. (5.57)
$C_\ell^{\Psi^w}(\boldsymbol{\eta})$	Equal-time power spectrum of Weyl potential	Eq. (5.82)
$\mathcal{K}_i(\ell_1, \ell_2)$	Nested double integrals of lensing effect	Eq. (5.91)

Table A.8 Miscellaneous

Symbol	Description	Equation
Subscripts b, c, n, r	Denoting baryons, CDM, neutrinos and photons	
Subscripts 1, 2	Acting on a first-order perturbation X means $X_i = X(\mathbf{k}_i, \tau)$ for $i = 1, 2$	
Header bar ‘ – ’	Denoting zeroth order perturbations	
Header dot ‘ · ’	Partial derivative on conformal time	
L		$2L \equiv 2\ell + 1$
N_ℓ		Eq. (C.2)
$\mathcal{T}_{\mathbf{k}_1, \mathbf{k}_2}(\mathbf{k})$	Convolution operator	Eq. (3.24)
$s\mathcal{D}_{\ell m}^n, s\mathcal{T}_{\ell m}^n, s\mathcal{U}_{\ell m}^n$	The symbols used in second-order Boltzmann equations	End of Appendix C.3

Appendix B

Table of Cosmological Parameters

Parameter	Best fit
\bar{T}	2.7255 K
$\Omega_b h^2$	0.022032
$\Omega_c h^2$	0.12038
$\Omega_\nu h^2$	0.00064
n_s	0.9619
A_s	2.215×10^{-9}
H_0	$67.04 \text{ km s}^{-1} \text{ Mpc}^{-1}$
Y_p	0.247695
N_{eff}	3.046
w_0	-1
τ	0.0925
z_{re}	11.37
Δz_{re}	0.5

Table B.1 The best-fit cosmological parameters are listed based on the Planck+WP dataset in [3]. For the primordial tensor modes, parameters come from the BICEP2's data in [2] with $n_t = 0$ and $k_* = 0.05/\text{Mpc}$. The definitions of these parameters can be found in Table 1 of [3]. As mentioned in [9], the tension between Planck and Bicep due to the tensor mode is mild. Thus, we do not re-fit the cosmological parameters using the data from the Planck and BICEP2 together.

Appendix C

Spin-weighted Spherical Harmonics

C.1 Properties of Spin-weighted Spherical Harmonics

Spherical harmonics, which are used to decompose functions on the surface of a sphere, are essential tools for studying the CMB signals projected in the full sky. Any function ${}_s f$ depending on the direction $\hat{\mathbf{n}}$ can be expanded into multipoles of spin-weighted spherical harmonics

$${}_s f(\hat{\mathbf{n}}) = \sum_{\ell m} \frac{1}{N_\ell} {}_s f_{\ell m} {}_s Y_{\ell m}(\hat{\mathbf{n}}), \quad (\text{C.1})$$

where we have, by following the normal modes in [51],

$$N_\ell \equiv i^\ell \sqrt{\frac{2\ell+1}{4\pi}}, \quad (\text{C.2})$$

and the spin-weighted spherical harmonic ${}_s Y_{\ell m}(\hat{\mathbf{n}})$ is defined as

$${}_s Y_{\ell m}(\hat{\mathbf{n}}) = \sqrt{\frac{(\ell-s)!}{(\ell+s)!}} \bar{\partial}^s Y_{\ell m}(\hat{\mathbf{n}}), \quad 0 \leq s \leq \ell, \quad (\text{C.3})$$

$${}_s Y_{\ell m}(\hat{\mathbf{n}}) = \sqrt{\frac{(\ell+s)!}{(\ell-s)!}} (-1)^s \bar{\partial}^{-s} Y_{\ell m}(\hat{\mathbf{n}}), \quad -\ell \leq s \leq 0, \quad (\text{C.4})$$

with $|m|, |s| \leq \ell$, $\ell \geq 0$ (otherwise equal to zero) and the Laplace's spherical harmonics $Y_{\ell m}$. The raising ($\bar{\partial}$) and lowering (∂) operators are defined as

$$\bar{\partial}_s f(\hat{\mathbf{n}}) = -(\sin \theta)^s \left[\frac{\partial}{\partial \theta} + \frac{i}{\sin \theta} \frac{\partial}{\partial \phi} \right] (\sin \theta)^{-s} {}_s f(\hat{\mathbf{n}}), \quad (\text{C.5})$$

$$\partial_s f(\hat{\mathbf{n}}) = -(\sin \theta)^{-s} \left[\frac{\partial}{\partial \theta} - \frac{i}{\sin \theta} \frac{\partial}{\partial \phi} \right] (\sin \theta)^s {}_s f(\hat{\mathbf{n}}), \quad (\text{C.6})$$

for a spin- s function ${}_s f$. By acting the operators on the spin-weighted spherical harmonics, we obtain

$$\bar{\partial}_s Y_{\ell m} = \sqrt{(\ell - s)(\ell + s + 1)} {}_{s+1} Y_{\ell m}, \quad (\text{C.7})$$

$$\partial_s Y_{\ell m} = -\sqrt{(\ell + s)(\ell - s + 1)} {}_{s-1} Y_{\ell m}. \quad (\text{C.8})$$

Here, we align the z -axis with the zenith.

There are many useful properties of the spherical harmonics. For example, the orthonormality and completeness of the spin-weighted spherical harmonics are

$$\int d\hat{\mathbf{n}} {}_s Y_{\ell m}(\hat{\mathbf{n}}) {}_s Y_{\ell' m'}^*(\hat{\mathbf{n}}) = \delta_{\ell \ell'} \delta_{m m'}, \quad (\text{C.9})$$

$$\sum_{\ell m} {}_s Y_{\ell m}(\hat{\mathbf{n}}) {}_s Y_{\ell m}^*(\hat{\mathbf{n}}') = \delta(\cos \theta - \cos \theta') \delta(\phi - \phi'), \quad (\text{C.10})$$

where the complex conjugation of spherical harmonic is ${}_s Y_{\ell m}^*(\hat{\mathbf{n}}) = (-1)^{m+s} {}_{-s} Y_{\ell, -m}(\hat{\mathbf{n}})$. The Legendre polynomial of degree ℓ is related to the spin-0 spherical harmonics

$$P_\ell(\hat{\mathbf{n}} \cdot \hat{\mathbf{n}}') = \frac{4\pi}{2\ell + 1} \sum_{m=-\ell}^{\ell} Y_{\ell m}(\hat{\mathbf{n}}) Y_{\ell m}^*(\hat{\mathbf{n}}'). \quad (\text{C.11})$$

In particular, when $\hat{\mathbf{n}} = \hat{\mathbf{n}}'$, we have Unsold's theorem

$$\sum_{m=-\ell}^{\ell} Y_{\ell m}(\hat{\mathbf{n}}) Y_{\ell m}^*(\hat{\mathbf{n}}) = \frac{2\ell + 1}{4\pi}. \quad (\text{C.12})$$

C.2 Properties of Wigner 3-j Symbols

The integral of three spin-weighted spherical harmonics can be expressed as

$$\int d\hat{\mathbf{n}} {}_{s_1}Y_{\ell_1 m_1}(\hat{\mathbf{n}}) {}_{s_2}Y_{\ell_2 m_2}(\hat{\mathbf{n}}) {}_{s_3}Y_{\ell_3 m_3}(\hat{\mathbf{n}}) = \sqrt{\frac{(2\ell_1+1)(2\ell_2+1)(2\ell_3+1)}{4\pi}} \begin{pmatrix} \ell_1 & \ell_2 & \ell_3 \\ -s_1 & -s_2 & -s_3 \end{pmatrix} \begin{pmatrix} \ell_1 & \ell_2 & \ell_3 \\ m_1 & m_2 & m_3 \end{pmatrix}, \quad (\text{C.13})$$

where the brackets are the Wigner 3-j symbols. In spin-0 case, the integral is defined as the Gaunt coefficient

$$\mathcal{G}_{m_1 m_2 m_3}^{\ell_1 \ell_2 \ell_3} \equiv \int d\hat{\mathbf{n}} Y_{\ell_1 m_1}(\hat{\mathbf{n}}) Y_{\ell_2 m_2}(\hat{\mathbf{n}}) Y_{\ell_3 m_3}(\hat{\mathbf{n}}). \quad (\text{C.14})$$

Wigner 3-j symbols $\begin{pmatrix} \ell_1 & \ell_2 & \ell_3 \\ m_1 & m_2 & m_3 \end{pmatrix}$ are non-zero only when the following conditions are satisfied

$$m_1 + m_2 + m_3 = 0, \quad (\text{C.15})$$

$$\ell_1 + \ell_2 + \ell_3 = N, \quad (\text{C.16})$$

$$|\ell_1 - \ell_2| \leq \ell_3 \leq |\ell_1 + \ell_2|, \quad (\text{C.17})$$

where N is a positive integer. In case of $m_1 = m_2 = m_3 = 0$, the symbols are non-zero if $\ell_1 + \ell_2 + \ell_3$ is an even positive integer. Moreover, the Wigner 3-j symbols are related to Clebsch–Gordan coefficients by

$$\begin{pmatrix} \ell_1 & \ell_2 & \ell_3 \\ m_1 & m_2 & m_3 \end{pmatrix} = \frac{(-1)^{\ell_1 - \ell_2 - m_3}}{\sqrt{2\ell_3 + 1}} \langle \ell_1 m_1 \ell_2 m_2 | \ell_3 - m_3 \rangle. \quad (\text{C.18})$$

The Wigner 3-j symbols possess some symmetries which can be used to simplify the calculation of its coefficients. For example, it is invariant under an even permutation of its columns

$$\begin{pmatrix} \ell_1 & \ell_2 & \ell_3 \\ m_1 & m_2 & m_3 \end{pmatrix} = \begin{pmatrix} \ell_2 & \ell_3 & \ell_1 \\ m_2 & m_3 & m_1 \end{pmatrix} = \begin{pmatrix} \ell_3 & \ell_1 & \ell_2 \\ m_3 & m_1 & m_2 \end{pmatrix}. \quad (\text{C.19})$$

In contrast, there is a phase factor under an odd permutation of its columns

$$\begin{pmatrix} \ell_1 & \ell_2 & \ell_3 \\ m_1 & m_2 & m_3 \end{pmatrix} = (-1)^L \begin{pmatrix} \ell_2 & \ell_1 & \ell_3 \\ m_2 & m_1 & m_3 \end{pmatrix} = (-1)^L \begin{pmatrix} \ell_1 & \ell_3 & \ell_2 \\ m_1 & m_3 & m_2 \end{pmatrix}, \quad (\text{C.20})$$

where $L \equiv \ell_1 + \ell_2 + \ell_3$. Similarly, a phase factor appears when changing the signs of ms

$$\begin{pmatrix} \ell_1 & \ell_2 & \ell_3 \\ -m_1 & -m_2 & -m_3 \end{pmatrix} = (-1)^L \begin{pmatrix} \ell_1 & \ell_2 & \ell_3 \\ m_1 & m_2 & m_3 \end{pmatrix}. \quad (\text{C.21})$$

Furthermore, we have the following orthogonality relations

$$(2\ell + 1) \sum_{m_1 m_2} \begin{pmatrix} \ell_1 & \ell_2 & \ell \\ m_1 & m_2 & m \end{pmatrix} \begin{pmatrix} \ell_1 & \ell_2 & \ell' \\ m_1 & m_2 & m' \end{pmatrix} = \delta_{\ell\ell'} \delta_{mm'}, \quad (\text{C.22})$$

$$\sum_{\ell m} (2\ell + 1) \begin{pmatrix} \ell_1 & \ell_2 & \ell \\ m_1 & m_2 & m \end{pmatrix} \begin{pmatrix} \ell_1 & \ell_2 & \ell \\ m'_1 & m'_2 & m \end{pmatrix} = \delta_{m_1 m'_1} \delta_{m_2 m'_2}. \quad (\text{C.23})$$

In particular, we have

$$\sum_{m_1 m_2 m_3} \begin{pmatrix} \ell_1 & \ell_2 & \ell_3 \\ m_1 & m_2 & m_3 \end{pmatrix}^2 = 1. \quad (\text{C.24})$$

C.3 Decomposition of Spherical Harmonics

To perform the decomposition of spherical harmonics, it is more convenient to use another basis which is related to that of a Cartesian coordinate system by¹

$$\bar{\mathbf{e}}_{(0)} \equiv -\bar{\mathbf{e}}_z, \quad \bar{\mathbf{e}}_{(1)} \equiv \frac{1}{\sqrt{2}}(\bar{\mathbf{e}}_x + i\bar{\mathbf{e}}_y), \quad \bar{\mathbf{e}}_{(-1)} \equiv \frac{1}{\sqrt{2}}(-\bar{\mathbf{e}}_x + i\bar{\mathbf{e}}_y), \quad (\text{C.25})$$

where the overhead bars denote the flat background space-time². It can be shown that the bases obey the orthonormality

$$\sum_{I=1}^3 \bar{e}_{(m)}^I \bar{e}_{(m')}^{*I} = \delta_{mm'}, \quad \sum_{m=-1}^1 \bar{e}_{(m)}^I \bar{e}_{(m)}^{*J} = \delta_{IJ}, \quad (\text{C.26})$$

¹Our definition is the same as that in [83]. See also [80] with a different definition.

²In the CMB study, all these bases live on the background manifold which has a trivial metric δ_{IJ} under the Cartesian coordinate system.

where $\bar{e}_{(m)}^* = (-1)^m \bar{e}_{(-m)}$. Any 3-vector \mathbf{v} with spin-0 can then be decomposed into

$$\mathbf{v} = \sum_m v_{(m)} \bar{\mathbf{e}}_{(m)} = -\frac{iv}{N_1} \sum_{m=-1}^1 Y_{1,m}^*(\hat{\mathbf{v}}) \bar{\mathbf{e}}_{(m)}, \quad (\text{C.27})$$

where the components are

$$v_{(0)} = -v_z = -\frac{iv}{N_1} Y_{1,0}^*(\hat{\mathbf{v}}), \quad (\text{C.28})$$

$$v_{(1)} = \frac{1}{\sqrt{2}}(v_x - iv_y) = -\frac{iv}{N_1} Y_{1,1}^*(\hat{\mathbf{v}}), \quad (\text{C.29})$$

$$v_{(-1)} = -\frac{1}{\sqrt{2}}(v_x + iv_y) = -\frac{iv}{N_1} Y_{1,-1}^*(\hat{\mathbf{v}}), \quad (\text{C.30})$$

with $\mathbf{v} = v \hat{\mathbf{v}}$. Using Eq. (C.1) and Eq. (C.27), we can perform the decomposition of the spin-0 spherical harmonics with respect to $\hat{\mathbf{n}}$ such that

$$[\hat{\mathbf{n}}]_{\ell m} = -i\delta_{\ell 1} \bar{\mathbf{e}}_{(m)}^*, \quad (\text{C.31})$$

$$[\hat{\mathbf{n}} \cdot \mathbf{v}]_{\ell m} = -i\delta_{\ell 1} v_{(m)}. \quad (\text{C.32})$$

Now, we consider expanding a product of two $\hat{\mathbf{n}}$ -dependent functions into spherical harmonics, e.g. ${}_s h(\hat{\mathbf{n}}) = {}_{s_1} f(\hat{\mathbf{n}}) {}_{s_2} g(\hat{\mathbf{n}})$ with $s = s_1 + s_2$. Using Eq. (C.1) and Eq. (C.14), we obtain the multipoles ${}_s h_{\ell m}$ as

$$\sum_{\ell_1 m_1} \sum_{\ell_2 m_2} i^{-\ell_1 - \ell_2 + \ell} (-1)^{m+s} (2\ell + 1) {}_{s_1} f_{\ell_1 m_1} {}_{s_2} g_{\ell_2 m_2} \begin{pmatrix} \ell_1 & \ell_2 & \ell \\ -s_1 & -s_2 & s \end{pmatrix} \begin{pmatrix} \ell_1 & \ell_2 & \ell \\ m_1 & m_2 & -m \end{pmatrix}. \quad (\text{C.33})$$

For example, if ${}_{s_1} f(\hat{\mathbf{n}}) = {}_{s_2} g(\hat{\mathbf{n}}) = \hat{\mathbf{n}}$, we have³

$$[\hat{\mathbf{n}}\hat{\mathbf{n}}]_{\ell m} = \begin{cases} \frac{1}{3} \sum_{m_1} \bar{\mathbf{e}}_{(m_1)} \bar{\mathbf{e}}_{(m_1)}^*, & \text{if } \ell = 0, \\ -(-1)^m \sum_{m_1 m_2} \sqrt{\frac{10}{3}} \begin{pmatrix} 1 & 1 & 2 \\ m_1 & m_2 & -m \end{pmatrix} \bar{\mathbf{e}}_{(m_1)}^* \bar{\mathbf{e}}_{(m_2)}^*, & \text{if } \ell = 2. \end{cases} \quad (\text{C.34})$$

³This decomposition is used when we derive the evolution equations of 2nd-order scalar, vector and tensor perturbations from the EFEs in Section 3.1.2.

It obeys the orthogonality that

$$\sum_{ij} [n^i n^j]_{2m} [n^i n^j]_{2m'}^* = \frac{2}{3} \delta_{mm'}. \quad (\text{C.35})$$

Moreover, if ${}_s f(\hat{\mathbf{n}}) = \hat{\mathbf{n}} \cdot \mathbf{v}$, we obtain⁴

$${}_s [(\hat{\mathbf{n}} \cdot \mathbf{v}) {}_s g(\hat{\mathbf{n}})]_{\ell m} = \begin{cases} -i \sum_{m_1} {}_s \mathcal{D}_{\ell m}^{m_1} v_{(m_1)} {}_s g_{\ell-1, m-m_1}, & \text{if } \ell_2 = \ell - 1, \\ -\sum_{m_1} {}_s \mathcal{T}_{\ell m}^{m_1} v_{(m_1)} {}_s g_{\ell, m-m_1}, & \text{if } \ell_2 = \ell, \\ i \sum_{m_1} {}_s \mathcal{U}_{\ell m}^{m_1} v_{(m_1)} {}_s g_{\ell+1, m-m_1}, & \text{if } \ell_2 = \ell + 1, \end{cases} \quad (\text{C.36})$$

where the coefficients are defined as

$${}_s \mathcal{D}_{\ell m}^0 = \frac{1}{\ell(2\ell-1)} \sqrt{(\ell^2 - m^2)(\ell^2 - s^2)}, \quad (\text{C.37})$$

$${}_s \mathcal{D}_{\ell m}^{\pm 1} = \frac{1}{\ell(2\ell-1)} \sqrt{\frac{(\ell \pm m)(\ell \pm m - 1)(\ell^2 - s^2)}{2}}, \quad (\text{C.38})$$

$${}_s \mathcal{T}_{\ell m}^0 = -\frac{ms}{\ell(\ell+1)}, \quad (\text{C.39})$$

$${}_s \mathcal{T}_{\ell m}^{\pm 1} = \pm \frac{s}{\ell(\ell+1)} \sqrt{\frac{(\ell \pm m)(\ell \mp m + 1)}{2}}, \quad (\text{C.40})$$

$${}_s \mathcal{U}_{\ell m}^0 = \frac{1}{(\ell+1)(2\ell+3)} \sqrt{[(\ell+1)^2 - m^2][(\ell+1)^2 - s^2]}, \quad (\text{C.41})$$

$${}_s \mathcal{U}_{\ell m}^{\pm 1} = \frac{1}{(\ell+1)(2\ell+3)} \sqrt{\frac{(\ell \mp m + 1)(\ell \mp m + 2)[(\ell+1)^2 - s^2]}{2}}, \quad (\text{C.42})$$

⁴This is useful when we derive the 2nd-order Boltzmann equation with ${}_s g(\hat{\mathbf{n}})$ as the photon intensity $I(\hat{\mathbf{n}})$ and the Stokes parameters $(Q \pm iU)(\hat{\mathbf{n}})$.

Appendix D

Perturbations of Tetrads and Ricci Rotation Coefficients

In this appendix, we calculate the perturbations of tetrads and Ricci rotation coefficients up to 2nd order. We will fix to the Newtonian gauge for 1st-order and 2nd-order perturbations and neglect the 1st-order vector and tensor perturbations.

D.1 Perturbations of Tetrads

Using Eq. (2.4), we can calculate the coefficients ${}_{\xi}X_{ab}$ order by order, i.e.

$$\begin{aligned}\eta_{ab} &= \lim_{\lambda \rightarrow 1} \phi_{\lambda, \xi}^* (\eta_{ab}) = \lim_{\lambda \rightarrow 1} \phi_{\lambda, \xi}^* (e_a^A) \phi_{\lambda, \xi}^* (e_b^B) \phi_{\lambda, \xi}^* (g_{AB}) \\ &= {}_{\xi}X_a^c \bar{e}_c^A \xi X_b^d \bar{e}_d^B \xi g_{AB},\end{aligned}\tag{D.1}$$

where ${}_{\xi}g_{AB}$ is the pulled-back physical metric on the background manifold, e.g. Eq. (2.1). Similarly, the coefficients ${}_{\xi}Y_{ab}$ can be solved by η^{ab} . We remark that the upper and lower indices of the coefficients are obtained by η^{ab} and η_{ab} .

There remain residual freedoms in determining the anti-symmetric part of the coefficients ${}_{\xi}X_{ab}$ and ${}_{\xi}Y_{ab}$ due to boost and rotation. In particular, we align ${}_{\xi}\hat{\mathbf{e}}^0$ with $d\eta$, i.e. ${}_{\xi}Y_{i0} = 0$. Physically, it means that the velocity of the chosen observer is orthonormal to the hypersurfaces of constant time. This fixes the boost freedom such that ${}_{\xi}Y_{[i0]} = -{}_{\xi}Y_{[0i]} = -{}_{\xi}Y_{(i0)}$ with (...) and [...] denoting the symmetric and anti-symmetric parts. On the other hand, the rotation freedom can be fixed by setting ${}_{\xi}Y_{[ij]} = 0$. With these conditions, we can determine

the coefficients uniquely. We can find that¹, for 1st order,

$$\xi X_0^{i[\text{I}]} = -\xi Y_0^{i[\text{I}]} = 0, \quad (\text{D.2})$$

$$\xi X_0^{0[\text{I}]} = -\xi Y_0^{0[\text{I}]} = -\Phi, \quad (\text{D.3})$$

$$\xi X_i^{0[\text{I}]} = -\xi Y_i^{0[\text{I}]} = 0, \quad (\text{D.4})$$

$$\xi X_j^{i[\text{I}]} = -\xi Y_j^{i[\text{I}]} = \Psi \delta^I_J, \quad (\text{D.5})$$

and for 2nd order,

$$\xi X_0^{i[\text{II}]} = -\xi Y_0^{i[\text{II}]} = 0, \quad (\text{D.6})$$

$$\xi X_0^{0[\text{II}]} = -\Phi^{[\text{II}]} + 3\Phi^2, \quad (\text{D.7})$$

$$\xi Y_0^{0[\text{II}]} = \Phi^{[\text{II}]} - \Phi^2, \quad (\text{D.8})$$

$$\xi X_i^{0[\text{II}]} = \mathcal{B}_I^{[\text{II}]}, \quad (\text{D.9})$$

$$\xi Y_i^{0[\text{II}]} = -\mathcal{B}_I^{[\text{II}]}, \quad (\text{D.10})$$

$$\xi X_j^{i[\text{II}]} = \Psi^{[\text{II}]} \delta^I_J - \mathcal{H}^I_J^{[\text{II}]} + 3\Psi^2 \delta^I_J, \quad (\text{D.11})$$

$$\xi Y_j^{i[\text{II}]} = -\Psi^{[\text{II}]} \delta^I_J + \mathcal{H}^I_J^{[\text{II}]} - \Psi^2 \delta^I_J. \quad (\text{D.12})$$

D.2 Perturbations of Ricci Rotation Coefficients

Using the definition of the Ricci rotation coefficients in Eq. (2.38), we can show that the coefficients are antisymmetric in their last two indices, i.e. $\omega_{abc} = -\omega_{acb}$ ². This implies that, for any order,

$$\omega_{000} = \omega_{i00} = 0. \quad (\text{D.13})$$

In background order, all the coefficients are zero except

$$\bar{\omega}_{ij0} = -\bar{\omega}_{i0j} = \frac{\mathcal{H}}{a} \delta_{ij}. \quad (\text{D.14})$$

¹We omit the the superscripts [I] denoting 1st-order perturbations.

²Here, the Ricci rotation coefficients are expressed in tetrad basis. Hence, the indices can be raised and lowered by multiplying with the Minkowski metric η^{ab} and η_{ab} respectively.

In 1st order, the non-zero coefficients are

$$\omega_{0i0}^{[\text{I}]} = -\omega_{00i}^{[\text{I}]} = \frac{1}{a} \partial_I \Phi, \quad (\text{D.15})$$

$$\omega_{i0j}^{[\text{I}]} = -\omega_{ij0}^{[\text{I}]} = \frac{1}{a} (\mathcal{H}\Phi + \dot{\Psi}) \delta_{IJ}, \quad (\text{D.16})$$

$$\omega_{ijk}^{[\text{I}]} = -\omega_{ikj}^{[\text{I}]} = \frac{1}{a} (\partial_J \Psi \delta_{IK} - \partial_K \Psi \delta_{IJ}). \quad (\text{D.17})$$

For 2nd-order Liouville terms, only the following coefficients are used

$$\omega_{0i0}^{[\text{III}]} = -\omega_{00i}^{[\text{III}]} = \frac{1}{a} (\partial_I \Phi^{[\text{III}]} - 4\Phi \partial_I \Phi + 2\Psi \partial_I \Phi), \quad (\text{D.18})$$

$$\omega_{i0j}^{[\text{III}]} = -\omega_{ij0}^{[\text{III}]} = \frac{1}{a} \left[\frac{1}{2} (\partial_I \mathcal{B}_J^{[\text{III}]} + \partial_J \mathcal{B}_I^{[\text{III}]}) - \mathcal{H}_{IJ}^{[\text{III}]} + (\dot{\Psi}^{[\text{III}]} + \mathcal{H}\Phi^{[\text{III}]}) \delta_{IJ} \right. \\ \left. - 3\mathcal{H}\Phi^2 \delta_{IJ} - 2\Phi \dot{\Psi} \delta_{IJ} + 4\Psi \dot{\Psi} \delta_{IJ} \right]. \quad (\text{D.19})$$

